The Study of Heavy Quark Production in High E_T Photoproduction at HERA using the ZEUS Detector.

Matthew Wing

University College London

January 1999

Thesis submitted in fulfillment of the
requirements for the degree of Doctor of Philosophy
in Elementary Particle Physics.

Abstract

The production of heavy quarks has been studied in dijet photoproduction at HERA. Two high transverse energy jets provide a hard scale as well as the quark mass itself. Using data collected by the ZEUS detector during 1996 and 1997 with a total luminosity of 36.9 pb^{-1}, we have performed two analyses to study heavy quark production. Firstly, we have considered decays of the $D^*(2010)$ meson in dijet events and measured the cross-section, $d\sigma/dx_\gamma^{\rm obs}$, where $x_\gamma^{\rm obs}$ is the fraction of the photon energy contributing to the two highest transverse energy jets. On comparison of the distribution with the predictions of Monte Carlo simulations, the component of *resolved* photon processes needed to describe the data is 43$\pm$5(*stat.*)%. Secondly, we have measured the same cross-section for the inclusive decays of quarks to electrons in the final state in a similar kinematic region. For this cross-section a significant contribution of resolved processes, equal to 29$\pm$5(*stat.*)%, was also required in the Monte Carlo to describe the data. Furthermore, to analyse the contribution of beauty quarks in the kinematic region, the cross-section, $d\sigma/dp_T^{rel}$, was measured, where p_T^{rel} is the momentum of the electron transverse to the axis of the jet which the electron is closest to. On comparison of the data with Monte Carlo predictions, the component from decays of beauty quarks required to describe the cross-section was $15.6 \pm 4.2(stat.)^{+12.9}_{-7.0}(syst.)$%. Therefore, the amount of beauty measured compared to the Monte Carlo is, $1.3 \times$ MC $<$ beauty $<$ $4.9 \times$ MC, in the one sigma limit. The 95% confidence level upper limit is, beauty $<$ $6.5 \times$ MC. In this thesis, we therefore obtain the first indication of *open beauty* production at ZEUS.

To Anke and My Parents

Outline

Two analyses of heavy quark production at HERA using 1996 and 1997 data are presented in this thesis. Chapter 1 briefly discusses the HERA machine and ZEUS detector with more detail given to specific components relevant to these analyses. Chapter 2 starts with a general resumé of the current understanding of QCD leading on to more detail about photoprodcution processes. Chapter 3 then discusses theoretical aspects and experimental results in heavy quark production. In Chapter 4 the reconstruction of the events is detailed and in Chapter 5 the Monte Carlo programs and samples used are discussed. In Chapter 6, the first analysis, the tagging of D^* mesons in dijet events is described. This analysis was performed as a second analysis in which the general method was already known. Chapters 7 and 8 form the major part of the thesis as it is the most significant work of this doctorate, defining the analysis described. Chapter 7 discusses the general method and signal extraction procedure, whilst Chapter 8 details the correction procedure and results and discusses the physics implications of the results. The thesis is summarised in Chapter 9.

Contents

List of Figures

List of Tables

Chapter 1

HERA and the ZEUS detector

1.1 The HERA Accelerator

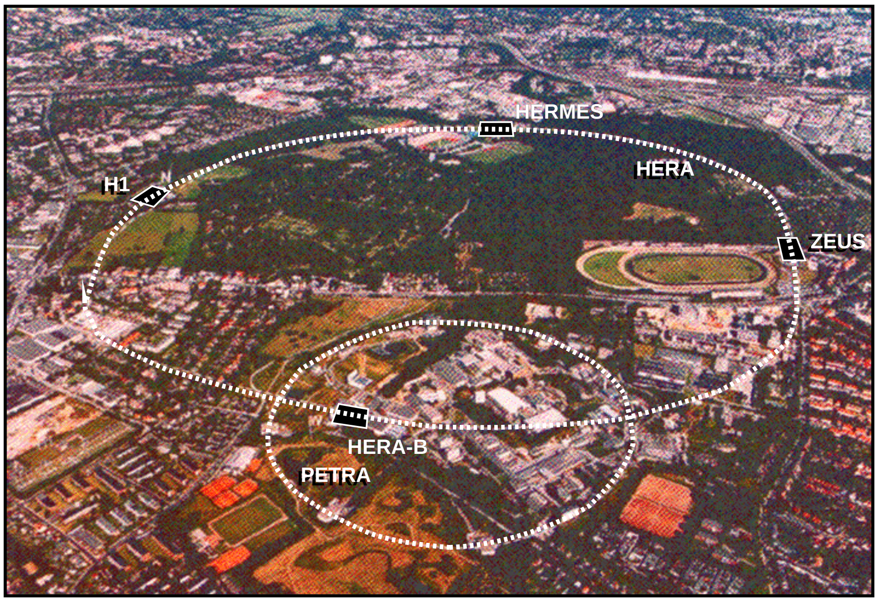

Figure 1.1: *The HERA collider enclosing the Volkspark in Hamburg, Germany shown with the pre-accelerator, PETRA and the four experiments.*

The Hadron Elektron Ring Anlage (HERA), the first lepton-proton collider, was constructed by Deutsches Elektronen-SYnchrotron (DESY). It is located under the Volkspark in Hamburg, Germany, enclosing the main DESY site (see Figure 1.1). The 6.34 km long accelerator was designed to collide 820 GeV protons with 30 GeV electrons, yielding a centre of mass energy, $\sqrt{s} = 314$ GeV. The two general purpose experiments, H1 and ZEUS, are located in the north and south halls. The east and west halls are now occupied by the HERMES and HERA-B collaborations respectively, which are both fixed target experiments. The HERMES collaboration uses an electron beam to investigate the origin of the spin of the nucleon. HERA-B uses a proton beam and is designed for studies of $\mathcal{C}P$ violation.

HERA has been colliding protons and positrons between 1994 and 1997 due to the short lifetime achieved with electrons. Positrons of energy, 27.52 GeV, slightly below the design value, are currently used, yielding a centre of mass energy, $\sqrt{s} \sim 300$ GeV. Electrons are now being used for the 1998 running period. The HERA history is shown in Table 1.1 where the colliding particles and the luminosity delivered by the HERA machine are displayed.

Year	colliding particles	HERA delivered $\mathcal{L}$
1992	e^-P (26.7 GeV, 820 GeV)	33 nb^{-1}
1993	e^-P (26.7 GeV, 820 GeV)	1.1 pb^{-1}
1994	e^-/e^+P (27.5 GeV, 820 GeV)	1.1/5.1 pb^{-1}
1995	e^+P (27.5 GeV, 820 GeV)	12.3 pb^{-1}
1996	e^+P (27.5 GeV, 820 GeV)	17.2 pb^{-1}
1997	e^+P (27.5 GeV, 820 GeV)	36.4 pb^{-1}
1998	e^-P (27.5 GeV, 920 GeV)	8.1 pb^{-1}

Table 1.1: *History of HERA running.*

1.1.1 HERA Injection System

Figure 1.2 shows the HERA injection system which is done in two stages; the positron and proton acceleration.

The proton acceleration is initiated by accelerating H^- ions to 50 MeV in the proton LINear ACcelerator (LINAC). These then enter the DESY III storage ring, which yields protons by stripping off the electrons. This is filled with 11 bunches having a 96 ns bunch spacing, the same as in HERA, and accelerated up to 7.5 GeV. Acceleration of up to 70 bunches of 40 GeV protons is achieved in the PETRA ring. Passage of the protons to HERA is then performed, the whole process being repeated twice, thereby achieving 210 bunches of 820 GeV protons with a lifetime of a few days. The HERA proton storage ring uses superconducting magnets operating at approximately 4 K, producing a magnetic field of about 4.7 T.

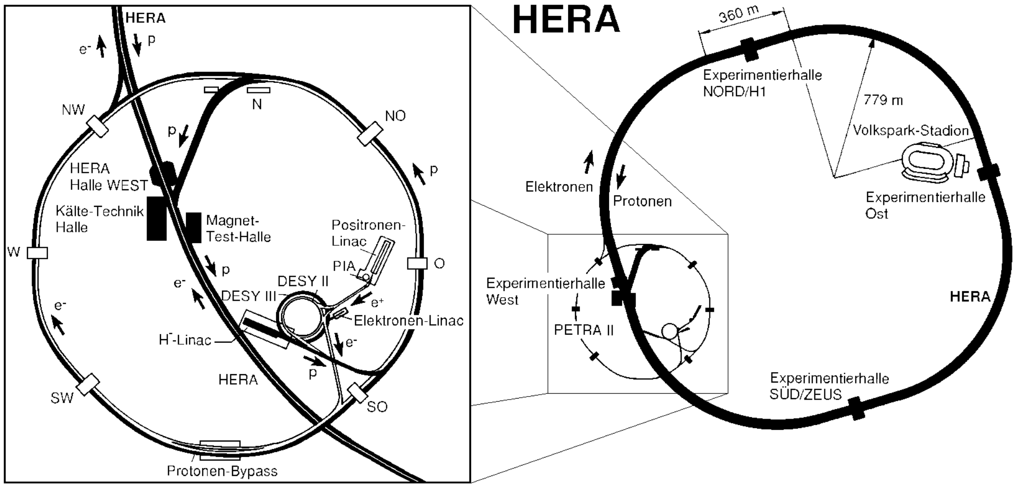

Figure 1.2: *Schematic view of the HERA collider, four experimental halls and the pre-accelerator ring with the injection system enlarged.*

Positron formation starts in the LINAC II and LINAC III machines where they are accelerated to 220 MeV and 450 MeV respectively. Passage into the DESY II ring allows acceleration of the positrons to 7.5 GeV. After transfer to PETRA II, 70 bunches at a spacing of 96 ns reach an energy of 14 GeV. Finally 210 bunches of 27.52 GeV positrons with a lifetime of about 8 hours exist in the HERA machine. The separate HERA storage ring for positrons operates at room temperature using normal conducting magnets.

1.2 The ZEUS Detector

In this section, an overview of the ZEUS detector will be given, followed, in the subsequent sections, by more detailed descriptions of components relevant to this thesis. For a more complete description of the ZEUS detector, see [1].

The ZEUS coordinate system is referenced from zero at the interaction point having the proton beam direction defining the z-axis. The x-axis is perpendicular to the beam direction pointing towards the centre of the ring and the y-axis upwards. The proton beam direction therefore defines the polar angle, $\theta = 0°$ and low values of polar angle are referred to as the forward direction, with $\theta = 180°$ being the extreme of the rear direction. The azimuthal angle is then defined with respect to the x-axis. Of importance in understanding measurements at ZEUS is knowledge of the definition of pseudorapidity, $\eta = -\log(tan(\theta/2))$.

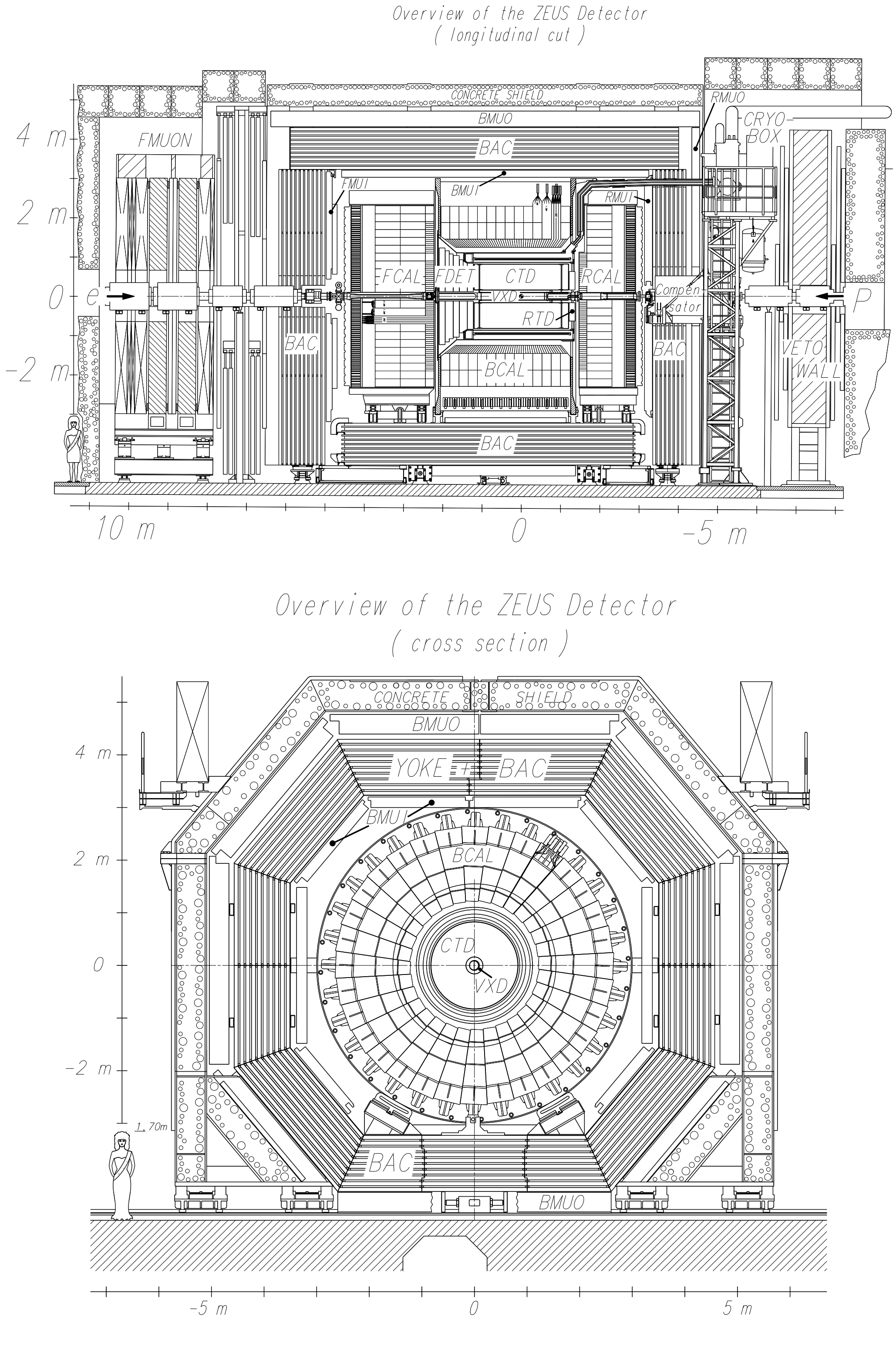

Figure 1.3: *Cross-sections of the ZEUS detector, shown along (top) and perpendicular (bottom) to the beam direction.*

Figure 1.3 shows two cross-sections through the ZEUS detector; in the zy-plane (along the beam direction) and in the xy-plane (perpendicular to the beam direction). This displays a schematic layout of the components within the detector. As can be seen in Figure 1.3, the detector is almost hermetic, with just the beam pipes preventing it from having 4π coverage.

Starting from the interaction point and moving radially outwards, the ZEUS detector consists of charged particle tracking detectors surrounding the beampipe. From Figure 1.3, we see that the innermost section is the VerteX Detector (VXD). However, this was removed at the end of 1995 so will not be discussed further. The innermost component is now the Central Tracking Detector (CTD) which is surrounded by a superconducting magnet providing a field of 1.43 T. The CTD is a central component for this analysis, providing the most tracking information for ZEUS, and so will be discussed in more detail in Section 1.3. At both ends of the CTD there are the Forward and Rear Tracking Detectors (FTD and RTD) which provide additional tracking and particle identification information. The final tracking detector is the Small angle Rear Tracking Detector (SRTD) which improves the position resolution for particles, particularly used for the scattered positron, in the rear direction. All the tracking components combined provide an angular acceptance of $7.5^\circ < \theta < 170^\circ$ for charged particles.

Immediately, outside the superconducting magnet lies the ZEUS calorimetry. The calorimeter is a high resolution Uranium CALorimeter (UCAL) and is divided into three sections; the Forward CALorimeter (FCAL), Barrel CALorimeter (BCAL) and Rear CALorimeter (RCAL). Allied to the UCAL, there is a further component of calorimetry; the BAcking Calorimeter (BAC), which provides an energy measurement of late showering particles. The calorimetry will also be discussed in more detail (Section 1.4) as it is important for the measurement of jets and cell clusters, which are used to aid electron detection. Between layers of the RCAL is a Hadron Electron Separator (HES) used for distinguishing between electromagnetic and hadronic objects.

Surrounding the UCAL and before the iron yoke are muon identification chambers (FMUI, BMUI and RMUI). Further muon chambers (FMUON, BMUON and RMUON) surround the iron yoke.

In the rear direction at $z = -315$ cm is the C5 counter, a lead scintillator around the beampipe which monitors synchrotron radiation and timing of the bunches.

Further to the rear is the VETO wall at $z = -750$ cm which rejects beam related background.

Further in the direction of the electron beam, two lead scintillators are located at $z = -34$ m and $z = -104$ m which provide ZEUS with its luminosity measurement and tagged photoproduction events (photoproduction is covered in Chapter 2). The luminosity measurement will also be discussed in more detail near the end of this chapter.

1.3 The Central Tracking Detector (CTD)

The CTD [2] is a large volume cylindrical gas container with an inner and outer radius of 18.2 cm and 79.4 cm respectively and a length of 205 cm. The chamber was developed around the use of an argon (Ar), ethane (C_2H_6) mixture of Ar:C_2H_6 = 0.5 : 0.5 bubbled through ethanol or with carbon dioxide also included; Ar:CO_2:C_2H_6 = 0.85:0.13:0.02, also bubbled through ethanol. Both mixtures have similar properties of gain, drift velocity and Lorentz angle, the former offering better precision and the latter easier safety precautions and protection against whisker growth. For the last few years of running, the gas has been maintained at an approximate ratio; Ar:CO_2:C_2H_6 = 0.85:0.05:0.1 at near atmospheric pressure.

Of the total angular acceptance provided by the tracking detectors mentioned previously, the CTD provides a large portion of this angular coverage; $15° < \theta < 164°$. It provides high precision measurements of the position and momentum of charged tracks and particle identification through a measurement of ionisation energy loss, dE/dx.

The wire chamber consists of nine superlayers containing cells with eight sense wires per cell; see Figure 1.4. The odd numbered superlayers have wires parallel to the chamber axis; so-called axial layers, whereas the even numbered superlayers are at a small stereo angle ($\sim \pm 5°$), thereby providing good z position measurement. The first three axial layers are also equipped with a z-by-timing system for trigger purposes. This determines the z position of a hit by considering pulse arrival times at each end of the chamber. Each cell containing the eight sense wires has a surface field controlling the gas gain of the signal. The potential ensures a Lorentz angle of 45° controlling the drift electrons to follow radially transverse paths. The drift paths can be seen in Figure 1.4. Ionised electrons (caused by the passage of a charged particle) shower close to the sense wires, the positive ions being repelled and drifting towards the negative field wires, thereby giving a pulse which is measured and recorded via an electronic read-out.

The nominal resolution for full length tracks in the CTD is 180μm in $r-\phi$ and for tracks which have passed through at least three superlayers is given by, $\sigma(p_T)/p_T \approx 0.016 \oplus 0.005 p_T$. The momentum resolution will be discussed in Chapter 7.

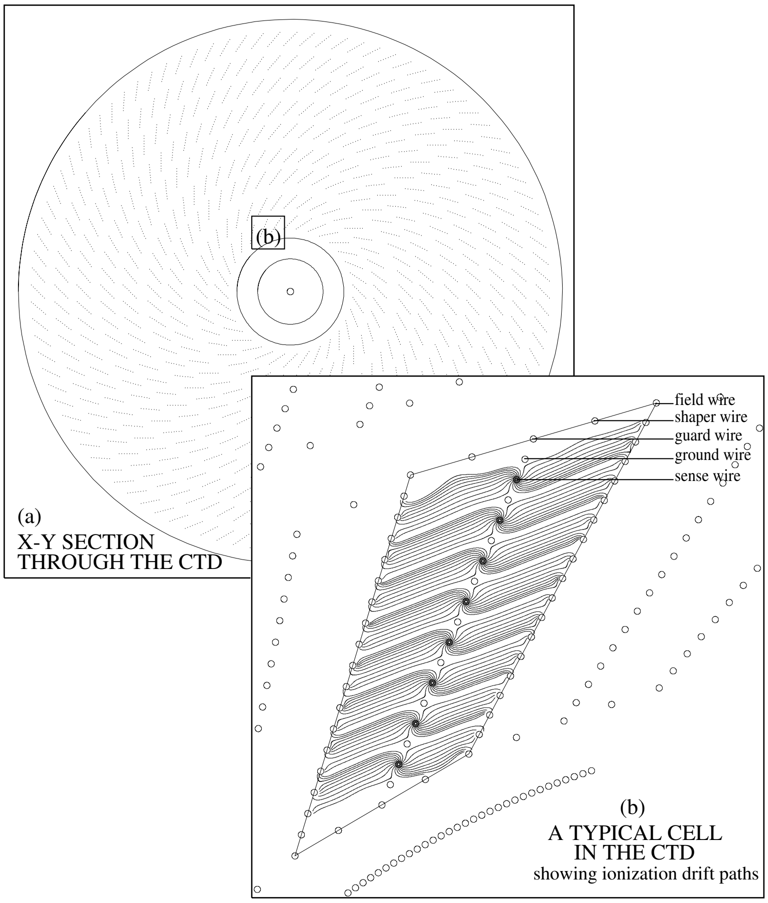

Figure 1.4: *(a) $r-\phi$ cross-section through the CTD, showing the nine superlayers. (b) A representation of a single cell.*

1.3.1 Track Reconstruction

A detailed description of track reconstruction can be found in [3], but is here briefly described.

Hits from the outer axial superlayers are combined to form a "seed", which is extrapolated back to the vertex. As the procedure of extrapolation occurs, more hits are gathered thereby increasing the precision. This pattern recognition procedure avoids bad parts of the CTD. Where the extrapolation is long, only the innermost superlayers are used as there is the least curvature from the magnetic field. This ensures a quality of track, reducing the incidence of split tracks.

The pattern recognition procedure is further refined to choose quality tracks which are fitted to a helix model. These tracks are then classified as VCTRHL tracks and are not required to have come from the vertex. However, in this thesis, we require the tracks to have come from the vertex, so we choose tracks from the VCTPAR table which are tracks from the primary vertex found by minimizing a fit to a subset of tracks.

1.3.2 Determination of dE/dx

The electronic read-out which records the pulse size from ionised electrons is the 8 bit $r-\phi$ Flash Analogue-to-Digital Converter (FADC), which is connected to all sense wires. The pulse height is sampled every 9.6 ns, digitised and stored, in order to be analysed by the second level trigger. Data accepted by the first level trigger is analysed by searching for "pulse trains" which are 9.6 ns bins of pulses from the passage of charged particles. Each pulse is then further analysed to achieve a pulse height for a given wire in FADC counts as displayed in Figure 1.5. Due to limitations of the read-out with 8 bits, there exists saturation in which the value of dE/dx exceeds that allowed. This leads to the large spike as seen in Figure 1.5, where values above 200 are considered saturated. A mean value of dE/dx is found from the pulse heights by calculating the "truncated mean", which removes the

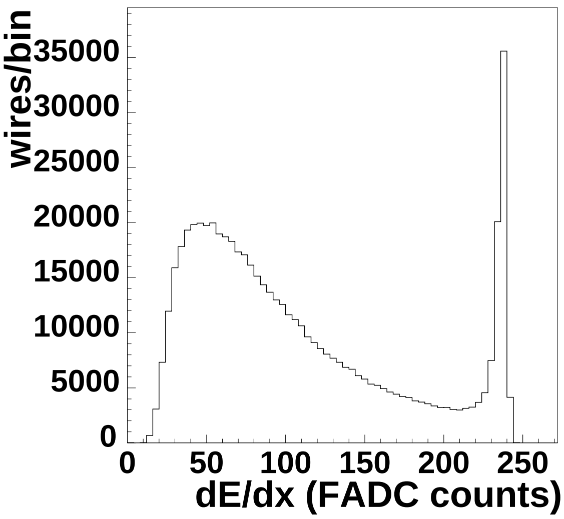

Figure 1.5: *Typical dE/dx pulse for a low momentum pion exhibiting the Landau shape and saturation at high dE/dx.*

use of saturated values. The calculation of the truncated mean will be returned to later.

Before a calculation of the mean dE/dx can be made, a correction procedure is first performed to remove any dependence on trajectory or detector response [4]. The raw pulse size of the i^{th} FADC hit is P_i. The normalised pulse size, P_i', is then given by,

$$P_i' = \prod_{\alpha} c_{i_\alpha} P_i,$$

where c_{i_α} are the empirical correction factors applied. Corrections are applied for the following;

- Polar angle, θ; this is a path length correction.
- The relative gain of the sense wires.
- The angle ψ', between the azimuthal angle ϕ_i and the planar drift measurement axis. This provides a correction for differences between positive and negative tracks being particularly important at low momentum.
- The local Lorentz angle.
- The hit position, z_i.
- The drift distance.

Distorted pulse size measurements can also be rejected if;

- The trajectory is nearly parallel to the measurement plane.
- The drift distance is near a cell boundary.
- Successive hits are too close together.

After this correction procedure, N hits remain, N_s of which are saturated hits. The N hits are then ordered by size and the lowest 10% and highest 30% are rejected, by way of truncation, leaving N_{used} hits. The number of hits then used in the calculation of the mean is $N_{used} - N_{sat}$, where N_{sat} are the remaining saturated hits. To perform the calculation, at least 4 hits are required and the mean is given by,

$$< dE/dx >= \sum_i P'_i/N_{used},$$

when $N_{sat} = 0$. When $N_{sat} > 0$, then a "variable" truncated mean is used [5] and the mean corrected back to the 10-70% "fixed" truncated mean. The average dE/dx is then given by,

$$< dE/dx >= \frac{F(0.7)}{F(R)} \sum_i \frac{P'_i}{N_{used} - N_{sat}},$$

where,

$$\begin{aligned} F(x) &= 26.95 + 30.92x + 55.685x^2 - 100.4x^3 + 71.508x^4, \\ R &= (N - N_s)/N. \end{aligned}$$

We are then provided with a reconstructed dE/dx value (in FADC counts) to be used in particle identification. An offline correction procedure to further refine the ionisation energy loss measurement will be discussed later in Chapter 7.

1.4 ZEUS Calorimetry

The ZEUS calorimeter [6] is a high resolution compensating calorimeter essential in this thesis for the reconstruction of jets and clusters of cells. In this thesis, the full reconstruction of jets is performed using the calorimeter cells. Clusters of cells are also used as an aid for the identification of electrons from semi-leptonic decays of heavy quarks.

As was said previously, the calorimeter is a *compensating* calorimeter, which implies the response of the calorimeter to electromagnetic and hadronic showers of the same energy should be the same. Typical showering can be seen in Figure 1.6. There were five main priorities for ZEUS with respect to the calorimeter, the most important being its hermiticity. The solid angular coverage is 99.7% of the possible 4π, the first priority therefore being achieved. The energy resolution hoped for was also achieved, being,

$$\frac{\sigma(E)}{E} = \frac{35\%}{\sqrt{E}} \oplus 2\%,$$

for hadrons, and

$$\frac{\sigma(E)}{E} = \frac{18\%}{\sqrt{E}} \oplus 1\%,$$

for electrons where the energy, E, is measured in GeV. The calibration of absolute energy scale is 1% with that between different sections being slightly more. Good jet separation is essential for this thesis, which heavily relies on jets. The hadron-electron separation is also good, although for low energy electrons, we require more information than just the calorimeter provides.

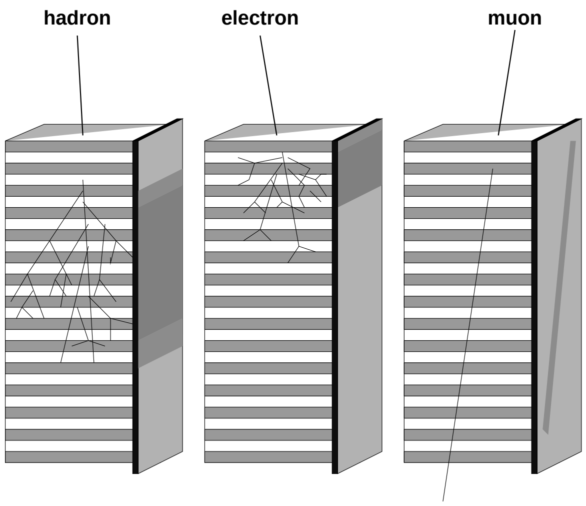

Figure 1.6: *Typical showering for hadronic, electromagnetic and muonic matter in the ZEUS calorimeter.*

The almost total solid angular coverage is achieved by three subsections of the calorimeter, the FCAL, BCAL and RCAL, which provide the coverage (in polar angle and pseudorapidity) shown in Table 1.2.

	θ range	η range
FCAL	$2.2^\circ \rightarrow 39.9^\circ$	$4.0 \rightarrow 1.0$
BCAL	$36.7^\circ \rightarrow 129.1^\circ$	$1.1 \rightarrow -0.74$
RCAL	$128.1^\circ \rightarrow 176.5^\circ$	$-0.72 \rightarrow -3.5$

Table 1.2: *Angular and pseudorapidity acceptance for the three sections of the calorimeter.*

Each calorimeter section consists of modules; vertical for the FCAL and RCAL, and radial for the BCAL, each consisiting of towers. These can be further subdivided into electromagnetic (EMC) and hadronic (HAC) sections. Each HAC cell is approximately 20×20 cm and each EMC cell is approximately 5×20 cm. A typical FCAL module with EMC and HAC divisions can be seen in Figure 1.7.

The EMC is the inner section of the tower, with two hadronic sections (HAC1 and HAC2) outside this. The alternating layers of Depleted Uranium (DU) (providing absorption and hence equal electromagnetic and hadronic response) and scintillator (for allowing readout) can also be seen. The unequal response is due to hadronic showers producing fewer photons than electromagnetic showers for a particle of the same energy. The uranium, therefore, acts as a compensator by absorbing neutrons and emitting photons which the scintillator can then detect. By choosing a suitable thickness of uranium, the same number of photons are produced for hadronic and electromagnetic showers of the same energy. The readout is performed by two photomultipliers (coupled to the scintillator by wavelength shifters) per cell; the pair ensuring the measurement to be independent of the impact point of the particles.

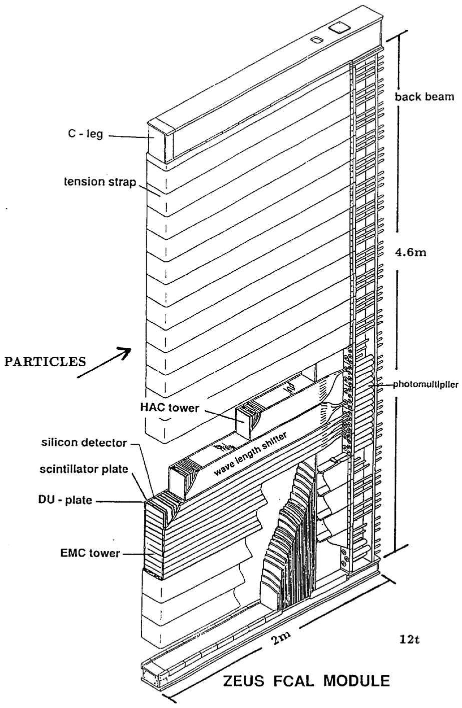

Figure 1.7: *Cut-away view of an FCAL module.*

1.4.1 Island Finding

Consideration of cell clusters can and has been done in several ways. Initially in ZEUS, condensates [7] and islands [8] were used, both being clustering packages based on tower geometry. However, neither were capable of joining clusters across calorimeter boundaries. It has also been found [9] that showers from single hadrons often result in multiple clusters in the calorimeter. In Figure 1.8, the island clustering algorithm is depicted, which is as follows. For each tower we determine which neigbouring tower has the highest energy and draw an arrow from each tower to its highest energy neighbour. When the tower has no neighbour of higher energy than itself, this is then considered a “peak”, which will be the centre for an island. Then considering all towers again and following

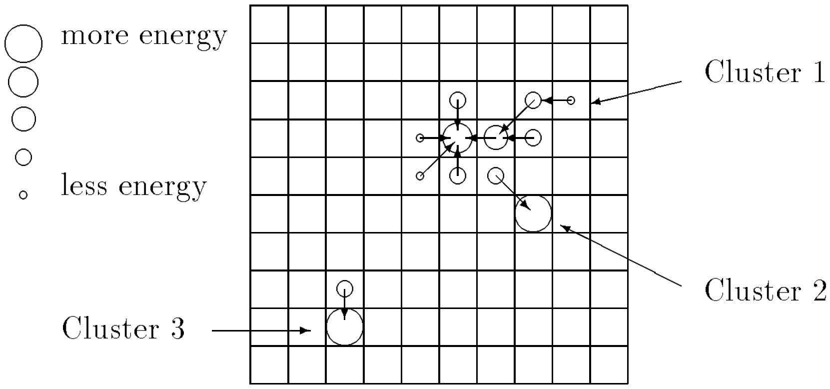

Figure 1.8: *Schematic of the island clustering algorithm.*

the arrows until we reach a peak, we find that all towers are uniquely associated with some peak and all those associated with a peak are classified as islands.

Improvements have now been made on the above two procedures, such that island finding is now performed on the cell rather than tower level. The basic concept is, however, that of the island algorithm. The island finding is done for each calorimeter section individually, and they are then joined across boundaries. This is the clustering algorithm used in this thesis to aid in the identification of electrons.

1.5 The Luminosity Monitor

The luminosity measurement is essential for any cross-section calculation and is measured at ZEUS from the rate of bremsstrahlung processes from the Bethe-Heitler [10] process;

$$ep \rightarrow e'p\gamma.$$

Integrating over scattering angles, the cross-section can be accurately calculated and is given by,

$$\frac{d\sigma}{dk} = 4\alpha r_e^2 \frac{E'}{kE}\left(\frac{E}{E'} + \frac{E'}{E} - \frac{2}{3}\right)\left(\log\frac{4E_pEE'}{Mmk} - \frac{1}{2}\right),$$

where k is the photon energy, E and E' are the initial and final electron energies, E_p is the proton energy, M and m are the proton and electron masses, α is the fine structure constant and r_e is the classical electron radius.

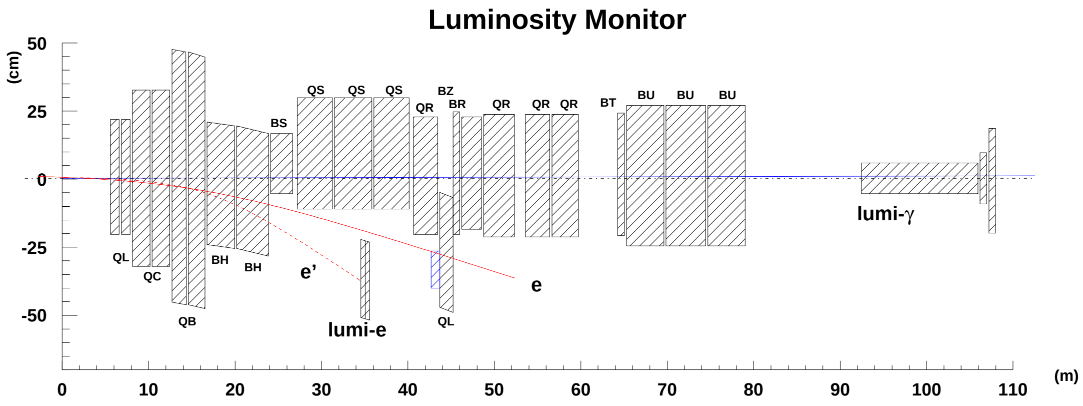

Figure 1.9: *The Luminosity Monitor.*

Figure 1.9 shows the luminosity monitor comprising the electron calorimeter (LUMI-e) and the photon calorimeter (LUMI-γ). Electrons leave an exit window at $z = -27$ m hitting the LUMI-e at $z = -34$ m. The acceptance of the LUMI-e limits the detection of electrons to $0.2E_{\rm beam} < E'_e < 0.8E_{\rm beam}$ with a resolution of $\sigma(E)/E = 0.18/\sqrt{E}$ (E is in Gev).

Photons leave an exit window at $z = -92$ m being detected by the LUMI$-\gamma$ at $z = -104$ m. The detector is protected from synchrotron radiation by a lead shield which reduces the energy resolution from $\sigma(E)/E = 0.18/\sqrt{E}$ to $\sigma(E)/E = 0.25/\sqrt{E}$ (E again measured in GeV).

1.6 The ZEUS Trigger System

The nominal crossing rate of the HERA accelerator is $\sim$ 10 MHz which poses challenges for the Data AcQuisition (DAQ) and trigger systems. The interaction rate is dominated by the proton beam interacting with residual gas, contributing about 10-100kHz, whilst the rate written to tape for ep interactions is between a few and 10 Hz.

To reduce the rate to less than $\sim$ 10 Hz whilst efficiently selecting ep events, ZEUS uses a three stage trigger system [11] and is shown in Figure 1.10.

The rate is initially reduced to $\sim$ 1 kHz by the First Level Trigger (FLT) which is a hardware based trigger. Each component used at the FLT has its own FLT and stores the data in a pipeline awaiting a decision. The decision is made within

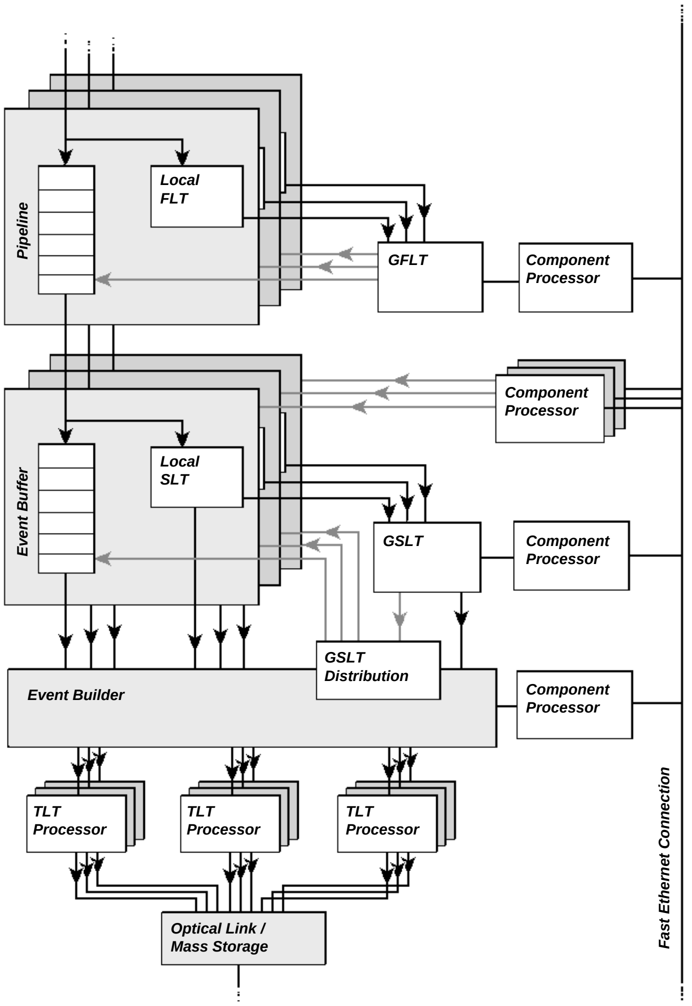

Figure 1.10: *The ZEUS Data Acquisition and Trigger System.*

$\sim 2\ \mu$s after the bunch crossing and passed onto the Global First Level Trigger (GFLT) which then makes a final decision in 4.4 μs passing the decision back to the component readout.

The events which pass the FLT proceed onto the Second Level Trigger (SLT). The SLT is a software based trigger run on a network of transputers, designed to reduce the rate by approximately a factor of ten. Analagously to the FLT, each component can have its own SLT, which passes decisions onto the Global Second Level Trigger (GSLT) [12].

Each component then passes the filtered events to an event builder which fills the data structure for the Third Level Trigger (TLT). The TLT runs a crude version of the full reconstruction software and is able to make decisions concerning global event properties, jet properties and event kinematics. The event rate is now reduced to a managable $\sim$ 1 Hz. The final stage is to then transfer the events by an optical fibre link for storage to then be processed by the full ZEUS reconstruction software.

Chapter 2

QCD and Photoproduction

2.1 Preamble

All particles which are subject to the strong nuclear force, *hadrons*, consist at an elementary level of quarks and gluons. The gluons are the propagators of the strong force, having no charge, but possessing colour. Analagously to Quantum ElectroDynamics (QED), which describes electromagnetic interactions, the strong force is described by Quantum ChromoDynamics (QCD) which is the field theory of quarks and gluons and their interaction. The coupling of the strong force, α_s, increases with distance due to an anti-screening effect. As gluons can couple to each other, then a gluon can fluctuate into a gluon-gluon pair, which causes the anti-screening effect.

The *ep* collider at HERA provides an opportunity for tests of QCD. For performing QCD calculations a larger momentum scale yields more reliable results. This momentum scale, referred to as the *hard scale*, is achieved in these analyses through the production of jets above a certain transverse energy threshold and through the study of heavy quarks.

In this chapter an introduction to HERA physics and specifically photoproduction will be given. The effects and properties of heavy quarks will be reserved for the next chapter.

2.2 Electron Proton Scattering

The fundamental, lowest order process in lepton-proton scattering is mediated either by the electromagnetic or weak forces through the exchange of a photon

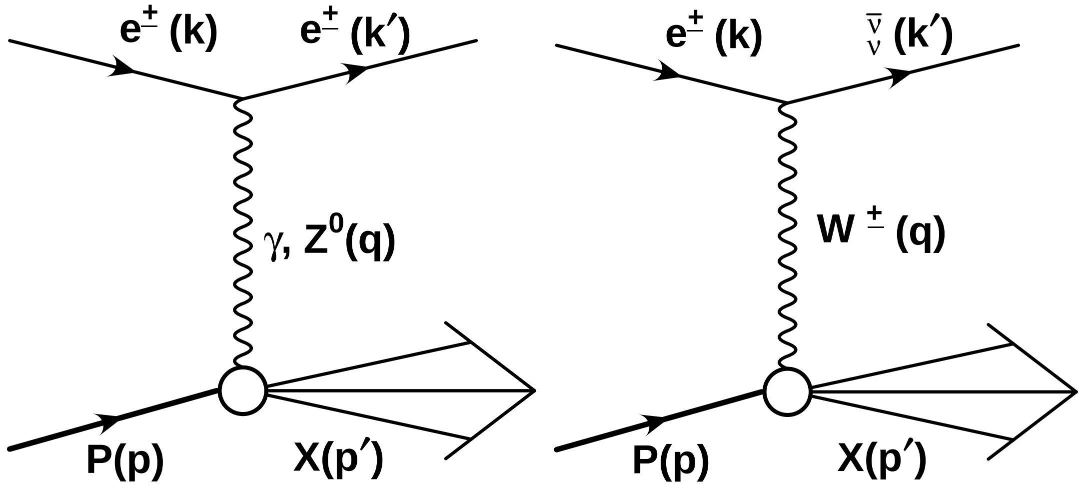

Figure 2.1: *Lowest order processes for neutral current (left) and charged current (right) reactions.*

in the first or a Z^0 or a $W^{\pm}$ in the second case. The result of this scattering process, in which the particle exchanged from the electron interacts with the proton, can be a high multiplicity hadronic final state, X. These processes can be reasonably placed into two classes; neutral current (NC), where the photon or Z^0 is exchanged and charged current (CC), where the $W^{\pm}$ is the exchanged boson. The processes can be summarised as:

$$e^{\pm} + P \rightarrow e^{\pm}X \quad (\text{NC}); \qquad e^{+}(e^{-}) + P \rightarrow \overline{\nu}(\nu)X \quad (\text{CC}) \tag{2.1}$$

and are shown in Figure 2.1.

Using the four momenta of the incoming and scattered lepton, $k = (E, \mathbf{k})$ and $k' = (E', \mathbf{k}')$, and the four momenta of the proton and photon, $p = (E_p, \mathbf{p})$ and $q = (E_{\gamma}, \mathbf{q})$, we can define the kinematics of the process. For a given centre of mass energy, $\sqrt{s} = \sqrt{(k+p)^2}$, two of the following three Lorentz invariant quantities completely describe electron-proton scattering kinematics.

$$Q^2 = -q^2 = -(k-k')^2, \tag{2.2}$$

$$y = \frac{q \cdot p}{k \cdot p}, \tag{2.3}$$

$$x = \frac{-q^2}{2p \cdot q}. \tag{2.4}$$

Q^2 is the negative square of the momentum transfer of the exchanged boson and defines its virtuality. In the proton rest frame, y is the fraction of the energy transferred from the lepton to the proton; $y = \frac{E-E'}{E} = \frac{E_\gamma}{E}$. In the parton model, x is the fraction of momentum carried by the struck quark. It is referred to as the Bjorken scaling variable.

The above three quantities are related to each other and the centre of mass energy squared, s, via the simple relation,

$$Q^2 = s \cdot x \cdot y, \tag{2.5}$$

where the energies are high and the masses can thus be neglected.

An understanding of the variable Q^2 is essential for this thesis, so will be discussed in more detail. It can be thought of as a measure of the resolving power of the photon. The wavelength of the virtual photon, λ, is given by,

$$\lambda = \frac{h}{|\mathbf{q}|}.$$

From this relation, one can see that an increase in Q^2 yields a decrease in wavelength and hence the photonic probe can resolve smaller objects.

In the exchange of a photon, the cross-section falls rapidly as a function of Q^2, as the propagator is given by $\frac{-ig_{\mu\nu}}{q^2}$. At low Q^2, the photon dominates the cross-section over the weak bosons. Only when Q^2 is sufficiently large are the contributions from the Z^0 and $W^\pm$ bosons significant. Indeed, when $Q^2 \geq M^2_{Z,W}$ (where $M_{Z^0} = 91.2$ GeV and $M_{W^\pm} = 80.2$ GeV) the neutral and charged current cross-sections are found to be of comparable size. This feature can be seen in Figure 2.2. The converging of the two cross-sections is a justification of electroweak theory. The high Q^2 region is, however, not relevant to the analysis work covered herein so will not be discussed further.

For large Q^2, the scale is provided by this variable and allows perturbative calculations to be performed. This is applicable down to a scale called $\Lambda_{\rm QCD}$ which has been experimentally determined to be $\Lambda_{\rm QCD} = 0.2 \pm 0.1$ GeV [13]. For values $Q^2 \gg \Lambda_{\rm QCD}$, the events are referred to as *Deep Inelastic Scattering* (DIS).

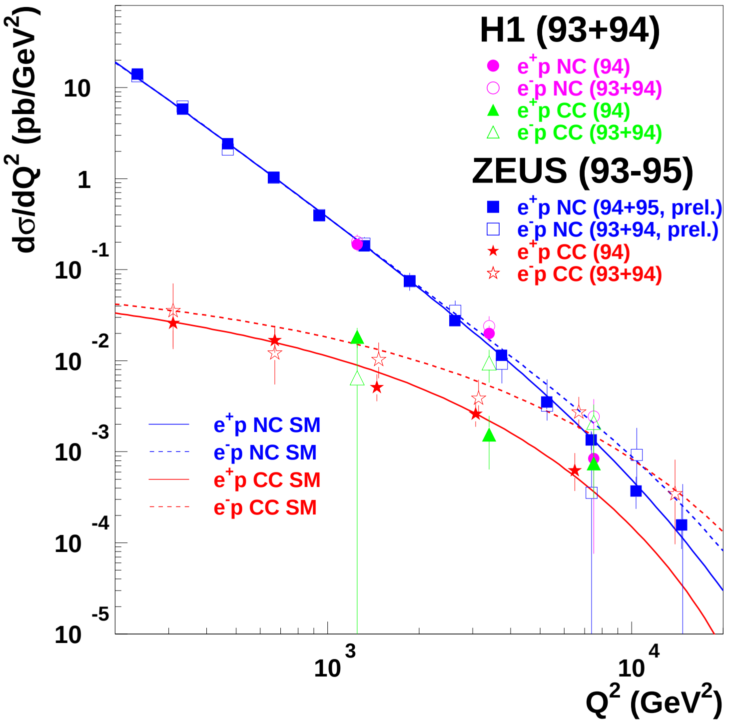

Figure 2.2: *Measurement of the NC and CC cross-sections at HERA.*

For low Q^2, there is an exchange of an almost real photon and the process is referred to as *photoproduction*. It is obvious that here Q^2 is not a hard scale, however the transverse momentum of jets may define a scale in the event. This hard scale allows the possibility of comparing experimental results with perturbative QCD calculations.

2.3 Structure Functions and the *ep* Cross-section

In the region of low Q^2, single photon exchange dominates the cross-section and so it can be approximated to,

$$d\sigma^{ep} \sim L_{\mu\nu} W^{\mu\nu}, \tag{2.6}$$

where $L_{\mu\nu}$ is the leptonic, and $W^{\mu\nu}$ the hadronic tensor. In Leading Order (LO) QED, $L_{\mu\nu}$ is given by;

$$L_{\mu\nu} = 2\left[k'_\mu k_\nu + k'_\nu k_\mu + \frac{q^2}{2} g_{\mu\nu}\right], \tag{2.7}$$

where $g_{\mu\nu}$ is the metric tensor and the mass of the electron has been ignored ($Q^2 \gg m_e^2$). The hadronic tensor, $W^{\mu\nu}$, describes all that happens at the propagator's other vertex, with the proton. In its most general form, $W^{\mu\nu}$ can be expressed in terms of the photon and (initial) proton four momenta, q and p, such that,

$$W^{\mu\nu} = -W_1 g^{\mu\nu} + \frac{W_2}{M^2} p^\mu p^\nu + \frac{W_4}{M^2} q^\mu q^\nu + \frac{W_5}{M^2} \left(p^\mu q^\nu + q^\mu p^\nu \right), \tag{2.8}$$

where M is the mass of the proton. By imposing current conservation at the hadronic vertex, $q_\mu W^{\mu\nu} = 0$, only two of the four structure functions, W_i, remain independent, since under the conservation of current condition;

$$W_5 = \frac{-p \cdot q}{q^2} W_2, \qquad W_4 = \left(\frac{p \cdot q}{q^2} \right)^2 W_2 + \frac{M^2}{q^2} W_1.$$

The ep cross-section can then be re-written as;

$$\frac{d^2\sigma^{ep}}{dx dQ^2} = \frac{4\pi\alpha^2}{xQ^4} \left[\frac{y^2}{2} 2xF_1(x, Q^2) + (1-y) F_2(x, Q^2) \right], \tag{2.9}$$

where the structure functions, W_i, have been renamed;

$$F_1(x, Q^2) \equiv M W_1(x, Q^2);$$

$$F_2(x, Q^2) \equiv \frac{p \cdot q}{M} W_2(x, Q^2).$$

F_1 and F_2 are now the structure functions which contain the information about the incalculable part of the hadronic vertex or alternatively the formalism, $F_L = F_2 - 2xF_1$ is also used yielding,

$$\frac{d^2\sigma^{ep}}{dx dQ^2} = \frac{2\pi\alpha^2}{xQ^4} \left[\left(1 + (1-y)^2 \right) F_2 + 2(1-y) F_L \right], \tag{2.10}$$

where $F_L = \frac{Q^2}{4\pi^2\alpha} \sigma_L$ and is referred to as the Longitudinal structure function.

2.4 The Quark Parton Model

2.4.1 The Simple Approach

Feynman's parton model [14] assumed the proton to be composed of free point-like objects, called partons. This model views the *inelastic* scattering of the electron off the proton as *elastic* scattering of the electron off the parton within the proton. Therefore the ep cross-section is given by the incoherent sum of the electron-parton scattering processes.

In the infinite momentum frame of the proton, the partons are assumed to have zero transverse momentum. When neglecting the masses of the proton and parton, the conservation of 4-momentum implies;

$$0 \approx m^2 = (\xi p + q)^2 = \xi^2 p^2 - Q^2 + 2\xi p \cdot q$$

$$\Rightarrow \xi = \frac{Q^2}{2p \cdot q} = x.$$

Therefore, the Bjorken scaling variable, x, is simply interpreted as the fraction of the longitudinal proton momentum, ξ, carried by the parton in the hard scatter.

In 1968, Bjorken predicted that the structure functions would depend on only one variable, x, in the limit $Q^2 \to \infty$, $\nu \to \infty$, where $\nu = \frac{p \cdot q}{M}$, the photon energy in the proton rest frame.

$$F_2(x, Q^2) = F_2(x) = \sum_i e_i^2 x f_i(x), \qquad (2.11)$$

$$F_1(x, Q^2) = F_1(x) = \frac{1}{2x} F_2(x), \qquad (2.12)$$

where $f_i(x)$ is the parton distribution function and Equation (2.12) is the Callan-Gross relation. This relation is a consequence of the partons having $spin - 1/2$ and implies that the cross-section for longitudinally polarised photons is zero.

This prediction, known as Bjorken scaling, was confirmed by results from SLAC [15] which then lead to the assumption that these $spin - 1/2$ partons were, in fact, quarks and so the name Quark Parton Model (QPM) was coined.

2.4.2 The QCD Improved Parton Model

The assumption that the proton consists solely of charged quarks implies that the sum of the momentum of the charged partons would be equal to that of the proton;

$$\sum_i \int_0^1 dx f_i(x) x = 1.$$

Experimentally, this value was found to be ≈ 0.5 [16], the implication being that the proton also consists of neutral particles. Evidence for the existence of these neutral particles, gluons, was provided in 1979 via the observation of 3-jet events in e^+e^- annihilation at DESY [17].

The QPM approach where the proton consists only of quarks was then modified to include gluons. This then became QCD, where quarks interact via the exchange of gluons. Gluons, themselves, can split into quark pairs or gluons. The radiated gluons result in the quarks having a component of transverse momentum. Coupling to longitudinally polarised photons is then possible, thereby violating the Callan-Gross relation. The value of the longitudinal structure function, F_L, is therefore no longer zero, but lies in the range $0 < F_L < F_2$.

As a result of the gluon radiation, exact scaling of the structure functions (i.e. dependence only on x) is violated and a logarithmic dependence on Q^2 is introduced. The photon at low Q^2 is then interpreted as resolving the valence quark substructure. At high Q^2 a quark may have radiated a gluon and consequently having a fraction of momentum, x, less than its original value, or alternatively, it may have arisen from gluon splitting.

At large values of x, where the valence quarks dominate, the quark density (and hence F_2) falls with increasing Q^2 whereas at low x, the number of "sea" quarks and gluons is larger, so F_2 increases with Q^2. This dependence of F_2 with Q^2 has been demonstrated at HERA [18].

2.5 The Evolution of Partonic Densities

The logarithmic Q^2 dependence of the structure functions can be predicted by accounting for the qqg vertex and modifying equation (2.11) to

$$\frac{F_2(x,Q^2)}{x} =$$

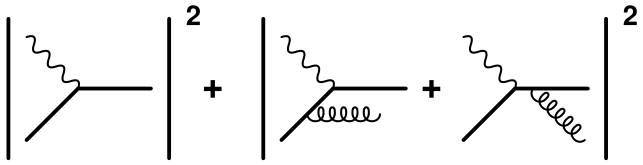

$$= \sum_q e_q^2 \int_x^1 \frac{dy}{y} q\left(y\right) \left(\delta\left(1-\frac{x}{y}\right) + \frac{\alpha_s}{2\pi} P_{qq}\left(\frac{x}{y}\right) \log\frac{Q^2}{\mu^2} \right), \quad (2.13)$$

where $q(y) = f_q(y)$ is the quark structure function, μ is a lower limit on the transverse momentum to regularise divergences which occur as the transverse momentum squared tends to zero and $P_{qq}(z)$ represents the probability of quark emitting a gluon and then having a momentum fraction z and is called a splitting function. Equation (2.13) can be re-written as

$$\begin{aligned} \frac{F_2(x,Q^2)}{x} &\equiv \sum_q e_q^2 \int_x^1 \frac{dy}{y} \left(q\left(y\right) + \Delta q\left(y,Q^2\right)\right) \delta\left(1-\frac{x}{y}\right) \\ &= \sum_q e_q^2 \left(q\left(x\right) + \Delta q\left(x,Q^2\right)\right), \end{aligned} \quad (2.14)$$

where

$$\Delta q\left(x,Q^2\right) \equiv \frac{\alpha_s}{2\pi} \log\frac{Q^2}{\mu^2} \int_x^1 \frac{dy}{y} q\left(y\right) P_{qq}\left(\frac{x}{y}\right). \quad (2.15)$$

At some $Q^2 \sim Q_0^2$, the photon starts to resolve the point-like valence quarks within the proton. QCD then predicts that with increasing Q^2, such that $Q^2 \gg Q_0^2$, the resolution power increases and the quark itself (surrounded by a sea of partons) is "seen". The quark structure function can be calculated for any value of Q^2, given some reference value $q(x,Q_0^2)$ by considering the change in $\Delta q(x,Q^2)$ for a small change in $\log Q^2$:

$$\frac{dq(x,Q^2)}{d\log Q^2} = \frac{\alpha_s}{2\pi} \int_x^1 \frac{dy}{y} q\left(y,Q^2\right) P_{qq}\left(\frac{x}{y}\right). \quad (2.16)$$

By then considering a quark evolved from a gluon in a pair production process, the evolution of the quark density distribution can be modified further. The

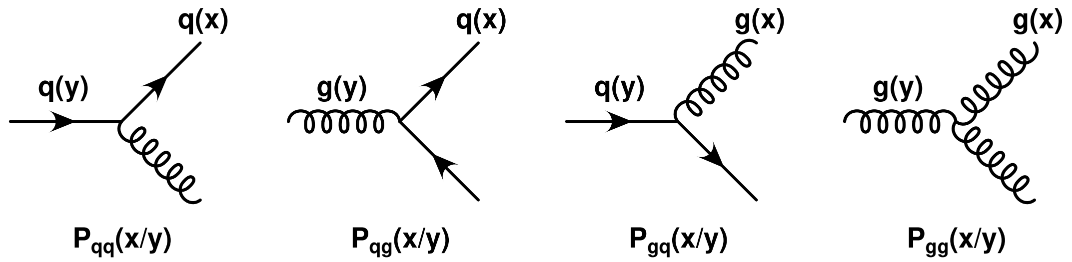

Figure 2.3: *The first order splitting functions* $P_{jk}\left(\frac{x}{y}\right)$ *used in the DGLAP equations.*

same procedure can also be applied to the evolution of the gluon density distribution by considering gluons resulting from quarks or gluons. The resulting equations describe partonic evolution and are called the Dokshitzer-Gribov-Lipatov-Altarelli-Parisi equations [19]:

$$\frac{dq_i(x,Q^2)}{d\log Q^2} = \frac{\alpha_s}{2\pi}\int_x^1 \frac{dy}{y}\left[q_i\left(y,Q^2\right)P_{qq}\left(\frac{x}{y}\right) + g(y,Q^2)P_{qg}\left(\frac{x}{y}\right)\right] \tag{2.17}$$

$$\frac{dg(x,Q^2)}{d\log Q^2} = \frac{\alpha_s}{2\pi}\int_x^1 \frac{dy}{y}\left[\sum_i q_i\left(y,Q^2\right)P_{gq}\left(\frac{x}{y}\right) + g(y,Q^2)P_{gg}\left(\frac{x}{y}\right)\right] \tag{2.18}$$

where $q_i(x,Q^2)$ is the quark density function, for each quark flavour i and $g(x,Q^2)$ is the gluon density function. There are now several splitting functions $P_{jk}\left(\frac{x}{y}\right)$ which are shown in Figure 2.3. They represent the probability of a parton k of momentum fraction y emitting a parton j of momentum fraction x.

The parton evolution can be seen as the sum of ladder diagrams where each "ladder" corresponds to a gluon emission as in Figure 2.4. Each diagram with n gluon emissions of momentum $k^2_{T_i}$ represent a term in $(\alpha_s \log Q^2)^n$, where $\alpha_s \log Q^2 \sim 1$, which is dominant at large x and Q^2. In this regime, each contribution is ordered in transverse momentum such that,

$$k^2_{T_1} \ll k^2_{T_2} \ll ... \ll k^2_{T_{n-1}} \ll k^2_{T_n} \ll Q^2.$$

With the knowledge of the x dependence at a minimum Q^2, Q_0^2, the evolution equations can be solved to give the parton distributions as a function of x for all Q^2. This minimum value Q_0^2, cannot presently be calculated so relies on an experimental determination.

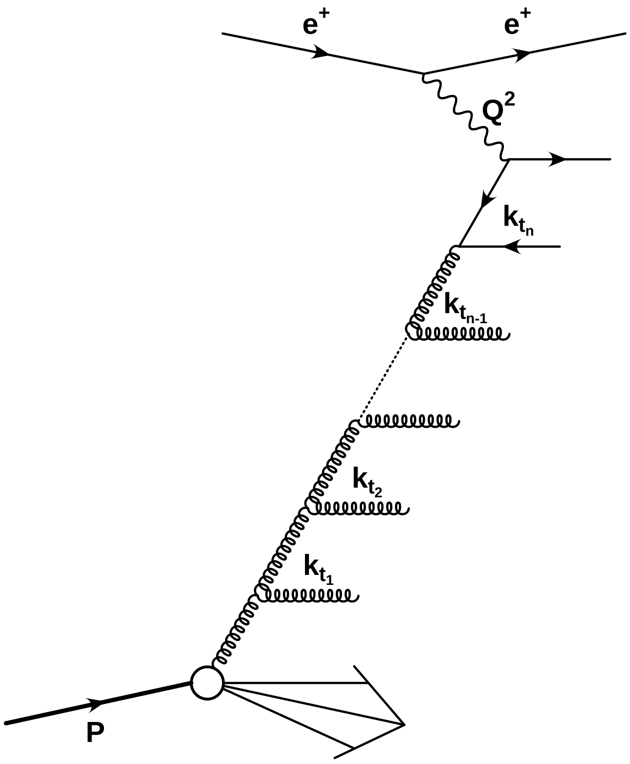

Figure 2.4: *Parton evolution diagram showing the k_t ordered gluon emissions.*

As was stated these evolution equations describe the physics at high x and Q^2 ignoring terms of $\log(1/x)$ whose importance arises at low x. The terms at low x have been taken into account by summing $(\alpha_s \log(1/x))^n$ gluon emission terms which are now not ordered in transverse momentum resulting in the Balitsky-Fadin-Kuraev-Lipatov (BFKL) equation [20].

A unification of the two methods leading to a complete description of the parton distribution function's x and Q^2 dependence is an obvious goal, but is experimentally as well as theoretically challenging.

2.6 Photoproduction Processes

Having given a description of the dynamics of electron-proton scattering and the processes at HERA, the aforementioned photoproduction will be discussed in detail. The processes under study in this analysis are termed photoproduction and so an understanding of its principles is required.

As we can now think of electron-proton scattering as photon-proton scattering due to the exchange of the virtual photon between the electron and proton, the total *ep* cross-section can then be expressed in terms of the γp cross-section. In the limit of low Q^2, i.e. photoproduction processes, the total γp cross-section, $\sigma_{tot}^{\gamma p} = \sigma_T^{\gamma p}$, the transversely polarised γp cross-section as the longitudinal component can be ignored. Using this condition, the *ep* cross-section can be written as

$$\frac{d^2\sigma^{ep}}{dydQ^2} = f_\gamma^e(y, Q^2)\sigma_{tot}^{\gamma p}(y, Q^2) \tag{2.19}$$

for a given photon flux, $f_\gamma^e(y, Q^2)$. This is known as the *equivalent photon approximation* (EPA). This can be interpreted as the probability to find a photon in the electron of energy $E_\gamma = yE_e$ which using the Weizsäcker-Williams Approximation [21] is given by,

$$f_\gamma^e(y, Q^2) = \frac{\alpha}{2\pi Q^2}\left(\frac{1-(1-y)^2}{y} - 2\frac{(1-y)}{y}\frac{Q^2_{min}}{Q^2}\right), \tag{2.20}$$

where Q^2_{min} is the kinematic lower bound.

Photoproduction can be studied at HERA at an energy of an order of magnitude higher than previous experiments. The two fundamental processes associated with photoproduction can be investigated. These two processes are the so-called “direct” and “resolved” photon interactions.

2.6.1 Direct Photoproduction

Direct photoproduction is so-called because in this process, the photon can be thought of interacting *directly* in the hard sub-process. The photon acts as a pointlike object interacting with the parton from the proton; a property which distinguishes photon-proton from hadron-hadron scattering. As all the photon's energy couples to the parton, the final state of the process is expected to be of higher transverse momentum than for hadronic type interactions in which only part of the photon's energy participates. The two LO direct photoproduction diagrams can be seen in Figure 2.5. The QCD Compton process in Figure 2.5a shows the photon coupling to a quark within the proton which then radiates a gluon before hadronisation. In Figure 2.5b, the photon couples to a quark coming from a “split” gluon in the proton which produced a quark-antiquark

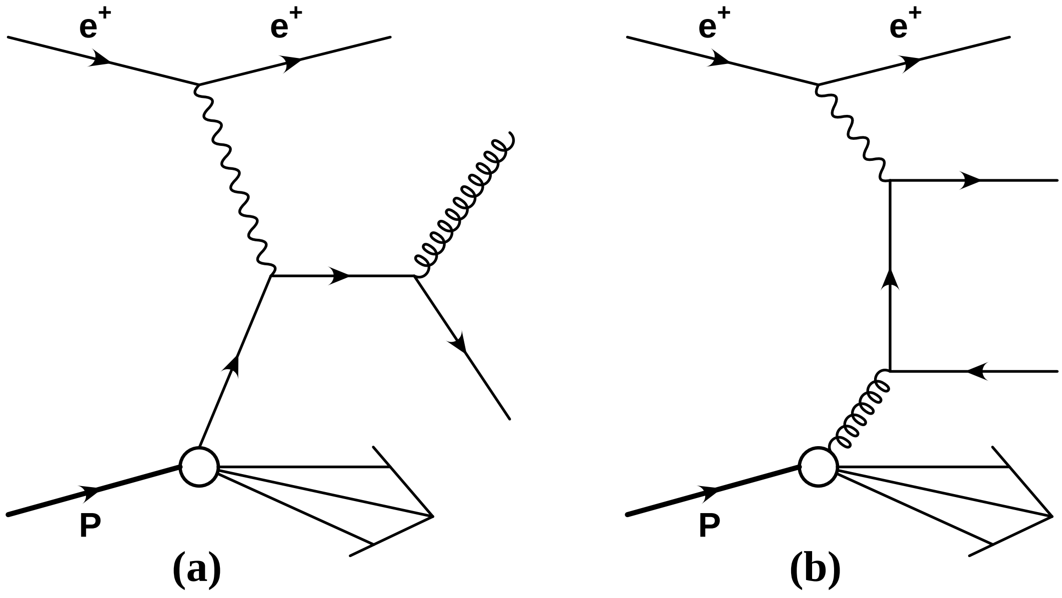

Figure 2.5: *Leading order direct processes; (a) QCD Compton and (b) Boson gluon fusion.*

pair. This is termed boson-gluon fusion. Both have final states consisting of two high transverse energy jets where in the case of the QCD Compton process one is a quark and the other a gluon jet and in boson-gluon fusion both are quark jets.

2.6.2 Resolved Photoproduction

In resolved photon processes, the photon acts as a source of partons one of which interacts with a parton from the proton in the hard sub-process. In the case of a resolved photon only a fraction of the photon's energy participates in the hard interaction. Examples of resolved photoproduction diagrams at LO can be seen in Figure 2.6. In Figure 2.6a, a gluon from the photon interacts with a gluon from the proton in what is termed gluon-gluon fusion. However, in Figure 2.6b it is a quark from the photon which interacts with the gluon from the proton. Again these two processes differ in that the final state consists of two quark jets in the case of Figure 2.6a and one quark and one gluon jet in the case of Figure 2.6b. It seems to therefore possess the same final state as direct processes. This, however, is not true as in addition to the two jets, proton remnant and scattered electron, there is a photon remnant.

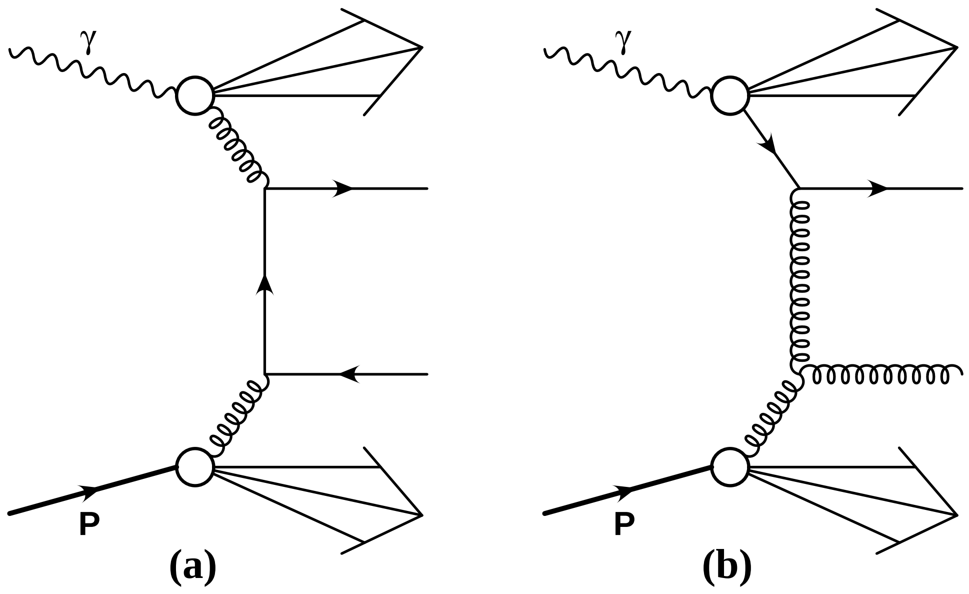

Figure 2.6: *Examples of leading order resolved processes.*

2.6.3 Generalised Photoproduction Model

Direct and resolved processes at LO and those diagrams shown in Figures 2.5 and 2.6 can be generalised and are shown in Figure 2.7 for jet production. The dotted line in the figure represent the cut-offs between the hard process which can be calculated perturbatively and the non-perturbative parton distribution functions. The factorisation scales, μ_P and μ_γ, are arbitrary, but are chosen to be $\sim p_T$, the transverse energy of the jet, allowing the incoming parton a large region of phase space in which to evolve. As the hard sub-process is independent of the factorisation scale, a variation of the scale would only effect the parton distribution functions.

The differential cross-section for the generalised model can be separated into direct and resolved components;

$$d\sigma_{\gamma p \to cd} = d\sigma^{dir}_{\gamma p \to cd} + d\sigma^{res}_{\gamma p \to cd}, \tag{2.21}$$

where the two separate components can be written as,

$$d\sigma^{dir}_{\gamma p \to cd} = \sum_b \int_{x_p} dx_p f_{p \to b}\left(x_p, \mu_p^2\right) d\hat{\sigma}_{\gamma b \to cd} \tag{2.22}$$

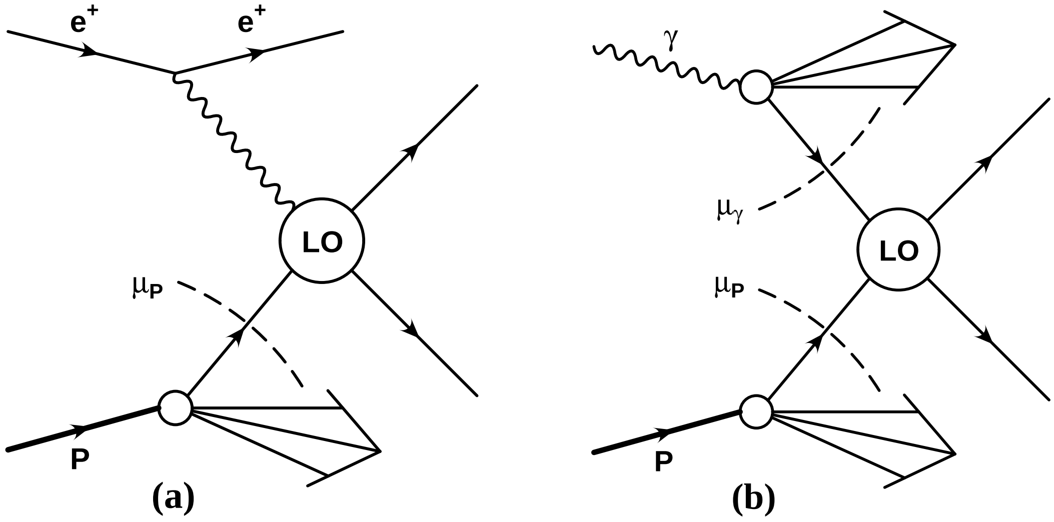

Figure 2.7: *General Leading Order picture for resolved and direct processes.*

and

$$d\sigma^{res}_{\gamma p\to cd} = \sum_{ab}\int_{x_p} dx_p \int_{x_\gamma} dx_\gamma f_{p\to b}\left(x_p, {\mu'_p}^2\right) f_{\gamma\to a}\left(x_\gamma, \mu_\gamma^2\right) d\hat{\sigma}_{ab\to cd}. \tag{2.23}$$

The $d\hat{\sigma}$'s represent the perturbatively calculable $2 \to 2$ scattering matrix element and $f_{p\to b}$ and $f_{\gamma\to a}$, the density functions of the proton and photon respectively.

At Next-to-Leading Order (NLO), there are also contributions from $2 \to 3$ parton scattering, which are dependent on the factorisation scale. By varying μ_γ, the amount of $2 \to 3$ processes at NLO and the amount which are in fact simply LO processes varies. More specifically an ambiguity between NLO direct and LO resolved arises and is dependent on μ_γ. The advantage of NLO over LO therefore lies in the reduction of the dependence on the factorisation scale.

2.6.4 The Structure of the Photon

Consider deep inelastic $e\gamma$ scattering as in Figure 2.8 which is formally analagous to deep inelastic ep scattering. The cross-section for a probing photon, virtuality, $Q^2 \equiv -q^2$, scattering off a real target photon with virtuality $P^2 \approx 0$ producing a final state eX is given by,

$$\frac{d^2\sigma_{e\gamma\to eX}}{dxdy} = \frac{2\pi\alpha^2 s}{Q^4}\left\{\left[1 + (1-y)^2\right] F_2^\gamma(x, Q^2) - y^2 F_L^\gamma(x, Q^2)\right\} \tag{2.24}$$

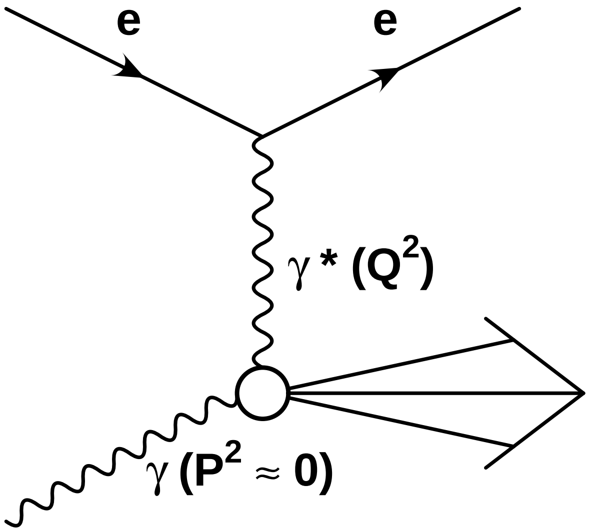

Figure 2.8: *Feynman diagram for $e\gamma$ diagram with a virtual photon, γ^*, probing an on-shell photon, γ.*

where $x \equiv Q^2/(2p \cdot q)$ and $y \equiv Q^2/(sx)$ with $\sqrt{s}$ being the total centre of mass energy.

The beauty of the $e\gamma$ cross-section is that unlike in ep scattering, the structure functions can be computed in the Quark Parton Model. Unfortunately the result depends on the mass of the constituent quarks which are not well defined in field theory.

However, analagously to ep scattering the structure function F_2^γ can also be written in terms of the quark densities in the photon, $q_i^\gamma(x, Q^2)$, such that (in LO)

$$F_2^\gamma(x, Q^2) = 2x \sum_i e_{q_i}^2 q_i^\gamma(x, Q^2), \tag{2.25}$$

where the sum runs over all quark flavours, i, of charge e_{q_i} and the factor of two accounts for quarks and antiquarks.

We can then compute the photonic parton densities Q^2 dependence [22];

$$\frac{dq_i(x, Q^2)}{d\log Q^2} = a(x) + \frac{\alpha_s(Q^2)}{2\pi} \int_x^1 \frac{dy}{y} \left[P_{qq}\left(\frac{x}{y}\right) q_i(y, Q^2) + P_{qg}\left(\frac{x}{y}\right) g(y, Q^2) \right], \tag{2.26}$$

$$\frac{dg(x,Q^2)}{d\log Q^2} = \frac{\alpha_s(Q^2)}{2\pi}\int_x^1 \frac{dy}{y}\left[P_{gq}\left(\frac{x}{y}\right)2\sum_i^f q_i(y,Q^2) + P_{gg}\left(\frac{x}{y}\right)g(y,Q^2)\right], \tag{2.27}$$

where,

$$a(x) = 3e_i^2\frac{\alpha}{2\pi}\left[x^2+(1-x)^2\right]$$

represents the $\gamma \rightarrow q\overline{q}$ splitting and the P_{jk} are the splitting functions as mentioned in Section 2.5.

At large values of x, the production of quarks comes predominantly via the $\gamma \rightarrow q\overline{q}$ splitting. As this coupling is electromagnetic, the number of u quarks produced is four times that of the d quarks due to their relative electronic charge. At low values of x however, the quarks are produced from the gluon splitting process and here there are an equal number of u and d quarks as the strong force does not differentiate between charge.

There are currently a large number of photon parton density parametrisations and usually involve some fits to data. With the large errors on F_2^γ, additional assumptions need to be made. These assumptions differ in different models and involve the treatment of heavy quarks, the choice of the scale Q_0^2 and the methods of deciding the form of the input densities. HERA could provide interesting information that would allow the testing of these different parametrisations. The study of heavy quarks will naturally be useful as assumptions of their contribution are made.

2.6.5 Dijet Photoproduction Results at HERA

The distinction between resolved and direct photon processes to LO as was shown previously is theoretically defined whereas at higher orders the distinction between the two becomes ambiguous. The relevant contributions from the two processes in the photoproduction of jets were compared to fixed target experiments in 1979 [23]. The contribution from the resolved photon processes was found to be small. With the building of HERA, the contribution from resolved processes would be large and consequently their observation possible. With the knowledge of their properties already espoused, an experimental distinction and observation can be made.

The observation of resolved photon processes was seen in the early stages at HERA [24] via the observation of large energy deposits in the rear (electron) direction consistent with a photon remnant. A distinction between the two was also seen [25] and an experimental separation of the two processes can be performed. This separation is based on the knowledge of the fraction of the photon's momentum, x_γ, participating in the interaction. For the LO QCD diagrams shown in Figures 2.5 and 2.6, energy and momentum conservation yield the following in a two parton scatter,

$$x_\gamma^{LO} = \frac{\sum_{partons} E_T^{partons} e^{-\eta^{partons}}}{2yE_e}, \tag{2.28}$$

where yE_e is the initial photon energy. For direct events, this value is one and for resolved events it is less than one. Translating this into an experimentally measurable quantity, we sum over jets instead of partons. Equation (2.28) then becomes in terms of our new variable, x_γ^{obs} [26],

$$x_\gamma^{\text{obs}} = \frac{\sum_{jets} E_T^{jet} e^{-\eta^{jet}}}{2yE_e}, \tag{2.29}$$

where the sum runs over the two highest transverse energy jets. Due to effects of hadronisation and/or higher order effects, the value of x_γ^{obs} is not one for direct events, but the events do populate the higher regions of x_γ^{obs}. By fitting the Monte Carlo simulations of resolved and direct and processes to the data measured, the two processes can be observed. This is shown in Figure 2.9 [27] where the experimental cut-off between the direct and resolved is also shown.

The agreement in shape between data and Monte Carlo is good except below $x_\gamma^{\text{obs}}= 0.3$ even when a MultiParton Interaction (MPI) model is included. The description of this region without MPI is poor using both generators.

Having found the existence of the two types of processes, the next question to then ask is of their form. In Figure 2.6, there are two examples of LO resolved processes and it is reasonable to ask if one dominates over the other. This can be determined by studying the dijet angular distribution which is dependent on the propagator of the process. The angle between the jet-jet axis and the beam axis,

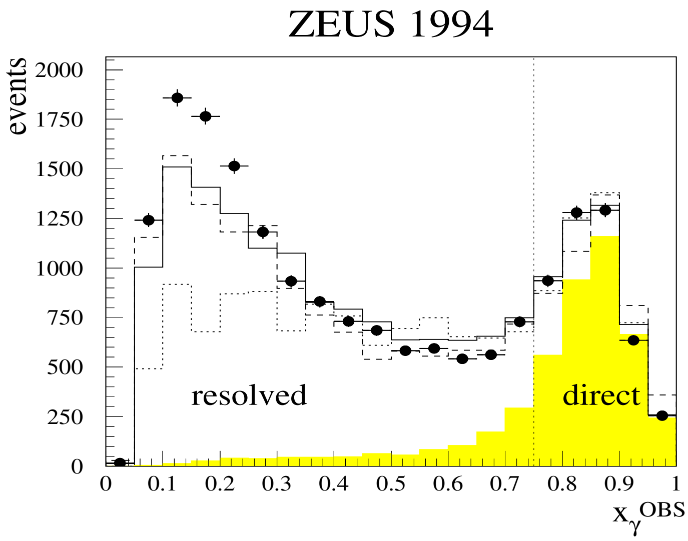

Figure 2.9: *The* x_γ^{obs} *distribution in dijet events for data (black dots) compared with HERWIG with and without MPI (solid line and dotted line), and PYTHIA with MPI (dashed line) Monte Carlo generators. The shaded area represents direct only events as generated by HERWIG and the vertical line is the experimental cut to separate direct and resolved processes.*

θ^* in the dijet centre of mass system can be calculated in terms of measurable quantities such that,

$$\cos\theta^* = \tanh\left(\frac{\eta^{jet1} - \eta^{jet2}}{2}\right), \tag{2.30}$$

where η^{jet1} is the pseudorapidity of the highest and η^{jet2} the pseudorapidity of the second highest jet in transverse energy. At LO, direct processes involve a quark as a propagator (see Figure 2.5) whereas resolved processes can have quark (Figure 2.6a) or gluon (Figure 2.6b) propagators. A quark propagator, with *spin*-1/2, leads to an angular dependence which is $\propto (1 - |\cos\theta^*|)^{-1}$ and a gluon with *spin*-1 gives an angular dependence which varies $\propto (1 - |\cos\theta^*|)^{-2}$. QCD predicts that in the case of resolved photon processes the angular distribution will rise rapidly in line with the gluon being the dominant process.

This was confirmed in dijet photoproduction at ZEUS [28] by measuring the dijet angular cross-section for resolved and direct events where the direct-resolved separation was achieved by a cut on x_γ^{obs}- $x_\gamma^{\mathrm{obs}} \geq 0.75$ (< 0.75) are classified as direct (resolved) - as previously mentioned, and is shown in Figure 2.10.

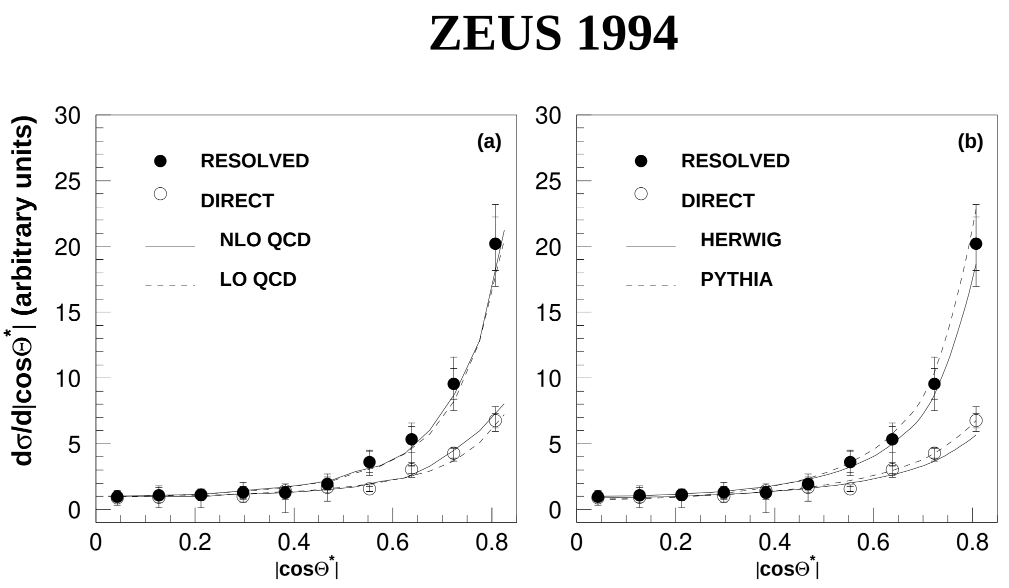

Figure 2.10: *Dijet angular cross-sections for resolved (black dots) and direct (open dots) compared to LO and NLO QCD predictions and HERWIG and PYTHIA Monte Carlo.*

These and other results from HERA are for inclusive dijet photoproduction, i.e. there are no other requirements. As the analyses in this thesis also tag heavy quarks *in* dijet photoproduction, the phenomenology of heavy quarks is discussed and is the subject of the next chapter. The results shown here, however, provide an interesting baseline for comparison with future results so the effect of a charm or beauty quark can be seen. The questions provoked are amongst others;

- Is there direct and resolved charm and beauty production at HERA?
- What are the dominant resolved and direct diagrams?
- Is there any charm or beauty in the photon?

These points will be discussed and some of them answered in the coming pages.

Chapter 3

Heavy Quark Production

The study of heavy quarks yields the opportunity of studying perturbative QCD with an additional hard scale to that of the transverse energy of the jets; that of the quark mass. The charm mass is approximately that of the hadronic scale and is at the (lower) limit of applicability for perturbative QCD. This implies the study of semi-perturbative effects may be better performed through measurements of the charm rather than the beauty quark. The mass of the beauty quark lies well above this value ($m_b \sim 3m_c$) so would theoretically provide the better tests of perturbative QCD.

Hadroproduction and photoproduction data from fixed target experiments agree qualitatively with QCD predictions but quantitative deviations remain. This prompts the question as to whether simple non-perturbative models such as fragmentation effects and intrinsic transverse momentum are sufficient to explain the deviations. The new possibilities provided by HERA are the wide kinematical range for photoproduction allowing the study of the photon and proton stucture functions and the study of heavy quark jets as in this thesis.

Initially, heavy quark production at fixed target experiments will be briefly discussed [29]. This is by way of introducing the history of heavy quark *photo*production. Theoretical aspects of photoproduction (and hadroproduction) allied to relevant results will then be discussed in the context of photoproduction at HERA. There is a large number of results on heavy quark production, particularly from LEP and the TEVATRON, but we will only consider those of direct relevance to the studies in this thesis. We will therefore omit any discussion on the wealth of data on for example, lifetimes, quarkonia production or $\mathcal{CP}$ violation.

3.1 Heavy Quark Production at Fixed Target Experiments

Heavy quark production has been extensively studied at a number of fixed target experiments at centre of mass energies of about 10 - 40 GeV. At this energy the cross-section for beauty quarks is low so most studies concentrated on the charm quark.

If one considers the photoproduction data for the total charm production cross-sections at fixed target experiments compared to pQCD calculations, qualitative agreement but quantitative deviations can be clearly seen (see Figure 3.1). These results from γN collisions clearly show a broad agreement with QCD predictions, but no consistent value of charm mass or renormalisation scale can be interpreted from the comparison. Looking at a data set from one experiment in isolation, one can see that the E687 data is consistent with a charm mass of 1.2 GeV and inconsistent with a value of 1.8 GeV whilst the E691 data is inconsistent with $m_c = 1.2$ GeV, but consistent with $m_c = 1.8$ GeV. To constrain the physical parameters, the (sometimes large) discrepancies between experiments need to be resolved.

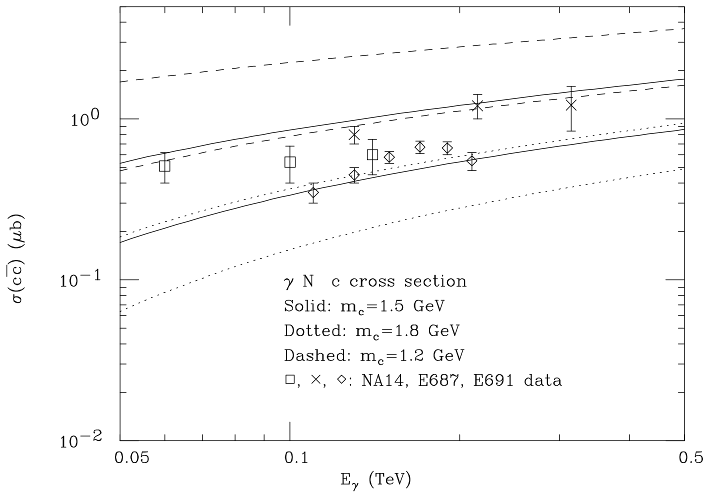

Figure 3.1: *Total pair cross-section for c production in γN collisions from the NA14 [30], E687 [31] and E691 [32] collaborations compared to QCD predictions. The bands represent (for a given charm mass) the variation due to the choice of the renormalisation scale, where the limits shown here are, $\mu_R = m_c/2$ and $\mu_R = 2m_c$ (from [29]).*

Single inclusive distributions have also been measured at fixed target experiments and compared to QCD predictions. The effect of non-perturbative phenomena coupled to the pQCD predictions have also been studied by, for example, introducing an intrinsic transverse momentum for the incoming partons (the so-called "k_T kick") and introducing a hadronisation for the charm quark. Figure 3.2 shows the inclusive p_T^2 distribution of charmed hadrons in γN collisions from the E687 (Left) and E691 (Right) collaborations. On comparison of the data with theoretical predictions, it can be seen that some non-perurbative component is needed to describe the data, although it is reasonably insensitive to the value of the "k_T kick" chosen. The convolution of the pQCD prediction with a fragmentation function is however necessary.

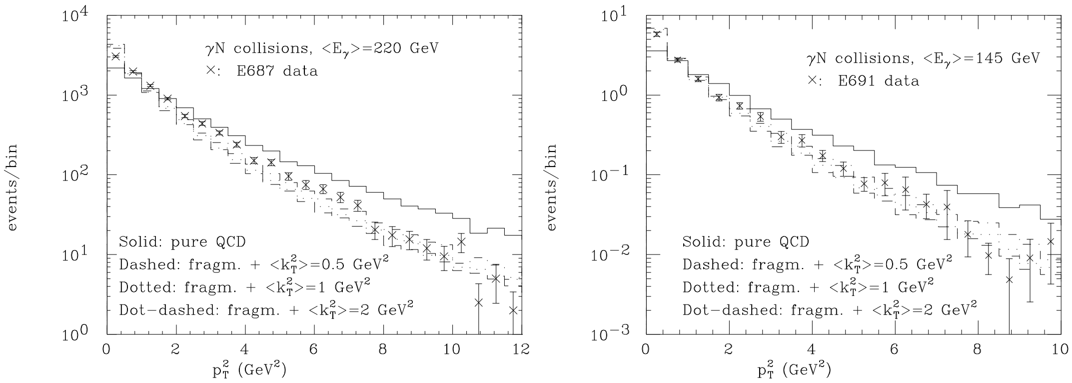

Figure 3.2: *Distribution in p_T^2 for charmed hadrons from the E687 [31] (left) and E691 [32] (right) collaborations compared to NLO pQCD (m_c = 1.5 GeV) and NLO pQCD with non-perturbative effects (from [29]).*

Correlations between charmed quarks have also been studied in photoproduction data; namely $\Delta\phi$, the angle between the momenta projections of the pair onto the transverse plane, and the transverse momentum of the pair $p_T(Q\bar{Q})$. These values are again thought to be sensitive to non-perturbative effects such as the "k_T kick". Photoproduction data has been compared to NLO QCD calculations with an added "k_T kick" [29]. Both distributions indicate a sensitivity to "k_T kick" but the value which gives the best description of the data is dependent on experiment and distribution.

From these results it can be seen that the data from fixed target experiments yields more questions than it answers being hindered by the limited kinematic range and differences between experiments. No serious kinematic constraints on the charm quark can be placed and no serious measurement of the beauty quark was made, due to lack of statistics.

3.2 Heavy Quark Production at HERA

There are two theoretical advantages to the study of heavy rather than light quarks in photoproduction. As mentioned at the beginning of the chapter, the large mass ($m_q \gg \Lambda_{\rm QCD}$) ensures that perturbative calculations are more reliable although corrections $\propto (\Lambda_{\rm QCD}/m_q)^n$ might be non-negligible for the charm quark. With accurate values of m_q and $\Lambda_{\rm QCD}$, reliable total cross-sections could be predicted. Secondly, the study of heavy quarks also reduces the number of contributing partonic processes such that the boson-gluon fusion (Figure 2.5b) process;

$$\gamma g \rightarrow Q\bar{Q},$$

is the only direct photon process at LO. To LO this process is directly sensitive to the gluon content of the proton. The question of the relative contribution of LO resolved processes is less clear. Heavy quark "excitation" processes;

$$Qg \rightarrow Qg,$$

(the charge conjugate being implied), where the heavy quark comes from the photon, may contribute. The size of the contribution relative to the gluon-gluon fusion process;

$$gg \rightarrow Q\bar{Q},$$

is a question that studies at HERA hope to answer. It is addressed in this thesis. Coupled to the unexplored kinematic region in photoproduction available at HERA, the study of heavy quarks promises to yield interesting results.

At LO, heavy quark production, like light quark production, is considered as the sum of direct (pointlike) and resolved (hadronic) components. Therefore, the general photoproduction description given by Equations (2.21 - 2.23), also describes photoproduction for heavy quarks. However, we must remember that approximations such as $p_T^2 \gg m_Q^2$ are not necessarily valid and the mass must be included. We should also consider that the pseudorapidity is a massless approximation of the rapidity, y, which is given by,

$$y = \frac{1}{2}\log\left(\frac{E+p_z}{E-p_z}\right).$$

The subsequent treatment of what constitutes direct and resolved and in which proportions is where differences in theoretical models occur. For example, the "excitation" process, stated in the previous paragraph, can be considered, at sufficiently high transverse momenta, as a LO resolved process or alternatively a NLO direct process.

3.2.1 Perturbative Formalism of Heavy Quark Photoproduction

The inclusive production of a heavy quark, Q, with momentum, p and energy E in the process,

$$\gamma(p_1) + H_A(p_2) \to Q(p) + X$$

has been calculated to $\mathcal{O}(\alpha\alpha_s^2)$ [33]. The total cross-section for a photon-hadron centre of mass energy, S, is given by,

$$\begin{aligned} \sigma(S) &= \sum_j \int dx \hat{\sigma}_{\gamma j}(xS, m^2, \mu^2) F_j^{H_A} \\ &+ \sum_{i,j} \int dx_1 dx_2 \hat{\sigma}_{ij}(x_1 x_2 S, m^2, \mu^2) F_i^{\gamma}(x_1, \mu) F_j^{H_A}(x_2, \mu), \end{aligned} \tag{3.1}$$

where $F_j^{H_A}$ and F_i^{γ} are the parton densities of the hadron and photon respectively and μ is the factorisation scale. The short distance cross-section, $\hat{\sigma}$ for a photon-parton collision is given by,

$$\hat{\sigma}_{\gamma j}(s, m^2, \mu^2) = \frac{\alpha\alpha_s(\mu^2)}{m^2} f_{\gamma j}(\rho, \mu^2/m^2), \tag{3.2}$$

where $\rho = 4m^2/s$ and s is the partonic centre of mass energy. The second term in Equation (3.1) is simply the cross-section for the hadroproduction process of heavy quarks, where the hadron parton density function is replaced by the photon parton density function. This has been calculated to $\mathcal{O}(\alpha_s^3)$ [34], where the short-distance cross-section is given by,

$$\hat{\sigma}_{ij}(s, m^2, \mu^2) = \frac{\alpha_s^2(\mu^2)}{m^2} f_{ij}(\rho, \mu^2/m^2). \tag{3.3}$$

The dimensionless function $f_{\gamma j}$ has the following perturbative expansion,

$$f_{\gamma j}(\rho, \mu^2/m^2) = f_{\gamma j}^{(0)}(\rho) + g^2(\mu^2)\left[f_{\gamma j}^{(1)}(\rho) + \bar{f}_{\gamma j}^{(1)}(\rho)\log(\mu^2/m^2)\right] + \mathcal{O}(g^4), \quad (3.4)$$

and the function f_{ij}, the following,

$$f_{ij}(\rho, \mu^2/m^2) = f_{ij}^{(0)}(\rho) + g^2(\mu^2)\left[f_{ij}^{(1)}(\rho) + \bar{f}_{ij}^{(1)}(\rho)\log(\mu^2/m^2)\right] + \mathcal{O}(g^4). \quad (3.5)$$

Details of the forms of the lowest order functions $f_{\gamma j}^{(0)}$ and $f_{ij}^{(0)}$ are given in [33] and [34]. The higher order corrections, $\bar{f}^{(1)}$ are the coefficients of $\log(\mu^2/m^2)$ and are determined by renormalisation group arguments and use the explicit forms [35, 36] of the Altarelli-Parisi kernels, P_{ij}. The quantities $f_{\gamma j}^{(1)}$ and $f_{ij}^{(1)}$ can be obtained by performing a complete $\mathcal{O}(\alpha\alpha_s^2)$ and a complete $\mathcal{O}(\alpha_s^3)$ calculation respectively or from numerical physically motivated fits. Results for both $\bar{f}^{(1)}$ and $f^{(1)}$ are again given in [33] and [34].

From our perturbative expansions in Equations (3.4) and (3.5), we see that the expansion parameter is that of the mass of the quark, m. Here we see clearly for the first time the reasoning behind statements about the mass being important in perturbative expansions. The above expansions are why the question of whether the mass of the charm is "big enough" ($m_c \gg \Lambda_{\mathrm{QCD}}$) for reliable perurbative calculations exists. Correspondingly, the equations demonstrate why the beauty quark with a larger mass provides a more reliable perturbative expansion. Allied to this we have an uncertainty in the actual quark mass, which then feeds into the perturbative expansion.

The above perturbative calculation (of which [37] is another) is for single particle inclusive cross-sections. This has been extended in [38] to provide fully exclusive cross-sections allowing more detailed comparisons with the data. This was extensively done in [29] a few examples of which appeared in the first section of this chapter. This benchmark calculation uses what is referred to as the *massive* scheme [39], with certain extensions thereof called the *massless* scheme [40, 41, 42]. These schemes will now be discussed in turn.

3.2.2 Massive Scheme

The massive scheme assumes the gluons and light quarks to be the only active partons in the photon, the heavy quarks not contributing to the evolution of the running coupling constant or the structure functions of the proton or photon. The heavy quark is produced dynamically in the hard sub-process. Therefore we have only two LO resolved processes,

$$gg \to Q\bar{Q}, \quad q\bar{q} \to Q\bar{Q},$$

where the former process is expected to dominate over the latter by significant factors of approximately three or four depending on the parametrisations used [43, 44].

The massive calculation for photoproduction [45] is heavily based on the hadroproduction calculations [38, 46]. The calculation is implemented as an effective "parton Monte Carlo" generator and can be used widely.

We can see the problem with our perturbative calculation; that of the mass in the perturbative expansion. Only when the coefficients of the coupling constant remain small will our expansion be reliable. However, a limitation of the method arises at high p_T, where terms of the form, $\log(p_T^2/m^2)$, become large, forcing the series to diverge. In the massive scheme, soft and collinear divergences are treated by generating sequences of correlated events such that cancellation of the divergences occurs. This method developed in [47] removes the need for artificial regularisation required when a light parton accompanies the heavy quark pair. Alternatively, these logarithms need to be resummed by treating the heavy quark as massless and leading to a reduced sensitivity to the renormalisation and factorisation scale. The scale at which the resummation of these logarithms becomes important is as yet uncertain, but phenomenological analyses show this is at large p_T of about 20−25 GeV [48].

3.2.3 Massless Scheme

The massless scheme treats the charm quark as an additional active flavour above some threshold. Below this threshold, $\mu^2 \sim m_c^2$, the quark reverts to an inactive flavour, the light quarks and gluons being the only active flavours as for the massive scheme. This massless scheme allows the resummation of the logarithms in p_T^2/m^2 providing perturbative fragmentation functions for the heavy quark containing the logarithmic dependence. However, the method is not reliable at

$p_T^2 \sim m^2$ [49] and so total cross-sections cannot be calculated. As a result of the method, we have extra LO resolved processes;

$$gQ \to gQ, \quad qQ \to qQ,$$

which are termed flavour excitation processes and an example is depicted in Figure 2.5b. These processes which are present in the massless scheme as part of the structure of the photon, also in some proportion contribute in the massive scheme, but only in the hard sub-process.

The fragmentation functions, D_k^Q, can be evaluated in perturbative QCD at a scale of the heavy quark mass and evolved up to the factorisation scale through the Altarelli-Parisi equations. They are given by the following,

$$D_Q^Q(x,\mu^2) = \delta(1-x) + \frac{\alpha_s(\mu)C_F}{2\pi}\left[\frac{1+x^2}{1-x}\left(\log\frac{\mu^2}{m^2} - 2\log(1-x) - 1\right)\right]_+, \tag{3.6}$$

$$D_g^Q(x,\mu^2) = \frac{\alpha_s(\mu)T_F}{2\pi}\left(x^2+(1-x)^2\right)\log\frac{\mu^2}{m^2}, \tag{3.7}$$

where the massive logarithms are contained in the fragmentation functions as stated previously. The QCD colour factors are, $C_F = 4/3$ and $T_F = 1/2$. The splitting functions from light quarks to heavy quarks are zero.

Comparison of the two schemes, massive and massless has been performed by one of the groups [48] and the two schemes found to yield similar results. The comparison of the (unphysical) direct and resolved however, shows differences but the (physical) sum of the two demonstrates good agreement as is shown in Figure 3.3.

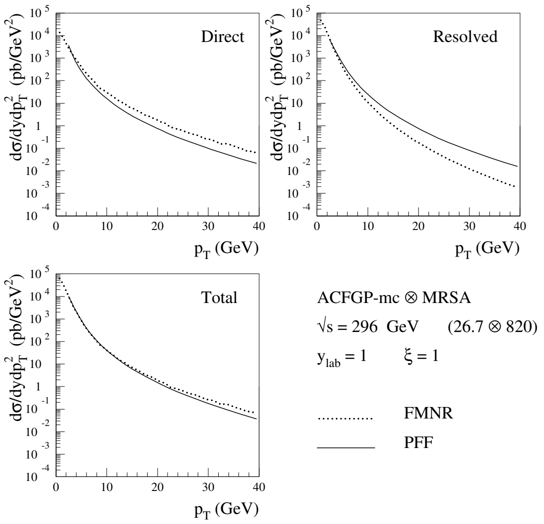

Figure 3.3: *Comparison between the massive (FMNR) and massless (PFF) calculations for charm photoproduction p_T distribution (from [48]).*

The two descriptions can be used for comparison with HERA data for all heavy quarks, c, b and t. The calculations themselves have been performed in the literature for predominantly charm and beauty and we can now start to compare particularly the charm calculations with HERA data. The quantity of data for the production of heavy quarks at HERA has so far been rather small but is increasing. Serious comparisons have now been made between data and the two schemes above espoused. In the next section we will discuss the methods for tagging heavy quarks at HERA and then discuss some results with respect to comparisons with the above schemes.

3.2.4 Identification of Open Heavy Quark Production at HERA

Identification of open heavy quarks at HERA has so far primarily been achieved through the tagging of decay products of the $D^*(2010)$ meson as a means of selecting charm. Most currently published data on open heavy quark production in photoproduction and DIS from both ZEUS and H1 have used the D^* tagging method. No published data on open beauty production from ZEUS or H1 currently exists. For the most recent publications on charm production from both collaborations, see [50] and [51]. The tagging method for the D^* meson relies on the identification of its decay products in two decay channels:

$$D^{*+} \rightarrow D^0\pi_s^+ \rightarrow (K^-\pi^+)\pi_s^+, \tag{3.8}$$

$$D^{*+} \rightarrow D^0\pi_s^+ \rightarrow (K^-\pi^+\pi^+\pi^-)\pi_s^+, \tag{3.9}$$

where the charge conjugate process is also implied. The small mass difference $\Delta M = m(D^*) - m(D^0) = 145.42 \pm 0.05$ MeV [52] yields a low momentum, “soft” pion, π_s. This value is just above the threshold of the $m(K\pi\pi_s) - m(K\pi)$ and the $m(K\pi\pi\pi\pi_s) - m(K\pi\pi\pi)$ distributions where the phase space contribution is small [53].

The only other method published in [51], by the H1 collaboration is the tagging of inclusive decays of the $D^0(1864)$ meson to a $K\pi$ pair. Without the use of a microvertex detector for the tagging of secondary vertices and the pre-1997 limitation in luminosity, further methods of tagging heavy quarks have proved difficult. The D^* meson tagging method also suffered from statistical limitations until the use of the 1996 and 1997 combined data sample as in this thesis and [50]. Considering the branching ratios of the above processes, we can understand why. The $c \to D^*$ ratio has been measured to be 22.2±0.2% [54]. The branching ratios for those decays in Equations (3.8) and (3.9) are $2.63 \pm 0.08\%$ and $5.2 \pm 0.3\%$ respectively [52]. The large increase in statistics now available at HERA has opened up the oppportunity to study other decay channels of heavy quarks. There is the possibility of tagging other meson decay channels via particle identification techniques or leptonic or semi-leptonic decays to electrons or muons. In this thesis, we investigate a new decay channel in photoproduction, that of inclusive decays to electrons. The inclusiveness of the decay implies a large branching ratio. Extensive work (although not yet published) has already been done on decays of charm to electrons in DIS at ZEUS [55, 56].

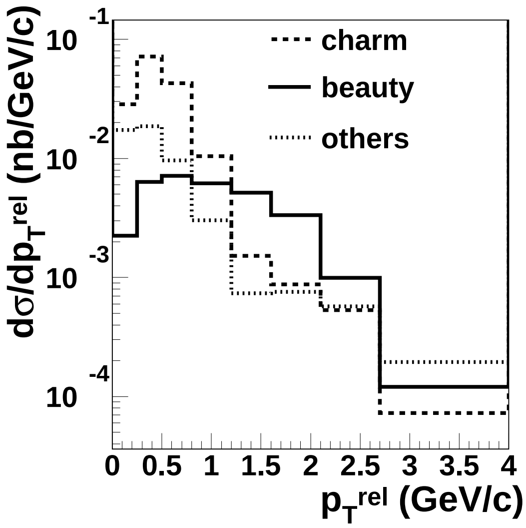

Figure 3.4: *Hadron level Monte Carlo predictions for p_T^{rel} in the cross-section region to be measured, Equation (8.2).*

The isolation of electrons uses particle identification information as will be detailed in Chapter 7. The identification of muons from heavy quark decays uses the muon chambers. The separation of those decays from different quarks then has to be addressed if we want to make a measurement of charm or beauty, the same method being used for both decays to muons and electrons. All further discussions on the quark separation will be specific to electrons unless otherwise stated. Naturally, the detection of secondary vertices would greatly simplify the procedure, but this information is not currently available at ZEUS. We therefore have to consider other methods and properties of the quarks and their decay products. For example, we would expect events containing beauty quarks to be more enhanced at high x_γ^{obs} than for charm or lighter quarks and so only considering high x_γ^{obs} events could be effective for a beauty measurement. However, the method of separation used in this thesis is by considering the momentum of the electron transverse to the axis of the jet which the electron is closest to. This quantity we henceforth refer to as p_T^{rel}. The quantity is larger for electrons decaying from beauty quarks than for charm or light quarks as can be seen in Figure 3.4. Figure 3.4 shows the p_T^{rel} distribution as predicted by Monte Carlo in the kinematic region under study; Equation (8.2). Shown are the contributions for charm decays (63%), beauty decays (16%) and other decays (21%). The separation of what constitutes the different contributions is explained in Chapter 5, where the Monte Carlo used is discussed. Figure 3.4 clearly demonstrates a marked difference with decays from beauty quarks populating large values. Then using Monte Carlo with the three components, we can allow their relative contributions to vary and fit them to the measured data. This will give us a percentage for the component of beauty required and hence the chance of a possible observation.

An advantage of looking at an inclusive electron sample is that we can measure properties of both charm and beauty quarks, containing both in our final sample. The second analysis performed in this thesis which looks for electrons provides us with another method for tagging charm at HERA allied to the reconstruction of D^* mesons. Perhaps more significantly, decays to leptons currently provide us with the only method available to tag beauty at ZEUS.

3.2.5 Heavy Quark Results from HERA

Recent results on the production of D^* mesons [50] have allowed an extensive comparison with massive and massless calculations. This paper has superceded the previous 1994 results [57] in which comparisons were also made to massive [39] and massless calculations [40]. In [50], inclusive cross-sections for the D^* meson were measured and the properties of dijet events with a tagged D^* meson were investigated. Before discussing the measurements and comparisons with data we first discuss how the NLO calculations are interfaced to be directly comparable with a cross-section in terms of a hadron and not the quark itself.

For the massive calculation, the MRSG [58] structure function for the proton and the GRV-G HO [59] structure function for the photon were used. The renormalisation scale was set to, $\mu_R = \sqrt{m_c^2 + p_T^2}$ and the factorisation scale twice this value, where the value for the charm mass, $m_c = 1.5$ GeV was used. The charm is then fragmented into a D^* meson using the Peterson fragmentation function [60], $f(z) \propto [z(1 - 1/z - \varepsilon/(1 - z))^2]^{-1}$, where z is the fraction of the momentum of the charm quark taken by D^* meson. We then achieve a cross-section in terms of the D^* meson by convoluting the partonic cross-section with the fragmentation function. The value of ε was initially chosen to be $\varepsilon = 0.06$ from [39] as recommended to be the central value for D mesons [61]. Recent fits to e^+e^- data [42] have suggested a lower value of $\varepsilon = 0.02$ is more appropriate and so was also used.

In the case of the massless calculations, the CTEQ4M [62] structure function for the proton and the GRV-G HO [59] structure function for the photon were used by both sets of authors. The renormalisation and factorisation scales and the charm mass are the same as before. The non-perturbative component of the fragmentation is fitted to the Peterson function [60], the perturbative fragmentation has the forms as in Section 3.2.3. The fit to the Peterson function was performed using recent e^+e^- data [63] on D^* production to extract the ε parameter. The two fitted values for the specific calculations are $\varepsilon = 0.116$ [40] and $\varepsilon = 0.02$ [42]. Alternative fitting functions, besides the Peterson form, for the description of the e^+e^- data were also used, yielding similar results.

The decays of the D^* meson have been discussed in the previous section and the experimental techniques will be discussed in Chapter 6. In [50] D^* mesons were reconstructed through the decay channels in Equation (3.8) and (3.9). For the inclusive cross-section measurements, candidates were selected with $p_T(D^*) > 2$ GeV/c in the pseudo-rapidity region, $|\eta(D^*)| < 1.5$. Photoproduction events were defined by a photon virtuality, $Q^2 < 1$ GeV^2 and a photon-proton centre of mass energy, $130 < W < 280$ GeV.

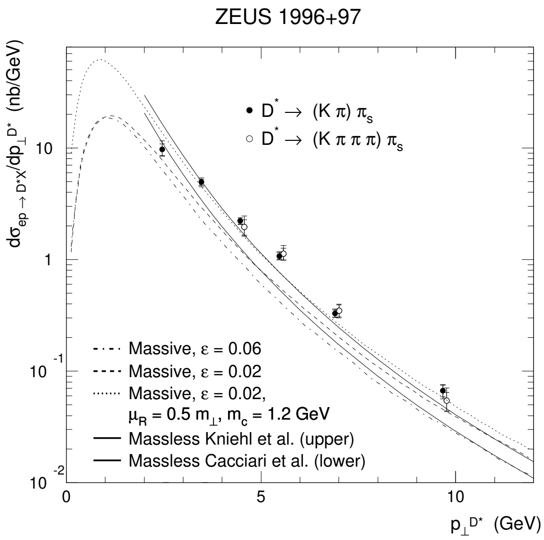

Figure 3.5: *Differential cross-section, $d\sigma/dp_T^{D^*}$, for D^* photoproduction for two decay channels. The data is compared to massive calculations and the two massless calculations.*

The differential cross-section, $d\sigma/dp_T^{D^*}$, is shown in Figure 3.5. The displayed data are for the two decay channels and they are compared to the massive and massless calculations. The two lowest massive curves lie consistently below the data for all $p_T(D^*)$. The two curves are for the different ε parameters,

$\varepsilon = 0.06$ (dot-dashed line) and $\varepsilon = 0.02$ (dashed line), with the nominal values for the scales and charm mass. Choosing extreme values of the scale and charm mass (dotted line) displays reasonable agreement but still lies too low for the three central points in $p_T(D^*)$. The massless calculations (solid) also generally lie below the data. Of significance is the disagreement between the two massless calculations in normalisation which must be resolved, the shapes being similar. Also of significance is the comparison between the massless and massive calculations as a function of $p_T(D^*)$. The low $p_T(D^*)$ data is better described by the massless than the massive calculations, with the two converging at higher $p_T(D^*)$. However, as was mentioned previously, the massive calculation is supposed to be more relevant at $p_T \sim m_Q$ and the massless at $p_T \gg m_Q$, which does not appear to be the case in Figure 3.5. The hardening of the massive calculation relative to the massless calculation as we increase in p_T is however expected (see Figure 3.3). Before making firmer statements we will move onto the cross-sections as a function of $\eta(D^*)$ in Figure 3.6.

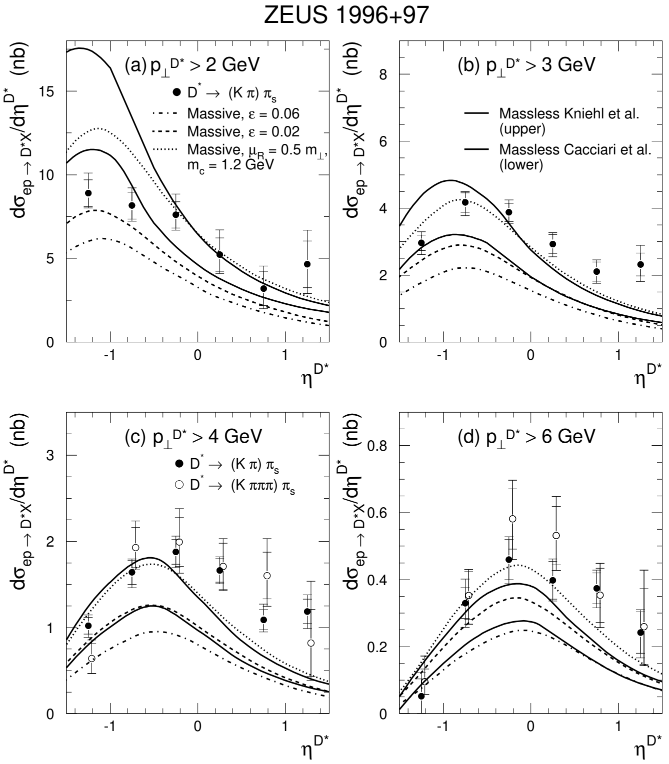

Figure 3.6: *Differential cross-section, $d\sigma/d\eta^{D^*}$, for D^* photoproduction for two decay channels in ranges of $p_T^{D^*}$. The data is compared to massive calculations and the two massless calculations.*

In Figure 3.6 the differential cross-sections, $d\sigma/d\eta^{D^*}$, are shown for four minimum $p_T(D^*)$ values. The massive and massless curves are again displayed as for the $p_T(D^*)$ cross-section. For the nominal scale and charm mass values, the massive calculations generally lie below the data. By choosing the extreme values we again receive a higher cross-section but this lies below the data in the forward region. As was performed when comparing to the fixed target data, a "k_T kick" was folded into the massive calculation. This had little effect, increasing the cross-sections by about 10%. In the case of the massless calculations, we again see a difference in the overall normalisation. The calculations agree generally in shape, but lie below, the measured data paricularly at high $p_T(D^*)$ and forward $\eta(D^*)$.

The above results represent the most significant comparison of data with massive and massless NLO calculations for charm production published at HERA. Clearly more measurements and hence comparisons to theory are needed for a more complete understanding of charm quark production. Measuring the beauty quark would also be of benefit providing us with a more rigourous test of QCD, being less dependent on non-perturbative factors. A measurement of Υ production has been preformed by the ZEUS collaboration [64]. The measured elastic Υ photoproduction cross-section was found to lie above QCD predictions. However, a more recent calculation [65] shows good agreement between the data and the QCD prediction. Open beauty production has been observed at HERA by the H1 collaboration and a preliminary cross-section measured [66]. The cross-section was found to be a factor of ~ 5 higher than calculations based on LO QCD models. This will be discussed further in Chapter 9 and compared to the results shown in this thesis. Also, results from hadron colliders have caused much speculation as reviewed in the next section.

3.3 Beauty Production at Hadron Colliders

The beauty quark differential p_T spectrum has been measured at hadron colliders by integrating over a rapidity range, y_{max}, above a given momentum threshold p_T^{min}, such that,

$$\sigma(p_T^{min}) = \int_{|y|<y_{max}} dy \int_{p_T>p_T^{min}} dp_T \frac{d^2\sigma}{dy dp_T}. \tag{3.10}$$

NLO QCD calculations exist for this distribution [67, 68] and the cross-section has been measured by the UA1 experiment at CERN and the CDF and D0 experiments at the TEVATRON. The UA1 measurement restricted the rapidity to $|y| < 1.5$ with a centre of mass energy, $\sqrt{s} = 630$ GeV [69]. The experiment measured four different decay channels, but all with a muon in the final state, finding reasonable agreement between the data and QCD calculation. Through extensive study of many decay channels, the CDF experiment has also measured the cross-section in Equation (3.10), for a rapidity limit, $|y| < 1$ and a centre of mass energy, $\sqrt{s} = 1800$ GeV [70]. Similarly, the D0 collaboration has also produced results in the above rapidity region for the same centre of mass energy [71]. The results from the three collaborations have all been compared to the NLO QCD calculations and collected together in [29]. We show the comparison with the NLO calculations for the CDF collaboration by way of example in Figure 3.7. From Figure 3.7, we see that the data lies consistently above the central theoretical prediction, whilst being compatible with the upper limit predictions for extreme values of the beauty mass and scale as detailed in the caption.

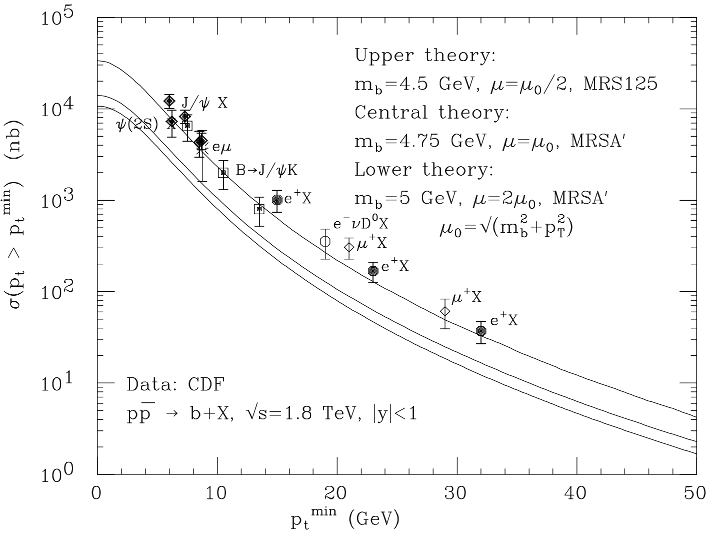

Figure 3.7: *CDF data on the integrated b-quark p_T distribution compared to NLO QCD (from [29]).*

A more revealing comparison was performed in [29], in which the ratio of the measured data to the theoretical prediction was analysed as a function of p_T^{min} for the results from all three collaborations. The results are shown in Figure 3.8.

The dotted line is a constant fit to the data points, the value given in the top right-hand corner for each experiment, and the solid lines are the upper, central and lower theoretical predictions. From Figure 3.8, we see that the three experiments differ in the factor they lie above the theoretical prediction, the CDF data being particularly high and having a large spread especially at low p_T^{min}. The general shape of the data is predicted by perturbative QCD, the upper limit reproducing the magnitude in the case of the UA1 and D0 data.

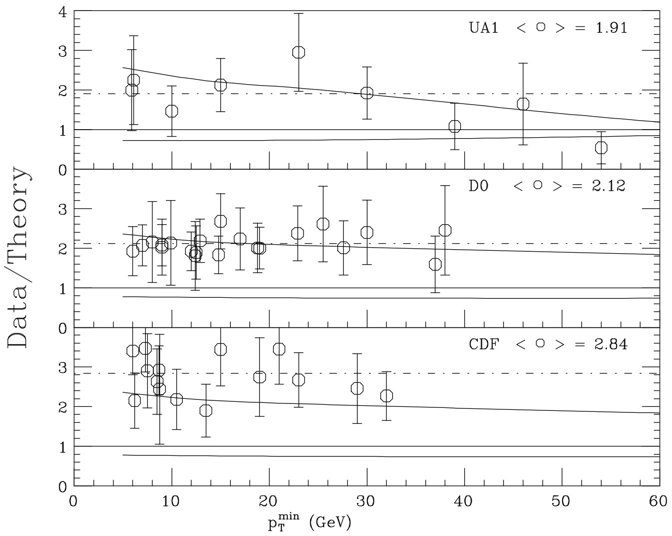

Figure 3.8: *Comparison between experimental data and theory for the integrated b-quark p_T distribution (from [29]).*

The results from hadroproduction shown are reasonably provocative representing an "upper limit" of pQCD predictions and question what the results in photoproduction would be. As was said no measurements or even observations of open beauty production have so far been published at HERA and results compared to NLO calculations is an obvious goal.

3.4 Heavy Quark Jets

The study of jets containing heavy quarks, should allow us to test perturbative QCD predictions more thoroughly than inclusive measurements. The transverse energy distribution of a jet containing a heavy quark should be more reliable than the transverse momentum of the heavy quark. As we have seen previoulsy, at large quark momentum, we have large logarithms of the form $\log(p_T^2/m^2)$ in the perturbative expansion due to the emission of collinear gluons. However, in the measurement of E_T of the jet, these collinear gluons are included in the jet along with the heavy quark so analagous large logarithms do not appear.

The limitation in statistics so far achieved at HERA prevented the study of heavy quark jets until [50]. In [50] the $x_\gamma^{\rm obs}$ distribution for dijet events with a tagged D^* meson was measured. The measurement forms part of this thesis and is discussed in some detail in Chapter 6 so will not be further discussed here.

The use of jets is also essential to this thesis for the study of direct and resolved processes and for the identification of beauty quarks.

3.5 Summary

From this chapter, we can see that the knowledge of heavy quark production, both experimentally and theoretically, in photoproduction is somewhat mixed and limited. Elements of charm production have been measured but do not reveal a consistent picture, whilst little information exists on beauty production. The aim of this thesis is to make measurements of heavy quark production and provide us with at least the start of a coherent picture at HERA.

Chapter 4

Event Reconstruction

Event and jet kinematics are reconstructed from measured quantities with a particular resolution and may suffer from systematic shifts. We discuss the reconstruction of the relevant event variables, y and Q^2, and the jet variables, E_T^{jet}, η^{jet} and ϕ^{jet}. Having defined these kinematic variables we then discuss the reconstruction of our measured cross-section quantities, $x_\gamma^{\rm obs}$ and p_T^{rel}.

4.1 Reconstruction of y and Q^2

There are many ways of reconstructing the variables, y and Q^2 [72], two of which are here discussed. The two used in this thesis are the so-called "electron-method" and the "Jacquet-Blondel method" and are described in the following sections.

4.1.1 Electron Method

The electron method is theoretically simple and relies only on the knowledge of the energy of the scattered lepton, E_e' and the angle of the scatter, θ_e. For a given initial lepton energy, E_e, we can write our variables, y and Q^2 as the following:

$$y_e = 1 - \frac{E_e'}{2E_e}\left(1 - cos\theta_e\right), \tag{4.1}$$

$$Q_e^2 = 2E_eE_e'\left(1 + cos\theta_e\right). \tag{4.2}$$

Photoproduction events are defined by seeing no scattered lepton in the calorimeter, that is, high values of θ_e. At ZEUS, the angles through which the lepton scatters when it is not seen in the calorimeter are greater than $\sim 177°$. From Equation (4.2), we can see that this corresponds to low values of the photon virtuality, Q^2. In this thesis (and for ZEUS photoproduction analyses in 1996 and 1997 in general) Q^2 is limited to be less than 1 GeV^2. The region of photoproduction then allows us to approximate y_e to be,

$$y_e \approx \frac{E_e - E'_e}{E_e} = \frac{E_\gamma}{E_e}, \tag{4.3}$$

where E_γ is the energy of the incoming photon. We can therefore interpret y_e to be the fraction of the incoming lepton's energy carried by the photon. In Monte Carlo simulations where we know all about the scattered lepton, the above formulae can be used. However, in the data, we have an effective *anti-tag* on the lepton as it is scattered down the beam-pipe. Consequently, we consider another method of reconstructing our kinematic variables.

4.1.2 Jacquet-Blondel Method

The Jacquet-Blondel method [73] calculates the variables y and Q^2 from the hadronic final state. The hadronic final state is all particles except the scattered lepton and summing over these gives:

$$y_{JB} = \frac{\sum_i (E_i - p_{z_i})}{2E_e}, \tag{4.4}$$

$$Q^2_{JB} = \frac{(\sum_i p_{x_i})^2 + (\sum_i p_{y_i})^2}{1 - y_{JB}}. \tag{4.5}$$

Obviously, the above sum cannot experimentally be over hadrons, but is for calorimeter cells. If the scattered lepton is found in the calorimeter, then the cluster of cells associated with it are eliminated from the calculation. The identification of the scattered lepton is not 100% efficient, so its energy deposit will sometimes enter into the above summations. This will yield high values of $y_{JB} \sim 1$, which are removed in the case of photoproduction events as DIS contamination. Before calorimeter cells can be used for the calculation of y_{JB} and Q^2_{JB}, their positions are first corrected for the position of the event vertex. This process is essential before any quantity can be reconstructed from calorimeter cells such as islands and jets which are discussed in the next section.

4.2 Jet Reconstruction

Within the ZEUS Collaboration, use is made of two types of jet algorithm for photoproduction analyses. These are the "cone" and the "cluster" algorithms. Two variants of the cone type are used - EUCELL [74] and PUCELL [75] - wheras the cluster algorithm used is the so called "k_T" algorithm [76] implemented in the KTCLUS library of routines [77].

Detailed discussions of each of these can be found elsewhere [78], so only a brief discussion of these will be included here.

4.2.1 Cone Algorithms

Two cone algorithms are used, defined in a standard form by the Snowmass Convention [79]. The Snowmass Convention defines the transverse energy and the coordinates of a jet as;

$$E_T^{jet} = \sum_i E_{t,i}$$

$$\eta^{jet} = \frac{1}{E_T^{jet}} \sum_i E_{t,i}\eta_i \tag{4.6}$$

$$\phi^{jet} = \frac{1}{E_T^{jet}} \sum_i E_{t,i}\phi_i$$

where the sum runs over all hadron or calorimeter cells within the cone defined by a given prescribed radius, R, in $\eta - \phi$ space.

PUCELL is an adaptation of the jet algorithm used at CDF. Both it and EUCELL use the concept of pre-clustering, but then diverge in the method of combination.

In PUCELL, a pre-cluster is formed by combining all objects within a radius, R, with the highest E_T object. This is done until all objects are assigned to a pre-cluster. The centre of the pre-clusters are then recalculated and the process repeated until some stable situation (or some maximum number of iterations) is reached. The formation of clusters is then complete and those that have a transverse energy above a certain threshold are considered jets.

In EUCELL, clusters are determined using a grid in $\eta - \phi$ space. The size of the cells that make up the grid is determined such that $\Delta\eta^{gridcell} \approx \Delta\phi^{gridcell} \approx R/2$. By then sliding a 3×3 cell window over the grid, a potential pre-cluster is then formed. To be called a pre-cluster, it must be above some prescribed transverse energy. A cone of radius R is then placed around the pre-cluster and an iterative process as in PUCELL is performed. The first jet is defined as the cone with the highest transverse energy. Successive jets are then determined from the remaining objects by the same procedure until there exist no more cones above a certain energy threshold.

4.2.2 Clustering Algorithm

The use of the aforementioned cone algorithms leads to ambiguities. The treatment of overlapping jets is *not defined* within the Snowmass convention, nor is the question of seed finding for the initial jets. This leads to theoretical ambiguity with respect to jet merging in the final state and the process is not infra-red safe at NNLO without modification [80].

These problems are avoided by the use of the k_T algorithm, as the merging criterion is completely defined for any given final state. As such, in these analyses we avoid the problems inherent in the use of the cone algorithm and use only the k_T algorithm.

The k_T algorithm was initially designed for use in e^+e^- annihilation, wheras the presence of hadron remnants in hadron-hadron, DIS or photoproduction events means that it must be used in a modified form which maintains the property of factorisation of initial state radiation [77].

For a cluster algorithm we must specify some distance measure which determines *which* particles will be merged, together with a recombination scheme which defines *how* they will be merged. In photoproduction we run the algorithm in the laboratory frame using the inclusive recombination scheme of Ellis and Soper [81] in a mode which is invariant under longitudinal boosts, the recombination scheme being similar to that of the Snowmass Convention (the so-called "*pt*" mode). The algorithm scheme depends on a parameter R and is analagous to a cone radius.

To decide which particles should be merged, for each particle i we form the quantity,

$$d_i = E_{T,i}^2$$

and for each pair of particles, ij, we form the quantity

$$d_{ij} = \min(E_{T,i}^2, E_{T,j}^2)\left[(\eta_i - \eta_j)^2 + (\phi_i - \phi_j)^2\right]/R^2.$$

The d_i is the limiting case of small angles of the "distance" between particle i and a large mass remnant travelling along the z direction.

If the smallest of all the d values is a d_{ij}, then particles i and j are merged into a single object, k. If however, the smallest value is a d_i then this particle is considered "complete" and is removed from further clustering. This process is then repeated until all the objects have been removed, producing an E_T ordered list of objects.

The scheme for merging the objects is similar to the Snowmass Convention, and is,

$$E_{T,k} \equiv E_{T,i} + E_{T,j} \tag{4.7}$$

$$\eta_k \equiv \frac{E_{T,i}\eta_i + E_{T,j}\eta_j}{E_{T,k}} \tag{4.8}$$

$$\phi_k \equiv \frac{E_{T,i}\phi_i + E_{T,j}\phi_j}{E_{T,k}}. \tag{4.9}$$

Therefore the scheme assigns objects to jets in a well-prescribed manner, and as each quantity $E_T, \Delta\eta, \Delta\phi$ in the distance parameter are each invariant under longitudinal boosts, so the property of boost invariance of the jet finding itself is retained.

4.3 Reconstruction of $x_\gamma^{\rm obs}$ and p_T^{rel}

Having discussed how we reconstruct jets and y, the formation of $x_\gamma^{\rm obs}$ as in Equation (2.29), is then reasonably trivial. We simply replace y with y_{JB} and we then have our value for $x_\gamma^{\rm obs}$ from calorimeter quantities. In the Monte Carlo, we measure y directly so can use Equation (2.29) with no further adaptation.

The quantity p_T^{rel} is reconstructed from the electron momentum and the jet axis and is simply given by,

$$p_T^{rel} = |\mathbf{p_e} \wedge \hat{\mathbf{p}}_\mathbf{j}|,$$

where $\mathbf{p_e}$ is the electron momentum and $\hat{\mathbf{p}}_\mathbf{j}$ is the unit jet axis, simply being $\hat{\mathbf{p}}_\mathbf{j} = \mathbf{p_j}/|\mathbf{p_j}|$, where $\mathbf{p_j}$ is the jet momentum.

Chapter 5

Monte Carlo Simulation

5.1 Monte Carlo Overview

From our experimentally measured observables, we need to apply a correction procedure which converts these observables from being calorimeter or tracking based quantities into hadron quantities and hence cross-sections. We also need to account for acceptances and efficiencies of measurements made. To do the above we rely on Monte Carlo techniques to simulate aspects of the physics under investigation and of the ZEUS experiment.

The initial procedure is the simulation of the actual physics events themselves. We therefore rely on the Monte Carlo to describe in some way the physics espoused in Chapters 2 and 3. They use principles of pQCD to simulate LO hard sub-processes and use models of non-perturbative phenomena to simulate soft physics processes such as parton density functions and hadronisation.

Following this, we then take what is a collection of hadronic states for a certain physics process we are interested in and simulate their path through the ZEUS detector. The MOZART package [1] which is based on the GEANT program [82] simulates all detector components using all our current understanding of each specific component and the detector as a whole. The trigger decision procedure is then simulated by the ZGANA [83] program and the full offline reconstruction by the ZEPHYR package.

In the above way we simulate the physics processes and ZEUS detector for the analyses in this thesis. For this thesis we use two Monte Carlo programs for simultaion purposes - the HERWIG [84] and PYTHIA [85] Monte Carlo generators which are now discussed.

5.2 HERWIG Monte Carlo

The HERWIG (Hadron Emission Reactions With Interfering Gluons) Monte Carlo [84] is a general purpose generator with a large predictive power as a result of the relatively small number of free parameters. Particular attention is paid to being as independent as possible from non-perturbative parameters.

The factorisation scale for the hard sub-process, μ^2, is given by,

$$\mu^2 = \frac{2\hat{s}\hat{t}\hat{u}}{\hat{s}^2 + \hat{t}^2 + \hat{u}^2},$$

where, $\hat{s}, \hat{t}$ and $\hat{u}$ are the Mandelstam variables. The resultant cross-section is divergent in the limit of transverse momentum of the outgoing partons, $\hat{p}_T^2 \to 0$, so we introduce a minimum transverse momentum cut, $\hat{p}_T^{min}$. The value chosen, $\hat{p}_T^{min} > 2.5$ GeV should not bias our results as we measure jets of $E_T^{jet} > 6$ GeV.

The incoming and outgoing partons go through a process of showering in which hadrons are formed from the partons. The showering is initiated by each single parton splitting into many partons. Logarithms of the form $(\alpha_s \log(\mu^2/\mu_0^2))^n$ are resummed and the partons ordered in terms of their opening angle. The ordering is continued until the hadronisation scale is of the order of the lightest mesons.

Parton showers from the initial hadrons to the partons of the hard sub-process are treated differently. Backwards evolution from the hard sub-process proceeds until some cut-off and is matched to the parton density parametrisations of the initial hadrons.

Resolved photoproduction has an initial photon spectrum as generated by the EPA. The backwards evolution in HERWIG allows at each stage the possibility for a $\gamma \to q\bar{q}$ vertex in resolved events. For direct events, the LO matrix elements for 2$\to$3 scattering are used.

The transition from partons to hadrons after the parton shower then proceeds via a non-perturbative model called the *cluster* model, which groups the partons into colour neutral objects. The gluons are split into $q\bar{q}$ pairs and these are subsequently clustered into colourless objects via the colour connections generated in the parton shower. Each cluster is then fragmented into two hadrons or the lightest hadron for its flavour if the cluster is not massive enough. Finally the decay of unstable particles is simulated.

For the evolution of heavy quarks in the hard sub-process back to the photon, there are three possibilities. A heavy quark pair can result from the photon splitting directly, $\gamma \to Q\bar{Q}$, from a gluon splitting, $g \to Q\bar{Q}$, or be present when the evolution terminates. The latter represents heavy quark excitation below the factorisation scale as shown in Figure 2.6b. As the factorisation scale is set to be at the hard sub-process, the question of whether excitation processes occur is dependent on whether $p_T^2 > m_Q^2$. We can then see that with sufficiently high p_T jets, we will have "bottom excitation".

HERWIG version 5.9 is used throughout this thesis.

5.3 PYTHIA Monte Carlo

The PYTHIA Monte Carlo [85] is also a general purpose generator, sharing many common features with HERWIG, but also significant differences. There are two main differences in the perturbative phases of the respective models. For photoproduction events, the photon spectrum in PYTHIA is generated using the WWA for both direct and resolved photon processes. Secondly, the factorisation scale, μ^2, used is the transverse mass of the two outgoing partons, m_T^2, given by,

$$\mu^2 = m_T^2 = \frac{1}{2}\left(m_1^2 + p_{T_1}^2 + m_2^2 + p_{T_2}^2\right).$$

The parton shower is conceptually the same in both generators, but in PYTHIA the evolution is ordered in the virtuality of the radiated partons. The partons are hadronised using the Lund Symmetric String Fragmentation model [86]. In the Lund model, partons are connected by "strings", the strength of which is about 1 GeV/fm. As the partons move away from each other, the strings become more energetic, finally breaking to produce $q\bar{q}$ pairs. When the energy of a string is too small to enable further separation of the partons, hadrons are formed. Finally the unstable hadrons are decayed as in HERWIG.

PYTHIA version 5.7 is used throughout this thesis.

5.4 Monte Carlo Samples Generated

As two analyses are performed in this thesis, separate sets of Monte Carlo events were required for each. Consequently, HERWIG and PYTHIA Monte Carlo was generated for dedicated studies of D^* mesons and for dedicated studies of decays of quarks with an electron in the final state. A sample of dijet photoproduction Monte Carlo events was also generated for the study of jet energy corrections where a large sample of jet events were required.

The Monte Carlo generated for the D^* mesons was filtered to require a true D^* meson in the event. No impositions on jets were made as the Monte Carlo was also used for inclusive measurements [50]. Direct and resolved photon charm events were generated with the MRSG [58] structure function for the proton and the GRV-G HO [59] structure function for the photon. A suitably low value for the D^* transverse momentum of, $p_T(D^*) > 1.7$ GeV/c was used to filter events.

For the analysis of semi-leptonic decays to electrons, an electron filter combined with a jet filter was used. Events were selected at the hadron level if they contained at least two jets with,

$$E_T^{HADjet} > 3 \text{ GeV}; \quad |\eta^{HADjet}| < 3. \tag{5.1}$$

Consideration of the resolution of these events as in Chapter 7, Figure 7.26 and the cuts used in the analysis; $E_T^{CALjet} > 4$ GeV and $|\eta^{CALjet}|$ <2.4, demonstrates that the filter requirements will not impose a bias on our final sample. Similarly for the electrons, where the resolutions (Figure 7.25) are good and the analysis cuts are $p_T^{trk} > 1.6$ GeV/c and $|\eta^{trk}| < 1.1$ filtering electrons such that,

$$p_T^{e^-} > 0.5 \text{ GeV/c}; \quad |\eta^{e^-}| < 1.9, \tag{5.2}$$

also imposes no bias.

The HERWIG Monte Carlo generated was an inclusive dijet photoproduction sample with five active flavours using the CTEQ4D [62] structure function for the proton and the GRV-G LO [59] structure function for the photon. Default masses of $m_c = 1.55$ GeV and $m_b = 4.95$ GeV were used. We therefore accept all events which pass the jet and electron cuts in Equations (5.1) and (5.2) thereby keeping a sample with decays from beauty, charm and light quarks. As we expect contributions from all three in our final cross-section, this Monte Carlo sample provides us with what we would hope to be a reasonably complete description.

We use our generated PYTHIA Monte Carlo as a systematic check for our unfolding procedure and so was not used as completely as the HERWIG Monte

Carlo. We therefore only generated decays from heavy and not light quarks; the generation of which is fast. The generation procedure for light quarks is extremely time consuming and was therefore thought not necessary because the shapes of the "charm" and "other" p_T^{rel} distributions are similar as can be seen in Figure 3.4.

When we display a distribution in p_T^{rel} for Monte Carlo we classify it into and refer to it as three different samples; beauty, charm and other Monte Carlo. How the classification is peformed is important as using this classification, we determine our amount of beauty production in the data. We consider the outgoing partons in the hard sub-process. If one or both partons are beauty quarks then this is termed "beauty Monte Carlo". If one or both partons are charm quarks, then it is termed "charm Monte Carlo". If the two partons are neither beauty nor charm, then this is termed "other" Monte Carlo.

To gain extra events in our final cross-section comparison of data and hadron level Monte Carlo, we make use of the HZTOOL package [87]. HZTOOL allows us to generate large amounts of events for a given cross-section quickly for many different Monte Carlos and provided us with substantially more events to compare with than if only the standard Monte Carlo generation method was used. All cross-section comparisons use this generated Monte Carlo which has the GRV 94 LO [88] structure function for the proton and the GRV-G LO [59] structure function for the photon.

Comparison of physical quantities between data and Monte Carlo, will be reserved for the respective analyses chapters.

5.5 Jet Energy Corrections

5.5.1 Jet Resolutions

The measurement in the calorimeter of the jet parameters - transverse energy, E_T^{jet}, pseudorapidity, η^{jet} and azimuthal angle, ϕ^{jet} - deviate from the true values of the hadron jets. This is due to dead material in front of the calorimeter, the resolution of the calorimeter and particles which do not deposit energy in the calorimeter such as muons and neutrinos. Monte Carlo statistics are studied to account for these systematic effects. In the following sections for corrections, we use HERWIG.

Jet finding is performed on the final hadronic state and on the calorimeter cells. The calorimeter jets and hadron jets are then matched in $\eta - \phi$ space. A pair is considered matched when,

$$\Delta R(\eta, \phi) = \sqrt{(\eta^{CALjet} - \eta^{HADjet})^2 + (\phi^{CALjet} - \phi^{HADjet})^2} \tag{5.3}$$

is a minimum and $\Delta R(\eta, \phi) < 1$. For these matched jets, resolutions in η and ϕ and the energy ratio between hadron and calorimeter jets were considered.

By considering Figure 5.1, the dependence of the jet parameters on each other is demonstrated. Direct and resolved processes are displayed separately and the error shown is the spread on the mean. We can clearly see that the jets measured in the calorimeter have a smaller transverse energy than the hadron jets. The value of E_T^{CALjet} is typically 20% too low. Considering the dependence on η^{CALjet}, we see that the energy loss exhibits a dependence, ϕ^{CALjet} and η^{CALjet} itself showing no dependence; all variations or non-variations are the same for both direct and resolved processes. We also see a non-dependence of all variables on ϕ^{CALjet} and so we seek a correction as a function of E_T^{CALjet} and η^{CALjet}. These results are consistent with previous dijet analyses; for example, see [78].

5.5.2 Correction of Jet Energy

The transverse energy of the jets are corrected using the Monte Carlo such that the average energy of the hadron jets and those in the calorimeter are equal.

As was said previously, the transverse energy of the jet varies with the jet pseudorapidity and jet energy. Therefore a correction function of the form $C(E_T^{CALjet}, \eta^{CALjet})$ was determined such that:

$$E_T^{CORjet} = C(E_T^{CALjet}, \eta^{CALjet}).E_T^{CALjet} \tag{5.4}$$

where E_T^{CORjet} is the corrected transverse energy of the jet.

Figure 5.2 shows the variation of $E_T^{HADjet}/E_T^{CALjet}$ as a function of E_T^{CALjet} in bins of η^{CALjet} for matched calorimeter and hadron jets. The curves for the resolved and direct are shown separately and are consistent with those of the combined curves. For a bin, i, in η^{CALjet}, the correction function fitted, $C(E_T^{CALjet}, \eta^{CALjet})$, is of the form:

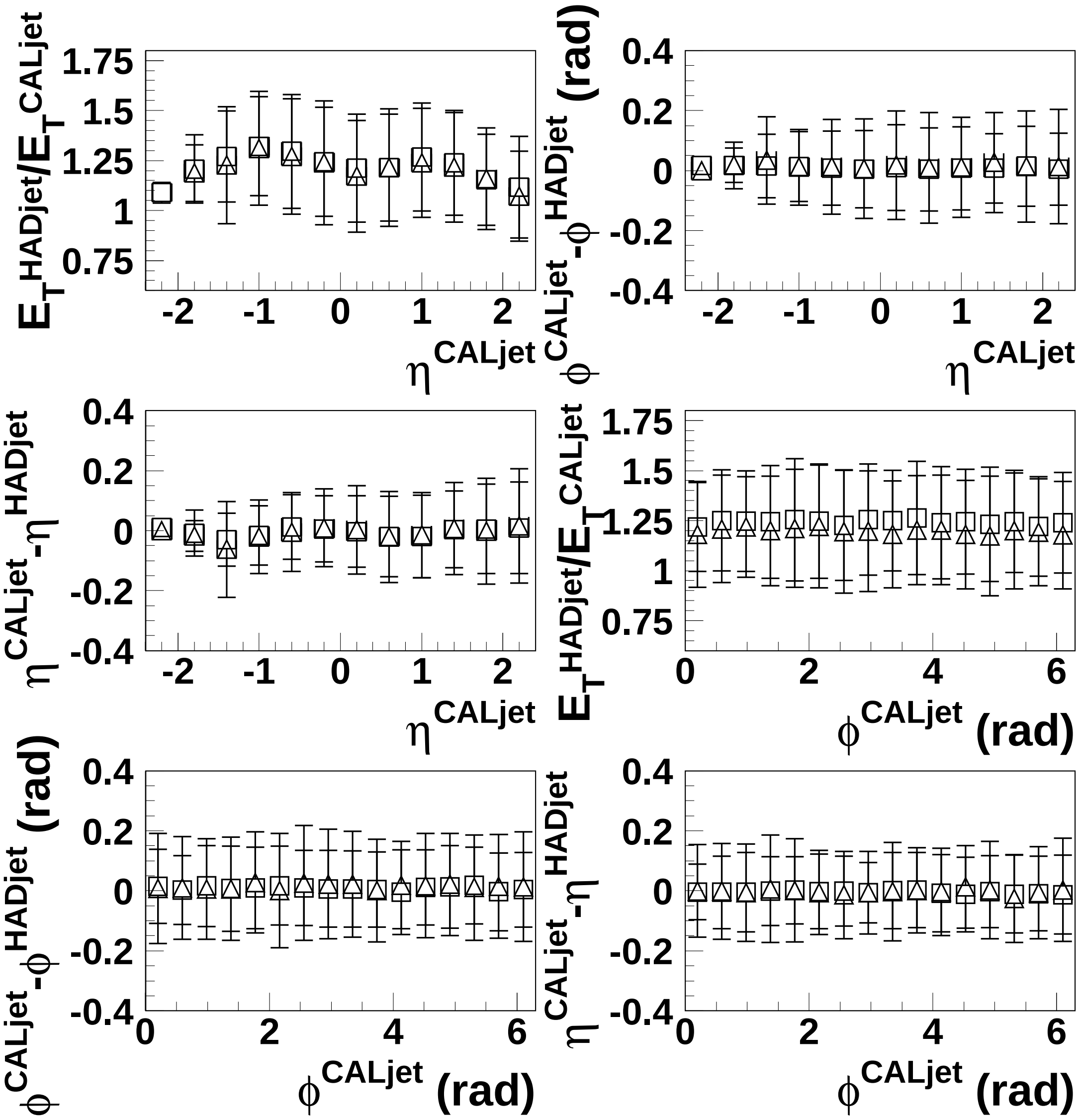

Figure 5.1: *Jet resolutions. The dependence of jet parameters on each other shown separately for direct (open squares) and resolved (open triangles). The dependence of* $E_T^{HADjet}/E_T^{CALjet}$, $\phi^{CALjet}-\phi^{HADjet}$ *and* $\eta^{CALjet}-\eta^{HADjet}$ *on* η^{CALjet} *and* ϕ^{CALjet} *is shown.*

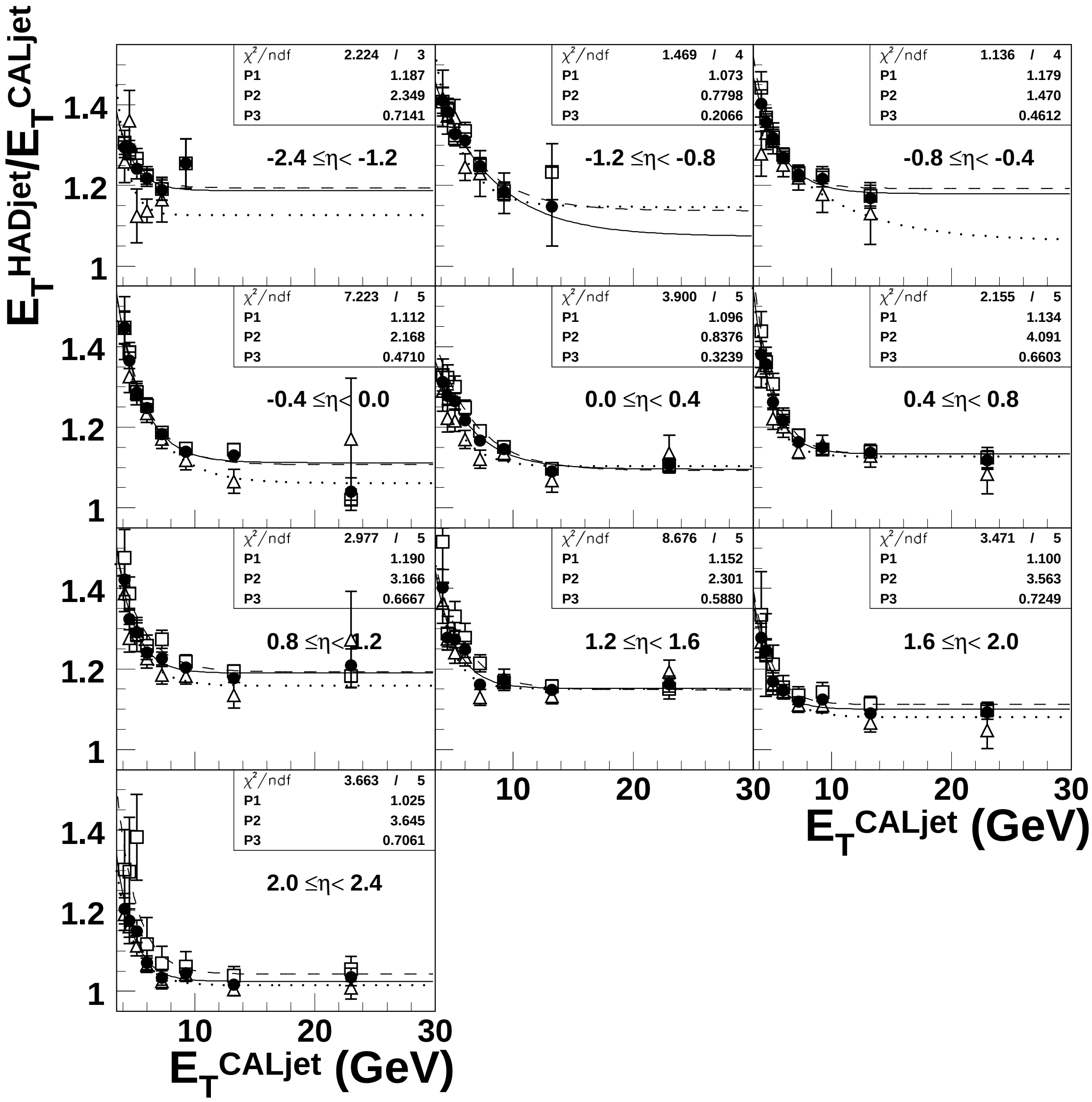

Figure 5.2: *The ratio of* E_T^{HADjet} *and* E_T^{CALjet} *versus* E_T^{CALjet} *in bins of* η. *The points and fit lines are shown for direct (open squares, dashed line), resolved (open triangles, dotted line) and resolved and direct combined (solid dots, solid line). The fit parameters shown are for the fit to the combined sample using the correction function,* $C(E_T^{CALjet}, \eta^{CALjet})$

$$C\left(E_T^{CALjet}, \eta^{CALjet}\right) = a_1\left(\eta_i^{CALjet}\right) + \exp\left(a_2\left(\eta_i^{CALjet}\right) + a_3\left(\eta_i^{CALjet}\right) \cdot E_T^{CALjet}\right) \tag{5.5}$$

With a maximum correction factor of about 1.48 for low E_T^{CALjet}, a cut of $E_T^{CORjet} > 6$ GeV for the lowest transverse energy jet is justified. We will in fact use asymmetric cuts on the corrected jets in both analyses of,

$$E_T^{CORjet1,CORjet2} > 7.0, 6.0 \text{ GeV}.$$

The reasoning behind this procedure of choosing asymmetric cuts will be explained later in Chapter 6.

The result of using these combined correction factors can be seen by applying them back to the Monte Carlo. This is achieved by plotting the ratio of the corrected calorimeter values of transverse energy and the hadron level values as a function of η^{CALjet} and ϕ^{CALjet}; Figure 5.3.

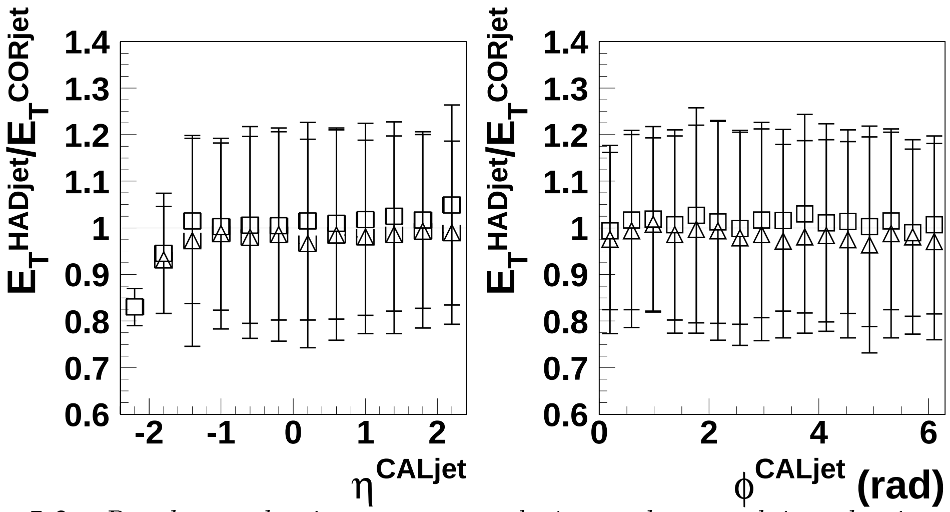

Figure 5.3: *Result on the jet energy resolutions when applying the jet energy corrections. The resolutions are shown again for direct (open squares) and resolved (open triangles) separately.*

As can be seen in Figure 5.3, the mean value is about 1 and not 1.2 and the pseudorapidity dependence is removed. The low values in the first two bins in η^{CALjet} arises from a lack of statistics in the rear direction. The same correction factor was used for the first three bins, with the result that the third bin dominates the first two. This was chosen as using three bins in the rear direction would be unreliable due to the inadequate statistics due to the large boost in the proton direction. By applying the overall correction on direct and resolved separately, one can see the justification in using a combined correction factor. The resolution of E_T remained roughly the same after as before correction.

5.6 Correction of y_{JB}

The value of y as calculated from the Jacquet-Blondel method, y_{JB}, clearly deviates from the true value of y, y_{true}; see Figure 5.4.

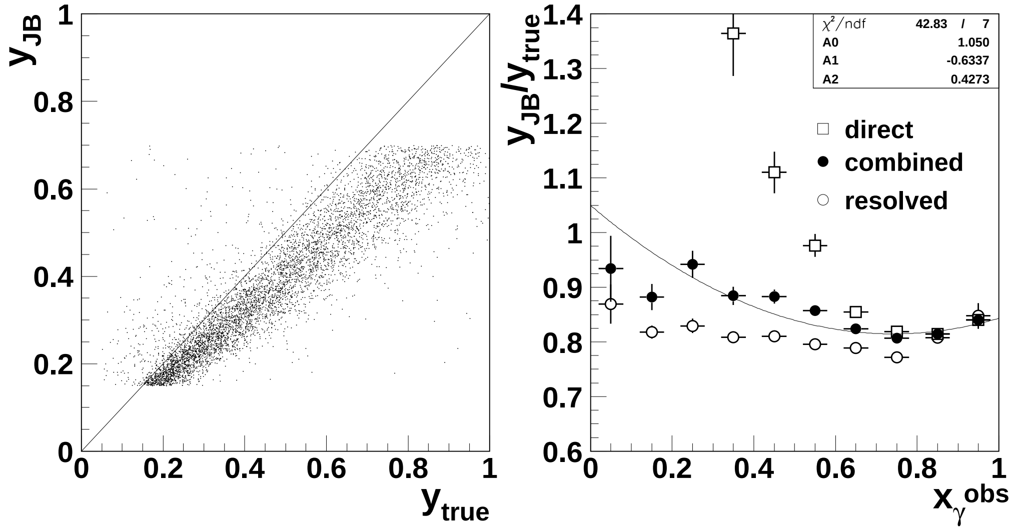

Figure 5.4: *Correction of the measurement of y. The correlation of y_{JB} and y_{true} (Left) is shown. Also displayed is the dependence of y_{JB}/y_{true} on $x_\gamma^{\rm obs}$ for direct (open squares) and resolved (open circles) and the combined sample (solid points) with the polynomial fit.*

The value of y_{JB} is systematically lower than y_{true}, as expected, due to energy losses as particles pass through dead material in front of the calorimeter or are lost down the rear beam-pipe. The resulting shift in y_{JB} is about 10%. This dependence can be corrected by studying the ratio of y_{JB}/y_{true} as a function of $x_\gamma^{\rm obs}$, as the shift is dependent on the presence of the photon remnant. The dependence on y_{JB} itself, E_T^{jet} and η^{jet} were also studied and found not to be significant. A dependence of y_{JB}/y_{true} on $x_\gamma^{\rm obs}$ can clearly be seen.

A polynomial was fitted to the sum of the direct and resolved components. The polynomial correction factor, $P(x_\gamma^{\rm obs})$ has the following form:

$$y_{corr} = y_{JB}/P(x_\gamma^{\rm obs}); \quad P(x_\gamma^{\rm obs}) = p_1 + p_2 x_\gamma^{\rm obs} + p_3 {x_\gamma^{\rm obs}}^2. \tag{5.6}$$

The correction to y_{JB} was then applied back onto the calorimeter level Monte Carlo. As the correction factor was determined from the combined direct and resolved samples, then its effect on direct and resolved separately was considered. As can be seen in Figure 5.5 the results of applying separately to resolved and direct yield similar results. There is an improvement in the resolution for both direct and resolved; the previous rms values were 0.085 and 0.094 for direct and resolved respectively. The value of y_{JB} is now closely correlated to y_{true} with a mean of about zero. This justifies the use of the overall correction factor even when applying it to direct and resolved samples separately.

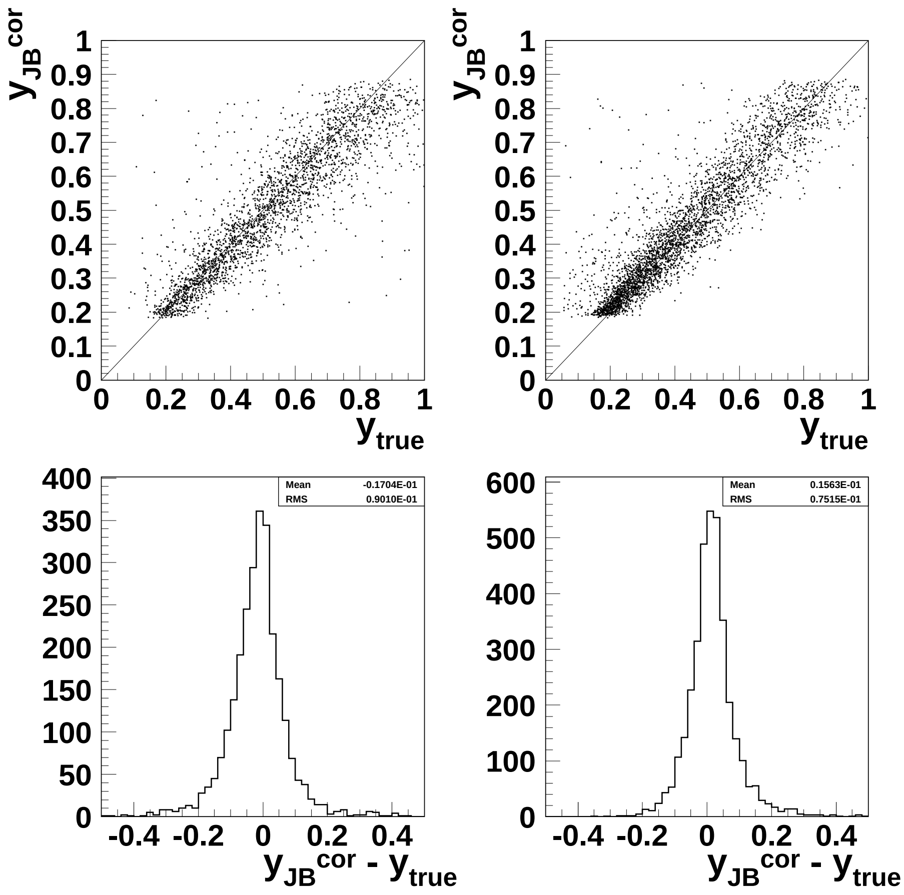

Figure 5.5: *Effect of the y_{JB} correction for direct (right) and resolved (left) separately on the correlation (top) and projection (bottom).*

Chapter 6

D^* in Dijet Photoproduction Analysis

Using data from the 1996 and 1997 running periods, studies of open charm production were made by looking for decays of the $D^*(2010)$ meson in dijet photoproduction events. Initially, dijet events were selected, and then D^* mesons were reconstructed within these events, through the observation of the decay chain,

$$D^{*\pm} \rightarrow D^0\pi_s^{\pm} \rightarrow (K^{\mp}\pi^{\pm})\pi_s^{\pm}. \tag{6.1}$$

By considering the mass of the D^0 meson, $m(D^0)$, and the mass difference,

$$\Delta m = m(D^0\pi_s) - m(D^0) \tag{6.2}$$

two mass resonances can be achieved. Using these tagged D^* mesons in jets, properties of heavy quarks can be found. In particular, the nature of the processes in charm production - direct and resolved photoproduction - was studied by determining the cross-section defined below.

6.1 Definition of the Cross-section

By considering photoproduction events with at least one D^* meson produced in the final state, $ep \rightarrow D^*X+$ dijets, a cross section in $x_\gamma^{\rm obs}$, the fraction of the photon's momentum participating in the hard process can be measured. With at least two jets in the final state, one of which is associated with one of the D^* mesons, a differential cross-section can be defined as:

$$\frac{d\sigma_{ep\rightarrow D^*X}}{dx_\gamma^{\mathrm{obs}}} \quad ; \quad 0 < x_\gamma^{\mathrm{obs}} < 1 \tag{6.3}$$

This was done in the kinematic region defined by the following;

$$0.2 < y < 0.8$$

$$Q^2 < 1 \text{ GeV}^2$$

$$E_T^{jet1,jet2} > 7, 6 \text{ GeV} \tag{6.4}$$

$$|\eta^{jet}| < 2.4$$

$$p_T(D^*) > 3 \text{ GeV/c}$$

$$|\eta(D^*)| < 1.5$$

The y interval corresponds to a γp centre-of-mass energy, $W_{\gamma p} \approx \sqrt{y.s}$ of $(134 < W < 269)$ GeV. The cut on Q^2 will be explained in the next section. An asymmetric cut on the transverse energy was chosen to allow the cancellation of soft gluon emission which accompanies jets as recommended in [89]. This arises from a purely theoretical constraint and is required for a calculation to be compared to the data measured. A symmetric cut of say, $E_T^{jet} > 6$ GeV, only allows one-loop contributions to be integrated out and not complete cancellation. The cut on the transverse momentum of the D^* was chosen to be this high as this provides a cleaner signal than a lower cut. The cut on pseudorapidity ensures all tracks are within the range of good reconstruction in the central tracking detector.

6.2 Trigger and Data Selection

Data was used from the years 1996 and 1997 giving a combined integrated luminosity of $36.9 \pm 0.5\text{pb}^{-1}$; 10.7pb^{-1} from 1996 and 26.2pb^{-1} from 1997. This total is the useful luminosity acquired by ZEUS, representing an efficiency of the data taking procedure when compared with the values delivered by the HERA machine as detailed in Table 1.1. These two years only were used as no change in the trigger or significant change in the detector occurred. Between 1995 and 1996, the VXD was removed which throughout 1995 did not function and was therefore only dead material.

The selection procedure can be separated into two parts - the selection using the First, Second and Third level online triggers and a tighter offline selection on quantities after full reprocessing of the data where the events are calibrated based on constants obtained.

6.2.1 First Level Trigger (FLT)

To pass the slot used at the FLT, slot 42, one of four thresholds at the Calorimeter FLT (CFLT), five vetoes and a track quality demand must be satisfied.

- The four CFLT thresholds are:
  - Total calorimeter energy > 14.968 GeV,
  - Total ElectroMagnetic Calorimeter (EMC) Energy > 10.068 GeV.

  The "total" energies are calculated by excluding the 3 inner rings around the FCAL and the inner ring around the RCAL beampipe, corresponding to a region in pseudorapidity of approximately $-3.66 < \eta < 2.2$.

  - RCAL EMC energy > 2.032 GeV.

  This also excludes the inner ring around the RCAL beam-pipe.

  - BCAL EMC energy > 3.404 GeV.

- The criteria for the event to pass the vetoes are:

  - The timings observed in the two C5 counters should match with physics timing, but not with that of the beam gas.
  - Two vetoes requiring that no coincidence of the inner and outer veto wall is detected.
  - The timing in the SRTD should match with physics events and not with beam-gas events.
  - Events should have `TrKclass>2`. These are events with a relatively high ratio of vertex to total number of tracks. The exact value of the ratio is dependent on the number of vertex and non-vertex tracks, but is approximately $> 25 - 30\%$.

- The tracking demand requires the event to have at least one track found by the CTD-FLT coming from the nominal interaction region, $-50\text{cm} < z_{vtx} < 80\text{cm}$.

6.2.2 Second Level Trigger (SLT)

The SLT used, the so-called "high-E_T" trigger, designed for hard photoproduction, has selection criteria that ensures high transverse energy events are accepted (whence the name). The following is required:

- $-60\text{cm} < z_{vtx} < 60\text{cm}$.
- there must be at least 1 vertex track. This is the same condition as demanded at the FLT, where the CTD SLT information is ignored;
- $E - P_z > 8.0$ GeV, where E is the energy sum of calorimeter cells and P_z the vector sum of longitudinal momentum of all cells;
- $E_T(\text{box}) > 8.0$ GeV, where $E_T(\text{box})$ is the sum of transverse energy, E_T in all calorimeter cells excluding the first ring around the FCAL beampipe (outside a value of about $\eta = 3$)
- $(E - P_z > 12.0 \text{ GeV})$ or $(p_z/E < 0.95)$.

6.2.3 Third Level Trigger (TLT)

At the TLT, more time is available and a software trigger is used. There are essentially two *independent* TLT's that could be used for the analysis; one based on tracking and the finding of D^* candidates (bit27) and the other on calorimeter quantities and the finding of dijet events (bit77). The D^* trigger relies on a modified version of the offline tracking reconstruction package to form D^* candidates.

In order to pass the "dijet" TLT the following criteria must be satisfied:

- -60 cm $< z_{vtx} <$ 60 cm;
- number of bad tracks is less than 6 where a bad track is so termed if it does not meet the following:
  - the number of degrees of freedom should be > 20,
  - $p_T \geq 0.2$ GeV,
  - -3.13 $< \eta <$ 1.75,
  - the number of hits used in CTD axial superlayers > 5
  - the number of hits used in CTD stereo superlayers > 5
  - the distance of closest approach in z to the vertex must be ≤ 75 cm.
- 5.0 GeV $< E - P_z <$ 75.0 GeV which is equivalent to a y_{JB} demand of: $0.09 < y_{JB} < 1$;
- $E_T(10°\text{cone}) > 5.0$ GeV, where $E_T(10°\text{cone})$, is the sum of all the E_T in the calorimeter cells outside a 10° cone ($\eta < 2.44$) around the FCAL beampipe;
- $p_z/E < 1.0$;
- a simplified version of the EUCELL jet cone algorithm is run at the TLT and there must be at least two jets with the following:

$$E_T(jet) > 4 \text{ GeV};$$

$$\eta(jet) < 2.5.$$

For studies of inclusive D^* production [90, 50], the use of the D^* trigger is necessary. However, when considering D^* production associated with dijet events, it is not obvious which to choose. It is therefore necessary to look at the number of events of the type under study passing each trigger. The most obvious way to do this is to compare the number of events passing each third level trigger - both passing the same FLT and SLT slot - which then enter the uncorrected $x_\gamma^{\rm obs}$ distribution. A simple comparison of the ratio of D^* trigger to dijet trigger events, N_{bit27}/N_{bit77}, and the exclusivity of both provides the information necessary to assess which should be used. The ratio of events per bin, n_{bit27}/n_{bit77}, entering into the signal region (but not background subtracted) for 1997 data only compared to Monte Carlo is shown in Figure 6.1. This shows that the charm trigger only accepts about 85% of the total events tagged by the dijet trigger. The ratio of events passing the two triggers is well modelled in the Monte Carlo as can be seen from the shaded band compared to the data points. The charm trigger has about 6% of the total events tagged by the two triggers unique to it whereas the dijet trigger has about 20%. The same study was made for 1996 data, revealing similar results and the same conclusion [90].

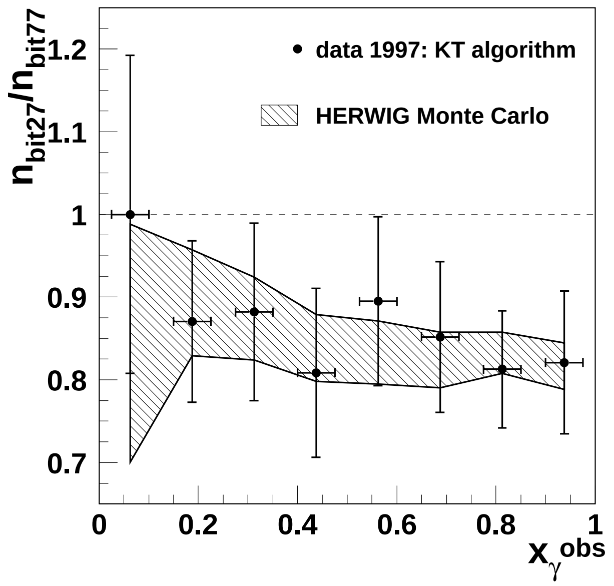

Figure 6.1: *Ratio of events passing the D^* trigger (bit27) to dijet trigger (bit77) as a function of $x_\gamma^{\rm obs}$.*

From this result, it is clear that the use of the dijet trigger yields more events and it is therefore the trigger of choice.

6.2.4 Efficiency of Trigger Chain

The efficiency of the above three stage trigger chain has been extensively studied in previous dijet analyses [78, 91]. We will therefore include only a brief summary of the method and conclusions.

FLT

The FLT slot was studied [78] by choosing an independent trigger which subsequently fed into the SLT and TLT as described. A LUMI branch of the FLT was chosen which required the observation of a scattered positron in the LUMI detector with some low energy calorimeter thresholds. The fraction of events passing the LUMI branch which also pass the calorimeter triggers was found to agree reasonably well between data and Monte Carlo.

SLT

Similarly an independent trigger was used to test the efficiency of our SLT. The LUMI SLT was studied [78], which has events from our FLT which then pass our TLT. The LUMI SLT has the same requirements as the LUMI FLT with the additional criterion that the energy in the LUMI is more than 5 GeV. Reasonable agreement between data and Monte Carlo was again seen.

TLT

The TLT has been studied extensively in [91] by considering an independent sample of events which have passed the charm TLT (bit 27). The overall efficiency of our trigger was found to be good and increase with E_T, such that for $E_T > 6$ GeV, the efficiency is almost 100%. The Monte Carlo models the efficiency reasonably well.

6.2.5 Offline Selection and D^* Reconstruction

Jet and Photoproduction Selection

Before cuts on quantities based on calorimeter values can be made, corrections for noise and the energy scale are implemented. Within the calorimeter, a number of cells are described as being "noisy". The effect is corrected for using standard routines for each year [92]. The correction falls into distinct categories; the removal of noisy cells according to lists provided each year in [92], a cut on the relative cell imbalance, and the removal of isolated EMC and HAC cells with energies below 80 and 140 MeV respectively. The noise associated with the imbalance and isolation cuts arises predominantly due to sparks in the PMT's, whereas the noisy cells are mainly from electronic malfunctions.

Differences in the energy scale of the calorimeter exist between data and Monte Carlo. Studies have shown that the calibration of the BCAL (RCAL) is 5% (2.5%) lower in the data than the Monte Carlo. Consequently the energies of each cell in the BCAL are scaled up by +5% and in the RCAL by +2.5% in the data [93]. No scale is used for those cells in the FCAL as present results suggest that these cells are consistent with not requiring a scaling factor [94]

After the trigger selection and calorimeter corrections, a tighter offline selection was applied with the cuts detailed below.

$$0.15 < y_{JB} < 0.7$$

No positron as found by the electron finder SINISTRA [95] satisfying requirements on y_e and the energy, E_e;

$$y_e < 0.7, E_e > 5 \text{ GeV}$$

The event must contain at least two jets as found by KTCLUS with:

$$E_T(jet) > 4 \text{ GeV};$$

$$\eta(jet) < 2.4$$

The effect of the cut on y_{JB} is two-fold. The rejection of low values eliminates proton-beam gas background. At high y_{JB}, there is a large DIS background due to the positron entering into the sum with the result that $E - p_z \to 2E_e$. The cut on y_e using the electron finder SINISTRA is also to eliminate DIS candidates. The effect of this cut on the scattered electron can be seen on application to a combined resolved and direct Monte Carlo sample; Figure 6.2. Shown is a sample of heavy flavour events, having only loose requirements on the D^* meson.

There are, however, jet cuts applied; requiring two jets with $E_T^{jet} > 4$ GeV and $|\eta^{jet}| < 2.4$. These cuts lead to the spike at high Q^2 in the "generated" sample as there is an enhancement of events because the scattered positron can form one of the jets. When the cut on the scattered positron is applied (dashed line), it can be seen that a large number of high Q^2 events are removed. Applying the cut on y_{JB} (dash-dotted line) further reduces the number of high Q^2 events. At a value of $Q^2 \approx 1$ GeV^2, as indicated by the dotted line at $\log_{10}(Q^2) = 0$, and below, the number of events passing the cut is greater than the number failing. This justifies the value of $Q^2 < 1$ GeV^2 as defined in the cross-section.

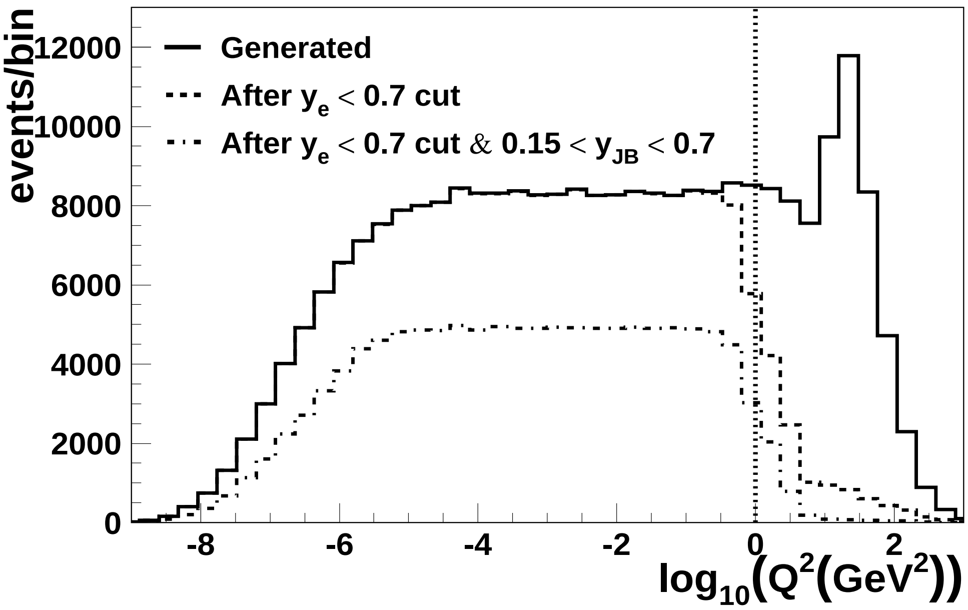

Figure 6.2: *Effect of the cut to remove DIS electrons on Q^2 (Q in GeV) of the event simulated using HERWIG Monte Carlo.*

The demand on the pseudorapidity of the jets is slightly harder than that for the trigger by 0.1 units. The requirement for the transverse energy of the jets although the same value is also effectively higher due to the jet finder used. As was mentioned in section 6.2.3, the jets are found at the TLT with a modified version of the EUCELL cone jet finder. This has a cone radius, $R = 1$, compared to the effective cone radius for KTCLUS of $R = 0.7$ [90]. Therefore, the jets found by KTCLUS are, on average, lower in energy than for the jets found by EUCELL. A cut of the same value is therefore harder for the jets found by KTCLUS.

D^* Reconstruction

Having successfully reconstructed dijet photoproduction events with the aforementioned trigger and data selection, the process of D^* "finding" is then carried out. This is based entirely on the tracks in the CTD by combining all permutations of three tracks (K, π, π_s candidates) such that they pass certain criteria.

Within an event, all pairs of tracks are analysed and assigned to be either of type "kaon" or of type "pion". All the combinations of tracks with opposite charge and,

$$p_T(K, \pi) > 0.5 \text{ GeV/c}$$

are combined and kept if their mass is within a loose selection criteria of:

$$1.5 \text{ GeV} < m(D^0) < 2.4 \text{ GeV}.$$

These pairs of tracks are then combined with a track of type "pion", called the *slow pion*, π_s due to its low energy, which has the opposite charge to the track of type "kaon" and,

$$p_T(\pi_s) > 0.2 \text{ GeV/c}.$$

This combination of three tracks then forms a D^* candidate which is accepted if the following is satisfied:

$$p_T(D^*) > 3 \text{ GeV/c},$$

$$|\eta(D^*)| < 1.5,$$

$$m(D^0\pi_s) - m(D^0) < 0.17 \text{ GeV}.$$

The cut on the pseudorapidity of the D^* requires that it and consequently the tracks used to form it lie within a well-understood region of the CTD. The cut on the p_T gives a large reduction in the background compared to a lower cut of say 2 GeV, whilst retaining a relatively large statistical sample. The two cuts mentioned above on the masses are loose and therefore lead to large backgrounds. Thus in the final selection and analysis of the mass distributions, tighter windows are then used. For the analysis of the Δm distribution, a cut around the central value of the mass of the D^0 meson; 1864.5 ± 0.5 MeV [52], was made of:

$$1.80 \text{ GeV} < m(D^0) < 1.92 \text{ GeV}.$$

Similarly a cut around the central value of the mass difference; 145.42 ± 0.05 MeV [52], was made for the analysis of the $m(D^0)$ distribution:

$$0.143 \text{ GeV} < m(D^0\pi_s) - m(D^0) < 0.148 \text{ GeV},$$

The initial "loose" selection criteria was made so that events used for an estimation of the background are kept. To estimate the backgrounds associated with the signals, two methods are employed, the so-called *control region* and *wrong charge* backgrounds, which provide independent measurements.

The control region is found by taking events which lie outside (but close to) the signal region in the mass distributions. The control region is defined as,

$$1.95 \text{ GeV} < m(D^0) < 2.20 \text{ GeV},$$

for events to be accepted into the distribution in Δm and for the background estimation in the $m(D^0)$ distribution events in the region,

$$0.150 \text{ GeV} < m(D^0\pi_s) - m(D^0) < 0.165 \text{ GeV}$$

are used.

The wrong charge background is found by considering the combinations of tracks mentioned previously, but with the two tracks forming the D^0 meson having the same charge - the other criteria remaining the same. Events which pass this criteria must then pass the same mass cuts as for the signal region. This then appears to be a better estimator of the background as the events lie within the same area of phase space as for the signal region. This is not true for the control region, and consequently the wrong charge estimator will be used for all distributions shown. A check of the consistency of the backgrounds with respect to the distributions shown will be discussed later.

6.3 Signal Mass Distributions

By considering Figure 6.3 clear signals for Δm and $m(D^0)$ with wrong charge background estimates can be seen. The background estimate is area normalised to the observed background in the regions $0.150 < \Delta m < 0.165$ and $1.95 < m(D^0) < 2.20$.

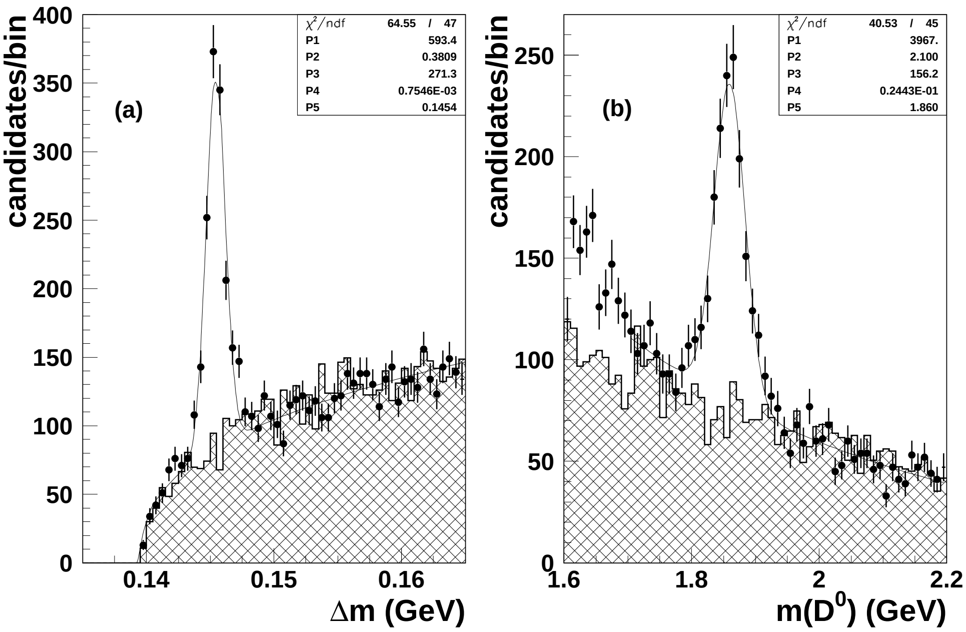

Figure 6.3: *Data mass signals for (a) $m(D^0\pi_s) - m(D^0)$ and (b) $m(D^0)$, where the background (hatched histogram) is estimated from the control region and is of the form $A(x - m_\pi)^B$ in (a) and Ae^{-Bx} in (b) and the fit is this background plus a Gaussian.*

A clean signal would produce a Gaussian distribution for the masses, but as a combinatorial background also passes the cuts detailed, then the shape is a Gaussian plus some background function. In the case of the mass difference, the background is described by, $A(x - m_\pi)^B$, where A and B are to be determined from the fit and m_π is the mass of the pion, which provides an obvious cut-off in x. The resulting Gaussian plus the function mentioned is shown in Figure 6.3a. For the mass of the D^0, the background is described by Ae^{-Bx}, where again A and B are determined from the fit. The result of adding this function to a Gaussian is shown in Figure 6.3b. The results of the fits are shown in the top right-hand corner of each plot where A and B correspond to the first two and the Gaussian the last three parameters given by the fit. In both cases, the fifth parameter, represents the value of the mass from the fits described. The overall fits and background estimates describe well what is seen. However, at low $m(D^0)$, the estimated does not well describe the observed backgound. This is due to another resonance in which the D^0 meson decays to a kaon, pion and a π^0 with the π^0 not included in the calculation, hence the lower invariant mass of the D^0 meson. Therefore, the fit was not performed over the full region of the plot.

The fits to the data give the following results for the masses;

$$\begin{aligned} m(D^0\pi_s) - m(D^0) &= (145.43 \pm 0.02)\ \text{MeV}, \\ m(D^0) &= (1859.6 \pm 1.3)\ \text{MeV}. \end{aligned}$$

The value for the mass difference is in excellent concordance with the value given by the particle data group [52]; $m(D^0\pi_s) - m(D^0) = (145.42\ \pm\ 0.05)$ MeV. The width of the distribution, $\sigma_{data} = 0.71 \pm 0.03$ MeV is in agreement with the value obtained from the Monte Carlo simulation of $\sigma_{MC}\ =\ 0.73 \pm 0.01$ MeV. The mass of the D^0 significantly contradicts the nominal value; $m(D^0) = (1864.5{\pm}0.5)$MeV [52]. This is consistent with a systematic uncertainty in the magnetic field of the central tracker [96] and does not effect the results of the analysis.

Having established clear signals, one can then extract some physical knowledge about the charm quark or D^* meson. The next section discusses the extraction of $x_\gamma^{\rm obs}$ from the D^* signal.

6.4 Extraction of $x_\gamma^{\rm obs}$

The determination of $x_\gamma^{\rm obs}$ was performed by considering those events in the *signal region*. This *signal region* is defined as $0.143 < \Delta m < 0.148$ GeV. For the 1996 and 1997 running period, a total of 1104 ± 52 D^* mesons were observed in this signal region *after* background subtraction. For every event that enters this region the value of $x_\gamma^{\rm obs}$ is calculated. Naturally, in the resulting distribution, there exists the background contribution which gives the mass peak its pedestal. Therefore, using the wrong charge combinations for the estimate of the background, all events that enter the signal region for this background estimator, also have a value of $x_\gamma^{\rm obs}$; this is calculated. The distribution for the background is normalised by the same factor as for the mass signal; Figure 6.3a. The distributions can be seen in Figure 6.4a where the background and signal region values are shown. The signal region points show a larger direct component than for the background. This demonstrates how the charm quark in the signal region enhances the direct peak and suppresses the resolved contribution.

To achieve a distribution in which there is no background and therefore is a distribution for D^* mesons, the two are bin-by-bin subtracted. This subtracted region is then normalised for comparison with Monte Carlo statistics. Figure 6.4b shows the normalised subtracted distribution with Monte Carlo statistics overlayed. Good agreement is seen between the data and Monte Carlo.

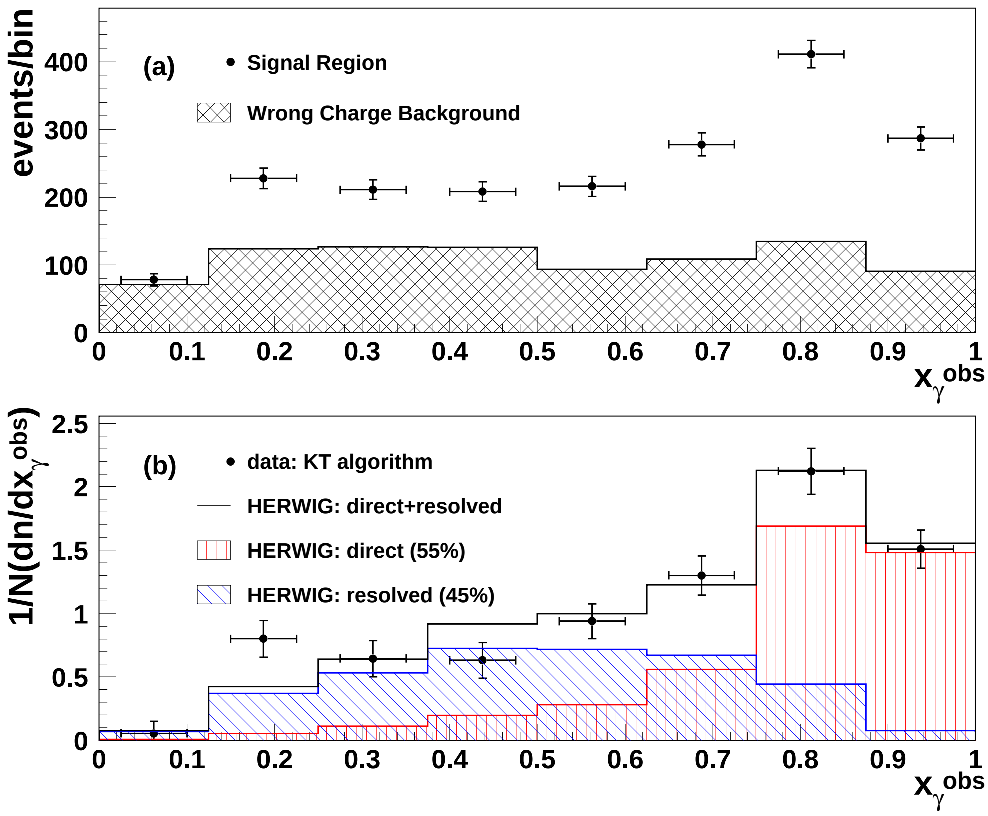

Figure 6.4: *Uncorrected distributions of* x_γ^{obs} . *(a) shows the number of events for the signal region (black dots) and the wrong charge background (histogram). (b) shows the subtracted distibution with Monte Carlo statistics overlayed where the black dots are data and the histograms Monte Carlo (vertically hatched; direct, diagonally hatched; resolved and open; direct plus resolved.*

For a given bin i in x_γ^{obs}containing n_i^{dir} and n_i^{res}, the combined number of events in the bin, n_i^{com} is given by;

$$n_i^{com} = a.n_i^{dir} + (1-a).n_i^{res}$$

such that the total number of Monte Carlo events summed over all bins, $n^{tot} = \sum_{i=1}^{bin} n_i^{com}$ is normalised to the total number of data events. Therefore the proportion of direct and resolved to be combined is given by a and is determined by performing a χ^2-minimisation. For a value of $a = 1$ the sample corresponds to an entirely direct and for $a = 0$ an entirely resolved sample. The fit resulted in a 54.9% direct and a 45.1% resolved component with an error of 4.2%. These values are important in future combinations of direct and resolved Monte Carlo statistics.

Before any correcting procedures are applied, it is interesting to look at the Δm mass distribution in the bins of $x_\gamma^{\rm obs}$. This is shown in Figure 6.5 again with the background estimation (normalised with the global scale factor from all bins) also shown.

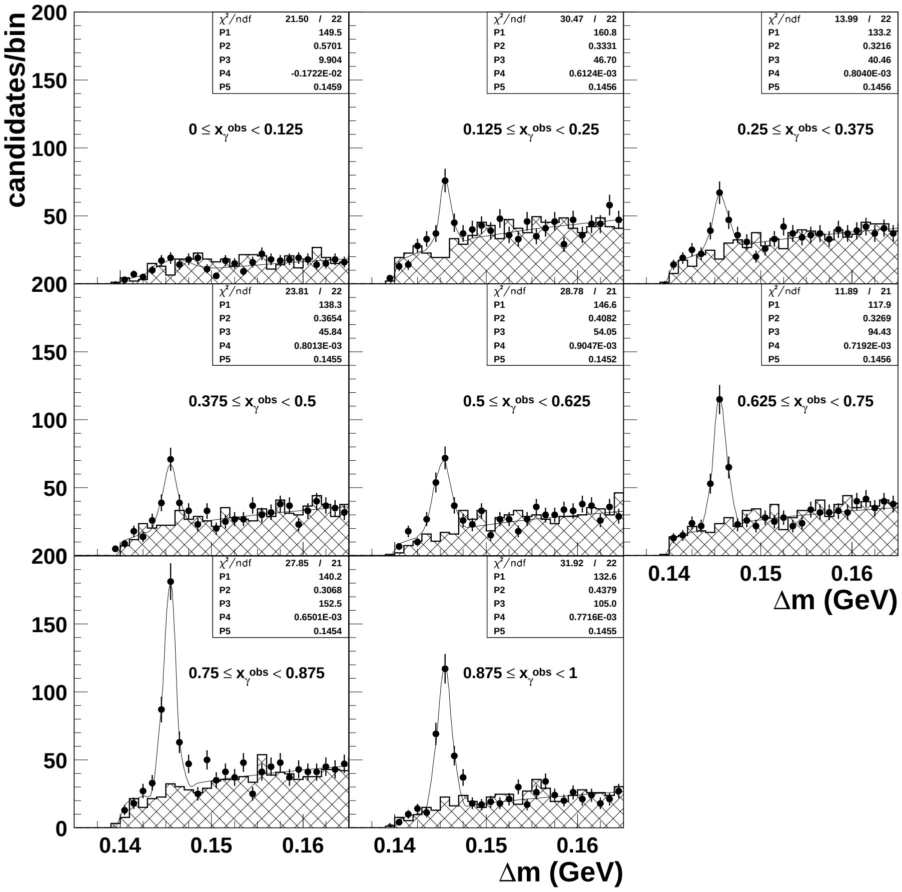

Figure 6.5: *Mass distributions, Δm, in bins of $x_\gamma^{\rm obs}$*

Clear signals in all but the first bin are seen where there is a faint hint of a signal even with the low statistics obtained. It is interesting to note the difference in the amount of background in each bin relative to the size of the signal. The size of the background in the second bin in $x_\gamma^{\rm obs}$ ($0.125 < x_\gamma^{\rm obs} < 0.25$) is slightly larger than in the seventh bin, where the signal is over twice the size. However, the global scale factor gives a good description of the background in all the bins.

6.4.1 Consistency of the Two Backgrounds

Having introduced two methods of estimating the background and proceeding to choose one of them, it is interesting to then compare the two. This is a necessary check of their consistency, as has been indicated, and by implication, a check that the control region background is consistent with the observed background. This we do by looking at the two backgrounds as a function of Δm and $x_\gamma^{\rm obs}$ in Figure 6.6.

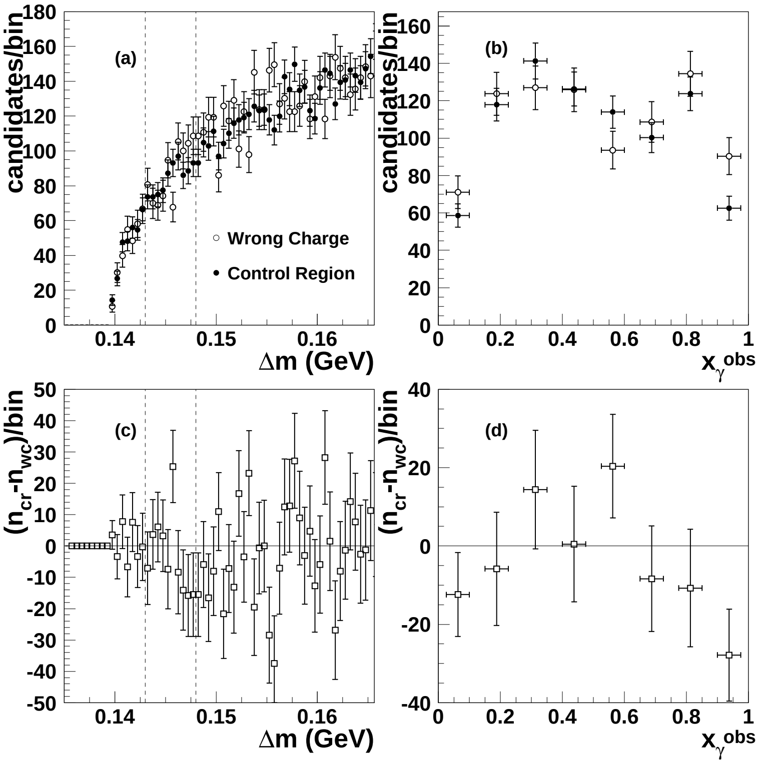

Figure 6.6: *Comparisons of the background estimators. (a) shows the background as a function of Δm for the wrong charge (open dots) and control region (closed dots) and their difference in (c). (b) shows the two as a function of $x_\gamma^{\rm obs}$ and the difference between the two in (d).*

By considering Figure 6.6a, we can see the two as a function of Δm, with the difference of the two distributions shown in Figure 6.6c where the line at zero is not a fit but is only to guide the eye. It should again be noted that both are normalised to each other in the region $0.150 < \Delta m < 0.165$. The region within the dashed lines ($0.143 < \Delta m < 0.148$) is of particular interest as this is the signal region from which the distribution in $x_\gamma^{\rm obs}$ is extracted. Within this region the agreement is good, with fluctations about zero and no systematic trends as can seen in Figure 6.6c.

Any differences arising in the mass difference distribution could then effect the distribution in $x_\gamma^{\rm obs}$. It is therefore necessary to consider the extracted signal. The two can be seen in Figure 6.6b with the difference shown in Figure 6.6d. Again, the two distributions compare well, with neither being significantly more or less "direct" or "resolved" than the other.

The result of this is that we are confident that we have two estimators of the background that are consistent with each other. This also confirms the previous statements about the direct nature of the charm quark, as two independent background estimators yield a compatible distribution in $x_\gamma^{\rm obs}$.

6.5 Comparison of Data and Monte Carlo

As was explained previously, the effects of energy loss due to the dead material in front of the calorimeter can be corrected for in the determination of the jet transverse energy and the y_{JB} of the event. This was carried out using the method detailed in Chapter 5. After correcting the transverse energy of the jets, a "new" cut on the η and E_T independent, recalculated quantity, E_T^{COR}, is made, replacing the 4 GeV cut on the measured jets:

$$E_T^{COR}(jet1, jet2) > 7.0, 6.0\text{GeV},$$

where the highest transverse energy jet is said to be $jet1$ and the second highest, $jet2$. Due to the constraints of the trigger and the correction factors used, a cut of 6 GeV is the minimum permissible. With the added constraint of an asymmetric cut on the jet transverse energy (as mentioned earlier in the chapter), the highest of the two jets must then have an (increased) corrected jet energy of greater than 7 GeV. An analagous "re-defining" of the cut is also used for the new value of y_{JB}, y_{JB}^{COR}, such that,

$$0.2 < y_{JB}^{COR} < 0.8.$$

After this procedure, a comparison of quantities between data and Monte Carlo was performed. The quantities compared can be seen in Figure 6.7 where a number of jet and event quantities are plotted for data (points) and Monte Carlo (histograms) both having passed the same selection cuts as detailed for the data.

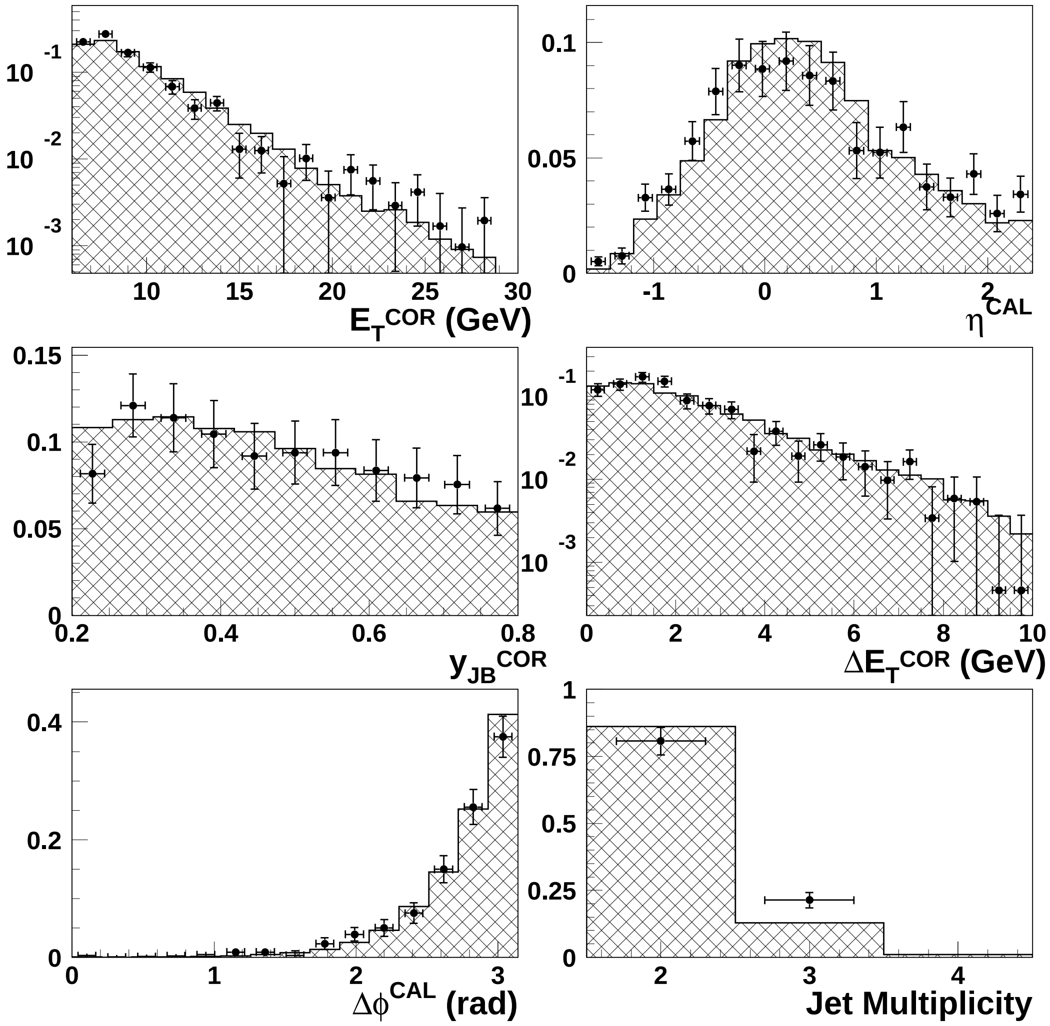

Figure 6.7: *Comparison of data (solid points) with Monte Carlo (histograms) for events passing the data selection criteria*

The two are area normalised to unity, so no relevance should be drawn from the y-axis and only a shape comparison should be made. The direct and resolved contributions have again been combined in the ratio from the fit to the uncorrected distribution. All quantities are in reasonable agreement between data and Monte Carlo.

The important features of the distributions to note will now be detailed. The comparison of the corrected E_T of the jet shows a rapid fall off with increasing E_T with the turnover at low values arising from the asymmetric cut on the E_T of the jets. The distribution in pseudorapidity of the jets is peaked in the central region, as a consequence of the cut on the pseudorapidity of the D^*. In standard dijet photoproduction the tendency is for the jets to be forward, so with a cut of η <2.4, the peak should be at this value, however one of the jets is confined approximately to within 1.5 units in pseudorapidity as it is associated with the D^*. The data is shifted slightly to lower values in pseudorapidity and is slightly broader, but the effect is not large. The agreement between data and Monte Carlo for the corrected y_{JB} is good with no systematic shifts observed. The last three histograms demonstrate that the jets measured are of roughly equal transverse energy (ΔE_T^{COR} is small) with usually two back to back (in angle ϕ) jets per event. The jet multiplicity of the events is higher in the data; $\sim$ 20% are three jet events compared to $\sim$ 10% in the Monte Carlo. This probably arises because the Monte Carlo only includes leading order QCD matrix elements with parton showers, which does not allow the possibility of processes with three roughly equal high transverse energy jets.

The quantities here compared are all (with the exception of y_{JB}^{COR}) associated with jets. Comparisons have been made of the quantities of the D^* in detail elsewhere [90] so are not shown here.

6.6 Unfolding to the Cross-section

A bin-by-bin unfolding procedure was then performed to achieve the cross-section defined in Section 6.1. This was performed using the HERWIG Monte Carlo sample by calculating the efficiency, ε, purity, p, and correction factor, C, in each bin of $x_\gamma^{\rm obs}$. Therefore, for a given bin, i, in $x_\gamma^{\rm obs}$, the efficiency and purity are given by,

$$\varepsilon(i) = \frac{T(i) \cap R(i)}{T(i)}, \tag{6.5}$$

$$p(i) = \frac{T(i) \cap R(i)}{R(i)}, \tag{6.6}$$

where $T(i)$ is the number of "true" hadronic events in a given bin i that pass the cross-section cuts defined in Section 5.1. $R(i)$ is the number of reconstructed events in a given bin i which pass the data selection criteria as outlined previously. The quantity, $T(i) \cap R(i)$ is the number of events which pass the hadronic criteria and are then reconstructed such that they pass the data selection cuts in the given bin i. Therefore, one can think of the efficiency as the fraction of true events in a given bin which are *also* reconstructed in that bin and the purity as the fraction of events reconstructed in a given bin which are *also* generated in that bin.

The correction factor is related to the purity and efficiency by the following expression;

$$C(i) = \frac{p(i)}{\varepsilon(i)} = \frac{T(i)}{R(i)}, \tag{6.7}$$

The errors associated with the purity, $\delta p(i)$, and efficiency, $\delta\varepsilon(i)$, are given by a binomial expression, thus not allowing them to be (meaninglessly) greater than one:

$$\delta\varepsilon(i) = \sqrt{\frac{(1-\varepsilon(i)).\varepsilon(i)}{T(i)}}; \tag{6.8}$$

$$\delta p(i) = \sqrt{\frac{(1-p(i)).p(i)}{R(i)}}. \tag{6.9}$$

The error on the correction factor, $\delta C(i)$, is less trivial, taking into account correlations between $T(i)$ and $R(i)$, and is given by,

$$\delta C(i) = \sqrt{\frac{T(i)}{R(i)^3}\left[T(i) + R(i) - 2T(i) \cap R(i)\right]} \tag{6.10}$$

The differential cross-section, $\sigma(i)$, is then calculated from the number of events passing the selection cuts after background subtraction, $N(i)$, for a given integrated luminosity, $\int dt\mathcal{L}$, such that;

$$\sigma(i) = \frac{N(i).C(i)}{\int dt\mathcal{L}.\text{bin width.BR}} \tag{6.11}$$

where BR is the branching ratio of the process $D^* \to K\pi\pi_s$.

To unfold using the Monte Carlo the separately generated direct and resolved need to be combined in some proportion. This we do by taking the values of the global fit carried out previously on the uncorrected distribution; 0.549 direct and 0.451 resolved. These values are used in combining the direct and resolved contributions in all eight bins of x_γ^{obs} in which the unfolding process is taking place.

To assess the validity of this combination the unfolding was also carried out with a fraction equal to the value plus its error. Consequently, unfolding with $a = 0.591$ and $a = 0.507$ gives an estimation of the systematic error associated with the combining of resolved and direct. This was found to be small even if the values taken were of the order of five times the error.

The results for the efficiency, purity and correction factor are shown in Figure 6.8.

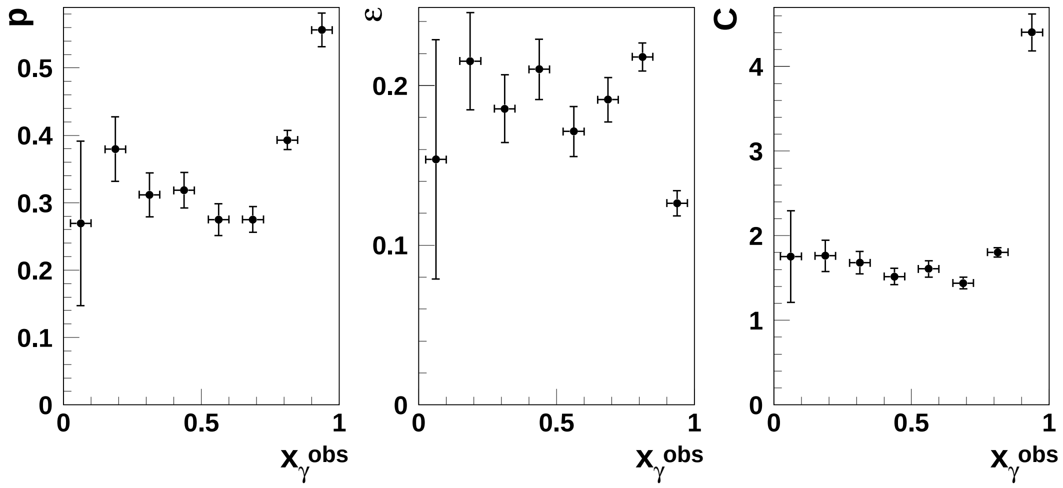

Figure 6.8: *Purity, efficiency and correction factors shown for the unfolding procedure as a function of* x_γ^{obs}.

The purity rises with x_γ^{obs} as the events at high x_γ^{obs} are predominantly direct events which are purer due to the jets being harder and consequently having more jets in the calorimeter above the threshold that are also above the hadronic threshold. The efficiency is reasonably flat, although slightly low in the final bin, which contributes to the rise of the correction factor in the last bin in x_γ^{obs}.

The extreme situation for the purity in this last bin can also be explained by "edge effects" due to migrations between bins in $x_\gamma^{\rm obs}$. As $x_\gamma^{\rm obs}$, by definition, cannot exceed one, then in this final bin, migrations can only occur to and from one and not two bins (assuming that migrations only occur across one bin). In the case of the purity where the value is high in the last bin, there can only be migrations from the bin below and none from above, thereby giving a pure sample. Consequently, fewer events are reconstructed when the true value lies outside this bin.

Using these correction factors, we can then unfold to the cross-section, $d\sigma/dx_\gamma^{\rm obs}$, which is shown in Figure 6.9. The points from this analysis (solid points) are compared with the ZEUS published results (open points) using 36.9 pb^{-1} of data. The ZEUS published results use a slightly larger y range of $0.19 < y < 0.87$ and hence the points lie systematically higher. The ZEUS points are displayed to give an idea of the systematic effects which are discussed in the next section. The data from this analysis is also shown compared with LO, hadron level, HERWIG Monte Carlo. The combined Monte Carlo is shown as the open histogram and the vertically hatched and diagonally hatched the direct and resolved components respectively. A fit to the data was performed on the Monte Carlo in the same way as for the uncorrected data. The component of resolved obtained from the fit is (42.8 $\pm$ 4.6) % a similar figure to that obtained with the uncorrected fit; (45.1 $\pm$ 4.2) %.

6.7 Study of Systematic Uncertainties

By considering Figure 6.9, a number of conclusions can be drawn. Naturally systematic studies need to be performed before strong conclusions are possible. As this cross-section was measured as a second analysis, a complete systematic study can be found in detail elsewhere [90, 50]. Of those studied, the major sources of systematic error arose from:

- the model dependence (HERWIG or PYTHIA) in the evaluation of the correction factors, contributes up to -4.5%
- the uncertainities in the tracking procedure yields a combined uncertainty of $^{+7.1}_{-2.2}\%$,

- using different photon structure functions, the largest uncertainty being $^{+4.1}_{-0.6}\%$,

- the uncertainty in the calorimeter energy scale gives a change in the cross-section of $^{+12.2}_{-9.8}\%$,

After full systematic studies, the physics conclusions remained the same so they were not fully assessed here.

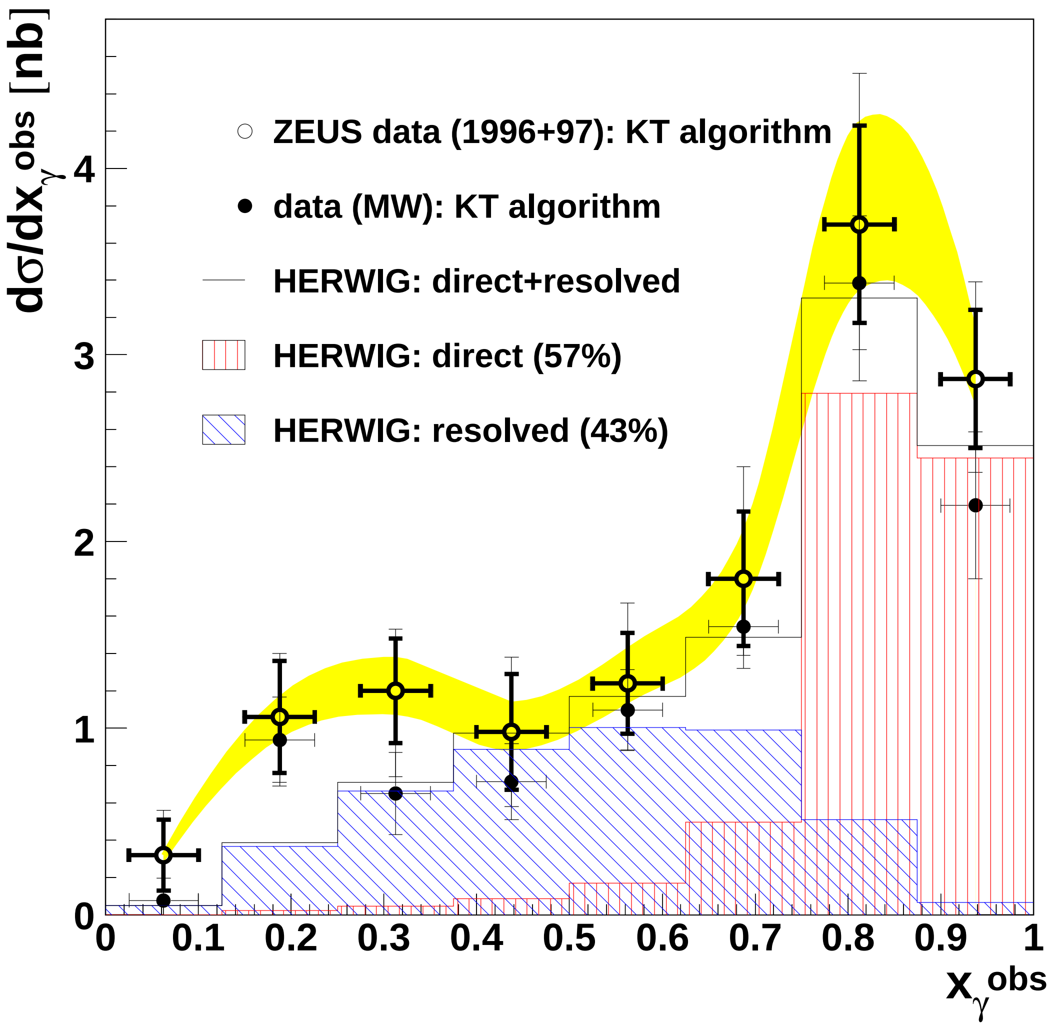

Figure 6.9: *The cross-section, $d\sigma/dx_\gamma^{\rm obs}$, for $ep \to D^*X +$ dijets in the kinematic regions defined in Section 6.1. The data (points) is compared with HERWIG Monte Carlo showing direct (vertically hatched) and resolved (diagonally hatched) separately and the two combined (open histogram).*

6.8 Conclusions and Discussion

From Figure 6.9 the first and most obvious conclusion is that the HERWIG Monte Carlo agrees well with the data in the shape comparison here shown. The LO direct-only processes are incapable of describing the results seen; a component of resolved is required to describe the events at low $x_\gamma^{\rm obs}$. More specifically a *significant* and *large* component of resolved is needed to explain the measurement; *greater than* 40%. With the statement that resolved charm exists at LO, the next question to ask is whether this is also true at NLO or can NLO direct-only describe the data here presented. One may also pose the question as to the nature of the "resolved" charm with reference to the two current schemes used to describe it; *massive* and *massless*. Is the charm quark in these processes arising from flavour excitation or processes where the quark is not an active flavour in the proton or photon?

While the overall description is good, the point in the second bin in $x_\gamma^{\rm obs}$ is poorly described, although this could be assigned to statistical fluctuations. However this is in the same region in $x_\gamma^{\rm obs}$ that standard dijet analyses [78] have seen disagreement with the Monte Carlo. This was attributed in part to the possible presence of multiparton interactions with a further excess attributed to some unknown physical process. This same unknown process could also be present in charm jets even though they have an extra hard scale due to the mass of the quark.

The understanding of the D^* meson through the analysis of dijet photoproduction is now starting to yield interesting results and can be taken further. An obvious final goal would be an extrapolation to the charm cross-section and not just the D^* cross-section. This would be an interesting measurement but requires an understanding of the hadronisation and fragmentation of the D^*. With a measurement of the fragmentation function of the D^* this would be possible. The fragmentation function is now something that could be measured at ZEUS although it is not modelled "correctly" in the (HERWIG) Monte Carlo. Figure 6.10 shows the fragmentation function $z(c \to D^*)$ at an uncorrected level and the separation in $\eta - \phi$ space, R, for the D^* and its closest jet.

The separation in $\eta - \phi$ space, R, is defined simply as:

$$R = \sqrt{(\Delta\eta)^2 + (\Delta\phi)^2}.$$

It can be seen in Figure 6.10a that the oft-said statement " ...(the) jet associated with the D^*..." is vindicated, with almost all events having a D^* meson close to the jet axis. This is consistent with the predicted hard fragmentation of heavy quarks [60]. The Monte Carlo models the data reasonably well at high values of R, but the distribution is narrower than the data, with more events with a harder D^* or indeed softer jet in the Monte Carlo. This would then also be reflected in the fragmentation function which can be seen in Figure 6.10b.

At e^+e^- experiments, the definition of the fragmentation function is simple as the invariant mass and total energy of the system is known. With an ep collider, this is not so easy as the system is boosted and has a remnant which requires us to look for another way of defining fragmentation. Therefore, we define the fragmentation function of the D^*, $z(c \to D^*)$, in terms of the variables relevant to this analysis, namely $p_T(D^*)$ and E_T^{jet}, such that,

$$z(c \to D^*) = \frac{p_T(D^*)}{E_T^{jet}}. \tag{6.12}$$

For the calculation of this fragmentation function, the asymmetric cut on the jets was taken out and a cut on the jets of $E_T^{COR} > 7$ GeV was required. As can be seen from the definition of the formula, the distribution is biased below a cut-off value defined by the cuts on the two quantities used. So the unbiased region is $z > 0.43$ (as indicated by the dashed line in Figure 6.10) which would have been confusing had there been an asymmetric jet transverse energy cut. Another factor determining the jet transverse energy cut is again relevant to the (un)biased region. The biased region should be minimised and to do this, one can raise the jet transverse energy or lower the p_T of the D^*; hence the choice of $E_T^{COR} > 7$ GeV rather then $E_T^{COR} > 6$ GeV.

The distribution in z clearly demonstrates that the Monte Carlo is harder than the data as was indicated in the distribution in R. This effect is the result of the $p_T(D^*)$ spectrum not being correctly modelled in the Monte Carlo. The jets in data and Monte Carlo are approximately the same, as was seen in the comparison of E_T^{COR} in Figure 6.7. Clearly this discrepancy needs to be addressed and the extraction of the fragmentation function performed, by also going to a lower p_T for the D^* of say 2 GeV, thereby making the unbiased region $z > 0.28$.

Extrapolation to a charm cross-section would provide a measurement independent of the particle tagged, leading to a more fundamental result. This is a technically challenging procedure and another way to make more definite statements about the charm quark is to look at an independent decay channel and analyse those results. This is done in the next chapters through the study of inclusive semi-leptonic decays of heavy quarks to electrons.

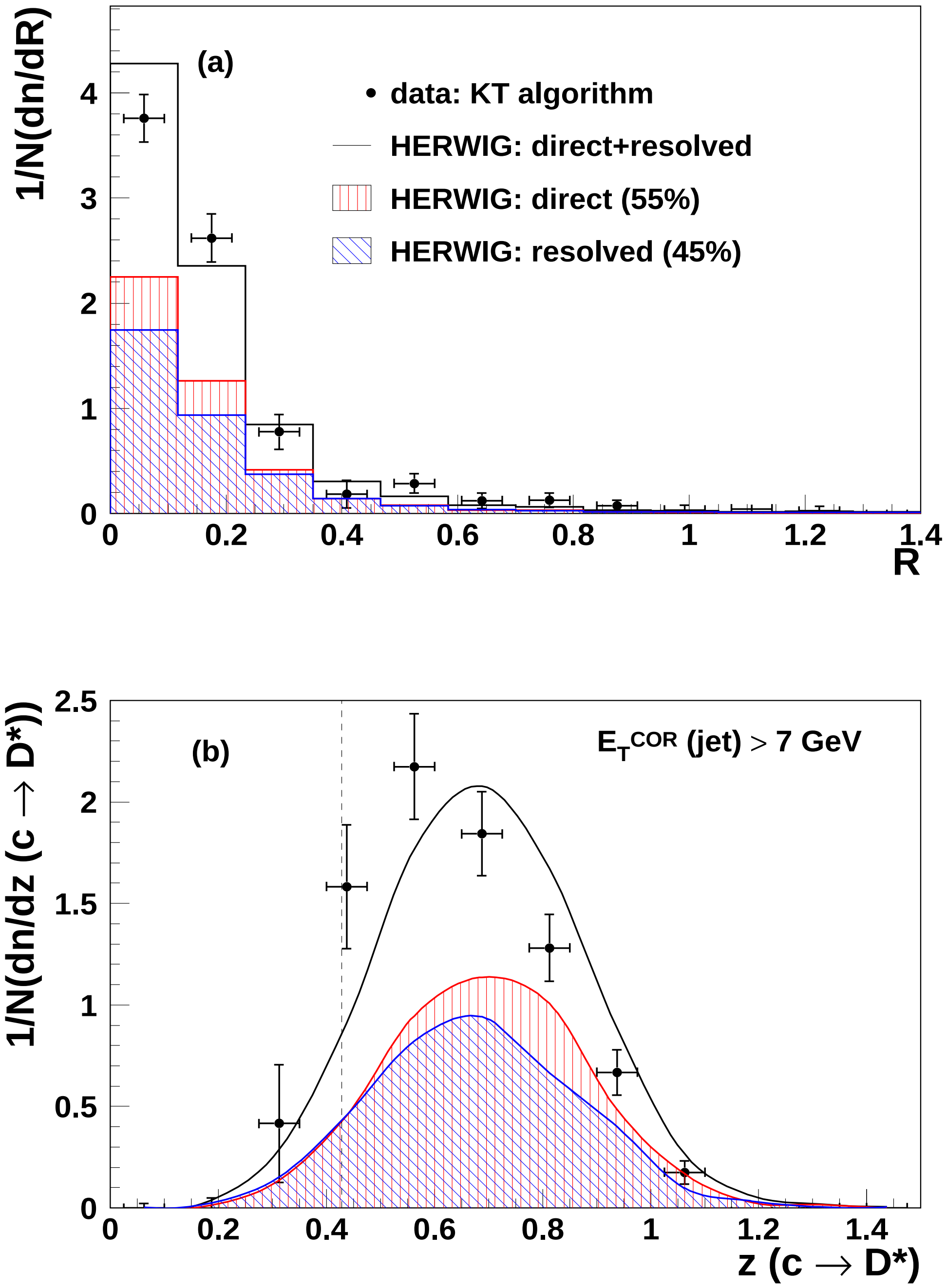

Figure 6.10: *Separation in $\eta - \phi$ space, R (a) and $z(c \rightarrow D^*)$ (b) of the D^* and the jet closest in R.*

Chapter 7

Extraction of Semi-leptonic Decays to Electrons

The study of semi-leptonic decays of (mostly) heavy hadrons with an electron in the final state was performed using 36.9 pb^{-1} data from the 1996 and 1997 running periods. Analogously to the study of D^* mesons, photoproduction events containing at least two jets were reconstructed. Electrons in the final state were then found within these events. The procedure for identifying electrons in the final state is not by directly tagging them via the use of (for example) a neural network electron finder, but by performing a method of statistical subtraction. This identification method for electrons is heavily based on the use of the ionisation energy loss, dE/dx, of particles traversing the CTD. This aspect will therefore be covered in detail first in this chapter.

7.1 Ionisation Energy Loss, dE/dx, for Particle Identification

Particles traversing the CTD lose energy by ionising the atoms within the gas in the detector. A raw pulse size is measured, which then has to be converted into a more meaningful and useful quantity, the "dE/dx" of the particle traversing the CTD. A description of the reconstruction of this quantity can be found in Chapter 1 in the description of the detector. External factors also exist which alter the "true" value of dE/dx, with pressure, gas composition and angular variations (thought to be due to a space-charge effect) being the largest. How the quantity is scaled (run-by-run "corrections") - to enable comparisons over a time period

- and pressure corrections within a run are discussed. The angular variation of the energy loss and the correction procedure is also discussed in detail. A brief introduction of the theory of ionisation energy loss is first espoused.

7.1.1 Ionisation Energy Loss

The theory of energy loss of charged particles traversing a medium is well documented [13, 97]. For all charged particles, except for electrons and positrons (due to their small mass), ionisation losses dominate over radiation losses at all but the highest attainable energies. These ionisation losses are dominated by Coulomb scattering off atomic electrons. There is some scattering from the nucleus but this is a negligible effect since the recoil energy of the nucleus is much smaller because of its greater mass. The theory is encompassed in the Bethe-Bloch equation [98], formulated in the 1930s. In the computation, it is essential to take into account the binding of electrons to the atoms; therefore, one should consider the system formed by the atom and by the incident particle and then compute the probabilities for the various possible transitions leading to excitation or ionisation of the atom. Bethe's formulation was based along these lines using Born's approximation.The original result was updated and went through more accurate calculations [99] and is given below in its modern form.

For a scalar $spin - 0$ boson with charge equal to plus or minus the electron charge, the Bethe-Bloch equation states the energy loss of a particle, $-dE/dx$ (in MeV/cm), to be,

$$\frac{-dE}{dx} = \frac{Dn_e}{\beta^2}\left[\log\left(\frac{2mc^2\beta^2\gamma}{I}\right) - \beta^2 - \frac{\delta(\gamma)}{2}\right], \tag{7.1}$$

where x is the distance travelled through the medium, m is the electron mass, β and γ have their standard relativistic definitions, Z is the atomic number and

$$D = \frac{4\pi\alpha^2\hbar^2}{m} = 5.1.10^{-25}\mathrm{MeVcm}^2 \tag{7.2}$$

The other terms are properties of the medium; $\delta(\gamma)$ is a dielectric screening correction which is important for highly relativistic particles; I is the mean ionisation potential of the atoms averaged over all electrons, which is given approximately by $I = 10Z$ eV for $Z > 20$; and n_e is the electron density and is given by,

$$n_e = \frac{\rho N_A Z}{A} \tag{7.3}$$

where N_A is Avogadro's number, ρ is the mass density and A is the atomic weight of the medium.

For $spin - 1/2$ particles the main features of the Bethe-Bloch equation are the same and the effects of the differences small, so can be ignored in this general discussion of ionisation energy losses.

By considering Figure 7.1, the important features of the Bethe-Bloch equation for ionisation energy loss and its application to particle identification can be seen. Shown, is the variation of dE/dx (normalisation and units to be discussed in the next section) with momentum for well reconstructed particles traversing the CTD. Curves for classes of particles are superimposed to give an idea of how different particles can be distinguished.

For hadrons, there is a rapid fall in dE/dx as the momentum increases from zero due to the $1/\beta^2$ factor. Then there is the region of *minimum ionisation*, where the curves are at their minimum value. After the region of minimum ionisation, β tends towards one and the logarithmic factor gives a *relativistic rise* in dE/dx, which can be seen on inspection of the graph. There are two reasons for this rise: firstly as the velocity increases, the relativistic deformation of the Coulomb field of the incident particle causes the effects of this particle to be felt at larger distances from its geometric path, thereby increasing the upper limit of the impact parameter; and secondly as the momentum increases, the lower limit of the impact parameter decreases due to the uncertainty principle. This relativistic rise then slows down as the screening correction, δ, becomes important. Electrons do not exhibit the same behaviour, with a momentum independent value of dE/dx in the momentum region under consideration. Due to its low mass, the electron has already reached its relativistic asymptotic limit.

Since the value of dE/dx depends on the velocity of the charged particle, it is possible to distinguish different particles with the same momentum but different masses by a careful measurement of dE/dx.

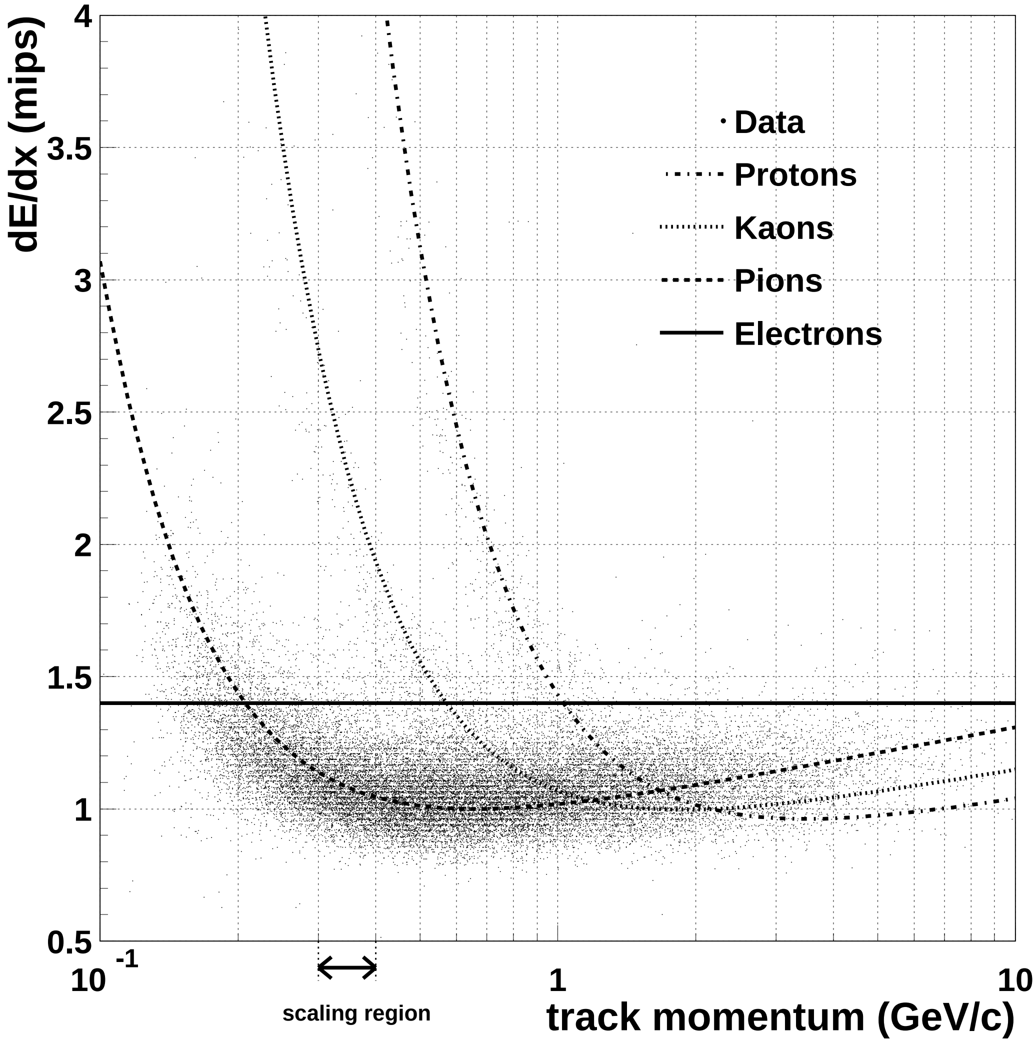

Figure 7.1: *The dE/dx versus momentum of well reconstructed tracks in the CTD with curves illustrating the particle classes.*

7.1.2 Scaling dE/dx Throughout the Year

Throughout the year and hence between runs, the value of dE/dx, for a given class of particles in a given momentum and angular region, changes. The major factors contributing to this change are the variations of pressure and gas composition throughout the year. A variation in pressure changes the gas density, which has a direct consequence on the average pulse size. The size of the pressure variation over the year can be seen in Figure 7.2 (Left) and its correlation with dE/dx is also demonstrated in Figure 7.2 (Right). The correlation of dE/dx with pressure can be clearly seen but also the large spread demonstrates that other factors affect the dE/dx value. The value of the pressure is an average value taken from the values recorded every ten minutes during the run. The average dE/dx value is explained below.

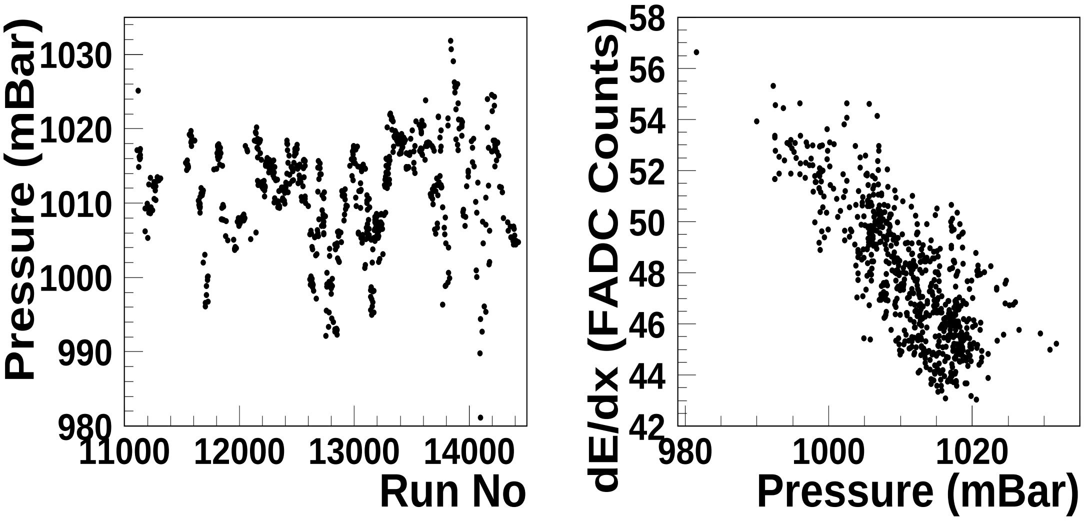

Figure 7.2: *Variation of atmospheric pressure with run number throughout the 1995 running period (Left) and the correlation of dE/dx with pressure (Right).*

For dE/dx to be then a useful quantity that is comparable between runs, a *scale* needs to be set. This scale needs to be a calibration value for a particular type of particle; the same for all runs.

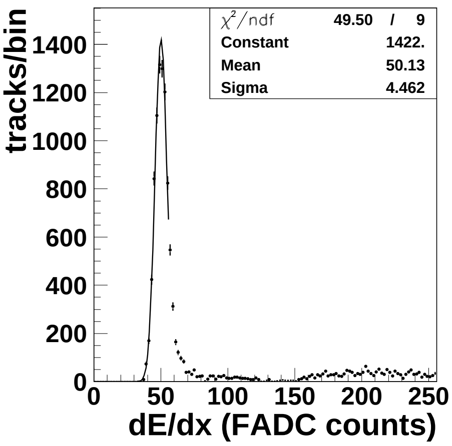

Figure 7.3: *Example fit to pions in the region $0.3 < p < 0.4$ GeV/c for run 22262 in 1996.*

This is achieved by determining the average dE/dx for pions around the minimum ionisation. Pions in the momenta range, 0.3 to 0.4 GeV/c, are used as, in this momentum region, they are most easily distinguishable from other particles. In this narrow momentum region the band of pions lies far from the other hadrons and is close to its minimum thereby being reasonably separated from electrons. In this momentum range a clear pion signal is achieved; see Figure 7.3. By performing a Gaussian fit to a sample of these pions for each run, an *average* value for this class of particle in a particular run is achieved. As can be seen the fit is not performed over the whole region but until half the height on the right hand side so as to avoid contamination from electrons. The mean value is then used as the scale and all values are with reference to this. The normalisation takes out the effects of pressure and gas composition *averaged over the run*. Henceforth when a normalised value of dE/dx is used the units will be called *mips* - minimum ionising pions - as was previously shown in Figure 7.1.

7.1.3 Pressure Corrections *within* a Run

There is also the consideration of dE/dx varying *within* a run. A method of correcting for the pressure will be explained. Then it will be shown that, in fact, the corrections to the pressure within a run are not significant. They had previously been so, but changes in the gas mixture used between years provided a more stable situation.

In long runs, some lasting up to 8 hours, the variation in pressure can be about 6 mBar. It was assumed that dE/dx and the pressure were correlated as in Figure 7.2 (Right). The gradient from this was used to correct the values back to atmospheric pressure. The correction factor, *corfact*, is applied to the uncorrected (VCTrak value), dE/dx_{VC}, (or the scaled value as in the previous section) as follows,

$$dE/dx_{corr} = dE/dx_{VC}.corfact \tag{7.4}$$

where dE/dx_{corr} is the value corrected for pressure within a run. The correction factor, *corfact* is given by,

$$corfact = 1.0 + pcorevt.(presrun - presevt) \tag{7.5}$$

where *presrun* and *presevt* are the (average) pressure of the run and the pressure of the event respectively. The multiplicative factor, *pcorevt*, is given by,

$$pcorevt = \frac{pcor_{1013}}{1.0 + pcor_{1013}.(presevt - 1013)} \tag{7.6}$$

where the value 1013 represents atmospheric pressure (in mBar) and $pcor_{1013}$ is a constant value for each event. By finding the gradient, *grad*, of the average dE/dx

against the average pressure (Figure 7.2 (Right)), $pcor_{1013}$ can be determined and is given by,

$$pcor_{1013} = \frac{grad}{dE/dx_{1013}} = -0.006. \tag{7.7}$$

where dE/dx_{1013} is the dE/dx value at 1013 mBar.

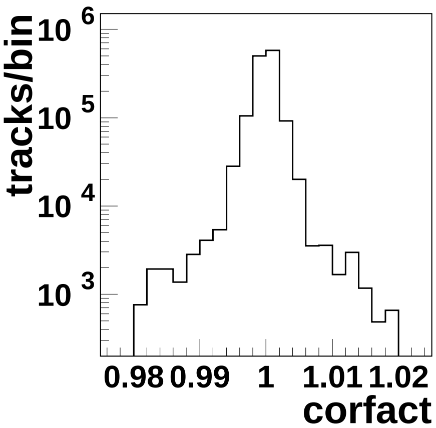

Figure 7.4: *The size of the correction factor,* corfact*, for an unbiased sample of tracks from events during 1995.*

By considering Figure 7.4, one can see the value of the correction factor, *corfact*. The sample of tracks is an unbiased one and represents data from all times during 1995. The sample is those events selected as possible semi-leptonic decays from heavy quarks and all tracks within these events enter into the distribution. Therefore, although the *event* sample has to pass certain criteria the *track* sample does not and it is not temporally biased, i.e. they occurred evenly throughout the year. As one can see, the the correction factor is peaked at a value of one (i.e. no correction), the largest being 2%. The significance of this value can be understood by considering the value of dE/dx stored in the VCTrak tables, which is an integer (for reasons of the 8-bit readout device, i.e. FADC counts range from 0 to 255), yielding an uncertainty on the value of $1/\sqrt{12}$, due to the readout method. It can therefore be clearly seen that the pressure correction is significant at this level. However, on comparison of tracks in which *corfact* was and was not applied, no significant change in resolution or mean value were observed. A sample of scattered DIS positrons was used and its mean and sigma found to be 1.392 mips and 0.1153 mips respectively before correction and 1.391 mips and 0.1145 mips after correction.

7.1.4 Space-charge Correction for Electrons

An additional and significant effect of the angular dependence of dE/dx also has to be taken into account. This is not a simple $1/sin\theta$ path length effect which has been accounted for in the reconstruction, but an additional dependence thought to be due to the so-called "space-charge" effect. This effect causes a reduction in gain through a screening of ions in the avalanche which is most significant at central values of the detector through simple geometric effects [100].

By considering electrons which have come from photons which converted in the beam-pipe, via the simple $\gamma \to e^+e^-$ process, the effect can be clearly seen. As they are electrons their dE/dx is momentum independent, so electrons over the full momentum spectrum can be used. To study this effect with hadrons, narrow bins in momentum would need to be considered. Electrons from photon conversions represent both a source of calibration and the major background for this analysis and will be explained in detail further in the chapter. For now it is sufficient to say that a clean sample of electrons from photon conversions is obtained by a statistical subtraction of same charged from opposite charged track pairs passing certain quality criteria. The dE/dx distribution of the electrons before and after the statistical subtraction and the background estimator from the same charged track pairs is shown in Figure 7.5 (Left). The dashed histogram for the same charged pairs shows a peak at a dE/dx value consistent with hadrons and removing the shoulder as seen on the oppositely charged pairs when subtracted. The subtracted distribution then provides us with a measure of the dE/dx value for electrons of about ~ 1.4 mips and a resolution of just under 10%.

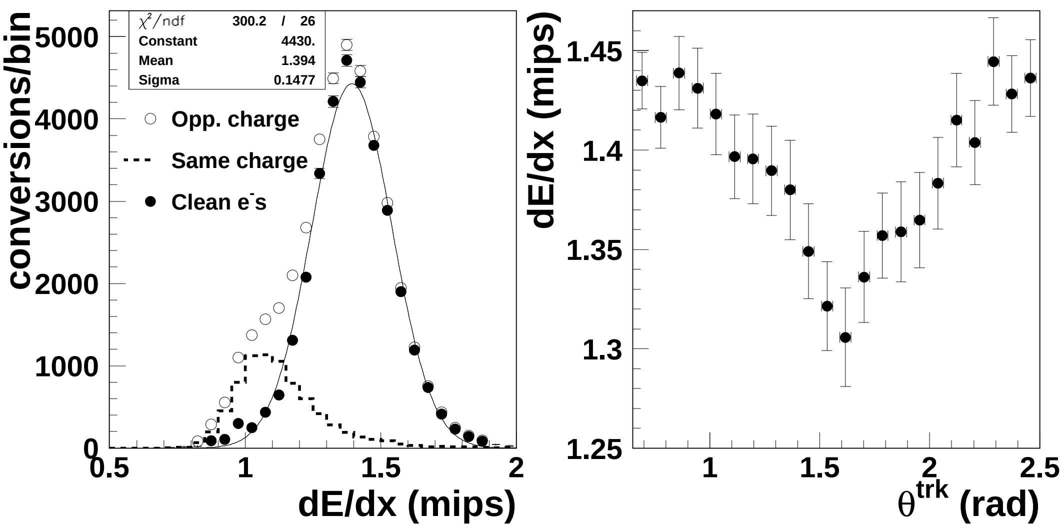

Figure 7.5: *Sample of conversion electrons' dE/dx value (Left) and their angular dependence of dE/dx (Right).*

Taking this sample of clean electrons and looking at the dE/dx dependence on the angle of the track, θ^{trk}, one receives the distribution shown in Figure 7.5 (Right).

This demonstrates a dramatic dependence with an approximate 10% effect on comparison of the edge of the angular region to the centre. The values at the edge are the more reliable, so a correction to about this value is performed for all electrons in this angular region, that is 1.4 mips. By doing this we now dictate that the mean dE/dx for electrons is exactly 1.4 mips. The correction is a simple bin-by-bin correction taken from the data points seen and not functionally based. However, if this angular dependence is the space-charge effect, then the effect is dependent on the dE/dx value itself and so this correction is only appropriate for electrons.

7.2 Trigger and Data Selection

For this analysis a similar procedure was used as for the D^* mesons in dijets analysis. At the trigger level, unlike with the D^* meson analysis, there is only one trigger option open for the analysis; using the jet trigger. No dedicated "semi-leptonic trigger" was available and, as has been shown in [91], the jet trigger is efficient for the jets under study. Consequently, the same trigger selection is used as described in Section 6.2 to select data from the years 1996 and 1997.

7.2.1 Offline Selection and Electron Detection

To select good dijet photoproduction events, the same criteria for jets and photoproduction was specified as in section 6.2.5. This includes the scaling of the energies and the correction for noise of calorimeter cells. These are particularly important as we are considering cell clusters.

The selection of events then (obviously) differs in order to find candidates for semi-leptonic decays to electrons. The essential method is a statistical subtraction of a *hadron enriched* from a *electron enriched* sample to achieve a sample of electrons. As the electrons under study are of low energy, $\sim 1-5$ GeV, a standard electron finder such as is used for the detection of the scattered positron was not used. Achieving the two enriched samples can be separated into many stages which are now detailed.

Tracking Requirements

Only tracks matched to the vertex which have entered the first superlayer and have subsequently passed through at least the first three superlayers [3] are selected. This ensures a certain quality of track which has come from the interaction point, ruling out cosmic tracks and other non-interaction point events. The following requirements are then made on the transverse momentum, p_T^{trk}, pseudorapidity, η^{trk}, and charge, q^{trk}, of the tracks:

$$p_T^{trk} > 1.6 \text{ GeV/c},$$

$$|\eta^{trk}| < 1.1,$$

$$q^{trk} = -1.$$

The reasoning behind the momentum cut is three-fold. Firstly it greatly simplifies the separation of electrons and hadrons as above an approximate momentum value, $p^{trk} \sim 1$ GeV/c, the hadrons are effectively in one band in dE/dx versus momentum below that of the momentum independent electrons. This can be seen in Figure 7.1. However, the cut used is harder and is applied to the transverse and not the full momentum. One effect is to reduce the background from conversion electrons and electrons from Dalitz decays ($\pi^0 \rightarrow e^+e^-\gamma$) - the major source of light quark background. These are primarily low momentum processes and conversion electrons will be discussed further, later in the chapter. As a goal of this analysis is also to look for the beauty quark, a raising of the transverse momentum of the track enhances this contribution from decays of beauty hadrons whilst reducing the contributions from decays of charm hadrons and lighter quark hadrons. Consideration of Figure 7.6 demonstrates the value of the cut on the p_T^{trk} of the track.

The sample was generated using the HERWIG Monte Carlo program which had a low cut on the transverse momentum of the electron, hence the distributions do not start at $p_T^{e^-} = 0$ GeV/c. Here are shown decays to electrons in which the mother was either a π^0 (Dalitz decay), a D meson ($\bar{D}^0$ or D^-) or a B meson ($\bar{B}^0$ or B^-). The distributions for Dalitz decays and decays from D mesons are area normalised to the distribution for B mesons to enable a shape comparison to be made. The D meson distribution is harder than for Dalitz decays with the distribution for B mesons being significantly harder than these two. This, therefore, clearly shows that the higher in $p_T(e^-)$, the larger the enhancement in decays from B hadrons.

The cut on the pseudorapidity is to select good quality, long tracks within the acceptance of the CTD. The reconstruction of dE/dx is good within this region, ensuring that the particle has a large number of hits. Within this region the resolution is reasonably constant at 10% but dramatically worsens outside the region. In general, this requires that the tracks have passed through a large number (at least seven) of the superlayers of the CTD. It does not, however, completely override the cut on the previously mentioned superlayer three demand. The cut also entails that after leaving the CTD the particles generally enter the BCAL, the RCAL and FCAL being largely redundant in the identification of electrons in this analysis.

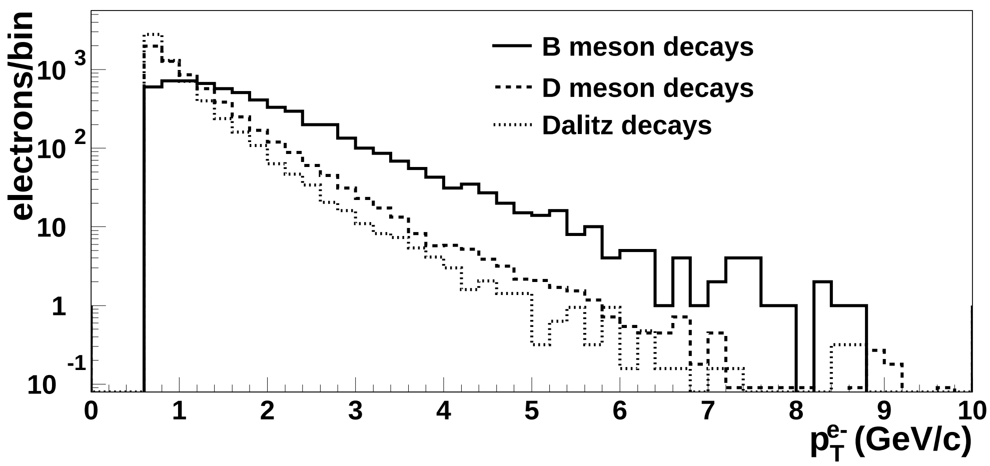

Figure 7.6: *Distribution for the p_T of an electron from a decays from a B meson (solid line) and D meson (dashed line) and Dalitz decays (dotted line).*

The charge requirement on the track is to select electrons, thereby removing the problem of having scattered positrons in the sample. Evidence for this problem will be demonstrated later in the chapter when the method has been completely explained. Requiring only electrons may reveal any $c\bar{c}$ production asymmetry on comparison with the analysis with D^* mesons which did not discriminate between charges. A large difference is not expected and the current accuracy of the measurements is unlikely to reveal a difference attributable to $c\bar{c}$ production asymmetry.

Island Requirements

The tracks selected are subsequently matched to cell clusters, which are called and will henceforth be referred to as islands [9]. Therefore, all tracks are compared with all islands reconstructed in the event and a distance of closest approach, *dca*, is assigned for all track-island combinations. The distance for a given track (or conversely a given island) dictates how well the track (or island) is matched to a given island (or track). The minimum distance for a given track for all the combinations is then considered to be its matched island. In this analysis a good match and hence a track-island combination is defined as having a distance of closest approach of;

$$dca < 20 \text{ cm}.$$

This value was chosen based on the size of a cell; as was mentioned in the chapter in the description of the detector, the cell sizes for the electromagnetic and hadronic sections are about 5×20 cm and 20×20 cm respectively. The value chosen, therefore seemed reasonable, roughly representing the width of a cell. Any value larger would be a questionable match whilst a smaller value would lead to a lower efficiency. As the analysis has a relatively low efficiency whilst having a reasonable purity (see later), a reduction in the distance of closest approach would only worsen the situation.

Using the track-island pairs, we define two samples on which the isolation of electrons is based. These samples will be referred to as *electron enriched* and *hadron enriched* and they are essentially achieved by a cut on the ratio of electromagnetic, E_{EMC}, to total energy, E_{ISL} of the island. Cleaning cuts are also applied to the actual energy of the island to reduce the chances of choosing an island containing only noisy cells. The electron enriched sample is defined as,

$$\left(0.9 < \frac{E_{EMC}}{E_{ISL}} < 1\right) \quad \cap \quad (E_{ISL} > 0.2 \text{ GeV})$$

$$\cup$$

$$\left(\frac{E_{EMC}}{E_{ISL}} = 1\right) \quad \cap \quad (E_{ISL} > 0.1 \text{ GeV}),$$

whilst the hadron enriched sample is achieved by placing the following criteria on the islands,

$$\left(\frac{E_{EMC}}{E_{ISL}} < 0.4\right) \quad \cap \quad (E_{HAC} > 0.3 \text{ GeV}) \, .$$

The distribution of this ratio, E_{EMC}/E_{ISL}, for all tracks which pass the tracking selection criteria defined previously and the island-track distance matching cut ($dca < 20$ cm) is shown in Figure 7.7 (Left). As can be seen the distribution is reasonably flat with a general rise to higher values and a peak at a ratio of one, corresponding to islands in which the energy deposited is totally contained in the electromagnetic section of the calorimeter. The inclusiveness of the tracks implies that a large proportion of hadrons deposit all their energy in the electromagnetic section of the calorimeter. This is particularly true for pions which provide the main source of fake electrons thereby rendering a cut solely on the ratio insufficient for identifying electrons. This implies that the sample enriched with electrons is still mainly hadrons. However, as can be seen in Figure 7.7 (Right) the number of electrons which enter into the hadron enriched sample is small with most being at high values of E_{EMC}/E_{ISL}. The electrons shown are from conversion pair production of which only 1% enter into the hadron enriched sample. The cut classifying the hadron enriched sample is therefore a highly efficient rejecter of electrons. The selection criteria for the electron enriched sample is reasonably efficient for tagging electrons, with most of the conversion electrons having $E_{EMC}/E_{ISL} > 0.9$. Consequently upon subtraction of the two a pure sample of electrons should be achieved with very few electrons in the hadron enriched sample being removed.

7.3 Extracting the Electron Signal

After the selection of tracks matched to one of two classes of islands, a signal of electrons is then achieved by considering the dE/dx of the matched track for both electron enriched and hadron enriched islands. As there is an excess of electrons in the electron enriched and practically none in the hadron enriched samples, a subtraction of the hadron enriched (appropriately normalised) from the electron enriched will realise a sample of electrons. However, this essential procedure cannot be applied directly. Certain aspects of the samples need to be first considered, as the method relies on the hadron enriched sample describing

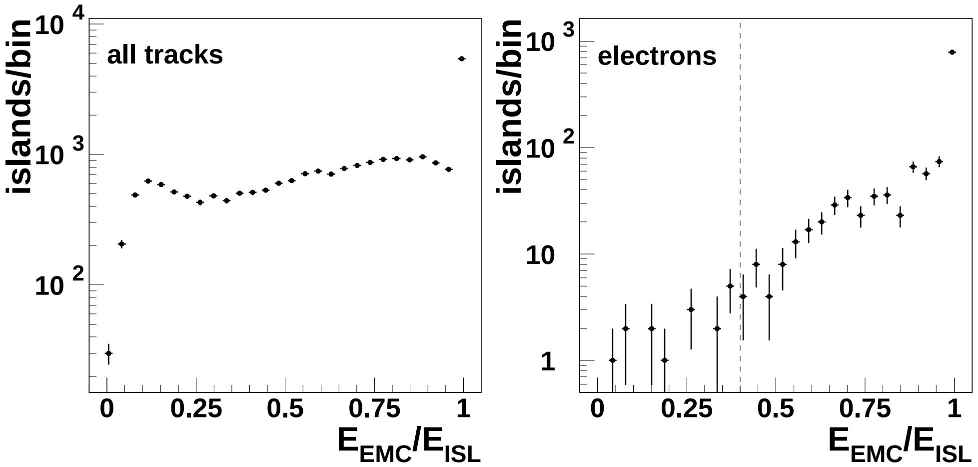

Figure 7.7: *Distribution of E_{EMC}/E_{ISL} for all tracks passing the previously mentioned tracking criteria (Left) and for a sample of electrons (Right).*

the background in the electron enriched sample. Therefore two points need to be addressed; the momentum and angular distributions of the two samples, recalling that there is a dE/dx dependence on both.

7.3.1 Momentum Dependence of Signal Extraction

By considering Figure 7.8, we can see that the momentum distributions for the electron and hadron enriched samples differ.

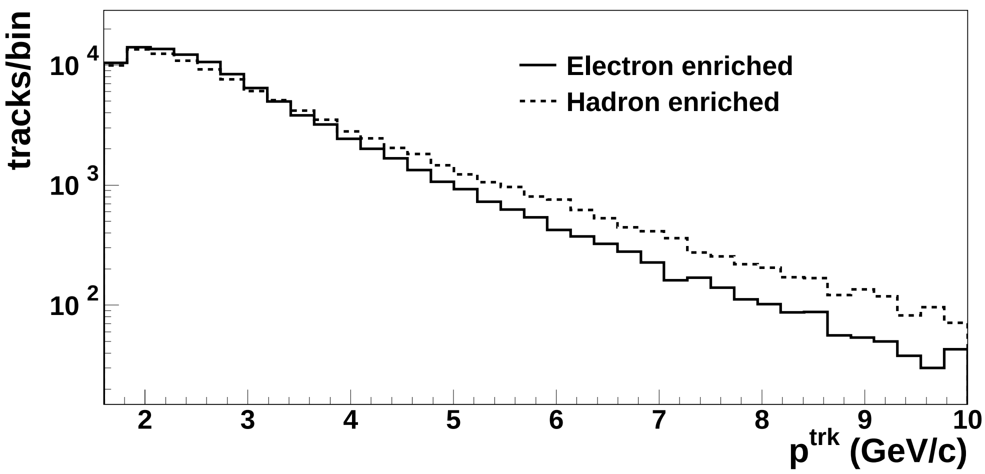

Figure 7.8: *Momentum distributions for all tracks in the electron and hadron enriched samples passing the final analysis criteria. The hadron enriched sample is area normalised to the electron enriched sample.*

The hadron enriched sample is area normalised to the electron enriched for a comparison of their shapes. From the figure we can see that the distribution for the hadron enriched sample is harder than for the electron enriched sample.

The difference has to be taken into account when considering the dE/dx of the respective samples. As was previously seen (Figure 7.1) dE/dx is momentum dependent, so if our estimation of the background (the hadron enriched sample) has a different momentum distribution to our actual background (*in* the electron enriched sample) then the dE/dx distribution will also be different and the consequent statistical subtraction wrong.

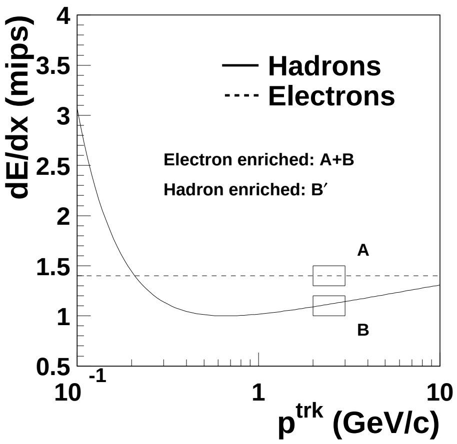

Figure 7.9: *Schematic picture of the constituents of the two samples in a given momentum region.*

Naively, one would think that a weighting factor applied to the hadron enriched sample, such that its momentum distribution matches that of the electron enriched sample, would solve the problem. This can be thought of by considering the electron enriched sample in a given momentum regime to be composed of two classes; electrons, class A and hadrons, class B; and the hadron enriched in the same momentum regime, one class; hadrons, class B'. This is simplistically shown in Figure 7.9, where the hadron band contains all hadrons. The actual distinction between A and B is (obviously) not so remarkable but is just for purposes of illustration. The naive weighting would result in the momentum distribution for B' matching that for $A + B$, which would then, upon subtraction, lead to a false momentum distribution for electrons. The electrons are then dictated to have the same momentum distribution as our hadronic background, which is almost certainly not so. However, what we require is that the hadron enriched sample describes the momentum distribution of the hadronic background in the electron enriched sample. Therefore we require the momentum distribution of B' to match B, A being the independent quantity we want to extract. This we achieve by binning the two samples and hence performing the analysis in momentum bins (or transverse momentum as this is how the analysis is defined). The logic and validity of the argument will become clearer once we perform the binning and extract the signals.

7.3.2 Angular Dependence of Signal Extraction

Allied to the difference in momentum of the two samples, there is also a difference in the angular distributions; Figure 7.10. Here we can see that the hadron enriched sample is more centrally peaked, or more specifically, is deficient at the edge regions; this is a simple geometrical artifact as a consequence of the restriction on the pseudorapidity of the track. As the hadron section of the calorimeter is behind the electromagnetic section, a track entering the hadronic section has an implicitly tighter cut. So we have less chance of having a matched island in the hadronic section at wide angles for a given track cut. The angular difference must also be accounted for because of the angular dependence of dE/dx as shown earlier in section 7.1.4. One could apply a direct correction to the data if the correction shown previously could be globally applied to all particles. However, as was said, this correction applies only to electrons, whereas our two samples are predominantly hadrons. Following a similar argument as in the case of momentum; as our final signal is electrons, we can then apply the correction for electrons only if class B' matches B in θ^{trk}. Therefore we apply the bin-by-bin correction from Figure 7.5 to the two samples in bins of polar angle (or pseudorapidity as this is how the analysis is defined).

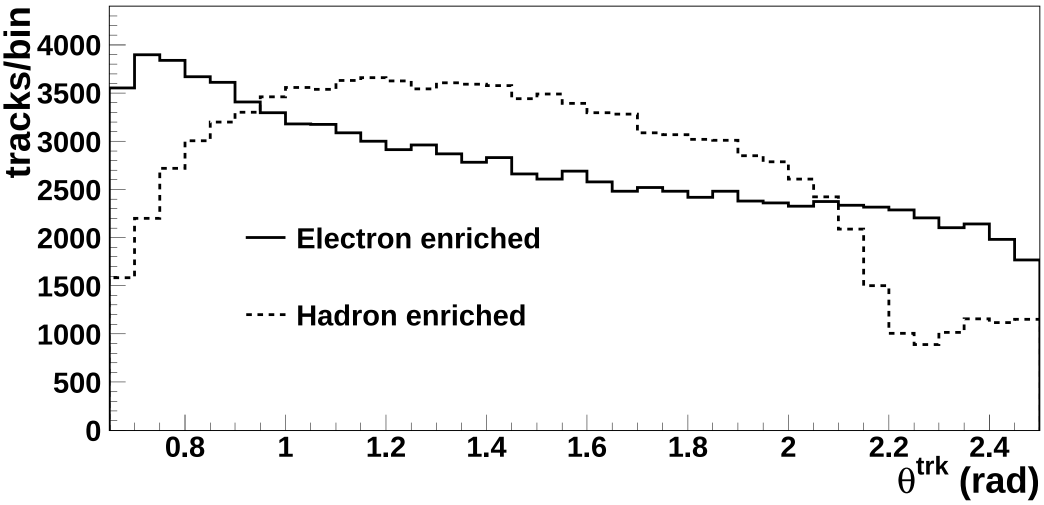

Figure 7.10: *Angular distributions for all tracks in the electron and hadron enriched samples passing the final analysis criteria. The hadron enriched sample is area normalised to the electron enriched sample.*

As a result of the differences in the electron and hadron enriched samples, we now perform the analysis in the following sixteen bins of p_T^{trk} and η^{trk}:

$$1.60 < p_T^{trk} < 2.00, \qquad -1.10 < \eta^{trk} < -0.55,$$

$$2.00 < p_T^{trk} < 2.45, \qquad -0.55 < \eta^{trk} < 0.00,$$

$$2.45 < p_T^{trk} < 3.00, \qquad 0.00 < \eta^{trk} < 0.55,$$

$$p_T^{trk} > 3.00, \qquad 0.55 < \eta^{trk} < 1.10.$$

Ideally the analysis should be performed in as large a number of bins as possible, but the above represents a balance between this and statistical limitation. By way of ensuring that the number of bins chosen is a good estimate of the large amount needed, one can compare the properties of the tracks between data and Monte Carlo. The angular dependence is not present in the Monte Carlo, thereby testing the correction procedure in the data. One can then choose a clean sample of electrons from semi-leptonic decays and compare the momentum and angular distributions. The angular dependence was first seen by comparing the data with the Monte Carlo, revealing that the two had a completely different shape. The data and Monte Carlo comparisons will be returned to later in the chapter.

7.3.3 Electron Signals in Bins of p_T^{trk} and η^{trk}

In Figure 7.11 we see the dE/dx distributions in the sixteen bins of p_T^{trk} and η^{trk} for the electron enriched and hadron enriched samples. The bins increase in transverse momentum from left to right and pseudorapidity from top to bottom. The normalisation of the hadron enriched to the electron enriched sample is performed in the region, $0.5 < dE/dx < 1.1$ mips. The region was chosen as it does not interfere with the electron signal and is essentially normalising the hadronic enriched sample to the hadrons in the electron enriched sample. The normalisation factor varies from bin to bin, being larger in the low momentum bins (up to 1.6) and smaller in the higher momentum bins (as low as 0.4).

From Figure 7.11, we observe an excess of the electron enriched over the hadron enriched samples in all bins for $dE/dx > 1.1$ mips. On consideration of the rise of the distribution on the left-hand side of the peak, we see that the two distributions are compatible with each other thereby providing some confirmation that the hadron enriched sample is a good estimator of our background in the electron enriched sample for all bins. Further justification of the background and its estimator and an excess at higher dE/dx, consistent with an electron signal, is gleaned by considering the subtracted distributions.

Figure 7.12 shows the subtracted distributions, and hence electron signal, in the same bins where again transverse momentum increases from left to right and pseudorapidity from top to bottom. The curves are simple Gaussian fits to the data by way of guiding the eye and are not used further in the analysis.

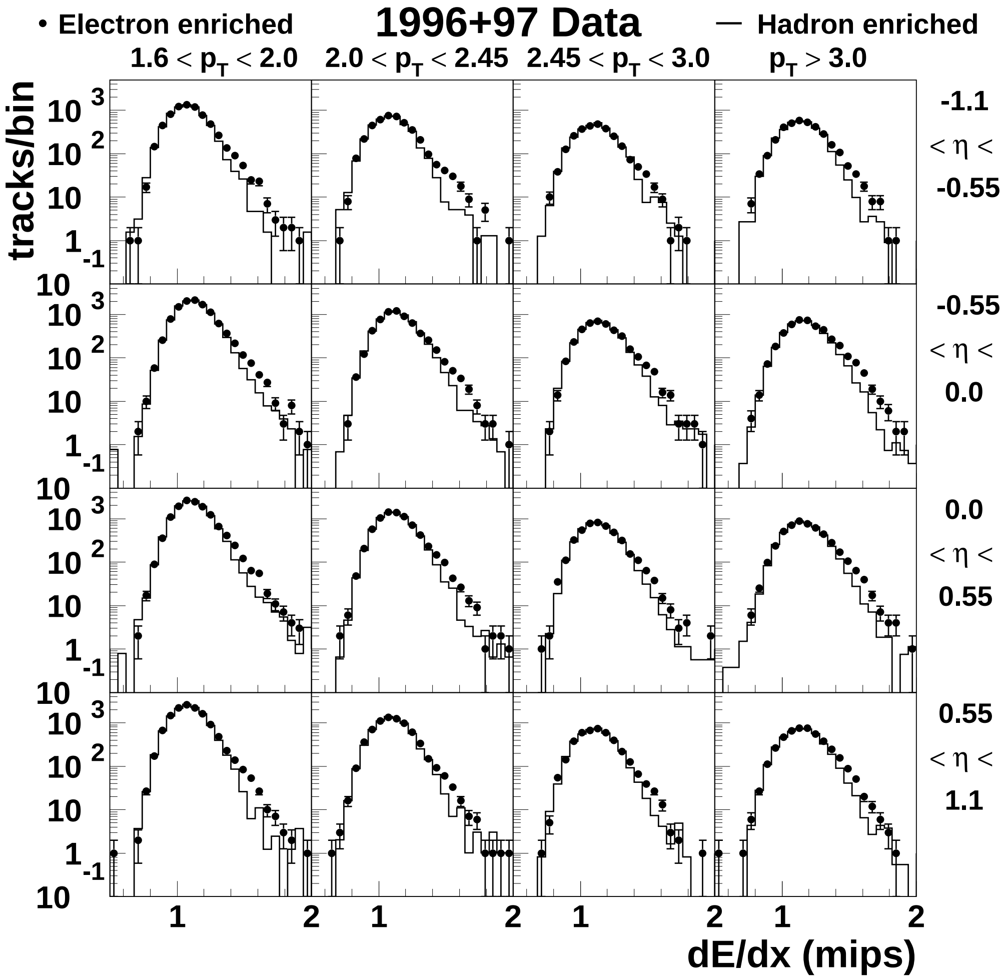

Figure 7.11: *Distributions of dE/dx for tracks matched to electron enriched (points) and hadron enriched (line) islands. The 16 bins are in increasing p_T^{trk} from left to right and increasing η^{trk} from top to bottom.*

In all bins of transverse momentum and pseudorapidity, we see a signal of electrons at about $dE/dx \sim 1.4$ mips, as expected. In the region of normalisation, $0.5 < dE/dx < 1.1$ mips, the data is consistent with zero, again indicating that our background estimator provides an appropriate description of our actual background.

The purpose of the binning; to remove the momentum and angular dependence of dE/dx and hence the analysis seems to have so far been successful. The background estimator provides a good description of the background and signals are achieved in each bin with none exhibiting a strange distribution consistent with a fault in the method.

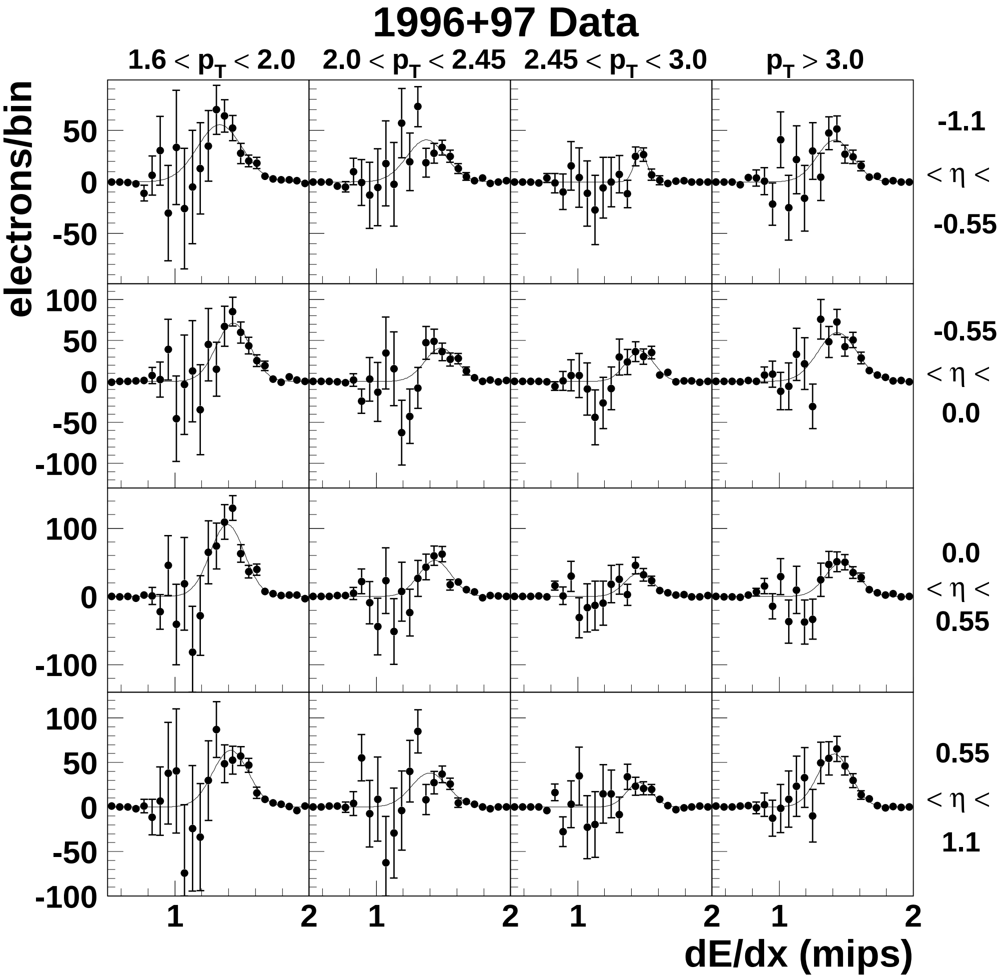

Figure 7.12: *Distributions of dE/dx for electrons from statistical subtraction of tracks matched to electron enriched (points) and hadron enriched (line) islands. The 16 bins are in increasing p_T^{trk} from left to right and increasing η^{trk} from top to bottom.*

7.3.4 Total Electron Signal

If we then take all the electron enriched signals in each bin and all the normalised hadron enriched signals in each bin and add them together to receive a total electron enriched and total hadron enriched signal we achieve the distribution in Figure 7.13 (Top). As with each bin separately, the agreement in dE/dx for the rising edge on the left-hand side between the two is good, indicating that our background is well described by our estimator. An excess is also seen at high dE/dx, which can be seen more clearly on subtraction of the two in Figure 7.13 (Bottom). Here we see a reasonably clean signal with the peak at $dE/dx \sim 1.4$, which shows that upon subtraction we are actually achieving a sample of electrons. The "cleanness" of the peak could possibly be improved by having more bins with increased statistics. However, the current procedure and statistical sample yields a promising signal with which to extract physics results.

To then extract physics results we make one final requirement on the data;

$$\frac{dE}{dx} > 1.4 \text{ mips}.$$

This cut on the mean value for electrons (as dictated by our previous correction) implies an efficiency of 50% and is chosen to remove the need for any fits to the data which would be affected by the uncertainties for $dE/dx < 1.4$ mips. Using the data below this value (even though doubling the statistics) also yields the problem of larger statistical errors due to the previous subtraction of large numbers. Also below this value the purity will be worse as it is the region in which the signal to background ratio decreases (down to $\sim 1:100$). Above this value we have 2476 ± 74 electrons, the error, $\sigma_{N_{tot}}$, being extracted by relating it to the number of electron enriched, x, and hadron enriched, y, tracks above $dE/dx = 1.4$ mips, to the number in the normalisation region ($0.5 < dE/dx < 1.1$ mips), x_1 and y_1 for electron and hadron enriched candidates respectively, such that,

$$\sigma_{N_{tot}} = \sqrt{\sum_{i=1}^{16} \left[x + \frac{x_1^2}{y_1^2} y + y^2 \left(\frac{x_1}{y_1^2} + \frac{x_1^2}{y_1^3} \right) \right]_i}, \tag{7.8}$$

where we have summed over the sixteen bins in p_T^{trk} and η^{trk}. The derivation of Equation (7.8) is shown in the Appendix.

With the signal now realised we can then unfold to the cross-section only after we have considered if there are any backgrounds. As the cross-section we are going to unfold to requires there only to be an electron in the final state, then the only background comes from electrons from the aforementioned photon conversions.

All other electrons inclusive of decays from beauty, charm and light quarks are included. Electrons from photons converting in the beampipe, however, provide a large source of background and involve a three stage procedure to remove them as detailed after a discussion of the dE/dx in the Monte Carlo.

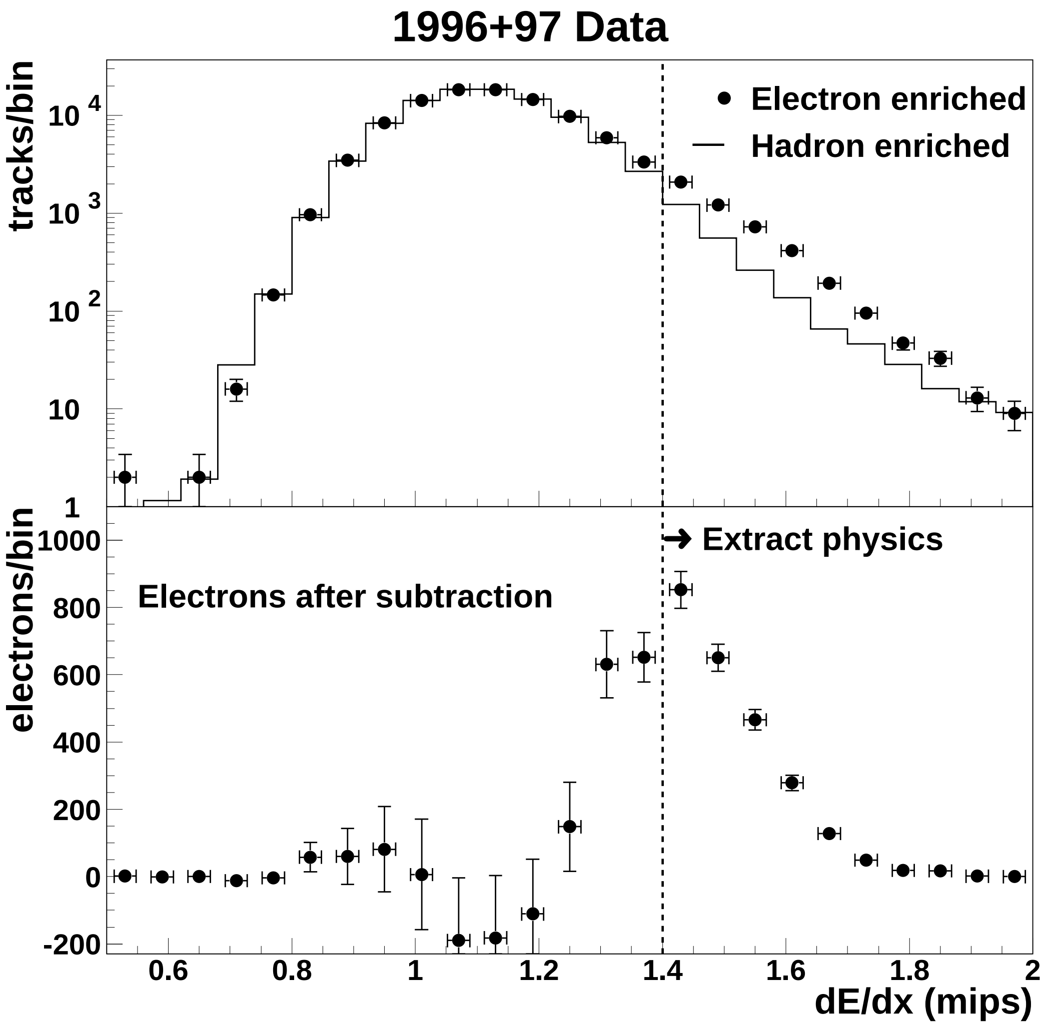

Figure 7.13: *Total distributions of dE/dx for tracks matched to electron enriched (points) and hadron enriched (line) islands (top) and for electrons from statistical subtraction of tracks matched to electron enriched and hadron enriched (bottom).*

7.4 dE/dx in the Monte Carlo

An important question in this analysis, is how good is the description of dE/dx in the Monte Carlo? To investigate this, we are going to follow the procedure as for the data and consider the distributions in bins of p_T^{trk} and η^{trk} and the total signal. We have used a Monte Carlo in which electrons in the final state were pre-selected, so the background in the electron enriched signal is small compared to that in the data. Performing the analysis and comparing electron enriched with hadron enriched results in Figure 7.14, where the dE/dx of the tracks is displayed in FADC counts as no *scaling* over runs is required in the Monte Carlo as there is only one run. The hadron enriched sample is normalised to the electron enriched sample in the region $25 < dE/dx < 55$ FADC counts.

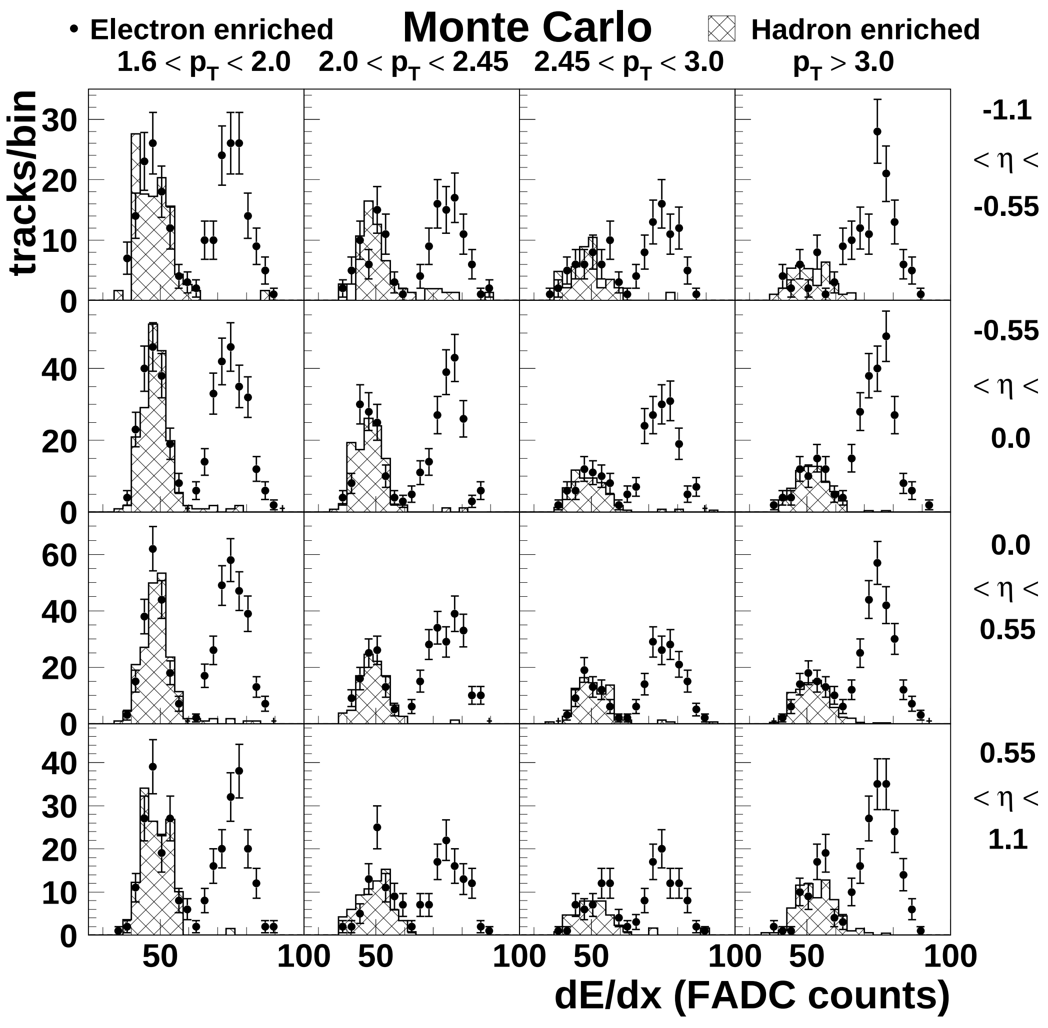

Figure 7.14: *Distributions of dE/dx for tracks matched to electron enriched (points) and hadron enriched (line) islands. The 16 bins are in increasing p_T^{trk} from left to right and increasing η^{trk} from top to bottom for HERWIG Monte Carlo.*

Figure 7.14 demonstrates one problem that exists with the Monte Carlo description of dE/dx, the relative value for electrons compared to hadrons is larger

(~ 1.6) than in the data (~ 1.4). However, it also shows that the cuts applied to the data do work in the Monte Carlo, with the hadron enriched sample providing a good estimate of the background. This can also be seen in Figure 7.15 in which the subtraction yields a signal in all bins and a cancellation of the background at low dE/dx values. This provides vindication of the subtraction method, albeit easier than in the case of the data. Simple Gaussian fits are again overlayed in order to guide the eye and are not used further in the analysis.

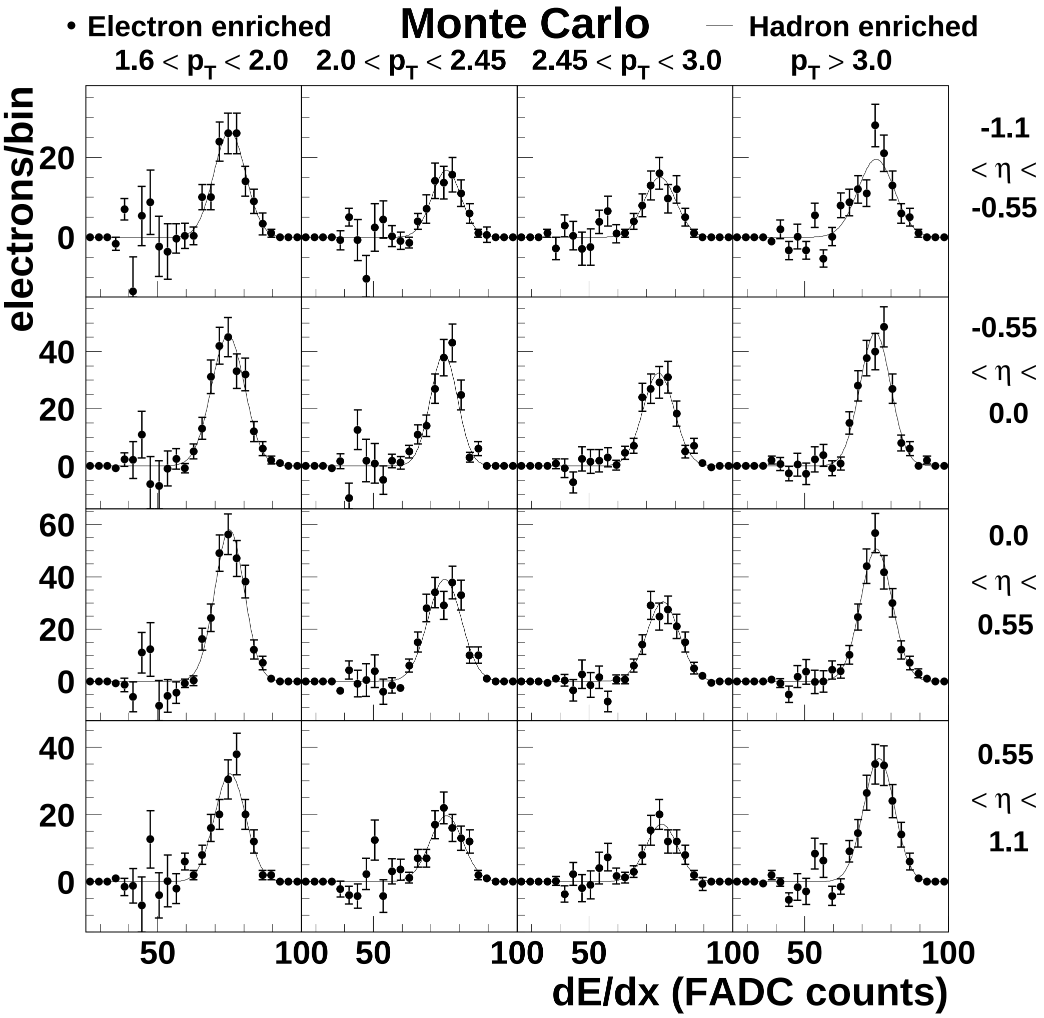

Figure 7.15: *Distributions of dE/dx for electrons from statistical subtraction of tracks matched to electron enriched (points) and hadron enriched (line) islands. The 16 bins are in increasing p_T^{trk} from left to right and increasing η^{trk} from top to bottom for HERWIG Monte Carlo.*

The procedure has also been performed using standard photoproduction Monte Carlo with no electron filter. This Monte Carlo, like the data, consists predominantly of hadrons in both the electron and hadron enriched samples. After application of the analysis criteria, the same results were seen; the hadron enriched providing an estimate of the background in the electron enriched sample and an electron signal remaining on subtraction of the two. The statistical sample for this was small, but large enough to see that the procedure worked. However, to get enough statistics for the Monte Carlo (without an electron filter) to be compatible with the data would require the generation of millions of events; there currently not being enough within the ZEUS collaboration, hence the electron filter.

Again, we add up all the bins for the electron and hadron enriched samples and compare the two (Figure 7.16 (Top)). As in each of the bins individually, the description of the background by the background estimator is good. The total subtracted electrons can also be determined (Figure 7.16 (Bottom)). The resulting signal for the Monte Carlo, is very clean with a mean at 75 FADC counts as indicated by the dashed line. With this signal, we see another problem with the Monte Carlo, that of the width of the distribution. The Monte Carlo distribution is narrower than in the data.

To extract the distribution we use this signal, but cut on the mean dE/dx of the signal (75 FADC counts) as in the data. By cutting on the mean and therefore requiring 50% of the sample we are removing any problem associated with the width of the signal. We can also see that the contamination from the hadron enriched sample in this region is small ($\mathcal{O}(1\%)$), so we are actually choosing an almost pure sample of electrons. This then allows us to be independent of the subtraction and test the efficiency of all the electron selection cuts.

In conclusion; although the dE/dx of a particle is not well modelled in the Monte Carlo, exhibiting many different properties compared to the data, we can perform the analysis by being largely independent of it.

7.5 Background from Conversion Electrons

Photons convert into electron-positron pairs in material in the ZEUS detector. Those converting in the beampipe and CTD inner wall constitute the major background for this physics study. The large majority of the photons arise from the decays of π^0 mesons, yielding a large number of photons over a large energy spectrum.

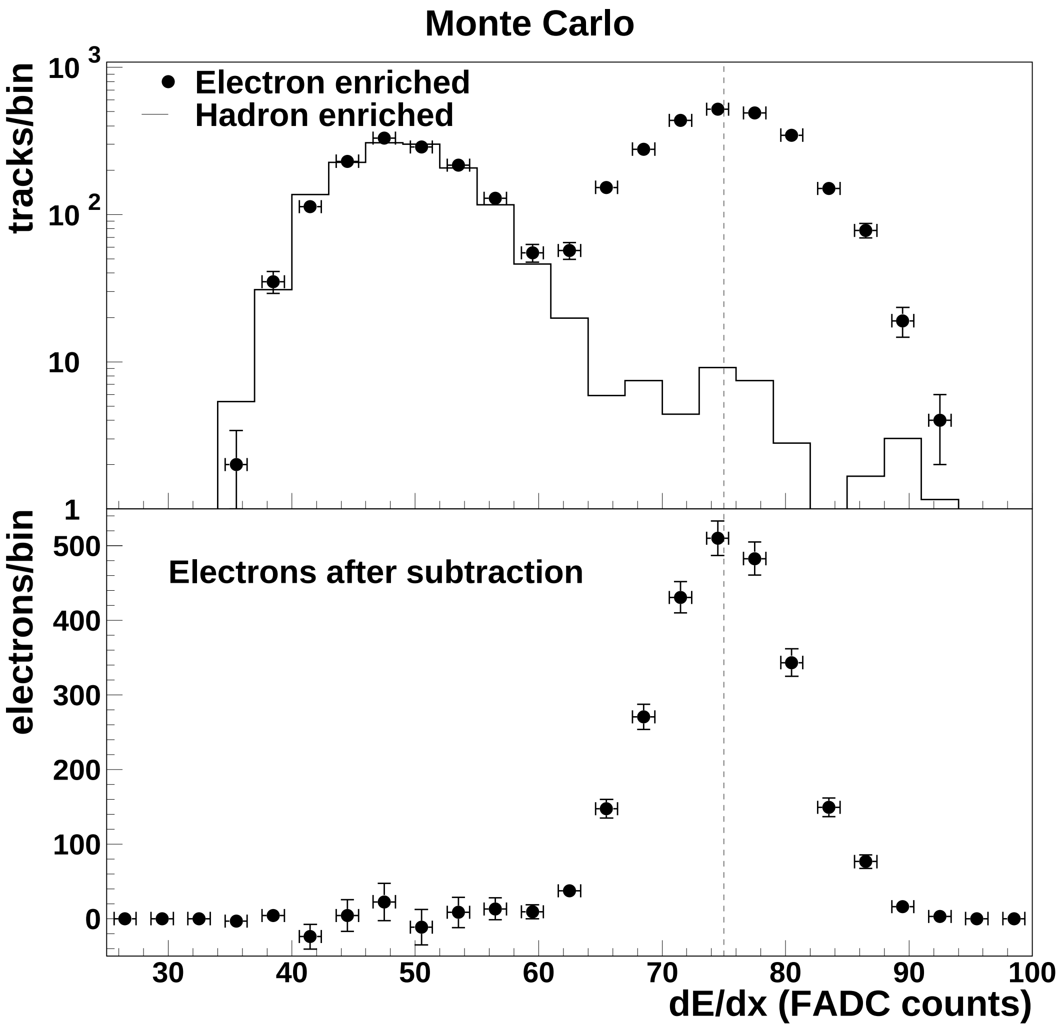

Figure 7.16: *Total distributions of dE/dx for tracks matched to electron enriched (points) and hadron enriched (line) islands (top) and for electrons from statistical subtraction of tracks matched to electron enriched and hadron enriched islands (bottom) for HERWIG Monte Carlo.*

7.5.1 Direct Identification of Photon Conversions

An electron-positron pair system arising from a converted photon has a distinct signature; the electron and positron have a distance of closest approach of zero and invariant mass of zero (neglecting the mass of the electron itself). A topological conversion finder, CONVERT2 [101], which takes combinations of oppositely charged track pairs (equally charged pairs being kept for background estimations) was used to identify those electrons in our sample which are from photon conversions. The topology of the system can be schematically visualised in Figure 7.17. The distance when the tangents of the two curves are parallel, Δxy, and the difference in polar angle, $\Delta\theta$, each provide quality tests of the conversion candidate, such that the following must be satisfied,

$$\Delta\theta < 0.1 \text{ rad}; \quad \Delta xy < 4\text{mm},$$

and when combined provide an additional, dimensionless quality factor, D, given by,

$$D = \sqrt{\left(\frac{\Delta xy}{\sigma_{xy}}\right)^2 + \left(\frac{\Delta\theta}{\sigma_\theta}\right)^2} \tag{7.9}$$

where, σ_{xy} and σ_θ are the resolutions of the Δxy and $\Delta\theta$ distributions. By cutting on this value, D, we can either select a highly pure sample with a low efficiency or an inclusive but impurer sample. The distribution in D for opposite and same charged tracks is illustrated in Figure 7.18 (Left). For electrons in our sample, we want to identify as many conversions as possible, therefore choosing a reasonably inclusive (efficient) sample by requiring,

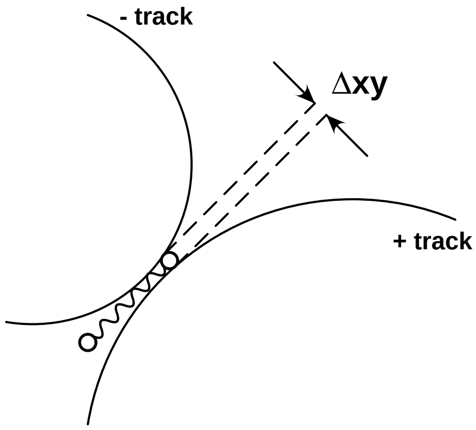

Figure 7.17: *Schematic diagram showing the distant of closest approach of a conversion pair.*

$$D < 15.$$

For purposes of calibration when a clean sample is required (for example, Figure 7.5), this requirement is tightened along with an invariant mass, $M_{e^+e^-}$, criteria;

$$D < 5; \quad M_{e^+e^-} < 0.025 \text{ GeV}.$$

The reasoning for the invariant mass requirement can be seen in Figure 7.18 (Right), where below this value the background (same charge pairs) lies well below the opposite charge track pairs.

Figure 7.5 (Left) shows how effective the same charged track pairs is as a background estimator. A statistical subtraction of the two provides us with the

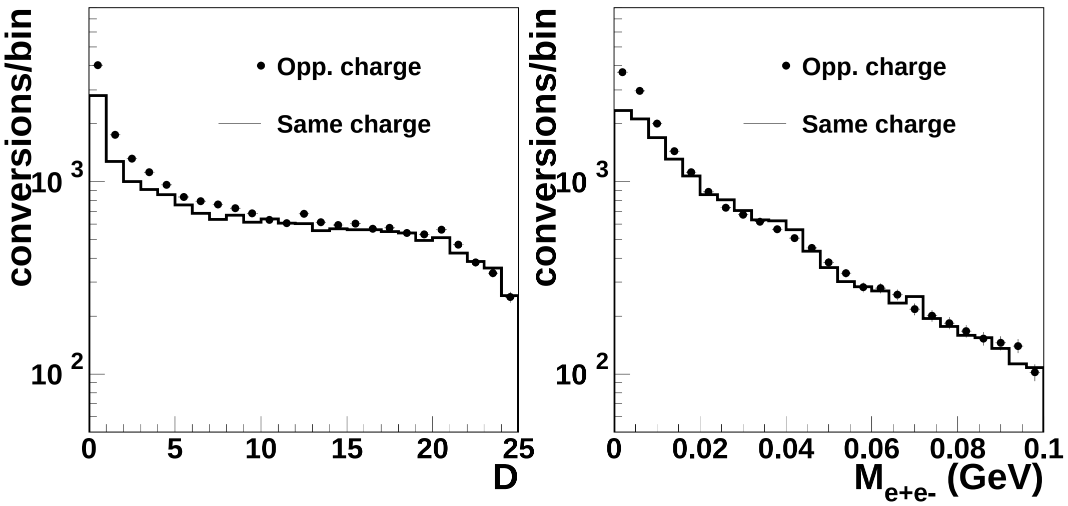

Figure 7.18: *Distributions of parameter, D (Left) and invariant mass of conversion pair system, $M_{e^+e^-}$ (Right) for opposite charged (points) and same charged (line) pairs.*

number of conversions seen. Of the 2476 electrons from potential quark decays, 599 ± 26 are identified as coming from photon conversions. The error has been calculated from the subtraction of the same charge from the opposite charge pairs assuming Poisson errors.

This summarises our first step in identifying conversion electrons, the next two being a determination of the efficiency of the procedure.

7.5.2 Conversion Finding Efficiency

To find the conversion efficiency, we have devised a two, rather than one step process, to be as independent from Monte Carlo as possible. The first step calculates the efficiency for those conversion pairs which are highly asymmetric as predicted by a theoretical calculation. The second step, however, relies on using the Monte Carlo, providing us with a global efficiency on top of the asymmetric efficiency, but extrapolating less than if the first step had not been used. The two steps will now be discussed.

Efficiency of Finding Asymmetric Pairs

The efficiency of the conversion finder is dependent on the momentum symmetry of the electron and positron tracks produced. For symmetric tracks the efficiency is high, but for asymmetric tracks, one of the tracks may lie outside the reconstruction region of the CTD. Therefore only one track is reconstructed and is indistinguishable from our quark decays and so an estimation of this efficiency is essential. To estimate this we look at the distribution of the energy fraction of the electron pair-produced from a photon by considering the calculation of Tsai [102]. This starts from the exact calculation for pair-production, accounting for screening and applying it to heavy atoms.

For a photon with momentum k producing an electron with momentum $p = x \cdot k$ (and positron with momentum $p' = k - p$), the cross-section for atomic number, $Z \geq 5$ is given by:

$$\begin{aligned} \frac{d\sigma}{dp} &= \frac{\alpha r_0^2}{k} \left\{ \left(\frac{4}{3}x^2 - \frac{4}{3}x + 1 \right) \left[Z^2 \left(\phi_1 - \frac{4}{3}\log Z - 4f \right) + Z \left(\psi_1 - \frac{8}{3}\log Z \right) \right] \right. \\ & \left. -\frac{2}{3}x\left(1-x\right) \left[Z^2(\phi_1 - \phi_2) + Z(\psi_1 - \psi_2) \right] \right\}, \end{aligned} \tag{7.10}$$

where α is the fine structure constant, r_0 the classical electron radius and;

$$\begin{aligned} \phi_1\left(\gamma\right) &= 20.863 - 2\log\left[1 + \left(0.55846\gamma\right)^2\right] - 4\left[1 - 0.6e^{-0.9\gamma} - 0.4e^{-1.5\gamma}\right], \\ \phi_2\left(\gamma\right) &= \phi_1\left(\gamma\right) - \frac{2}{3}\left(1 + 6.5\gamma + 6\gamma^2\right)^{-1}, \\ \psi_1\left(\varepsilon\right) &= 28.340 - 2\log\left[1 + \left(3.621\varepsilon\right)^2\right] - 4\left[1 - 0.7e^{-8\varepsilon} - 0.3e^{-29.2\varepsilon}\right], \\ \psi_2\left(\varepsilon\right) &= \psi_1\left(\varepsilon\right) - \frac{2}{3}\left(1 + 40\varepsilon + 400\varepsilon^2\right)^{-1}, \\ f\left(z\right) &= z\sum_{n=1}^{\infty}\frac{1}{n\left(n^2+z\right)} \approx 1.202z - 1.0369z^2 + 1.008\frac{z^3}{(1+z)}, \\ \text{with} \quad & \gamma = \frac{100m_e k}{E_e E_e' Z^{1/3}}, \quad \varepsilon = \frac{100m_e k}{E_e E_e' Z^{2/3}}, \quad z = \left(\frac{Z}{137}\right)^2 \end{aligned}$$

where E_e is the energy of the electron and E_e' the energy of the positron in the laboratory system.

The cross-section, $d\sigma/dx$, is shown in Figure 7.19 as a function of E_{e^-}/E_γ for $Z = 13$ (aluminium) for different photon energies.

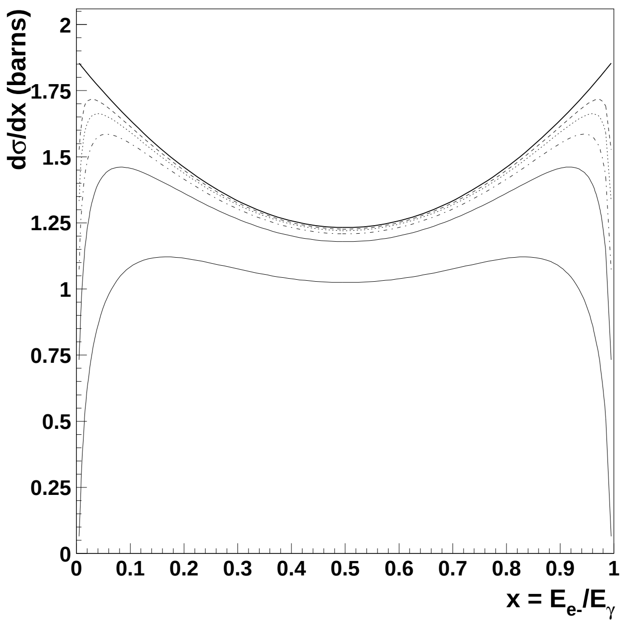

Figure 7.19: *Differential cross-section as a function of E_{e^-}/E_γ for aluminium using the equations from Tsai with photon energies, E_γ of ∞ (top curve), 5, 2.5, 1.2, 0.5, 0.1 (bottom curve) GeV.*

Using this theoretical prediction, the hope is then to determine the efficiency of the conversion finder for asymmetrically produced pairs. To do this it has to be demonstrated that the ZEUS conversion data is in agreement with the theoretical prediction. In this way a model independent efficiency can be determined by not relying on Monte Carlo expectations.

Within the range under study, $-1.1 < \eta(e^-) < 1.1$, the CTD reconstructs tracks with a momentum independent efficiency above 200 MeV/c. Below this momentum value, the efficiency is greatly reduced and so using the Monte Carlo introduces model-dependence. To estimate the number missed we therefore apply a cut to the positive track from the pair to be above this momentum value (the negative track is already required to be $p_T^{trk} > 1.6$ GeV/c) and compare to the situation when no momentum cut is applied.

To demonstrate the consistency of the ZEUS data and the theory, we take a sample of clean conversions, as defined previously, and a conversion energy, $E_\gamma > 1$ GeV with the additional criteria that the momentum of each of the two tracks is greater than 200 MeV/c. We then have a sample of conversions with different photon energies and we compare this to the theory by taking the photon distribution for the data and using it as the input for Tsai's equations.

The results can be seen in Figure 7.20 where the points are the data and the solid line the theoretical prediction.

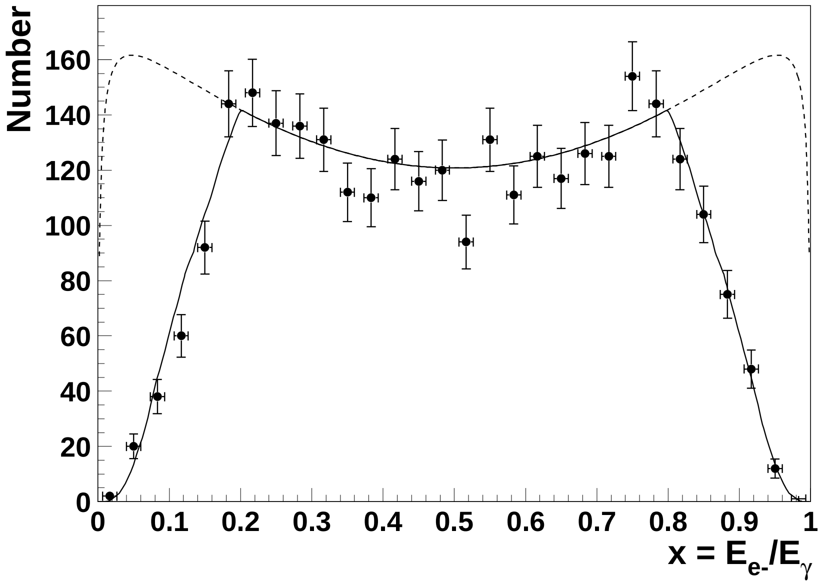

Figure 7.20: *Comparison of the number of events as found in the data (points) with the prediction from theory (solid line) for clean conversions with energy, $E_\gamma > 1$ GeV and the momentum of both tracks greater than 200 MeV/c. The prediction is also shown for no cut on the momentum of the tracks (dashed line).*

Also shown is the theoretical prediction if no track momentum cuts were imposed (dashed line). The data and theory describe each other well in both shape and normalisation. The dip at central values with a slow rise and then a sharp drop (due to the track momentum cuts) are all well-produced. With confidence in the compatibility of the data and the theory, we can assign an efficiency, which is the ratio of the two curves.

The ratio of these two curves is an overall efficiency which is not directly applicable to the measurement being made. Due to the cut on our candidate tracks of $p_T^{trk} > 1.6$ GeV/c, the efficiency is dependent on the energy of the converting photon. The ratio of the two curves was then found as a function of photon energy (Figure 7.21) for different minimum track cut-offs. As can be seen for the curve with the cut-off at 200 MeV/c (thick line), the minimum photon energy is (1.6 + 0.2 =) 1.8 GeV, with the efficiency rising rapidly before reaching a reasonably constant value around 3 GeV. Therefore, for a given photon energy, a weight taken from this curve can be assigned to ascertain the number of conversions corrected for asymmetric pairs which were not tagged.

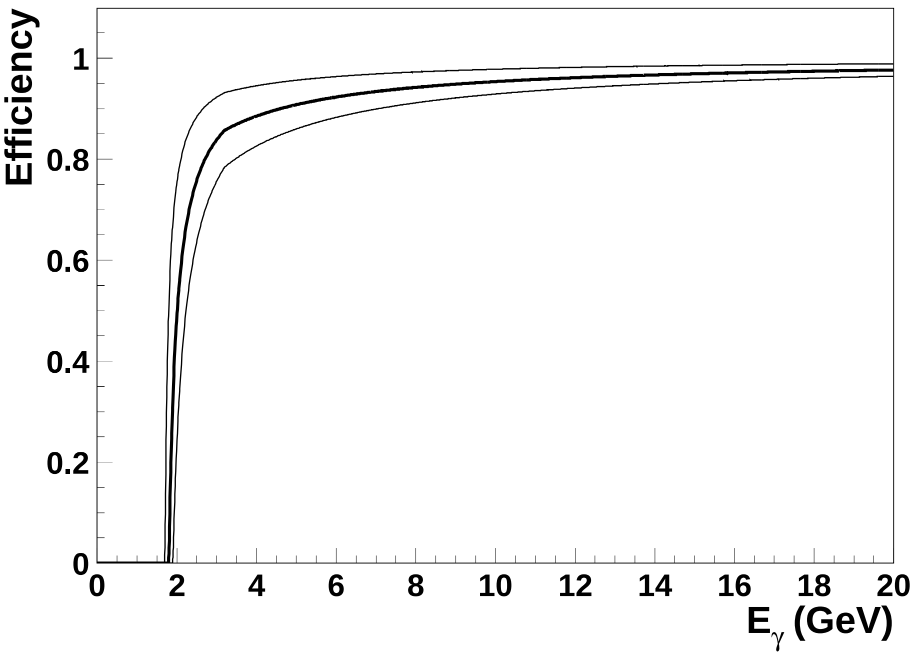

Figure 7.21: *The fraction of findable coversions (efficiency) as a function of photon energy for different track momentum cuts of 100 (top curve), 200 and 300 MeV/c (bottom curve).*

The procedure yielded an efficiency of 80%, thereby increasing the estimated number of conversions from 599 $\pm$ 26 to 748 $\pm$ 33.

Global Efficiency for Conversion Finder

As a final step to estimate the total number of electrons from photon conversions, we have to ascertain an overall, "global" efficiency. This is a Monte Carlo based procedure and we have to somehow estimate from all the true conversions, how many are found from our previous two steps. Within the ZEUS detector, there are a large number of photon conversions which could never enter into our sample of candidate tracks and can therefore be neglected. If we were not to remove them and simply count all the photon conversions as produced by GEANT, then our efficiency would be less than 1%. However, knowing exactly which true photon conversions to remove is non-trivial. Photons which convert at the edge of the CTD could have the electron passing through the CTD and into the calorimeter, the positron not entering the CTD. This may or may not then enter our sample but knowing which of these kind of true events to remove is impossible. We therefore choose not to define the undefinable true sample and seek another method.

The method used is in a sense analysis specific, being only relevant to the analysis requirements as detailed and cannot therefore be used in any other context although should be comparable for a similar kinematic region. By requiring *no* final state electrons and performing the analysis on these events, we find an effective total number of conversions. Applying the conversion finder and applying the asymmetric efficiency, we have the number of conversions our method so far finds. The ratio of the two therefore provides us with our global efficiency. This was found to be 90%, which upon application to the number so far ascertained in the analysis yields a total of 830 $\pm$ 36 electrons coming from photon conversions. The number of electrons estimated as arising from photon conversions represents about one-third of our total electron signal sample, reducing it to, 1646 $\pm$ 82 electrons. The identification of the number of electrons from photon conversions is summarised in Table 7.1.

	No. conversions	No. electrons
Initial	-	2476 $\pm$ 74
After CONVERT2	599 $\pm$ 26	1877 $\pm$ 79
Tsai weighting	748 $\pm$ 33	1728 $\pm$ 81
Global weighting	830 $\pm$ 36	**1646 $\pm$ 82**

Table 7.1: *Table showing the number of electrons from conversions and the subsequent number of electrons in the final sample.*

We have now fully estimated the background in our signal sample, the remaining electrons entering into our cross-section calculations.

7.6 Extraction of $x_\gamma^{\rm obs}$ and p_T^{rel} Distributions

Using the electrons now found, we can use them to calculate physics distributions, $x_\gamma^{\rm obs}$ and p_T^{rel} being the interesting ones in this analysis, where $x_\gamma^{\rm obs}$is defined in Chapter 2 and p_T^{rel} in Chapter 3. The basic method to extract them is the same in each case so we will initially concentrate on the $x_\gamma^{\rm obs}$ distribution by way of an example.

Each time we tag a track as being an electron or hadron enriched candidate we calculate the event property $x_\gamma^{\rm obs}$, where the hadron enriched sample is appropriately weighted from the normalisation factors. The result of this can be seen in Figure 7.22 (Top), where the $x_\gamma^{\rm obs}$ distribution is shown for the events containing the two classes of track-island matched quantities. The electron enriched is displayed as the open squares and the hadron enriched as the histogram. The first and most obvious point of the graph is that there is a peak at high $x_\gamma^{\rm obs}$ for the electron enriched sample consistent with direct photon events which is not as pronounced in the hadron enriched sample. The distribution for the hadron enriched sample is reasonably flat in $x_\gamma^{\rm obs}$, indicating that the presence of the electron and hence heavy quarks enhances the direct peak. The same conclusion was drawn in the analysis of D^* mesons in which the signal region was peaked at high $x_\gamma^{\rm obs}$ and the wrong-charge background estimator was flatter in $x_\gamma^{\rm obs}$.

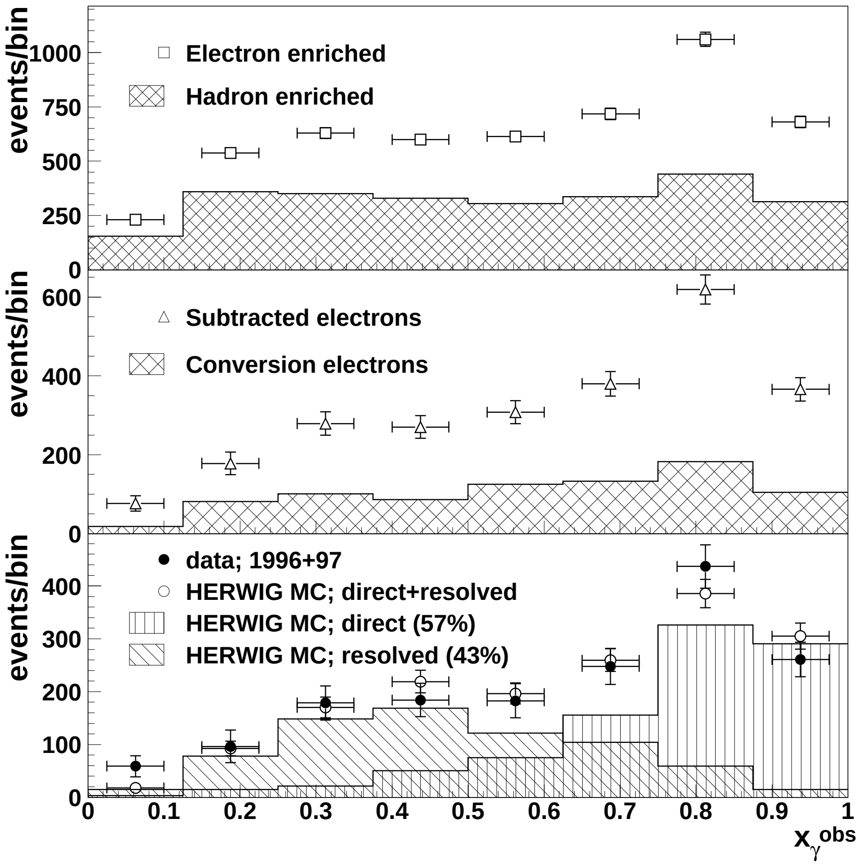

Figure 7.22: *Distribution in $x_\gamma^{\rm obs}$ for the electron (squares) and hadron (histogram) enriched samples (top) after all cuts. Also shown (centre) are the two subtracted (triangles) compared to the conversion electrons (histogram). The final electron signal (solid circles) is then compared to Monte Carlo (open circles) predictions (bottom) with direct and resolved also shown separately.*

Upon subtraction of the two distributions, we have the distribution shown as the open triangles in Figure 7.22 (Centre), which represents the $x_\gamma^{\rm obs}$ distribution for 2476 electrons in the signal region. Also shown is the distribution for those electrons identified as conversions appropriately weighted for the two-step efficiency procedure. The distribution for conversion electrons is also peaked at high $x_\gamma^{\rm obs}$, but not as remarkably as for the total electron signal. Subtraction of the two yields the distribution shown as solid points in Figure 7.22 (Bottom), which represents our uncorrected $x_\gamma^{\rm obs}$ distribution.

The uncorrected $x_\gamma^{\rm obs}$ distribution is compared to Monte Carlo predictions from HERWIG (open circles). The proportion of direct and resolved from a fit to the data are also separately shown. The fit reveals a value of 43±4% for resolved photon processes, the combined sample in good agreement with the measured data. The proportion of LO resolved photon Monte Carlo required is also vindication of the results for the analysis with D^* mesons (which is consistent with the predicted value) even though the kinematic range and the amount of charm events is different.

We can also follow the same process for a measurement of p_T^{rel} and it is shown in Figure 7.23. The same distributions are displayed as for the measurement of $x_\gamma^{\rm obs}$. The distributions have variable bin widths, due to a small amount of statistics in the higher bins, which then makes the performing of Monte Carlo fits to the data more reliable.

The comparison of the electron and hadron enriched samples Figure 7.23 (Top) reveals nothing of remark, both being of similar shape. The same applies to the comparison of the subtracted electrons and conversion electrons in Figure 7.23 (Centre), although the subtracted electrons are slightly harder in p_T^{rel}. However, on comparison with HERWIG Monte Carlo predictions the data shows an interesting trend Figure 7.23 (Bottom). The Monte Carlo has been area normalised to the data, and the proportion of direct and resolved from the fit to $x_\gamma^{\rm obs}$ used. No further fits for proportions of direct and resolved or quark content were made. From the Figure, we see that there is a tendency for the data to be harder than the Monte Carlo prediction. In the first two bins, the data lies below that of the Monte Carlo, this then inverts itself, with the data lying above the Monte Carlo in the last two bins. If we fit the amount of beauty and charm+other to the data we obtain a value for beauty of 42±6%. Is this an indication of the Monte Carlo predicting too much or too little of certain processes? We will first correct the data, reassess the comparison with Monte Carlo and then try and draw some conclusions.

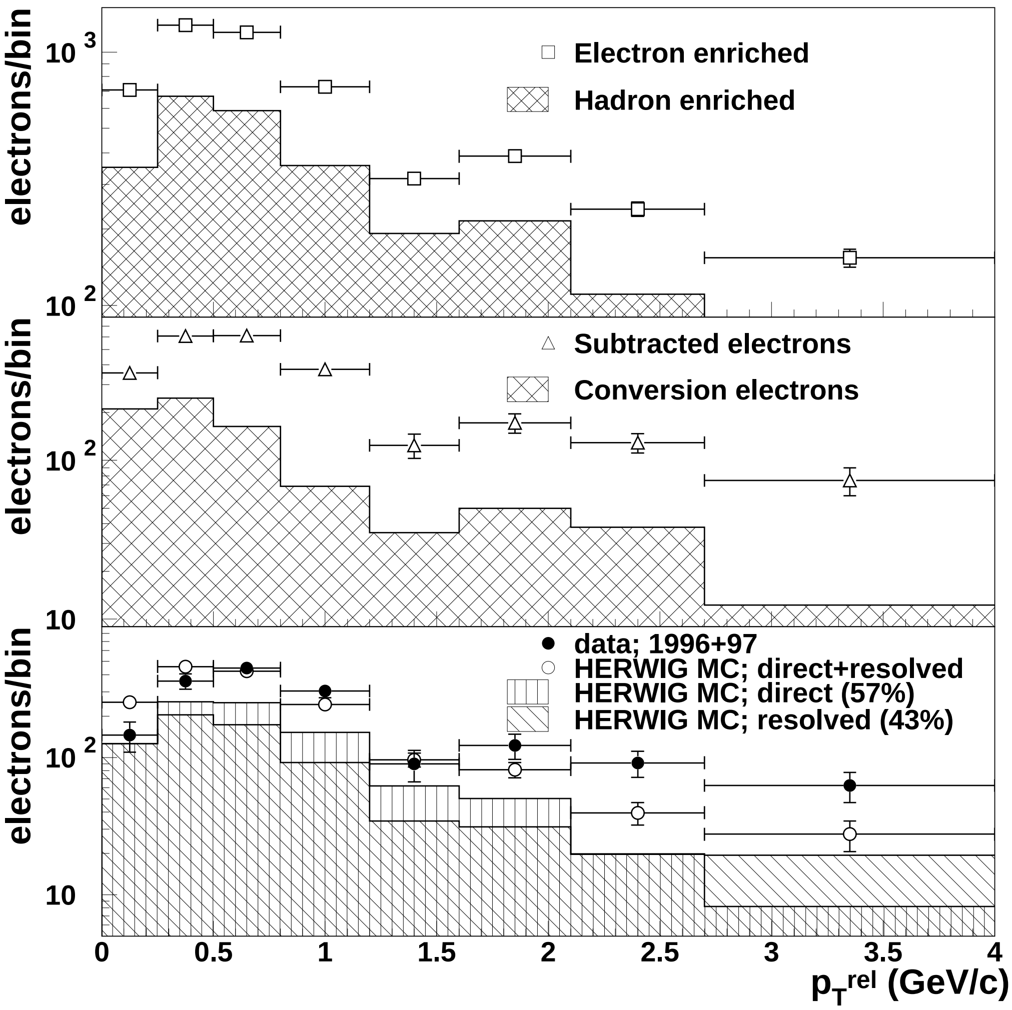

Figure 7.23: *Distribution in p_T^{rel} for the electron (squares) and hadron (histogram) enriched samples (top) after all cuts. Also shown (centre) are the two subtracted (triangles) compared to the conversion electrons (histogram) in the data. The final electron signal (solid circles) is then compared to Monte Carlo (open circles) predictions (bottom) with direct and resolved also shown separately.*

7.7 Other Sources of Background?

Having now achieved our uncorrected distribution in $x_\gamma^{\rm obs}$, we briefly return to the question of backgrounds apart from electrons from photon conversions. As was stated previously, there are no other backgrounds to subtract. The decays from light quarks remain as well as those from heavy quarks as only model dependent methods exist for their subtraction.

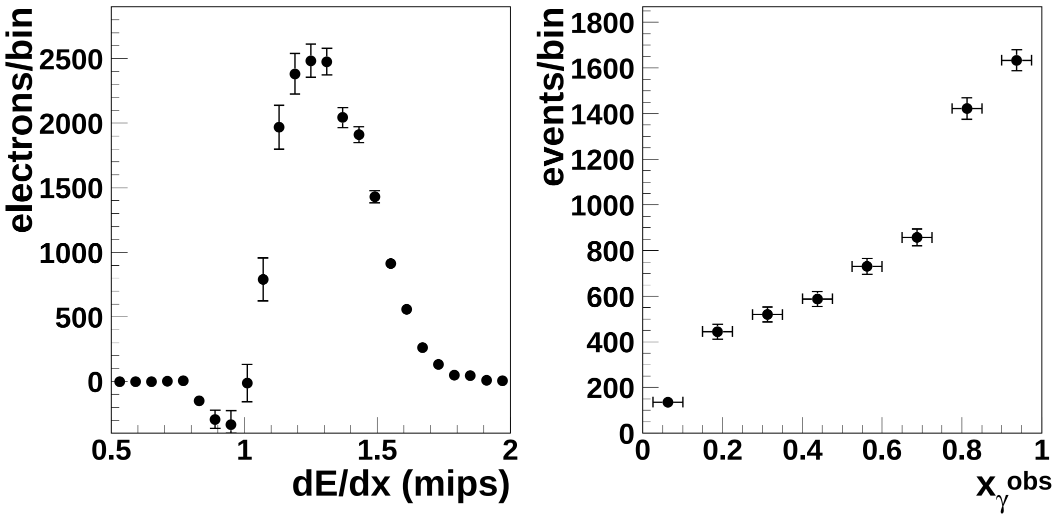

Figure 7.24: *Distributions in dE/dx for subtracted* positron *signal (Left) and subsequent $x_\gamma^{\rm obs}$ distribution (Right).*

If we were considering positrons as well as electrons, then we would have to think more carefully about backgrounds. In Figure 7.24 we see the distribution if we tag positrons rather than electrons with all other analysis criteria remaining the same. From the distribution in dE/dx, we can see that the result of statistical subtraction is poor. This has been influenced by the large amount of extra positrons (compared to electrons) observed, which shifts the peak value and affects the normalisation of the background. The method we have adopted is reliant upon the number of electrons being small particularly at high momentum. At high momentum the separation in dE/dx of electrons and hadrons becomes worse; consequently one has to start normalising the hadron enriched signal to the electron enriched signal in the region of the *electron signal* itself. As many of the extra positrons here observed are at higher momentum, the problem therefore arises. One has to then ask the question, what are these extra positrons? The first and obvious thought would be that they are scattered DIS positrons, which from the shape of Figure 7.24 (Right) is given some credance. The $x_\gamma^{\rm obs}$ distribution shows a similar shape to that for electrons (see Figure 7.22) except for the last bin which is high being indicative of DIS processes.

As we are specifically rejecting DIS and tagging photoproduction events, we should have no DIS scattered positrons, although there is always contamination in one from the other. However, this then puts into question the results using electrons and begs the question, how much DIS contamination do we have?

Obviously the number of extra positrons cannot be exactly stated as the method needs to be changed to perform the analysis, but it seems to be of the order of a few thousand. This may seem like a large number, but as the analysis is to specifically tag positrons, we find a large number of them. It also has to be taken into context of how many electron enriched tracks we have; $\sim$ 100000, which implies that the scattered positrons are a few percent of those tracks, indicating that the DIS contamination is not large.

The above explains why positrons have not been used. For them to be used, the method needs to be adapted with the following being important points which need to be addressed:

- Can we more efficiently eliminate scattered positrons?
- If not, can we estimate the number?
- Can we improve the resolution of the CTD?
- If we do have scattered positrons, then an upper limit on the momentum of the track will reject many.

The inclusion of the positron data obviously needs more study and will not be possible without solving the above problems. This is not covered further in this thesis and we will concentrate solely on the electron sample.

7.8 Comparison of Data and Monte Carlo

Before correcting our data to a cross-section, we would like to compare event properties and look at resolutions in the Monte Carlo.

We first consider the resolutions in pseudorapidity and transverse momentum of tracks which are our candidate tracks. The resolution distributions are shown in Figure 7.25 for all tracks. Both the distributions in pseudorapidity (Left) and transverse momentum (Right) show no average shift and both have good resolutions. Of particular interest is the resolution of the transverse momentum which is,

$$\frac{\sigma(p_T)}{p_T} = 0.011.$$

This represents an upper limit as we have assumed $p_T = 1.6$ GeV/c, which is the lower cut-off value. The p_T resolution of the CTD as stated in Chapter 1 is not in good agreement with this figure; again with $p_T = 1.6$ GeV/c, the resolution is predicted to be;

$$\frac{\sigma(p_T)}{p_T} \approx 0.005 p_T \oplus 0.016 = 0.018,$$

which in this case represents a lower limit.

Further research has been done [91] and found that the above form of the resolution is not a good estimator particularly for low transverse momentum tracks and as high as $p_T \approx 3 - 4$ GeV/c. An improved form was postulated such that,

$$\frac{\sigma(p_T)}{p_T} \approx 0.0058 p_T \oplus 0.008 \oplus 0.0014/p_T,$$

which predicts $\sigma(p_T)/p_T = 0.012$ for the distribution in question. We can therefore conclude that the resolution observed is in better agreement with the new postulated form than the quoted one.

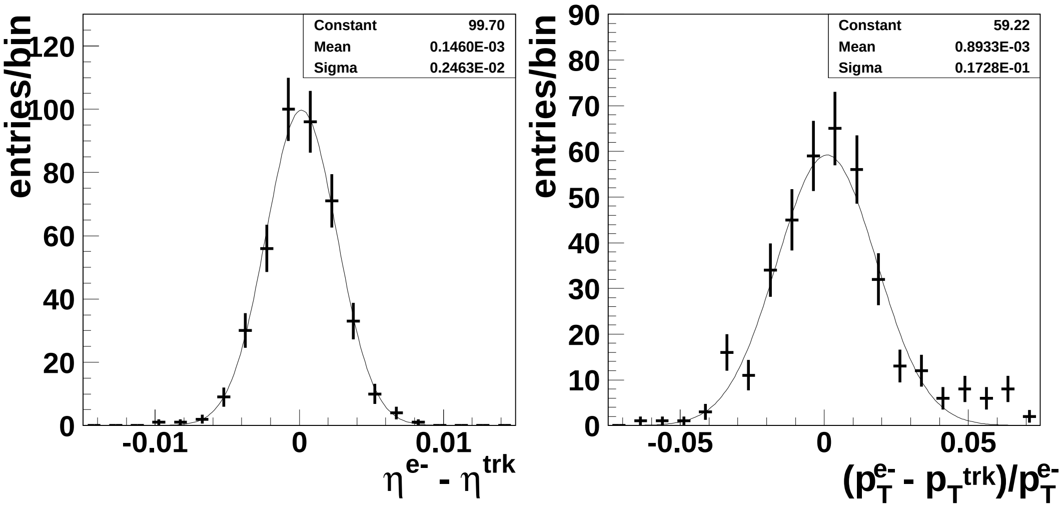

Figure 7.25: *Pseudorapidity (Left) and transverse energy (Right) resolutions of the tracks from semi-leptonic decays to electrons.*

Consideration of the jet resolutions (Figure 7.26) shows that the jets we are measuring are reasonable jets. They exhibit no mean shift in pseudorapidity and have a good resolution. The transverse momentum of the jets is shifted

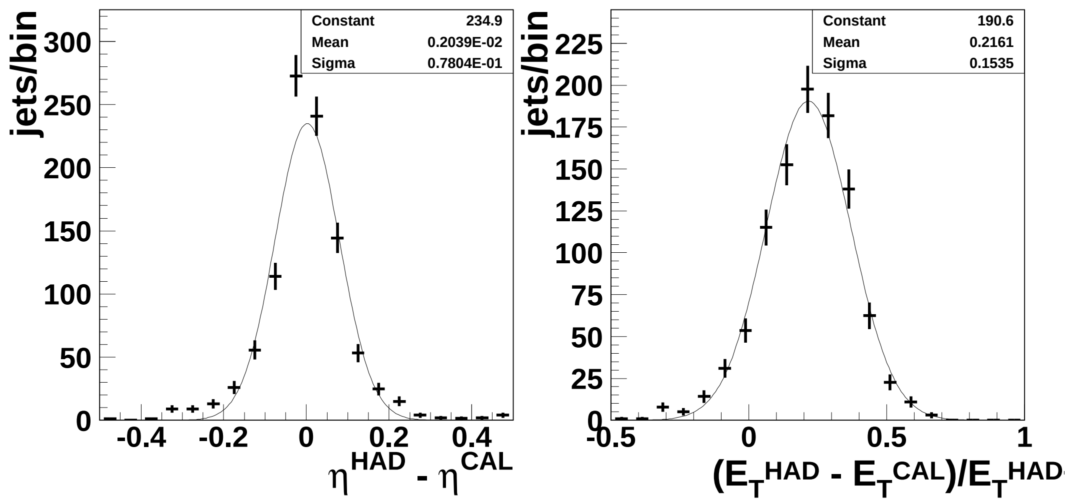

Figure 7.26: *Pseudorapidity (Left) and transverse energy (Right) resolutions of the two highest E_T jets in events containing a semi-leptonic decay to an electron.*

by 22% with respect to the true jets due to energy loss in the dead material with a resolution of 15%. Due to this energy shift, we correct our jets before proceeding further to a corrected cross-section. In exactly the same way as with the D^* analysis, we correct our jet transverse energies and y_{JB} using the method detailed in Chapter 5. Again we then have to redefine our cuts for jet transverse energy and y_{JB} such that,

$$E_T^{COR}(jet1, jet2) > 7.0, 6.0 \text{ GeV},$$

$$0.2 < y_{JB}^{COR} < 0.8.$$

Finally, we can then compare the resolutions of our cross-section variables, x_γ^{obs} and p_T^{rel}. These are shown in Figure 7.27. We see that considering x_γ^{obs} there is no shift in the absolute value and the fit gives a resolution of ~ 0.07. This resolution is commensurate with the bin width and previous jet results [50]. For p_T^{rel}, there is also no overall shift in the mean, but the resolution is reasonably poor at about 40%. The bin width was chosen accordingly.

We now compare data and Monte Carlo predictions for important quantities in the analysis.

In Figure 7.28, we compare a number of jet, event and track properties between data and Monte Carlo, where the Monte Carlo is area normalised to the data.

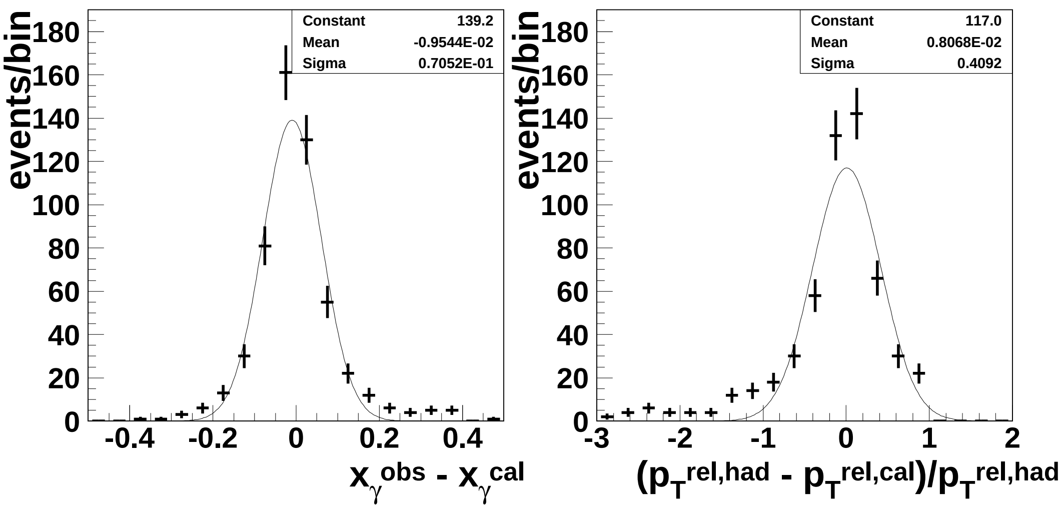

Figure 7.27: *Resolutions of* $x_\gamma^{\rm obs}$ *and* p_T^{rel} *of events containing an electron in the final state.*

Considering each distribution in turn; we see that the transverse energy of the two highest E_T jets is well described. There is a turnover in the second bin due to the asymmetric cuts above, which is modelled in the Monte Carlo. The pseudorapidity of the two highest transverse energy jets is reasonably well modelled for photoproduction events. Most of the jets are in the central region due to the pseudorapidity and transverse momentum tracking requirements. The data exhibits a slight excess over the Monte Carlo in the forward region and a deficiency in the central region. Improvements could possibly be realised with more binning in pseudorapidity of the tracks.

Both event properties, y_{JB}^{COR} and the Z vertex are also reasonably well described. The Z vertex is centrally peaked with few events outside ± 20 cm.

As the distance of closest approach of the track-island pairs is dependent on both the reconstruction of the tracks and islands as well as their interdependency, this could be expected to be the most sensitive distribution. However, good agreement between data and Monte Carlo is observed, the general features being well produced.

Finally the two track parameters, p_T^{trk} and η^{trk} both show reasonable agreement between data and Monte Carlo. This is especially poignant when one considers the somewhat crude binning in the two quantities, particularly for the pseudorapidity. They would both benefit from finer binning, but the current agreement is the vindication needed for the justification of the method.

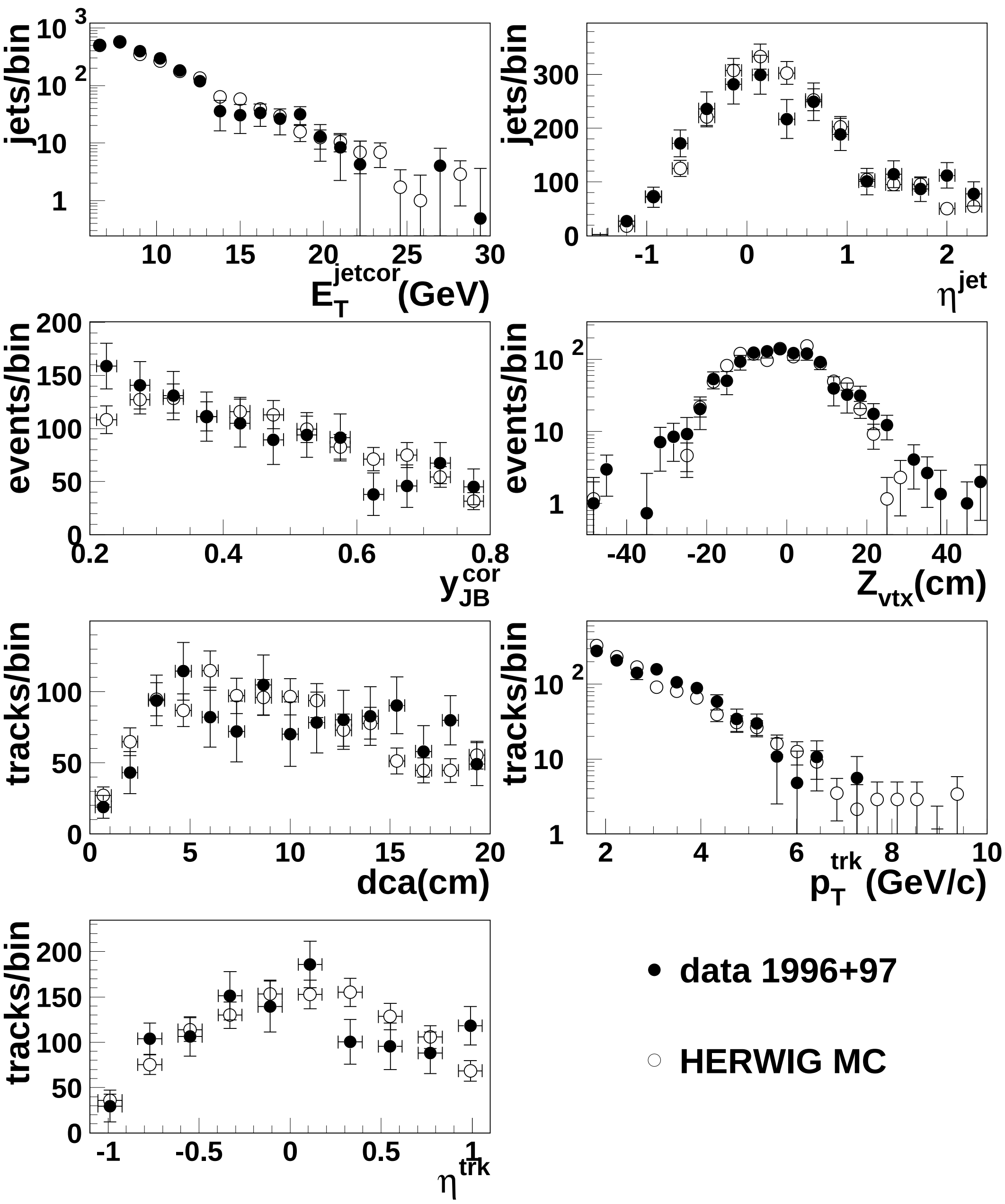

Figure 7.28: *Comparsion of data (solid points) and HERWIG Monte Carlo (open points) for event, jet and track properties of the semi-leptonic events entering the cross-section measurement.*

Having espoused and justified the analysis method, we can then unfold to cross-sections in $x_\gamma^{\rm obs}$ and p_T^{rel} and extract physics in the next chapter.

Chapter 8

Cross-section Measurements for Semi-leptonic Decays

8.1 Definition of the Cross-sections

By considering photoproduction events with at least one electron in the final state, we can define cross-sections in $x_\gamma^{\rm obs}$ and p_T^{rel}. Each event consists of at least two high transverse energy jets, one of which is generally associated with one of the electrons. The electron sample is an inclusive sample, being decay products of hadrons from light and heavy quarks alike. For the process,

$$ep \rightarrow e^- + \text{dijets} + X,$$

we measure the differential cross-sections:

$$\frac{d\sigma_{ep\rightarrow e^- + \text{dijets} + X}}{dx_\gamma^{\rm obs}} \; ; \; \frac{d\sigma_{ep\rightarrow e^- + \text{dijets} + X}}{dp_T^{rel}}. \tag{8.1}$$

This was done in the kinematic region defined by the following;

$$0.2 < y < 0.8$$

$$Q^2 < 1 \text{ GeV}^2$$

$$E_T^{jet1,jet2} > 7,6 \text{ GeV} \tag{8.2}$$

$$|\eta^{jet}| < 2.4$$

$$p_T(e^-) > 1.6 \text{ GeV/c}$$

$$|\eta(e^-)| < 1.1$$

The region defined by the jets, E_T and η, and the electron, Q^2 and y, are the same as for the D^* analysis so will not be discussed further. The momentum and pseudorapidity cut on the electron are dictated by the reasonings in the previous chapter in Section 7.2.1. It should be noted that here "electrons" is specific with the leptons required to have a negative charge.

8.2 Unfolding to the Cross-sections

To unfold to the cross-sections in x_γ^{obs} and p_T^{rel}, we again employ the bin-by-bin unfolding procedure as was performed in Section 6.6. Correspondingly, we use Equations (6.5 - 6.10) to determine the purities, $p(i)$, efficiencies, $\varepsilon(i)$, correction factors, $C(i)$, and their associated errors for a given bin i. However, we adapt Equation (6.11) slightly by removing the division of the branching ratio as we are measuring an inclusive cross-section with no assumed decay channel or assumed parental quark. For a given luminosity $\int dt\mathcal{L}$, the number of events, $N(i)$ is corrected to the differential cross-section, $\sigma(i)$ using the following expression:

$$\sigma(i) = \frac{N(i).C(i)}{\int dt\mathcal{L}.\text{bin width}}. \tag{8.3}$$

For the unfolding procedure, the direct and resolved Monte Carlo is combined in the proportions of the global fit to the uncorrected data obtained in the previous chapter; 56.9% direct and 43.1% resolved. The ratios of the quark content are those given by the Monte Carlo, so no further fitting of quark components is performed. Varying the ratios of the quark content from that predicted by the Monte Carlo will form a systematic check of the measurement.

8.2.1 Unfolding for $x_\gamma^{\rm obs}$ Cross-section

The results for the purity, efficiency and correction factor as a function of $x_\gamma^{\rm obs}$ are shown in Figure 8.1. Looking initially at the general trends of the plots, we see that the purity increases with increasing $x_\gamma^{\rm obs}$, the efficiency is reasonably flat and hence the correction factor represents the characteristics of the purity and also increases with increasing $x_\gamma^{\rm obs}$. If we reconsider the corresponding distributions for the analysis with D^* mesons (Figure 6.8), we see that the general trends of the three quantities for the two analyses are the same.

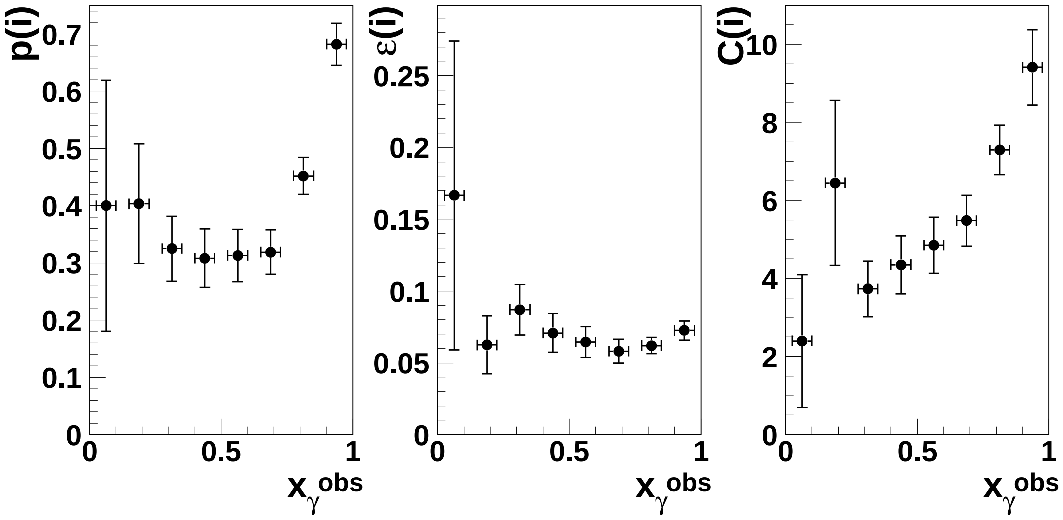

Figure 8.1: *Purity, efficiency and correction factors shown for the unfolding procedure as a function of $x_\gamma^{\rm obs}$.*

The purity in Figure 8.1 also corresponds in magnitude to that of the purity in Figure 6.8 indicating a consistency of reconstructing $x_\gamma^{\rm obs}$ for the two analyses. Comparison of the efficiencies of the two results shows that for the current analysis the efficiency is very much less, representing an overall (poor) efficiency of 5-10%. The lowness of this value needs some explaining and the following justifies its value in comparison with that obtained for the D^* analysis. In a multi-stage analysis, the efficiency will suffer the more cuts imposed. The D^* analysis had essentially a four stage process all of which contributed to an overall efficiency of $\sim 20\%$. These are:

- Trigger efficiency.
- Event reconstruction efficiency.

- Jet reconstruction efficiency.
- Track reconstruction efficiency.

All of these, in a general sense, also apply to the search for electrons from semi-leptonic decays of hadrons. However, the reduction in efficiency from $\sim$ 20% to $\sim$ 5-10% is a consequence of the three extra stages involved in the current analysis:

- Island reconstruction efficiency.
- Track-island matching efficiency.
- dE/dx cut efficiency.

With the knowledge of the imposed 50% efficiency of the cut on dE/dx, the values then become comparable to those obtained in the D^* analysis, the remaining deficit arising from the other two extra stages.

Having justified the values obtained for the purity and efficiency, the somewhat high correction factors can therefore be understood by virtue of the many stages of the analysis.

Applying these correction factors to the data using Equation (8.3) we obtain the cross-section shown in Figure 8.2. The data points are shown compared to hadron level Monte Carlo statistics with the contributions from direct and resolved photon processes shown separately. We first observe that the agreement between data and Monte Carlo is good. It is also clear that direct photon processes are not on their own sufficient to describe the data in the low $x_\gamma^{\rm obs}$ region; a component of resolved photon processes is required. In fact, the Monte Carlo predicts a value of 38% for the resolved photon processes and in a fit to the data the value achieved is 29$\pm$5 %, the two being in reasonable agreement. The fit was performed as in the case of the cross-section for the D^* meson in dijets $x_\gamma^{\rm obs}$ measurement - allowing the percentage of direct and resolved to float and minimising the χ^2 - yielding similar results. This gives vindication to the tagged D^* meson cross-section measurement result. It should be noted however, that the comparison of data and hadron level Monte Carlo is purely a comparison of shape, the absolute normalisation of the Monte Carlo being well below the data. More specifically, a normalisation factor of 2.8 is applied to the HERWIG Monte Carlo for the description shown in Figure 8.2. This value is also in reasonable

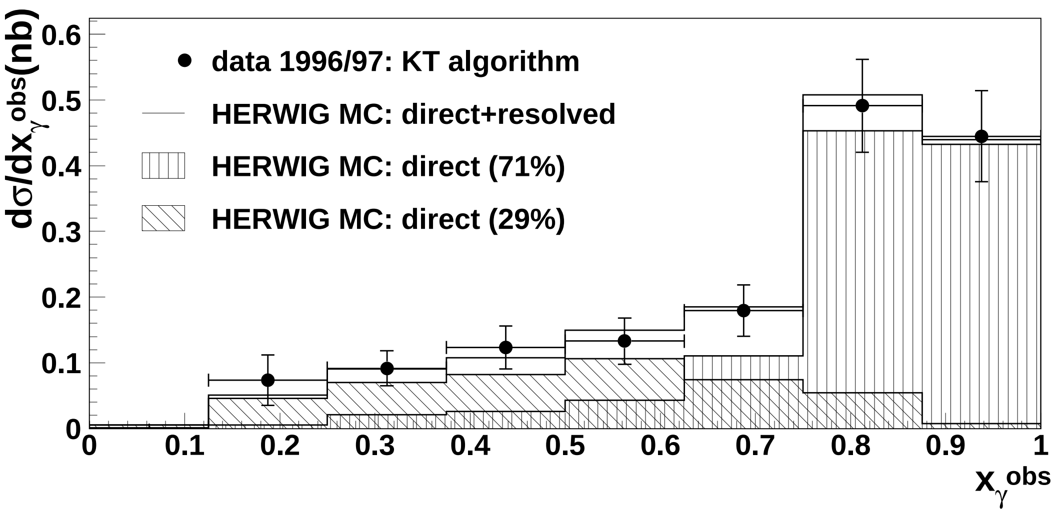

Figure 8.2: *Unfolded differential cross-section as a function of $x_\gamma^{\rm obs}$ compared to total, direct only and resolved only hadron level Monte Carlo.*

agreement with the normalisation factor obtained in the D^* analysis, which for HERWIG is 2.6 [103].

The purpose of the measurement of the cross-section in $x_\gamma^{\rm obs}$ has now been achieved. A resolved photon component is observed in agreement with that predicted from the Monte Carlo. The description of the data by the Monte Carlo is good in shape but much lower in absolute value. Both of these were seen in the analysis with tagged D^* mesons. Further analysis of the $x_\gamma^{\rm obs}$ distribution will not be performed except to estimate the systematic uncertainties. The estimation of systematic uncertainties is done for completeness and the distribution will not be further refitted nor will a systematic error for the resolved photon component be determined.

8.2.2 Unfolding for p_T^{rel} Cross-section

The results for the purity, efficiency and correction factor as a function of p_T^{rel} are shown in Figure 8.3. The purity, efficiency and correction factors for this quantity demonstrate more drastic trends than those as a function of $x_\gamma^{\rm obs}$. These trends, however, can be thought of in terms of the quantity itself being an underlying reflection of the relation between the electron and the jet.

All three distributions show a general decrease with increasing p_T^{rel}, with a flattening off at high values. The purity in the first bin is as high as ~ 0.8, decreasing to a reasonably constant ~ 0.1 for $p_T^{rel} > 1$ GeV/c. The efficiency also has its highest value in the first bin of about 0.09, decreasing to about 0.04 again for $p_T^{rel} > 1$ GeV/c. This is reflected in the correction factor, which has a highest value of 9 and levelling out to about 4.

It should be noted that the somewhat large errors in the purity and efficiency are correlated. Using Equation (6.10) accounts for these correlations leading to smaller errors in the correction factors.

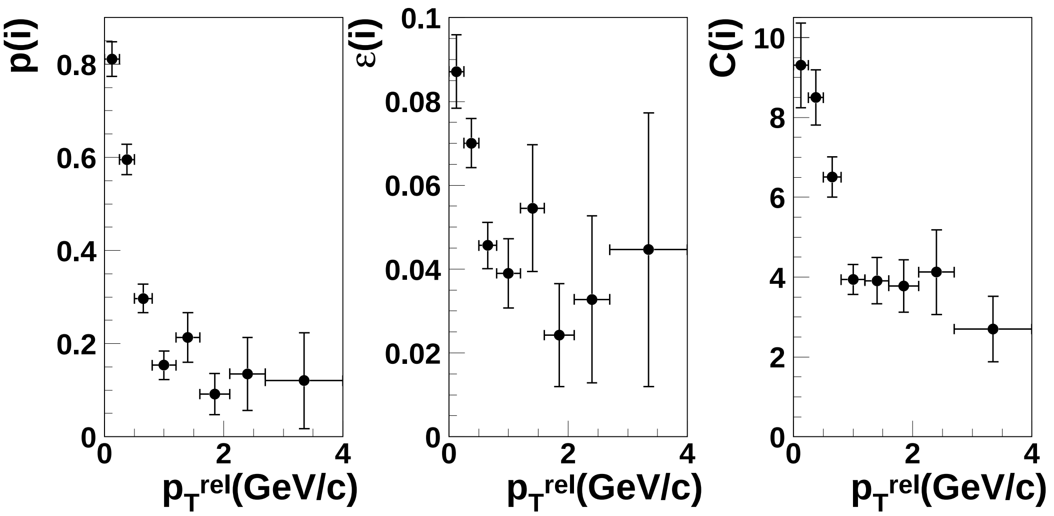

Figure 8.3: *Purity, efficiency and correction factors shown for the unfolding procedure as a function of* p_T^{rel}.

Considering first the correction factor, the high values for low p_T^{rel} seem intuitively reasonable. As low values of p_T^{rel} imply that the electron is reasonably centrally positioned within the jet, we would expect the identification of a specific particle to be "harder" as the multiplicity of particles is higher in this region. Therefore a larger correction factor would be required inside the jet, the quantity increasing the closer the tracks are to the jet axis. However when we reconsider the efficiency we see that it is higher for those tracks in the centre of the jet. Therefore we ask the question: in what sense is it "more difficult" to find tracks in the centre of the jet? The "difficulty" does not come from the inefficiency in finding the electrons but from the relative value in the ratio of the purity and efficiency. The shape in the efficiency can be explained in terms of track mismatching and the purity in terms of the geometry of the track trajectory as follows.

The implication for a higher efficiency is that for a given true electron, the chance of finding the reconstructed track in the same bin is higher. When considering the higher efficiency at low p_T^{rel} one again has to consider the multiplicity distribution in the event and within the jet. The actual high efficiency arises from misidentification of the reconstructed track as the true particle. The multiplicity is higher closer to the centre of the jet, and consequently the chances of the true electron being identified as another track are higher. Therefore, this misidentification has an effect on the efficiency but not the purity as the true electron *is in the bin* as well as the misidentified track. At higher p_T^{rel} (outside the jet) the distribution could be flat or could still be falling but the statistical errors are too large for a definitive statement. However, the multiplicity is definitely lower and a lower efficiency is therefore observed.

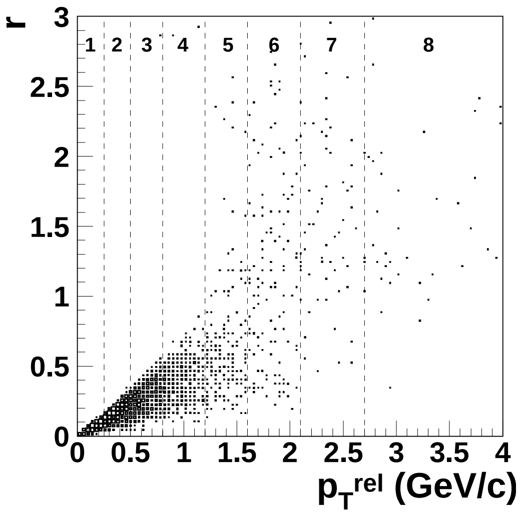

Figure 8.4: *Correlation of the electron-jet separation in $\eta - \phi$ space with p_T^{rel} in the Monte Carlo. The p_T^{rel} analysis bins are also shown.*

Higher purity entails that for a given candidate reconstructed in a given bin, the likelihood that the true event was in the same bin is higher. That is, the migrations from other bins is lower. We now have to explain the trend seen in the purity of the sample and here we have to consider the geometry of the trajectory of the electron and how this relates to migrations. As p_T^{rel} is strongly correlated to r (see Figure 8.4), then our argument can be based on the distance r from the jet axis. For our eight bins in p_T^{rel}, the lower edge of each bin corresponds to some coordinate, $r_{i,i=1,8}$ (where $r_1 = 0$), the outer edge, $r'_{i,i=1,8}$. For a bin i in p_T^{rel}, the distance in r space of the bin, Δr_i, is given by,

$$\Delta r_i = r'_i - r_i, \text{ where}, r'_i - r_i > r'_{i-1} - r_{i-1}.$$

As the trajectory can be within a specific area transverse to the jet axis given by the area of an anulus (which corresponds to a bin);

$$A_i = \int_{r_i}^{r'_i} 2\pi r dr,$$

then we can see that the area increases with increasing r and hence with a given bin. Accordingly for a bin at small p_T^{rel}, the amount of phase space (area of the anulus) is smaller than a bin at larger p_T^{rel}. A smaller area implies that there is less phase space for events to migrate into it. Therefore if an event is reconstructed in that bin then it is less likely for it to have come from a migration to that bin. For higher p_T^{rel}, the phase space is much larger for migrations into the bin to occur resulting in a lower purity. The inverse dependence of the purity on the available area of phase space leads to a rapidly falling distribution as seen in Figure 8.3.

The above explains the shape of the correction factors measured, which we now use to obtain a cross-section in p_T^{rel}. Applying these correction factors to the data via Equation (8.3) yields the cross-section shown in Figures 8.5 and 8.6, where it is compared to the hadron level Monte Carlo which is fitted in two different ways.

In Figure 8.5, the data is shown compared to the Monte Carlo with the contributions from direct and resolved photon processes shown separately. The percentages used are those from the fit to the $x_\gamma^{\rm obs}$ distribution with no further fits made. The overall description of the data by the Monte Carlo is reasonable with a slight excess in the last two bins.

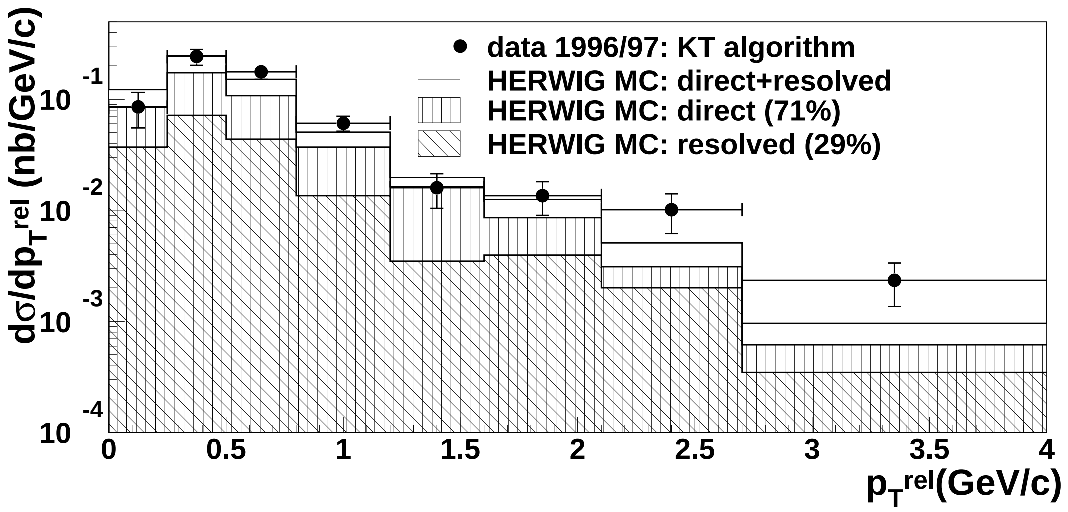

Figure 8.5: *Differential cross-section as a function of p_T^{rel} compared to total, direct only and resolved only hadron level Monte Carlo, where the direct/resolved components are taken from the fit to $x_\gamma^{\rm obs}$.*

As the shapes of direct and resolved photon processes are similar as a function of p_T^{rel}, then they are not really the most suitable quantities to compare to. We therefore consider how the data is best described by allowing the Monte Carlo to be dependent on the quark in the hard sub-process. The prediction from the Monte Carlo gives a beauty component in the measured cross-section region of 16%. When the Monte Carlo was fitted to the $x_\gamma^{\rm obs}$ distribution this percentage changed to 17%. If we then return to the original Monte Carlo prediction of the direct and resolved components and this time allow the amount of beauty and charm+other processes to vary we receive a beauty component of 16±4%, with a χ^2/d.o.f. $= 1$. The description of the data is again reasonable with a slight excess in the last two bins. However, the excess in the last two bins is somewhat misleading as the fit is dictated by the values in the first three bins. Any subsequent increases in the beauty cross-section to fit these last two bins would greatly reduce the charm plus other cross-section at low p_T^{rel}, yielding a poor fit. The charm and light quark component are included into one "charm+other" component as their shapes are very similar not allowing a good fit with the current statistics.

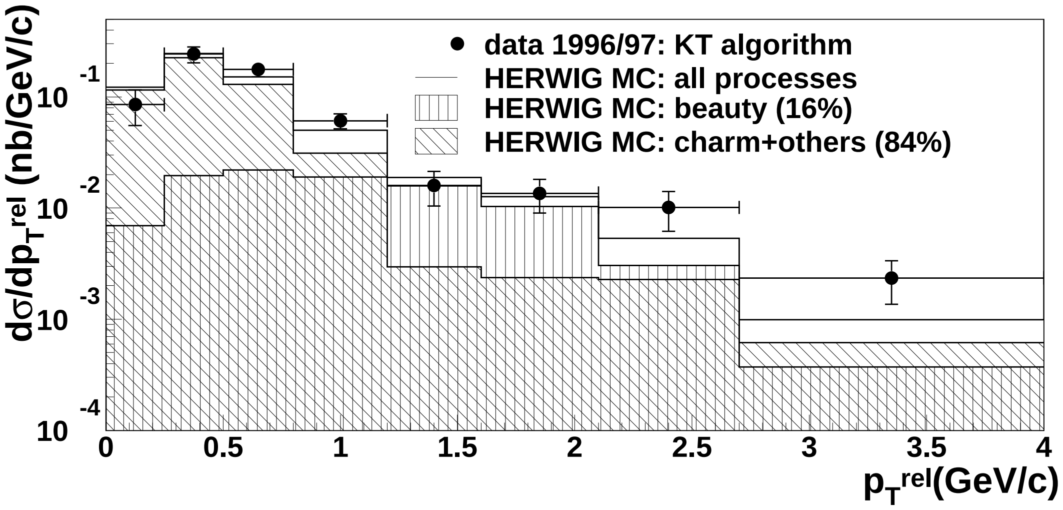

Figure 8.6: *Differential cross-section as a function of p_T^{rel} compared to total, beauty only and charm+other hadron level Monte Carlo.*

The different fits performed and the subsequent proportions of processes is summarised in Table 8.1.

From the above, Figures 8.5 and 8.6 and Table 8.1, we see that the measured cross-section as a function of p_T^{rel} is in good agreement with the Monte Carlo prediction for the fraction of beauty production in our kinematic region. A more definite statement, however, is reserved for when a full study of systematic uncertainities

	direct	resolved	charm+other	beauty
MC prediction	62%	38%	84%	16%
Direct/resolved fit	$71 \pm 5\%$	$29 \pm 5\%$	83%	17%
Quark component fit	62%	38%	$84 \pm 4\%$	$16 \pm 4\%$

Table 8.1: *Table showing proportions of direct and resolved processes and beauty and charm+other processes as predicted by the Monte Carlo, after allowing the direct and resolved fraction to vary and allowing the fraction of beauty and charm+other to vary.*

has been performed and a systematic error placed on the beauty component of 16±4% so far received. We study the systematic uncertainties in the next section for both cross-sections measured.

8.3 Study of Systematic Uncertainties

For any given measurement, a large number of systematic uncertainties could be studied, so one has to decide on a sensible amount of *uncorrelated* effects. We can somewhat artificially categorise the changes into four classes:

1. Variation of the kinematic cuts used to define the analysis. This we perform by varying the reconstructed variables, E_T^{jet} and y_{JB} in both the data and HERWIG Monte Carlo samples.

2. Variation of the kinematic cuts and quantities used to define the electron selection and the cuts used to subsequently remove the background. This is again performed by varying the cut values in the data and reconstructed Monte Carlo.

3. We also consider the systematic effect due to the uncertainty on the absolute calorimeter energy scale between the data and Monte Carlo. This we do by varying the calorimeter quantities (E_T^{jet}, y_{JB} and island energy) by some factor in the data only, whilst the Monte Carlo remains at its nominal value. This is therefore expected to systematically increase or decrease the cross-section.

4. Uncertainties arise from the dependence of the model used to unfold to the cross-section. We analyse this by considering Monte Carlo specific parts of the analysis and varying these.

When considering the resulting changes in the cross-sections and what constitutes a systematic trend, one should also consider the physics to be interpreted. For the cross-section in x_γ^{obs}, we are interested in the percentage of resolved photon processes as predicted by LO Monte Carlo generators. Any subsequent reduction in the low x_γ^{obs} tail coupled to an enhancement at high x_γ^{obs} would represent a problematic shift for interpreting any physics result. Correspondingly and more importantly for the p_T^{rel} cross-section, any dramatic change in the relative size of the low ($p_T^{rel} < 0.75$ GeV/c) to high ($p_T^{rel} > 1$ GeV/c) values would lead to a large change in the amount (if any) of beauty quarks as required by the Monte Carlo to describe the measured data.

8.3.1 Uncertainties Arising From the Kinematic Cuts

By way of analysing the effects of the of the quantities used to define the kinematic region we consider the transverse energy of the jets and the y_{JB} of the event. For our value corrected for energy loss as particles pass through dead material, y_{JB}^{corr}, we select those events satisfying:

$$0.2 < y_{JB}^{corr} < 0.8$$

This we vary by changing the lower and upper limits separately to:

$$0.15 < y_{JB}^{corr} < 0.8, \quad 0.2 < y_{JB}^{corr} < 0.85.$$

As the purpose of the lower and upper cuts on y_{JB} is different they have been varied separately, rather than choosing one extended window. The cut on the transverse energy of the jets has been varied by considering the resolution (Figure 7.26) and varying our central values by $\pm 1\sigma$. We therefore have the following cuts,

$$E_T^{CORjet1,2} > 8,7 \text{ GeV}, \quad E_T^{CORjet1,2} > 6,5 \text{ GeV},$$

where our resolution for low transverse energy jets is $\approx$15%. Here the 1σ variation is taken for the 7 GeV jet and is subsequently larger for the lower 6 GeV jet.

However, we also want to retain the 1 GeV difference between the cut on the highest and second highest transverse energy jet.

The effect of these four kinematic changes on the cross-section in $x_\gamma^{\rm obs}$ can be seen in Figure 8.7 and those for p_T^{rel} in Figure 8.8 where the quantity plotted is a fractional variation in the cross-section such that,

$$\frac{\Delta d\sigma}{d\sigma} = \frac{d\sigma_{syst} - d\sigma_{nominal}}{d\sigma_{nominal}},$$

where $d\sigma_{syst}$ and $d\sigma_{nominal}$ are our varied and central cross-sections respectively. As a result, a systematic variation of 1, is a 100% variation, however of more importance is the size of the variation with respect to the statistical error. The statistical error on the central cross-section is shown as the shaded band, being $\sim 20-50\%$ for the $x_\gamma^{\rm obs}$ cross-section and $\sim 10-40\%$ for the cross-section in p_T^{rel}. The percentage statistical error in the first bin in $x_\gamma^{\rm obs}$ is very large due to the small value in the bin. Subsequent systematic variations and errors in this bin are then also large but are somewhat insignificant in absolute values and so all further discussions will omit this bin.

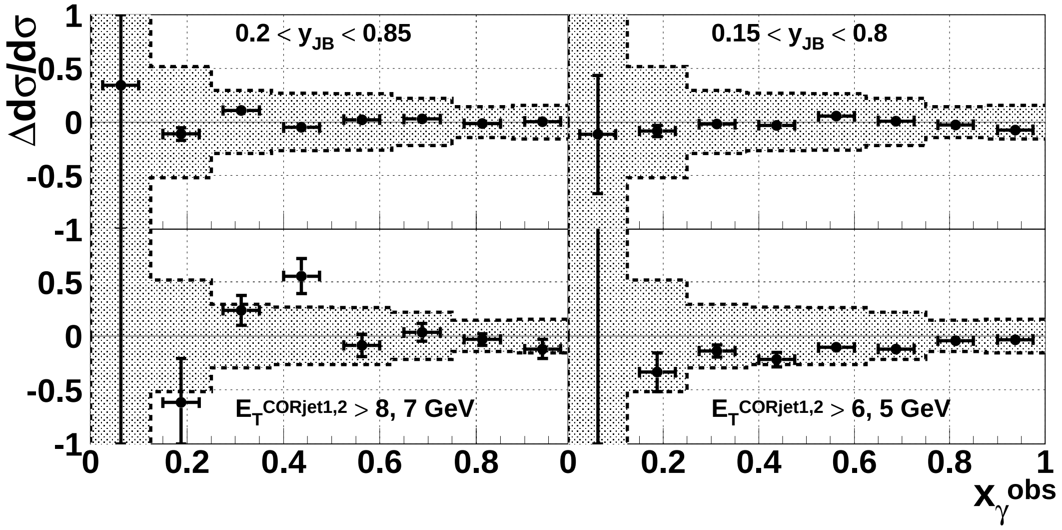

Figure 8.7: *Systematic uncertainties due to the kinematic cuts as a function of $x_\gamma^{\rm obs}$. The shaded band shows the statistical error on the central cross-section value.*

From Figure 8.7, we see that the systematic variations of y_{JB} have little effect on the cross-section. No systematic trends are exhibited and the absolute variations in all bins are small, all being less than half the value of the statistical error.

The effect of varying the cuts on the transverse energy is more marked. Consideration of when the cuts are increased by 1σ shows no systematic trend but does show absolute shifts of significant size. The absolute shifts are of the order of the statistical error and is twice the statistical error in the case of the fourth bin. However, within this variation we actually see an effect caused by the limitation of the statistics and not just the cuts themselves. Changing to these higher values of jet transverse energy results in a 41% reduction in events and so we are relying on correction factors of almost twice the size as the nominal ones and hence a large Monte Carlo extrapolation. Lowering the transverse energies by 1σ results in another situation. Here the resultant shifts from the central values are large, but this time the shifts are systematically downwards, therefore the cross-section with the lower reconstructed jet transverse energies is lower. By requiring jets with a corrected jet transverse energy of 5 GeV, we are allowing the jets measured in the calorimeter to be as low as ~ 3.4 GeV. Jets of this value are poorly modelled and as we are relying on extrapolation from the Monte Carlo as our trigger requires the jets to be greater then 4 GeV, such a trend is not wholly surprising.

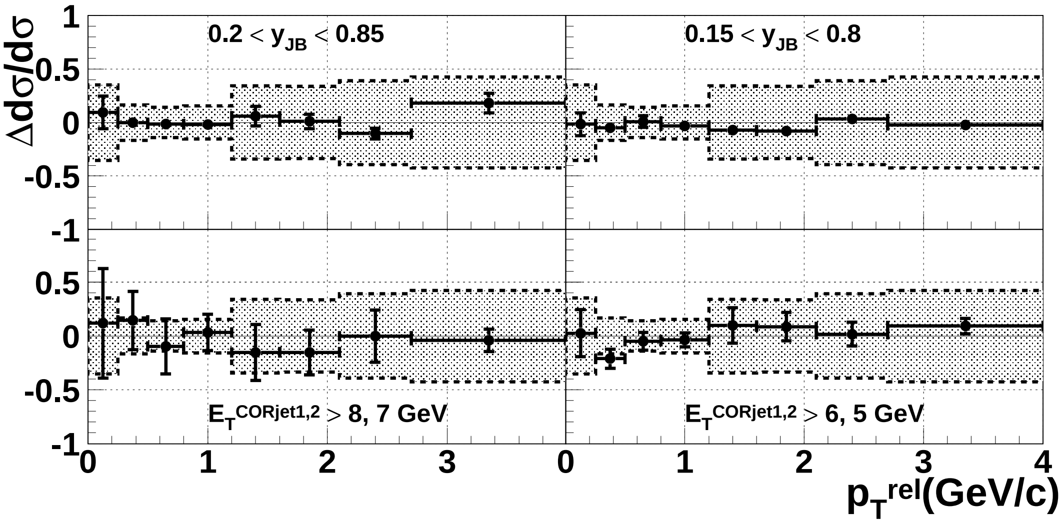

Figure 8.8: *Systematic uncertainties due to the kinematic cuts as a function of p_T^{rel}. The shaded band shows the statistical error on the central cross-section value.*

Similarly to the cross-section in $x_\gamma^{\rm obs}$, the cross-section in p_T^{rel} is largely unaffected by the the changes in y_{JB}. The percentage changes are again less than half that of the statistical error.

For the higher E_T^{jet} cuts, no systematic trend is again seen but shifts of the order of the statistical error are observed. For the lower pair of cuts, a lower cross-section is again observed, being concentrated in the second, third and fourth bins. The higher four bins are not shifted as much in relation to their statistical error as the first four. Interpretation of the effects of changing the lower limits on the transverse energy of the jets is difficult and must await the refitting procedure. However, the higher minimum requirements are suggestive of a smaller beauty component and the lower minimum requirements suggestive of a larger beauty component.

8.3.2 Uncertainties Arising From the Electron Extraction

Consideration of uncertainties related to the extraction of the electron signal can be separated into three sections and we perform one systematic check for each of these:

1. Variation of the kinematic cuts, by allowing the p_T^{trk} cut to change by $\pm 1\sigma$ in the same way as for the transeverse energy of the jets. From Figure 7.25, we see that the resolution of the transverse momentum of the tracks is good ($\approx 2\%$) leading to changes of the 1.6 GeV/c central value of ± 0.03 GeV/c.

2. So-called "cleaning" cuts are applied to achieve as *clean* a signal as possible for a given efficiency. One of these is the distance of closest approach allowed for a track-island pair to be considered matched. Changing the value should only result in variations of the purity and efficiency - a larger distance of closest approach criteria implies a higher efficiency and lower purity and vice versa for the smaller distance of closest approach - but no subsequent variation in the overall correction factor. The value is changed by $\pm$ 5 cm from the original, $dca = 20$ cm.

3. The removal of the background due to electrons from photon conversions also plays a significant rôle and the uncertainty related to the cuts which define it have to be estimated. We vary the quality factor, D (Equation (7.9)), by $+5(-5)$, thereby increasing (decreasing) the efficiency and decreasing (increasing) the purity of finding the electron from a photon conversion.

The results of these changes on the cross-sections are shown in Figures 8.9 and 8.10.

The difference in the cross-section as a function of $x_\gamma^{\rm obs}$ when changing the minimum transverse momentum cut of the track is small in all bins. The magnitude of the variation is far less than the statistical error and is insignificant in this analysis for this distribution.

Changing the value for the distance of closest approach for the track-island pair results in the largest systematic effect from those investigated in this section. The shifts in the cross-section are larger for the smaller distance cut, but are generally of the order of half the statistical error in all bins. There is also a decrease in the overall cross-section.

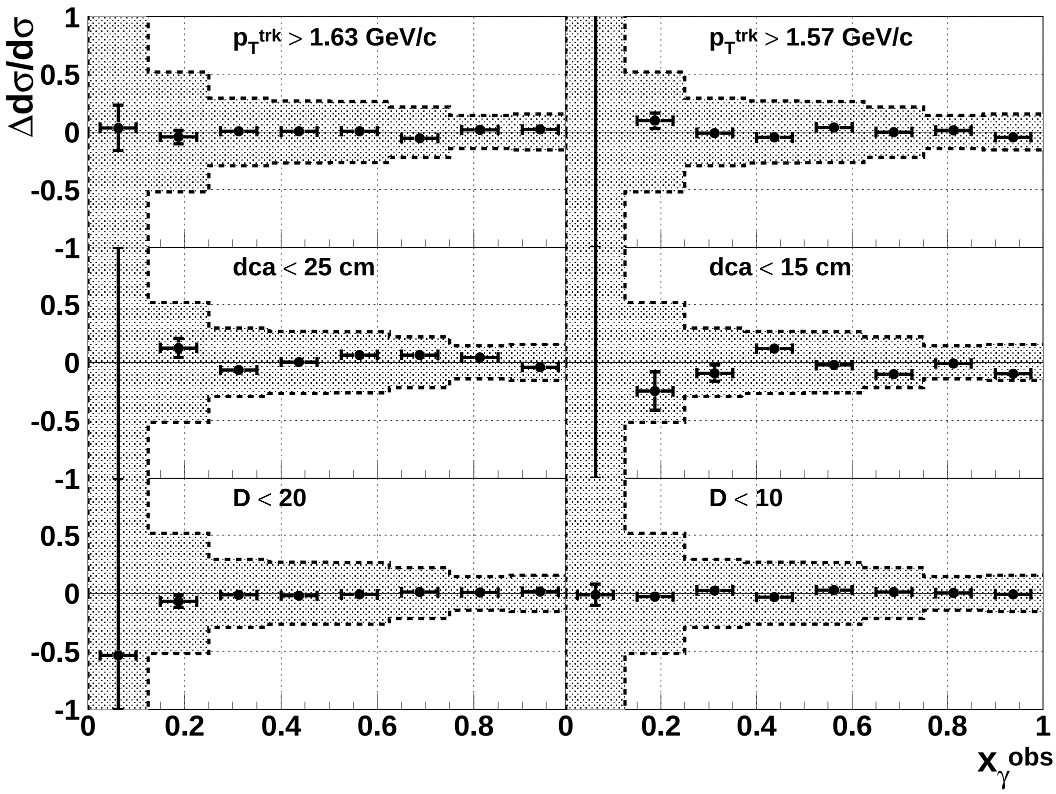

Figure 8.9: *Systematic uncertainties due to the electron finding as a function of* $x_\gamma^{\rm obs}$.

For the variation of the quality factor, D, no significant effect is seen, the largest shift being less than 10%.

When altering the minimum p_T^{trk} cut, for the cross-section as a function of p_T^{rel} (Figure 8.10) we see a slightly more noticable effect than was seen for the cross-section as a function of x_γ^{obs}. For the higher minimum requirement, three bins are shifted by ~ 10 %, however there is no systematic trend.

The change in the cross-section with varying distance of closest approach cut is also more noticable for the p_T^{rel} measurement. The variation is as much as 30%, but always less than the statistical error.

The quality factor, D, has very little effect in all bins for both changes of the upper limit.

Overall the effect of the changes to variables which yield the electron signal is small. The largest differences seen are for the distance of closest approach cut for the cross-section in p_T^{rel}, all differences being larger in the case of the cross-section in p_T^{rel} than as a function of x_γ^{obs}. This is reasonable as the quantity, p_T^{rel} is more dependent on the electron itself where x_γ^{obs} is an event quantity.

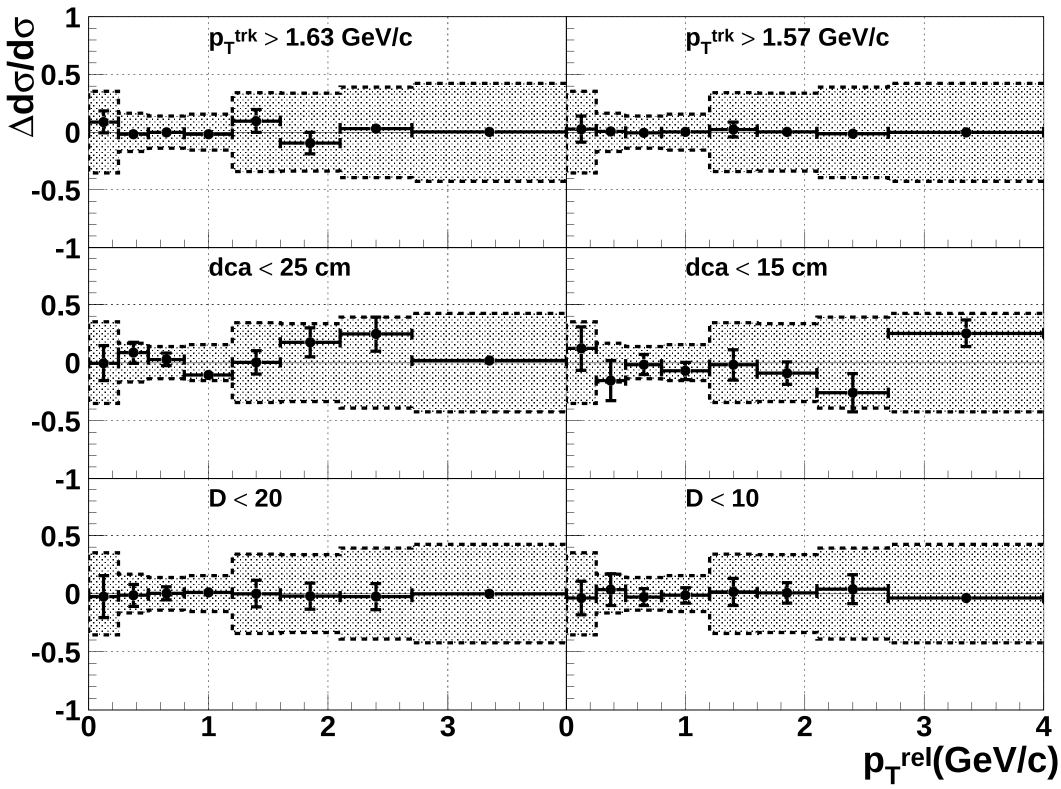

Figure 8.10: *Systematic uncertainties due to the electron finding as a function of* p_T^{rel}.

8.3.3 Uncertainties Arising From the Energy Scale

When we say uncertainties arising form the energy scale we mean an uncertainty in our knowledge of the calorimeter energy scale *between* data and Monte Carlo. In all of our systematic checks so far studied, a change in a quantity corresponded to the same change in both the data and the Monte Carlo. However, as the energy scale could be different between data and Monte Carlo, we apply a change to it in one and not the other. The Monte Carlo has been shown to reproduce the absolute energy scale of the calorimeter to within $\pm 3\%$ [104]. We therefore increase the calorimeter quantities, y_{JB} and the island energies, by $\pm 3\%$ in the data *only*, the Monte Carlo remaining in the nominal situation. However, jets are also measured via the calorimeter so they must also be subsequently changed as for y_{JB} and island energies. The magnitude of the scale factor is not the same for jets as for cell or island energies. For the measurements of the low energy jets under study we have extra uncertainties between the data and Monte Carlo. The scale uncertainty attributed to our relatively low energy jets is $\pm 5\%$ [27] and so the jet energies are scaled by $\pm 5\%$, also only in the data.

The effects of the uncertainty of our knowledge in the energy scale between data and Monte Carlo are shown in Figures 8.11 and 8.12.

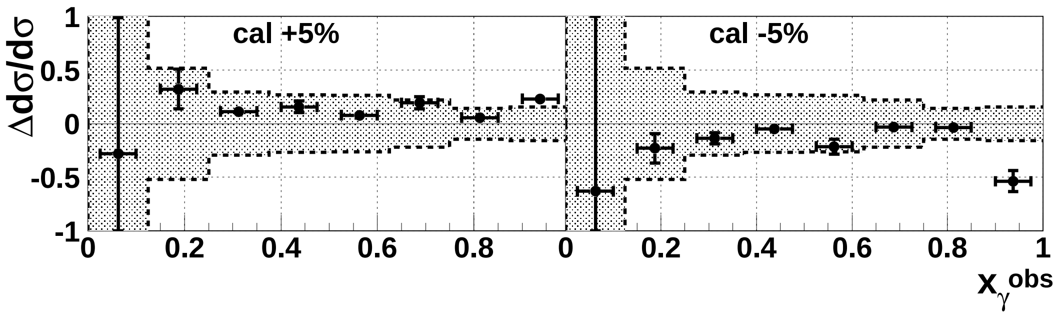

Figure 8.11: *Systematic uncertainties due to the uncertainty in the energy scale of the calorimeter as a function of* x_γ^{obs}.

Scaling the calorimeter energies in the data up and down produces the effect expected. In Figure 8.11, we see that all points lie above (below) zero for an increase (decrease) in the scale representing an increase (decrease) in the cross-section. The shift is generally slightly smaller than the size of the statistical error and is of the order of 20%. The largest uncertainty from the shift in calorimeter scale is in the final bin, which is thought to be due to the correction procedure for y_{JB}. The correction for y_{JB} for energy loss as particles traverse dead material is a fit to the combination of direct and resolved as a function $x_\gamma^{\rm obs}$. In this bin in $x_\gamma^{\rm obs}$ the fit underestimates the data, resulting in a sensitivity in this bin to the y_{JB} correction procedure.

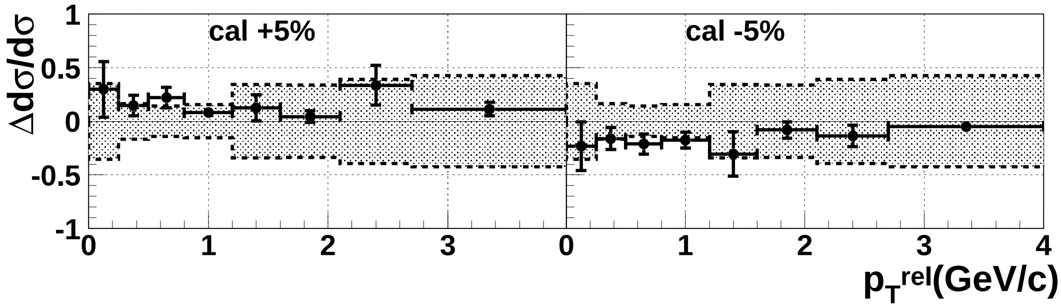

Figure 8.12: *Systematic uncertainties due to the uncertainty in the energy scale of the calorimeter as a function of* p_T^{rel}.

Similarly for the cross-section as a function of p_T^{rel} there is an overall shift, either up or down. Again the shift is generally slightly smaller than the statistical error. As the shift is systematically up or down, there may be no effect on the percentage of beauty required by the Monte Carlo to describe the cross-section and we await the fit to these cross-sections.

The uncertainty here gleaned from varying the energy scale measured in the data with respect to the Monte Carlo is large and is correlated between bins. For this reason it will not be added in quadrature with the other systematic checks but displayed as a separate band in the differential cross-section measurements.

8.3.4 Uncertainties Arising From the Monte Carlo

Using only one Monte Carlo to perform the unfolding procedure to a cross-section is not sufficient and may result in model dependence. Therefore, we use another independent Monte Carlo to perform the unfolding. The Monte Carlo used as a cross check for HERWIG is PYTHIA although calorimeter correction factors applied to E_T^{jet} and y_{JB} are those determined from the HERWIG Monte Carlo.

Our first step is to check the validity of the bin-by-bin unfolding procedure, by unfolding the PYTHIA Monte Carlo *with* the HERWIG Monte Carlo. We therefore unfold the raw PYTHIA distribution and then compare it to our true

PYTHIA distribution which should agree within statistical fluctuations. This is shown for the distribution in p_T^{rel} in Figure 8.13 (where we have not divided by luminosity or bin width). The corrected PYTHIA (solid points) shows good agreement with the true PYTHIA (open points). This gives us confidence in our correction procedure.

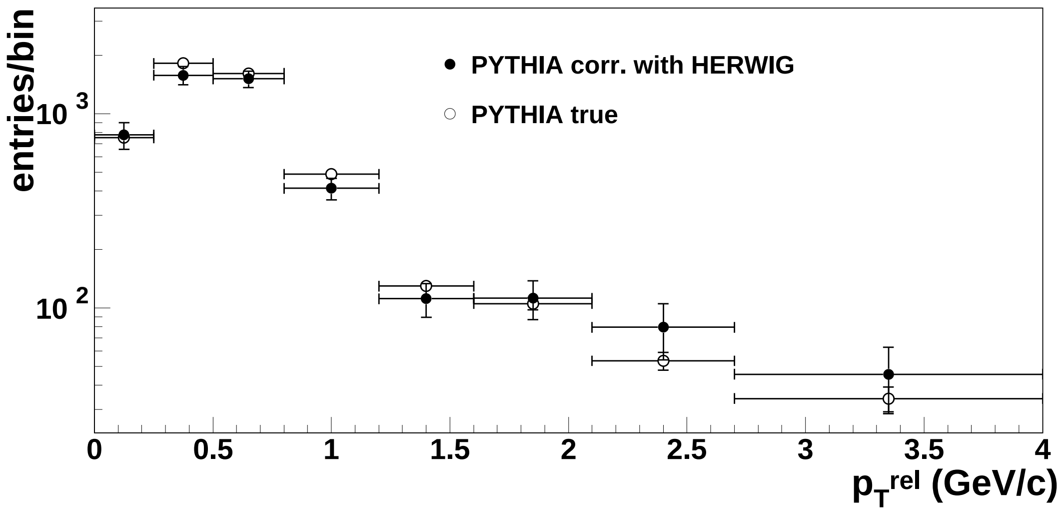

Figure 8.13: *Comparison of PYTHIA corrected with HERWIG (solid points) and the true PYTHIA (open points) for* p_T^{rel}.

We can also check the validity of the Monte Carlo modelling by looking at the correction procedure for our jets. As we use a Monte Carlo based correction procedure which is dependent on the transverse energy and pseudorapidity of the jet, this again could be model dependent. Using a much simpler crude correction procedure should provide us with an estimation of its independence from the Monte Carlo. Considering the uncorrected jets measured in the calorimeter with respect to the hadronic jets an average overall shift in the mean energy of 22% is observed (Figure 7.26). Our crude correction procedure is to simply multiply our uncorrected jets energies by a factor of 1.22, regardless of the position and transverse energy of the jet.

The results of the fractional differences in the cross-sections for these two studies are shown in Figures 8.14 and 8.15.

Consideration of Figure 8.14 demonstrates the importance of the checks on the model dependence, with the fluctuations reasonably large both when using PYTHIA and a constant jet energy correction. We see that when using PYTHIA

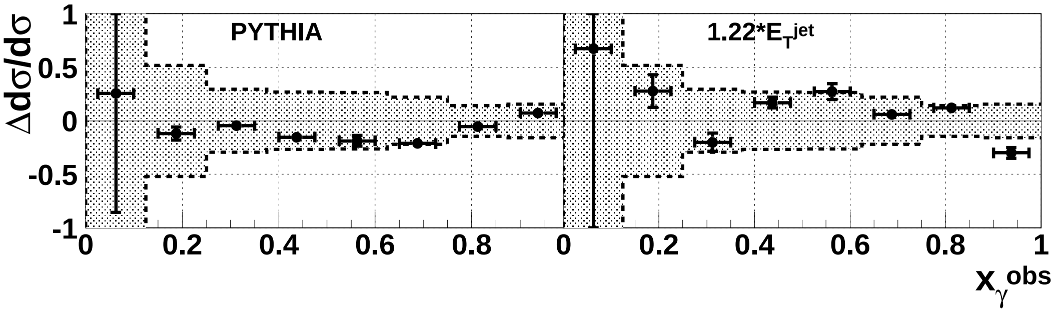

Figure 8.14: *Systematic uncertainties due to the uncertainty in the model and jet correction as a function of* $x_{\gamma}^{\mathrm{obs}}$.

the points lie below zero between bins two and seven, two of them of the order of the statistical error. This implies a larger cross-section when unfolding with the HERWIG Monte Carlo. Also of note is that the seventh bin has a smaller and the eighth bin a larger cross-section in the case of PYTHIA with respect to HERWIG. However, this is expected due to the peak in HERWIG being in the seventh and the peak in PYTHIA being the eighth bin in $x_{\gamma}^{\mathrm{obs}}$. This is a known feature of the respective Monte Carlo programs and is a problem the PYTHIA generator has in describing the data, with HERWIG providing the better description of the two.

The application of the constant jet transverse energy correction factor also exhibits reasonably large fluctuations of the order of the statistical error. The fluctuations are of a similar, if not greater, magnitude but in the opposite sense to those for PYTHIA. We therefore apply a reasonably large contribution to the systematic error for the dependence on the model.

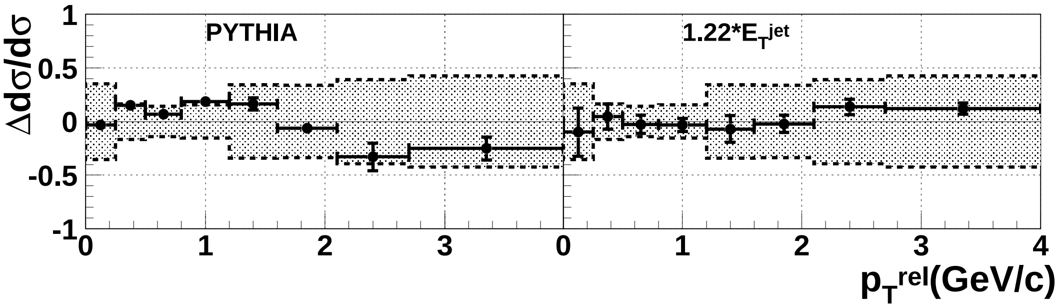

Figure 8.15: *Systematic uncertainties due to the uncertainty in the model and jet correction as a function of* p_T^{rel}.

Unfolding to the cross-section as a function of p_T^{rel} using the PYTHIA Monte Carlo also exhibits reasonably large fluctuations (Figure 8.15). The size of the fluctuations is as large as the statistical error in over half of the bins. It will be interesting to see what effect these rather large shifts have on the component of beauty required to describe the cross-section.

The constant correction factor applied to the jets yields small differences except in the last two bins and the first two. The effect is certainly smaller than in the case of the differences for the cross-section in x_γ^{obs}. The quantity p_T^{rel} is not reliant on the transverse energy of the jet, only the position of its axis, so as long as we are accepting "good" jets, the differences in the measured cross-section should only arise from the different statistical samples accepted.

The Monte Carlo (and the data) as has been said previously is an inclusive sample of decays to electrons including decays from beauty, charm and other hadrons. The goal of this analysis is to extract the actual quark content of the sample and more specifically the amount of beauty produced in the data compared to the Monte Carlo. Therefore we vary the quark content of the Monte Carlo from the nominal prediction and see if there are any systematic differences in the cross-section measurements. As the beauty content is the figure we are extracting and the value is completely unknown a sensible variation is difficult. We therefore choose situations putting upper and lower limits on the value. In the Monte Carlo we therefore require that the quark content in the hard sub-process takes the following two forms:

- All events contain beauty quarks in the hard sub-process.
- No events contain beauty quarks in the hard sub-process.

The procedure is also a test of systematic detector effects, but is not just accounting for detector anomalies. In some sense, this also represents some estimation of a theoretical error as we are then considering the physical properties of the events, the jets and the electrons themselves. For example the shape of the jets between different quarks will almost certainly be different and hence can have an effect on our ability to find the electron.

The percentage differences for the cross-sections by varying the quark content as indicated previously are shown in Figures 8.16 and 8.17.

The effect on the cross-section as a function of x_γ^{obs} in Figure 8.16 reveals reasonably large fluctuations. When excluding beauty processes from the Monte

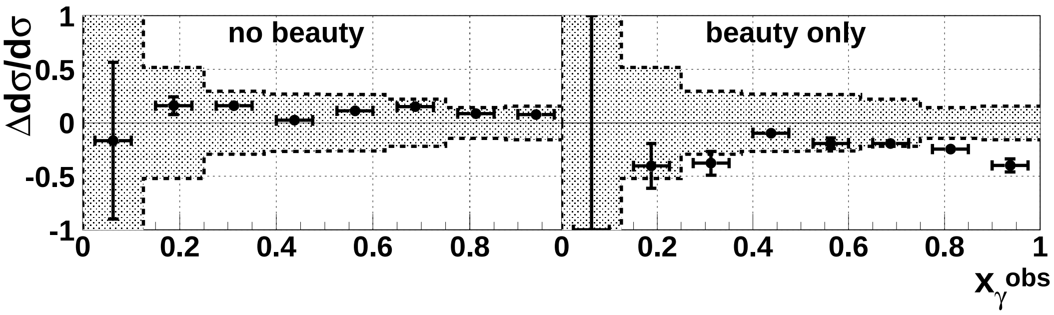

Figure 8.16: *Systematic uncertainties due to varaiation of the quark flavour in the hard sub-process as a function of* $x_\gamma^{\rm obs}$.

Carlo, the differences are slightly less marked than for the all beauty case. When there are no beauty events, there is an overall increase in the cross-section. Conversely when using Monte Carlo with beauty quarks in the hard sub-process, we obtain a lower cross-section, with every bin systematically shifted in the same direction by approximately the same value as the statistical error. The effects seen here are probably related to the properties of and our ability to reconstruct the jets themselves. A detailed study of the differences between charm and beauty jets is needed before the above can be explained. However, as the point of this analysis is to *separate*, for the first time at ZEUS, charm from beauty, then a study of them is difficult as we do not know which jets are which. The “Catch-22” [105] situation in which we are left requires further development. However we can place constraints on the measurement made, by using the above two distributions as upper and lower limits on our cross-section depending on the quark content. This will not be added in quadrature with the other errors but displayed as a separate band.

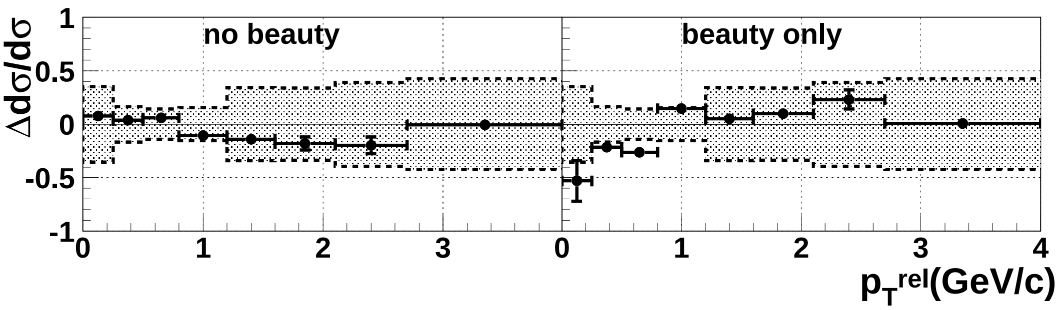

Figure 8.17: *Systematic uncertainties due to varaiation of the quark flavour in the hard sub-process as a function of* p_T^{rel}.

The effects on the p_T^{rel} distribution will be analysed more carefully and the percentage of beauty quarks found with the two distributions corrected in the different ways. As can be seen from Figure 8.17, the Monte Carlo containing no beauty produces significant fluctuations, all approximately half the size of the statistical error. The slightly higher values in the first three bins allied to the lower values in the higher bins is suggestive of a cross-section with a smaller fraction of beauty quarks than the nominal case. We will await the fit before making a more definite statement on the effect of the change.

However, the effect of using Monte Carlo from only beauty events is more transparent. The first three bins all lie well below zero, indicative of a lower cross-section in this region, and the last five all lie above zero, indicative of a higher cross-section in this region. More simply, the cross-section is lower at low p_T^{rel} (where charm and light quark decays dominate) and higher at high p_T^{rel} (where beauty decays dominate). We can also see this by comparing the correction factors of the nominal situation and the all beauty Monte Carlo situation as we do in Figure 8.18. Here we see that the correction factors for the all beauty quark sample is reasonably flat in p_T^{rel}, being significantly lower in the first three bins. The reasoning behind this is uncertain, and requires more detailed knowledge of the differences between charm and beauty decays and charm and beauty jets. The effect could also be due to the migrations of events between bins. The high correction factors at low p_T^{rel} come from high purities in these bins which are a result of migrations from other bins. In the case of the decays from beauty quarks, the events are at higher p_T^{rel} and so do not subsequently migrate to these lower bins as often as in the charm and light quark decays. This is somewhat speculative and needs further study.

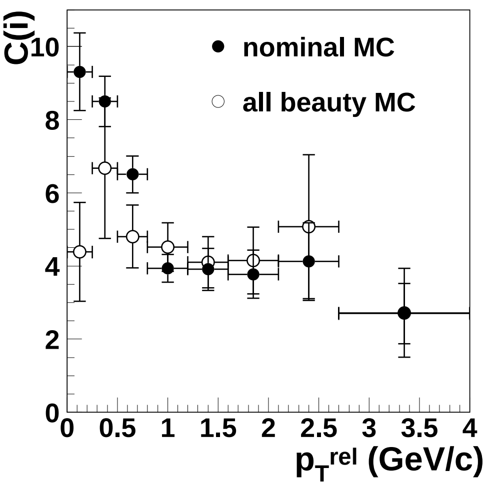

Figure 8.18: *Correction factors obtained when using the nominal Monte Carlo and when using only beauty quark Monte Carlo.*

This would suggest that unfolding with Monte Carlo containing beauty quarks in the hard sub-process increases our cross-section at high p_T^{rel} and hence our percentage component of beauty as gleaned from a fit with the Monte Carlo.

Having completed our systematic study, we will then add them to our cross-sections and in the case of the p_T^{rel} distribution analyse the consequences in depth.

8.4 Differential Cross-section Results

8.4.1 Final Cross-section for x_γ^{obs}

By considering the systematic errors, for the cross-section as a function of x_γ^{obs}, shown in Figures 8.7, 8.9 and 8.14, we add them in quadrature along with the statistical error in each bin. The resulting errors are shown as the thin, outer bars on our cross-section values in Figure 8.19, with the statistical errors shown as the thick, inner error bars. The energy scale uncertainty is shown as the lightly shaded band around the points. The error due to the uncertainty on the quark content of the Monte Carlo is shown as the darkly shaded band centred around the line at zero. The lower limit represents using Monte Carlo with only beauty quarks and the upper limit using Monte Carlo with no beauty quarks in the hard sub-process. For all three classes of error, the largest errors are in the high bins, the highest bin being particularly sensitive to the quark component in the Monte Carlo and the energy scale uncertainty. The errors on the low x_γ^{obs} points are generally small with only the fourth point having a significant (if asymmetric) error, which arises from the raising of the minimum jet transverse energy cuts.

The data is again shown compared to the area normalised hadron level Monte Carlo. The value of the direct and resolved fraction is again that from the χ^2-fit to the data obtained earlier with a value $29\pm5(stat.)\%$ for resolved processes. As was said previously we will not perform fits to all the systematic changes and determine a systematic error on the fraction of the resolved (and hence direct) component. If we performed the fits, then the value would be dictated by the seventh and particularly the eighth bins. The two high x_γ^{obs} points would change considerably whilst the low x_γ^{obs} points remain reasonably stable.

The shape of the distribution is also related to the quark component as the quark mass itself affects the distribution in x_γ^{obs}. From the definition of x_γ^{obs} (Equation (2.29)), we see that we calculate it using the pseudorapidity of the jets. However, in the case of heavy quarks we should use rapidity, particularly if we have beauty quarks. Consequently the high x_γ^{obs} peak is shifted to lower values for heavier masses. For a charm only sample of events, the peak is in the

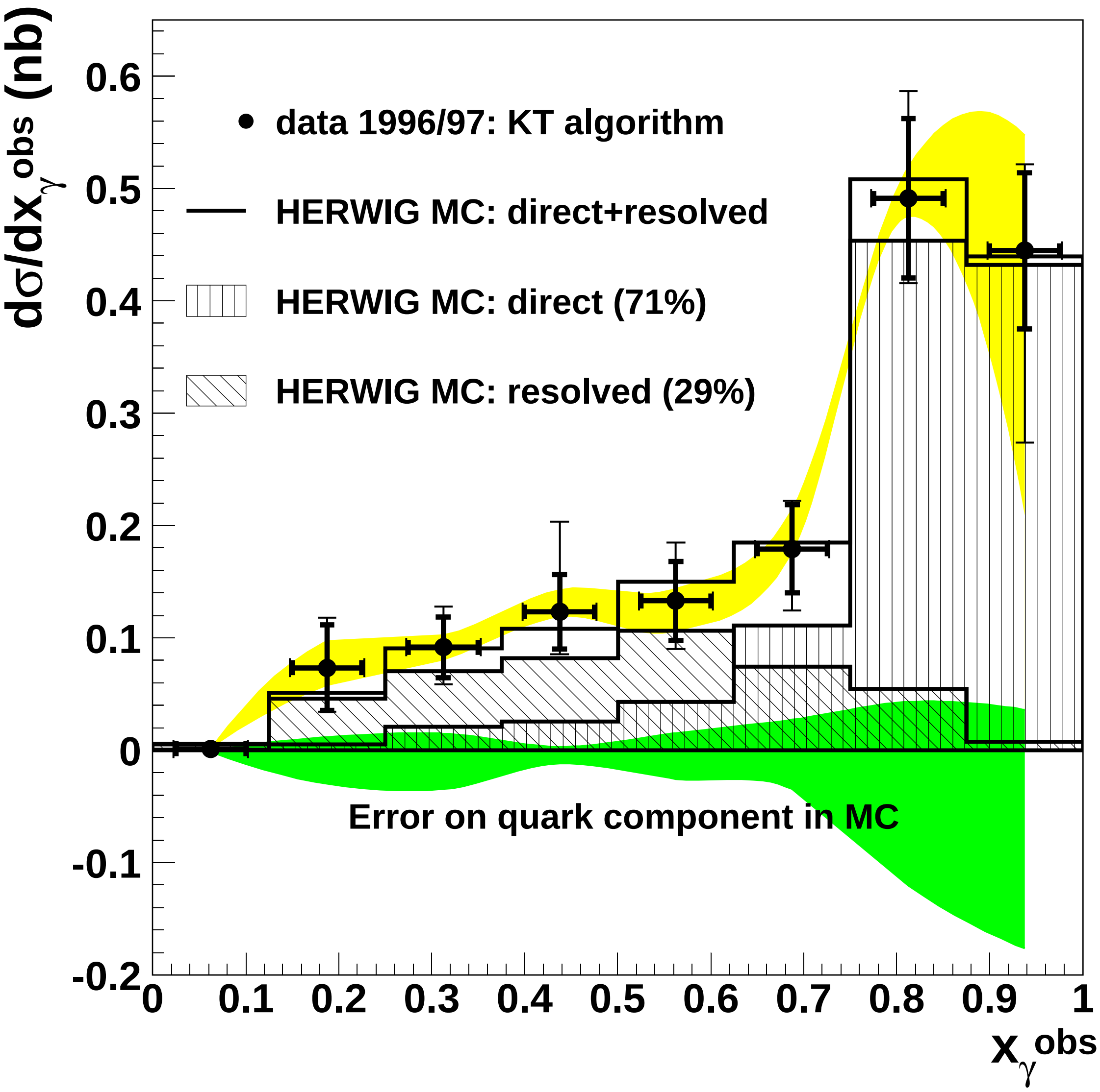

Figure 8.19: *Differential cross-section, $d\sigma/dx_\gamma^{\rm obs}$, compared to LO Monte Carlo (solid line). The contributions from direct (vertically hatched) and resolved (diagonally hatched) photon processes are shown separately. The points are shown with statistical errors (thick, inner bars) and statistical and systematic errors added in quadrature (thin, outer bars). The energy scale uncertainty is shown as the lighter band around the points. The uncertainty arising from the quark content of the hard sub-process is displayed as the darker band around the line at $d\sigma/dx_\gamma^{\rm obs} = 0$.*

seventh bin, but the seventh and eighth bins are of similar size. For a sample of only beauty events the peak is also in the seventh, but the seventh bin is much larger than the eighth. Therefore we receive the large uncertainty at high $x_\gamma^{\rm obs}$ due to different inputs of the quark content used for unfolding. We will discuss this further in the conclusions in the next Chapter.

In summary, we observe that the cross-section defined by the kinematic region in Equation (8.2) agrees well in shape with HERWIG Monte Carlo. However, an overall normalisation of ~ 2.8 needs to be applied to the Monte Carlo for the description. A component of LO resolved photon events in the Monte Carlo are required to describe the measured data. This component is predicted to be 38% by the Monte Carlo and a consistent value of 29$\pm$5(*stat.*)% is obtained when a fit to the data is performed. The systematic uncertainties are large.

8.4.2 Final Cross-section for p_T^{rel}

In the case of the cross-section as a function of p_T^{rel}, we combine the uncertainty from the quark content of the Monte Carlo into the total systematic error. Therefore we combine the errors in Figures 8.8, 8.10, 8.15 and 8.17 in quadrature with the statistical errors. The combined errors are shown as the thin, outer errors bars on our cross-section measurement in Figure 8.20 and the statistical only as the thick, inner error bars. The energy scale uncertainty is again shown as a shaded band around the points. The data is compared to the area normalised hadron level Monte Carlo with the beauty and charm plus other components shown separately where the percentages are from a χ^2-fit to the data where the amount of beauty was allowed to vary.

We combine the error from the uncertainty in the quark component as the cross-section in p_T^{rel} is being used to directly extract the ratio of quark components in the kinematic region and so cannot be ignored. The systematic errors displayed do not look as significant as in the $x_\gamma^{\rm obs}$ cross-section, but this is just an optical effect arising from the logarithmic scale. The combined total errors are in fact large in all bins. The significant bins, however, are the first three which are populated by most of the events and consequently have significant "control" over the fit. Here we observe a large lower systematic error arising primarily from the procedure of unfolding the distribution with only beauty quarks in the hard sub-process.

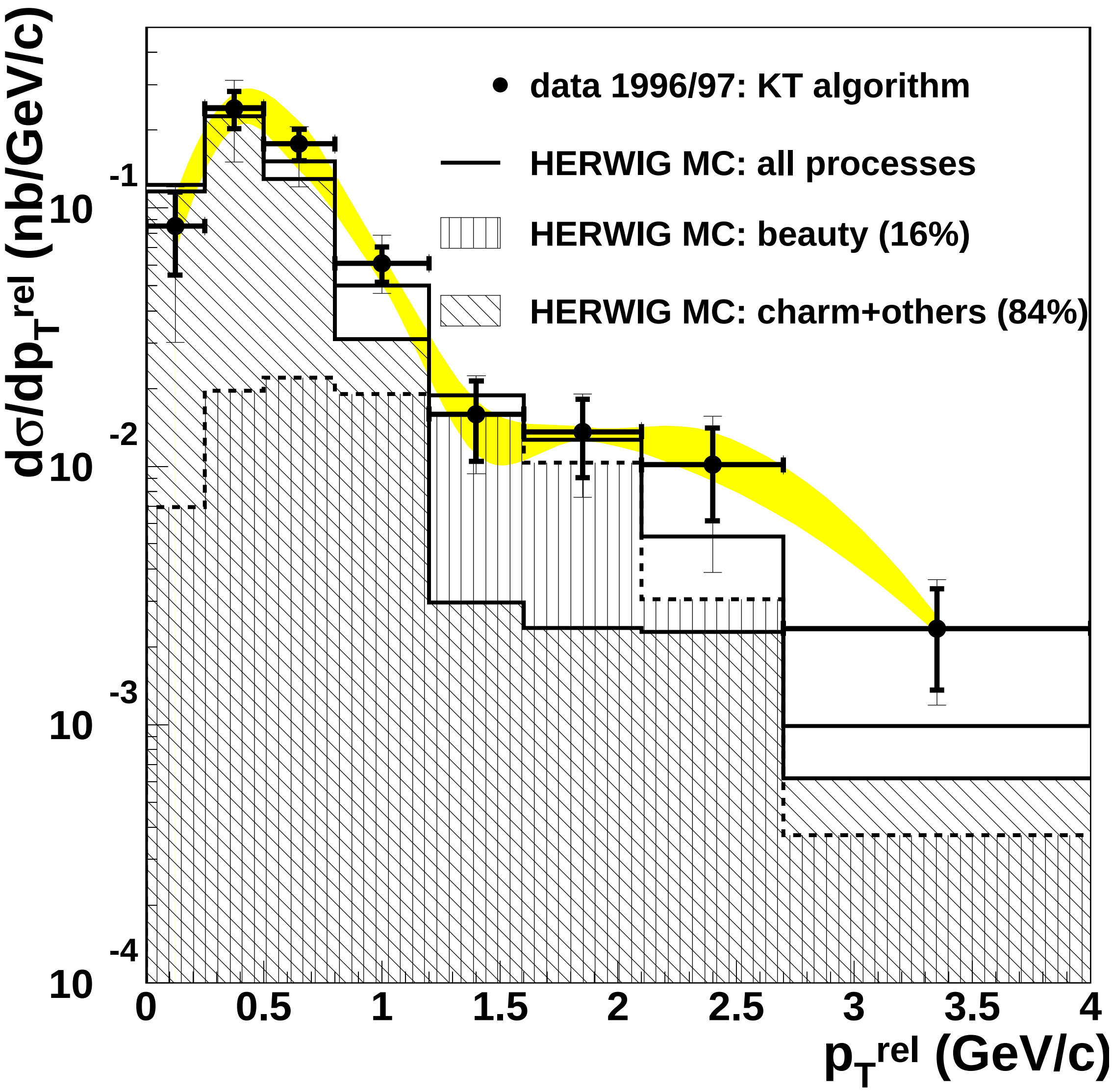

Figure 8.20: *Differential cross-section, $d\sigma/dp_T^{rel}$, compared to LO Monte Carlo (solid line). The contributions from beauty (vertically hatched) and charm+others (diagonally hatched) quarks in the hard sub-process are shown separately. The points are shown with statistical errors (thick, inner bars) and statistical and systematic (including the uncertainty from the hard sub-process quark) errors added in quadrature (thin, outer bars). The energy scale uncertainty is shown as the light band around the points.*

In summary, the differential cross-section measured is well described in shape by the HERWIG Monte Carlo, but with reasonably large errors. The Monte Carlo predicts a beauty component of 16% the same as when the Monte Carlo is fitted to the data: 16±4(*stat.*)%. The value is less than that from the fit to the uncorrected data. This arises as decays from beauty quarks have different correction factors to the other decays, but we are applying a global correction to the data. This is, however, accounted for in the systematic error by unfolding with all beauty and without beauty. This uncertainty and others will be analysed in more detail in the next section and a systematic error assigned by considering all the systematic checks performed.

8.5 Beauty Quark Contribution

We are now going to extract a systematic error on the percentage of beauty required by the Monte Carlo to describe the measured cross-section in our kinematic region. This we do by fitting the components of beauty and charm plus other in the Monte Carlo to all data cross-section results from all systematic checks. Therefore for every change which was made as a systematic check, we receive a "new" cross-section. We then refit the Monte Carlo to the "new" cross-section and receive a "new" value for the percentage of beauty. This is then compared to the central value for the percentage of beauty required and the difference of the two is our systematic error for that particular systematic check. Allied to our central percentage value, we then have sixteen subsequent values and sixteen systematic shifts *all* of which are combined to give us our total systematic error on the measurement of the percentage of beauty required by the Monte Carlo to describe the data. The results of these fits are shown in Table 8.2.

We see that the amount of beauty required in the Monte Carlo to describe the data for all the different criteria imposed in the systematic studies can vary by a large amount. Considering each new value in turn we can conclude the following. In varying the cuts on y_{JB}^{corr}, we receive small changes to our central value as was expected from the small shifts seen in Figure 8.8. Using higher (lower) minimum reconstructed jet E_T requirements has a significant effect on the value, yielding a lower (higher) percentage, the difference from the nominal value being $\sim \pm 5\%$. Each difference for changes in the method of electron extraction are small as was expected from Figure 8.10. Changing the distance of closest approach value

	charm+other	beauty		$b_{syst} - b_{nominal}$
Nominal value	**84.4±4.2%**	**15.6±4.2%**		-
Kinematic cuts				
$0.2 < y_{JB}^{corr} < 0.85$	$84.2 \pm 4.1\%$	$15.8 \pm 4.1\%$		$+0.2\%$
$0.15 < y_{JB}^{corr} < 0.8$	$85.2 \pm 4.1\%$	$14.8 \pm 4.1\%$		-0.8%
$E_T^{CORjet1,2} > 8,\ 7$ GeV	$89.1 \pm 4.2\%$	$10.9 \pm 4.3\%$		-4.7%
$E_T^{CORjet1,2} > 6,\ 5$ GeV	$79.2 \pm 4.2\%$	$20.8 \pm 4.2\%$		$+5.2\%$
Electron extraction				
$p_T^{trk} > 1.63$ GeV/c	$84.5 \pm 4.2\%$	$15.5 \pm 4.2\%$		-0.1%
$p_T^{trk} > 1.57$ GeV/c	$84.3 \pm 4.2\%$	$15.7 \pm 4.2\%$		$+0.1\%$
$dca < 25$ cm	$85.4 \pm 4.0\%$	$14.6 \pm 4.0\%$		-1.0%
$dca < 15$ cm	$84.6 \pm 4.3\%$	$15.4 \pm 4.3\%$		-0.2%
$D < 20$	$84.2 \pm 4.2\%$	$15.8 \pm 4.2\%$		$+0.2\%$
$D < 10$	$84.3 \pm 4.2\%$	$15.7 \pm 4.2\%$		$+0.1\%$
Energy scale				
cal +5%	$86.5 \pm 3.8\%$	$13.5 \pm 3.8\%$		-2.1%
cal -5%	$84.8 \pm 4.6\%$	$15.2 \pm 4.6\%$		-0.4%
Monte Carlo				
PYTHIA	$84.7 \pm 4.1\%$	$15.3 \pm 4.0\%$		-0.3%
$1.22 \times E_T^{jet}$	$85.5 \pm 4.2\%$	$14.5 \pm 4.3\%$		-1.1%
Quark content				
non beauty	$88.8 \pm 4.3\%$	$11.2 \pm 4.2\%$		-4.4%
beauty only	$72.6 \pm 6.0\%$	$27.4 \pm 6.0\%$		$+11.8\%$
Total				**+12.9%** **−7.0%**

Table 8.2: *Results of quark component fits to the cross-sections when a systematic check is made. The total systematic error and the energy scale uncertainty is also shown.*

has the largest effect of -1.0%. The uncertainty in the energy scale contributes small, but not insignificant, differences; both being in the same direction. The dependence on the model used is not large even though in the case of using PYTHIA the effect on the differential cross-section was large as was shown in Figure 8.15. The consequences of using all beauty or non beauty Monte Carlo in the unfolding procedure are significant in the final percentage. This is particularly so for the positive systematic in which we have a value $\sim 12\%$ in excess of the nominal percentage, the final value being 27.4% .

The relevance of the quark content factors and different minimum jet E_T requirements can be more clearly seen if we tabulate the percentage shifts by general category rather than individually as in Table 8.3.

	$b_{syst} - b_{nominal}$
Kinematic cuts	$^{+5.2\%}_{-4.8\%}$
Electron extraction	$^{+0.2\%}_{-1.0\%}$
Energy scale	$^{+0.0\%}_{-2.1\%}$
Monte Carlo	$^{+0.0\%}_{-1.1\%}$
Quark content	$^{+11.8\%}_{-4.4\%}$

Table 8.3: *Results of systematic error in beauty component for each general category.*

From Table 8.3 we clearly see that the total positive error is dominated by the uncertainty in the quark content and the negative error is a consequence of the quark content and the kinematic cuts. If the quark content error were not taken into account then the total systematic error would be reasonably symmetric at about $\pm$ 5%.

The percentage of beauty component required in the Monte Carlo to describe the data is,

$$\%\text{beauty} = 15.6 \pm 4.2 (stat.)^{+12.9}_{-7.0} (syst.)$$

If we then add the statistical error in quadrature with the total systematic error we receive a percentage which has a total error of $^{+13.6}_{-8.1}\%$. Therefore we have a non-zero percentage of beauty and therefore have the first indications of open beauty at ZEUS, the one sigma limits being $(7.5 < \text{beauty} < 29)\%$. When this translates into the amount of beauty measured relative to that predicted by the LO HERWIG Monte Carlo, we receive,

$$1.3 \times \text{MC} < \text{beauty} < 4.9 \times \text{MC}\ (1\sigma\ \text{range}),$$

remembering we have a normalisation factor of 2.8 and a Monte Carlo predicted value of 16.3%. These represent one sigma limits in the defined kinematic region of the beauty component from our error estimation and shows that in the data there are indications of a larger component of beauty than is predicted by the Monte Carlo. The 95% confidence level upper limit is,

$$\text{beauty} < 6.5 \times \text{MC}\ (95\%\ \text{CL}).$$

As was shown in Figure 8.18, we have inexplicable correction factors at low p_T^{rel}. We have therefore performed the analysis of the beauty component by removing the first two bins and fitting to just the region for $p_T^{rel} > 0.5$ GeV/c. We are then provided with two additional systematics of the choice of bin; that is fitting to the first and third bins. The results of the fits are shown in Table 8.4.

Using only those bins for $p_T^{rel} > 0.5$ GeV/c demonstrates a more stable systematic error as a fraction of the total value. This improvement however, is not so marked when one considers the reasonably large systematic errors from the choice of bin and the increased statistical error. It should be noted that the Monte Carlo predicts a beauty component of 24.4%. Adding the statistical to the systematic error in quadrature, we then have one sigma limits on the amount of beauty relative to the Monte Carlo:

$$0.87 \times \text{MC} < \text{beauty} < 3.9 \times \text{MC}(1\sigma\ \text{range}),$$

which gives us slightly tighter limits, than when the fit to the whole range is performed. The slight improvement in error is not sufficient however for us to prefer this result. We therefore revert back to our previous beauty component.

In summary, we have the first *indications of open beauty* at ZEUS but with reasonably large limits, the central value being consistent with the percentage predicted by LO Monte Carlo but requiring a scaling factor of ~ 2.7.

	charm+other	beauty		$b_{syst} - b_{nominal}$
Nominal value	**81.0±7.3%**	**19.0±7.3%**		-
Kinematic cuts				
$0.2 < y_{JB}^{corr} < 0.85$	$79.5 \pm 7.3\%$	$20.5 \pm 7.3\%$		$+1.5\%$
$0.15 < y_{JB}^{corr} < 0.8$	$83.4 \pm 7.0\%$	$16.6 \pm 7.0\%$		-2.4%
$E_T^{CORjet1,2} > 8$, 7 GeV	$83.5 \pm 8.4\%$	$16.5 \pm 8.4\%$		-3.5%
$E_T^{CORjet1,2} > 6$, 5 GeV	$76.4 \pm 6.8\%$	$23.6 \pm 6.8\%$		$+4.6\%$
Electron extraction				
$p_T^{trk} > 1.63$ GeV/c	$80.6 \pm 7.3\%$	$19.4 \pm 7.3\%$		$+0.4\%$
$p_T^{trk} > 1.57$ GeV/c	$80.4 \pm 7.4\%$	$19.6 \pm 7.4\%$		$+0.6\%$
$dca < 25$ cm	$81.0 \pm 7.2\%$	$19.0 \pm 7.2\%$		0.0%
$dca < 15$ cm	$82.4 \pm 7.4\%$	$17.6 \pm 7.4\%$		-1.4%
$D < 20$	$81.3 \pm 7.3\%$	$18.7 \pm 7.3\%$		-0.3%
$D < 10$	$79.7 \pm 7.4\%$	$20.3 \pm 7.4\%$		$+1.3\%$
Energy scale				
cal +5%	$84.3 \pm 6.7\%$	$15.7 \pm 6.7\%$		-3.3%
cal -5%	$80.9 \pm 8.1\%$	$19.1 \pm 8.1\%$		$+0.1\%$
Monte Carlo				
PYTHIA	$81.2 \pm 7.0\%$	$18.8 \pm 7.0\%$		-0.2%
$1.22 \times E_T^{jet}$	$81.9 \pm 7.6\%$	$18.1 \pm 7.6\%$		-0.9%
Quark content				
non beauty	$87.4 \pm 7.6\%$	$12.6 \pm 7.6\%$		-6.4%
beauty only	$71.0 \pm 9.3\%$	$29.0 \pm 9.3\%$		$+10.0\%$
bin change				
$p_T^{rel} > 0.25$ GeV/c	$84.7 \pm 4.6\%$	$15.3 \pm 4.6\%$		-3.7%
$p_T^{rel} > 0.75$ GeV/c	$73.0 \pm 16.6\%$	$27.0 \pm 16.6\%$		$+8.0\%$
Total				$\mathbf{+13.8\%}$ $\mathbf{-9.3\%}$

Table 8.4: *Results of quark component fits to the cross-sections for $p_T^{rel} > 0.5$ GeV/c when a systematic check is made. The total systematic error and the energy scale uncertainty is also shown.*

Chapter 9

Summary and Conclusions

In this thesis we have performed two analyses of heavy quarks; the first concentrating on open charm and the second on open beauty production. We will now try and summarise the measurements and their consequences. Allied to this we will also note future measurements of interest to increase our understanding of open heavy quark production.

9.1 Dijets with Tagged D^* Meson Analysis

In Chapter 6, we considered dijet photoproduction events containing a reconstructed D^* meson. The cross-section $d\sigma/dx_\gamma^{\rm obs}$ was measured in the kinematic region given by Equation (6.4). The data displayed a peak at high $x_\gamma^{\rm obs}$, consistent with direct photon processes, and a significant cross-section at low $x_\gamma^{\rm obs}$. The data was compared to LO HERWIG Monte Carlo predictions. Using only direct photon processes in the Monte Carlo did not provide a large enough cross-section at low $x_\gamma^{\rm obs}$. A component of resolved photon processes was required to describe the low $x_\gamma^{\rm obs}$ region. The amount of resolved processes predicted by a χ^2-fit to the data was 43±5%, in reasonable agreement with the HERWIG predicted value of 37%. The discussion of the fit is only with respect to the shape and does not rely on the absolute cross-section prediction. In fact, the Monte Carlo prediction lies below the data in its absolute value and is scaled by ~ 2.6 to describe the data.

Therefore, within LO QCD, we have a significant amount of resolved processes in charm photoproduction. The generally assumed fact that resolved processes are sub-dominant, with direct boson-gluon fusion processes dominating is therefore not true. From our LO description, we can then ask what are the LO resolved processes contributing to the total prediction. Do we simply have gluon-gluon fusion processes producing charm in the hard sub-process or are there so-called "excitation" processes present where we have charm in the photon? By looking at the hard sub-process in the Monte Carlo, we can determine the relative contribution of each process. The contribution from excitation processes is ~ 0.93 of the total sample indicating their existence, at least at LO. At LO, we are heavily dependent on the factorisation scale which then influences the production processes. As was stated in Chapter 5, the factorisation scale is set to be of the order of the scale of the hard sub-process and the possibility of excitation processes is dependent on the E_T^2 of our final state. In our measurement, we were studying jets with a minimum cut-off, $E_T^{jet} > 6$ GeV, showing that $E_T^2 \gg m_c^2$. To make firmer conclusions on the nature of the processes involved, we need to compare to higher order calculations or produce other measurements. We will first discuss moving to higher order predictions and discuss future measurements in the final section.

As was earlier discussed, there is an ambiguity between LO resolved and NLO direct, so what we refer to as resolved photon processes could simply be NLO direct processes. An NLO prediction compared to the data would then more solidly demonstrate that we have resolved charm production. In [50], a massive [39] NLO calculation was found to lie below the data for low $x_\gamma^{\rm obs}$. In the calculation, charm is generated in the hard sub-process and is not an active flavour in the parton densities. Large logarithms in p_T^2/m_c^2 are not resummed and may be significant. A massless calculation would be expected to provide a better description of the cross-section. In summary, the NLO prediction [39] provokes more questions than are answered and we await further developments.

9.2 Dijets with Electrons in the Final State

The cross-sections $d\sigma/dx_\gamma^{\rm obs}$ and $d\sigma/dp_T^{rel}$ were measured for dijet photoproduction events with an associated electron. For the cross-section as a function of $x_\gamma^{\rm obs}$ we again observe a peak at high $x_\gamma^{\rm obs}$ consistent with direct photon processes and a significant cross-section at low $x_\gamma^{\rm obs}$. As was observed in the D^* analysis, the Monte Carlo predictions give a good description of the data. Again, direct photon processes on their own cannot describe the observed low $x_\gamma^{\rm obs}$ cross-section. From a χ^2-fit, we require a component of resolved; 29±5%, which is again in reasonable agreement with the Monte Carlo prediction of 38%. The Monte Carlo was again significantly scaled up to match the data by ~ 2.8.

Consideration of the cross-section in p_T^{rel} allows us to compare the amount of beauty decays required to describe the data with the Monte Carlo prediction. A χ^2-fit to the data yielded a value of 16±4%, consistent with the Monte Carlo predictions. A full systematic study was performed and error on this value found:

$$\%\text{beauty} = 15.6 \pm 4.2\,(stat.)^{+12.9}_{-7.0}\,(syst.).$$

Coupled with the Monte Carlo prediction of 16.3% and the normalisation factor of ~ 2.8, this means the amount of beauty measured compared to the Monte Carlo is in the one sigma limit,

$$1.3 \times \text{MC} < \text{beauty} < 4.9 \times \text{MC} \ (1\sigma \text{ range}).$$

With this measurement, we have the first indication of open beauty at ZEUS, the value being more than predicted by LO Monte Carlo.

We then would like to consider these results in the context of the preliminary results from the H1 collaboration [66]. However, any direct comparison is difficult for a number of reasons which are now detailed. The results shown in this thesis are in a dijet kinematic region, whereas those from the H1 collaboration extrapolate out of the jet region. This can then influence any conclusions when one one considers the following two points:

- HERWIG requires a normalisation factor of 1.8 in inclusive dijet photoproduction [27].
- HERWIG requires a normalisation factor of 2.6 in charm dijet photoproduction [103].

These points indicates that the factor of 2.7 required by HERWIG for open beauty dijet photoproduction is not so remarkable. The Monte Carlo used by the H1 collaboration also contains only direct photon processes, where a resolved component for heavy quark production is clearly shown in this thesis. Clearly more work is needed for a comparison between experiments.

Further studies of open beauty production would prove difficult with the current statistics, but unfolding to a $b\bar{b}$ cross-section (with large errors) maybe possible and hence a comparison to NLO predictions.

As we have a first indication of open beauty production in our events, we should consider the massless nature of our jets. We can see in Figure 9.1 an effect of the mass of the quark in the calculation of x_γ^{obs}. Our jets are assumed to be massless and we use an appropriate massless recombination scheme. We see that for beauty production the events are shifted to lower x_γ^{obs} than for charm. The mass of the quark does not seem to effect the distribution in the case of the charm as its mass is one-third that of beauty. Changing the definition of x_γ^{obs} is not actually necessary unless we want to cut on the quantity, and is also not trivial. We could take into account the mass by considering massive jets and not the massless approximation of using transverse energy and pseudorapidity. However, simply changing this also requires us then to change the recombination scheme of the jet algorithm. This discussion does not effect our measurement and for purposes of cross-sections our x_γ^{obs} is still valid, but its appropriateness for heavy quarks is an interesting subject.

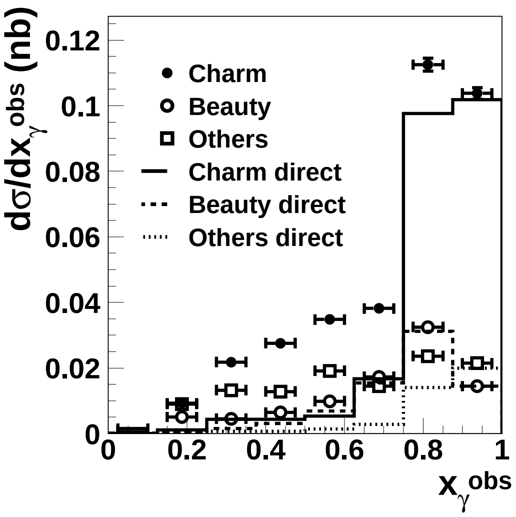

Figure 9.1: *Comparison of x_γ^{obs} for charm, beauty and light quark production.*

9.3 Future Prospects

From these results we see that the study of heavy quarks in dijet photoproduction is yielding interesting results and other measurements are now possible. With our clean sample of charm events provided by our sample of D^* meson events, we can measure charm jet cross-sections as has been done for inclusive jet measurements. Comparing these cross-sections to NLO massive and massless predictions would be instructive in developing a “best” way to consider charm production. Of particular interest is a measurement of jet shapes which could reveal which are the dominant resolved processes. As gluon-gluon fusion leads to two quarks jets and charm excitation has a charm and gluon jet, by considering the D^* tagged and other jet we may be able to discern which process is the dominant.

The beauty indication, would then ideally be extended to a measurement. Once a measurement has been achieved then further properties of beauty jet production could be discerned. By cutting on, for example, high p_T^{rel} we could isolate a beauty enriched sample with a reasonably small background from charm and light quarks. With our current method and acceptance for beauty quarks, detailed jet analyses would prove difficult. With the proposed HERA and ZEUS upgrades for the interaction region [106], there will be a significant increase in luminosity. Allied to these upgrades, the installation of a microvertex detector [107] will allow us to tag secondary vertices allowing us another method for the detection of decays of heavy quarks.

Preliminary Monte Carlo studies of heavy quark jets with the upgrades and inclusion of the microvertex detector have demonstrated that many interesting measurements could be made [108]. Coupling the detection of secondary vertices with current methods should lead to a greatly increased statistical sample and hence a deeper understanding of heavy quarks in photoproduction and the photon structure.

Acknowledgements

For his supervision and advice during this doctorate, I would like to thank Jon Butterworth. Both Mark Hayes and Mark Sutton, with whom I closely worked, also contributed much to my understanding. Other people who helped during the three years are Costas Foudas, Tegid Jones and John Lane.

Appendix A

Error calculation for number of electrons

For a given bin in track transverse momentum and pseudorapidity, we have x electron enriched tracks and y hadron enriched tracks above $dE/dx = 1.4$ mips, resulting in a total number of tracks, N;

$$N = x - f \cdot y,$$

where f is the normalisation factor which is given by:

$$f = \frac{x_1}{y_1},$$

where x_1 and y_1 are the number of electron and hadron enriched tracks in the normalisation region $0.5 < dE/dx < 1.1$ mips respectively. If we write $z = f \cdot y$, the error on the total σ_N is given by,

$$\sigma_N = \sqrt{\sigma_x^2 + \sigma_z^2},$$

where,

$$\sigma_z^2 = \left(\frac{\partial z}{\partial x_1}\sigma_{x_1}\right)^2 + \left(\frac{\partial z}{\partial y_1}\sigma_{y_1}\right)^2 + \left(\frac{\partial z}{\partial y}\sigma_y\right)^2$$

$$= \left(\frac{y}{y_1}\right)^2 x_1 + \left(\frac{-x_1 y}{y_1^2}\right)^2 y_1 + \left(\frac{x_1}{y_1}\right)^2 y$$

$$= y^2\left(\frac{x_1}{y_1^2} + \frac{x_1^2}{y_1^3}\right) + \frac{x_1^2}{y_1^2} y,$$

where Poisson errors have been assumed such that, $\sigma_{x_1}^2 = x_1$, $\sigma_{y_1}^2 = y_1$ and $\sigma_y^2 = y$.

$$\Rightarrow \sigma_N = \sqrt{x + \frac{x_1^2}{y_1^2} y + y^2\left(\frac{x_1}{y_1^2} + \frac{x_1^2}{y_1^3}\right)}. \tag{A.1}$$

If we then consider that the total signal, N_{tot} consists of i bins, each subject to Equation (A.1), we then have,

$$N_{tot} = \sum_i N_i.$$

The error on our total signal is therfore,

$$\sigma_{N_{tot}} = \sqrt{\sum_{i=1}^{16}\left[x + \frac{x_1^2}{y_1^2} y + y^2\left(\frac{x_1}{y_1^2} + \frac{x_1^2}{y_1^3}\right)\right]_i}. \tag{A.2}$$

Bibliography

[1] The ZEUS Detector Status Report 1993, DESY 1993.

[2] B. Foster et al., Nucl. Instrum. Methods, **A338** (1994) 254.

[3] G. F. Hartner, Y. Iga, J. B. Lane, N. A. McCubbin, "VCTRAK (3.06/20): Offline Output Information", ZEUS Note 96-013, 02/96.
G. F. Hartner, Y. Iga, J. B. Lane, N. A. McCubbin, M. Wing, "VCTRAK (3.07/04): Offline Output Information", ZEUS Note 97-064, 09/97.

[4] G. F. Hartner, "VCTRAK Briefing: Program and Math", ZEUS Note 98-058, 08/98.

[5] W. Verkerke, Minutes of Tracking Meeting, 8 May 1996.

[6] M. Derrick et al., Nucl. Instrum. Methods, **A309** (1991) 77.
A. Andresen et al., Nucl. Instrum. Methods, **A309** (1991) 101.
B. Bernstein et al., Nucl. Instrum. Methods, **A336** (1993) 23.

[7] P. de Jong, "Status of the Uranium Calorimeter Reconstruction Software", ZEUS Note 92-019 02/92.

[8] F. Sciulli, B. Straub, L. Wai, "Search for an 0(100 GeV) Mass Right-Handed Electron Neutrino with the 1993 and 1994 ZEUS Data", ZEUS Note 95-140, 10/95

[9] H. Beier, A. Caldwell, "Track-CAL Matching with Parametrized CAL Resolution and Inactive Material Effects", ZEUS Note 95-040.
H. Beier, "Update of the MATSCH Package", ZEUS Note 96-107.

[10] H. Bethe, W. Heitler, Proc. Roy. Soc., **A146** (1934) 83.

[11] W. H. Smith et al., "The ZEUS Trigger System", ZEUS Note 89-084.

[12] H. A. J. R. Uijterwaal, “The Global Second Level Trigger”, Ph.D. Thesis, University of Amsterdam, 1992.

[13] B. R. Martin, G. Shaw, “Particle Physics”, Wiley 1992.

[14] R. P. Feynman, Phys. Rev. Lett. **23** (1969) 1415.

[15] D. H. Perkins, “Introduction to High Energy Physics”, Addison Wesley (1987)

[16] T. Eichten et al., Phys. Lett. **B46** (1973) 274.

[17] TASSO Collab., R. Brandelik et al., Phys. Lett. **B86** (1979) 243.

[18] H1 Collab., I. Abe et al., Nucl. Phys., **B407** (1993) 515.
ZEUS Collab., M. Derrick et al., Phys. Lett., **B316** (1993) 412.

[19] V. N. Gribov, L. N. Lipatov, Sov. J. Nucl. Phys., **15** (1972) 438.
L. N. Lipatov, Sov. J. Nucl. Phys., **20** (1975) 96.
Y. L. Dokshitzer, Sov. Phys. JETP, **46** (1977) 641.
G. Altarelli, G. Parisi, Nucl. Phys., **B126** (1977) 298.

[20] Y. Balitsky, L. N. Lipatov, Phys. Rev. Lett., **28** (1978) 822.
E. A. Kuraev, L. N. Lipatov, V. S. Fadin, Phys. Rev. Lett. **44** (1976) 443.
E. A. Kuraev, L. N. Lipatov, V. S. Fadin, Phys. Rev. Lett. **45** (1977) 199.

[21] C. F. Weizsäcker, Zeits. f. Phys., **88** 612.
E. J. Williams, Proc. Roy. Soc. London, **A139** (1933) 163.
E. J. Williams, Phys. Rev., **45** (1934) 729.

[22] R. J. De Witt, L. M. Jones, J. D. Sullivan, D. E. Willen, H. W. Wyld, Phys. Rev. **D19** (1979) 2046.

[23] J. F. Owens, Phys. Rev. **D21** (1980) 52.

[24] H1 Collab., T. Ahmed et al., Phys. Lett. **B297** (1992) 205.
ZEUS Collab., M. Derrick et al., Phys. Lett. **B297** (1992) 404.

[25] ZEUS Collab., M. Derrick et al., Phys. Lett. **B322** (1994) 287.

[26] ZEUS Collab., M. Derrick et al., Phys. Lett. **B348** (1995) 665.

[27] ZEUS Collaboration; J.Breitweg et al. The European Physical Journal **C1** (1998) 109-122.

[28] ZEUS Collab., M. Derrick et al., Phys. Lett. **B384** (1996) 401.

[29] S. Frixione et al. “Heavy-Quark Production”, hep-ph/9702287.

[30] NA14/2 Collab., M. P. Alvarez et al., Zeits. f. Phys., **C60** (1993) 53.

[31] G. Bellini, Proc. of Les Rencontres de Physique de la Vallée d’Acoste, La Thuille, 1994.

[32] E691 Collab., J. C. Anjos et al., Phys. Rev. Lett., **62** (1989) 513.
E691 Collab., J. C. Anjos et al., Phys. Rev. Lett., **65** (1990) 2503.

[33] R. K. Ellis, P. Nason, Nucl. Phys., **B312** (1989) 551.

[34] S. Dawson, P. Nason, R. K. Ellis, Nucl. Phys., **B303** (1988) 607.

[35] G. Altarelli, Phys. Rep., **81** (1982) 1.

[36] Ya. I. Kogan, M. A. Shifman, Yad. Fiz. **38** (1983) 1045.

[37] W. Beenakker, H. Kuijf, W. L. van Neerven, J. Smith, Phys. Rev. **D40** (1989) 54.

[38] M. L. Mangano, P. Nason, G. Ridolfi, Nucl. Phys., **B373** (1992) 295.

[39] S. Frixione et al., Phys. Lett., **B348** (1995) 633.
S. Frixione et al., Nucl. Phys., **B454** (1995) 3.

[40] B. A. Kniehl et al., Zeits. f. Phys. **C76** (1997) 677.
J. Binnewies et al., DESY 97-241, hep-ph/9712482, Phys. Rev. D (1998) in print.

[41] J. Binnewies et al., Zeits. f. Phys. **C76** (1997) 677.

[42] M. Cacciari, M. Greco, Phys. Rev. **D55** (1997) 7134.
M. Cacciari, M. Greco, S. Rolli, A. Tanzini, Phys. Rev. **D55** (1997) 2736.

[43] M. Drees, R. M. Godbole, Phys. Rev., **D39** (1989) 169.

[44] R. K. Ellis, Z. Kunszt, Nucl. Phys., **B303** (1988) 653.

[45] S. Frixione, M. Mangano, P. Nason, G. Ridolfi, Nucl. Phys., **B412** (1994) 225.

[46] M. L. Mangano, P. Nason, G. Ridolfi, Nucl. Phys., **B405** (1993) 507.

[47] B. Mele, P. Nason, G. Ridolfi, Nucl. Phys., **B357** (1991) 409.

[48] M. Cacciari, "Hadronic Production of Heavy Quarks", DESY 97-156, To appear in the Proceedings of the Ringberg Workshop "New Trends in HERA Physics", 25-30 May 1997.

[49] M. Cacciari, M. Greco, Zeits. f. Phys. **C69** (1996) 459.

[50] ZEUS Collaboration; J.Breitweg et al., "Measurement of inclusive $D^{*\pm}$ and associated dijet cross sections in photoproduction at HERA", DESY 98-085 (July 1998), accepted by The European Physical Journal - MS 1017

[51] H1 Collaboration, C. Adloff et al., Zeits. f. Phys., **C72** (1996) 593 .

[52] R.M. Barnett et al., Physical Review **D54** , 1 (1996) and 1997 off-year partial update for the 1998 edition available on the PDG WWW pages (URL: `http://pdg.lbl.gov/`).

[53] S. Nussinov, Phys. Rev. Lett., **35** (1975) 1672.
G. J. Feldman et al., Phys. Rev. Lett., **38** (1977) 1313.

[54] OPAL Collaboration, K. Ackerstaff et al., Euro. Phys. J., **C1** (1998) 439.

[55] R. van Woudenberg, "Study of Charm Production at HERA using the ZEUS Detector", Ph.D. Thesis, September 1995.

[56] W. Verkerke, "Measurement of Charm Production in Deep Inelastic Scattering", Ph.D. Thesis, June 1998.

[57] ZEUS Collaboration; J.Breitweg et al., Phys. Lett. **B401** (1997) 192-206.

[58] A. D. Martin, W. J. Stirling, R. G. Roberts, Phys. Lett. **B354** (1995) 155.

[59] M. Glück, E. Reya, A. Vogt, Phys. Rev. **D46** (1992) 1973. M. Glück, E. Reya, A. Vogt, Phys. Rev. **D45** (1992) 3986.

[60] C. Peterson et al., Phys. Rev. **D27** (1983) 105.

[61] J. Chrin, Zeits. f. Phys. **C36** (1987) 163.

[62] CTEQ collaboration, MSUHEP-60416, CTEQ-604.
H. Lai et al., Phys. Rev. **D55** (1997) 1280.

[63] ARGUS Collab., H. Albrecht et al., Zeits. f. Phys., **C52** (1991) 353.
OPAL Collab., R. Akers et al., Zeits. f. Phys., **C67** (1995) 27.

[64] ZEUS Collaboration; J.Breitweg et al., Phys. Lett. **B437** (1998) 432.

[65] L. L. Frankfurt, M. F. McDermott, M. Strikman, "Diffractive Photoproduction of Υ at HERA", DESY 98-196.

[66] Y. Tsipolitis, "First Observation of Open b Production at HERA", Talk given at DIS98 and proceedings, Brussels, 1998.

[67] P. Nason, S. Dawson, R. K. Ellis, Nucl. Phys., **B327** (1989) 49.
erratum:
P. Nason, S. Dawson, R. K. Ellis, Nucl. Phys., **B335** (1990) 260.

[68] W. Beenakker, W. L. van Neerven, R. Meng, G. A. Schuler, J. Smith, Nucl. Phys. **B351** (1991) 507.

[69] UA1 Collab., C. Albajar et al., Phys. Lett. **B256** (1991) 121.
erratum:
UA1 Collab., C. Albajar et al., Phys. Lett. **B262** (1991) 497.

[70] CDF Collab., F. Abe et al., Phys. Rev. Lett. **71** (1993) 500.
CDF Collab., F. Abe et al., Phys. Rev. Lett. **71** (1993) 2396.
CDF Collab., F. Abe et al., Phys. Rev. Lett. **68** (1992) 3403.
CDF Collab., F. Abe et al., Phys. Rev. **D50** (1994) 4252.
CDF Collab., F. Abe et al., Phys. Rev. Lett. **69** (1992) 3704.
CDF Collab., F. Abe et al., Phys. Rev. Lett. **71** (1993) 2537.

[71] D0 Collab., S. Abachi et al., Phys. Rev. Lett. **74** (1995) 3548.
D0 Collab., S. Abachi et al., Phys. Lett. **B370** (1996) 239.

[72] S. Bentvelsen, J. Engelen, P. Kooijman, in "Physics at HERA", Vol.1, edited by W. Buchmüller, G. Ingelman (Proceedings of the Workshop, Hamburg 1991), p.23.

[73] F. Jacquet, A. Blondel, "Proceedings of the study of an *ep* facility for Europe", DESY 79-48 p.391.

[74] P. J. Bussey, EUCELL, ZEUS PHANTOM Users Library.

[75] P. de Jong, 'Status of the Uranium Calorimeter Reconstruction Software', ZEUS Note 92-019

[76] S. Catani, Yu. L. Dokshitzer and B. R. Webber, Phys. Lett. **B285** (1992) 291.

[77] S. Catani, Yu. L. Dokshitzer, M. H. Seymour, B. R. Webber, Nucl. Phys. **B406** (1993) 187.

[78] J. M. Butterworth, L. Feld, R. L. Saunders, 'Measurement of Dijet Cross Sections in Photoproduction at HERA', ZEUS Note 97-057.

[79] J. Huth et al., Proc. of the 1990 DPF Summer Study on High Energy Physics, Snowmass, Colorado, edited by E. L. Berger (World Scientific Singapore, 1992) p.134

[80] M. Seymour; pre-print hep-ph/9707349. "Jet Phenomenology". Contribution to "Proceedings of Les Rencontres de la Valee d'Acoste: Results and Perspectives in Particle Physics" La Thuile, Italy March 2-8, 1997.

[81] S. D. Ellis, D. E. Soper, Phys. Rev. **D48** (1993) 3160.

[82] GEANT 3.13, R. Brun, CERN DD/EE/84-1 (1987).

[83] ZGANA, ZEUS trigger simulation library, Els de Wolf (editor) et al.

[84] HERWIG 5.9; G. Marchesini, B. R. Webber, G. Abbiendi, I. G. Knowles, M. H. Seymour, L. Stanco, Computer Phys. Commun. **67** (1992) 465.

[85] PYTHIA 5.7; H.-U. Bengtsson, T. Sjöstrand, Computer Phys. Commun. **46** (1987) 43.

[86] B. Andersson, G. Gustafson, G. Ingelman, T. Sjöstrand, Phys. Rep. **97** (1983) 33.

[87] J. Bromley et al., “Future Physics at HERA”, Vol.1, edited by G. Ingelman, A. De Roeck, R. Klanner (Proceedings of the Workshop, Hamburg 1995/6), p.611.
see also: `http://dice2.desy.de/ h01rtc/hztool.html`

[88] M. Glück, E. Reya, A. Vogt, Zeits. f. Phys. **C53** (1992) 127.

[89] B. W. Harris, J. F. Owens, ’Photoproduction of jets at HERA in next-to-leading order QCD’, hep/ph/9704324.
B. W. Harris, private communication.

[90] C. Coldewey et al., “D* and associated dijet Photoproduction at HERA”, ZEUS Note 98-047, 07/98.

[91] M. Sutton, “Charm in Dijet Photoproduction at HERA”, Ph.D. Thesis, September 1998.

[92] `noise96s.cpp`, Noise suppression routine, PHANTOM Users Library.

[93] `calcorr.fpp`, Calorimeter correction routine, PHANTOM Users Library.

[94] J. Repond, “Jet Energy Corrections”, ZEUS Note 96-104.

[95] H. Abramowicz, A. Caldwell, R. Sinkus, “Neural Network Based Electron Idnetification in the ZEUS Calorimeter”, DESY 95-054.
R. Sinkus, Nucl. Instrum. Methods **A361** (1995) 290.

[96] S. Mengel, J. Lane, F. Corriveau, “The Magnetic Field in the ZEUS Central Tracking Region”, ZEUS Note 92-098 (06/11/92)

[97] B. Rossi; “High-Energy Particles”, Prentice-Hall (1952).

[98] H.A. Bethe; Annalen d. Physik **5** (1930) 325.
H.A. Bethe; Zeits. f. Phys. **76** (1932) 293.

[99] G.C. Wick; Ricera Scient. **12** (1941) 858.
G.C. Wick; Nuovo Cim. **1** (1943) 302.
O. Halpern and H. Hall; Phys. Rev. **73** (1948) 477.

[100] R. W. Hendricks, Rev. Sci Inst. **40** , (1969) 1216

[101] L. Köpke, R. van Woudenberg, "Photon Conversions in the ZEUS Detector", ZEUS NOTE 94-016.

[102] Y-S Tsai, Rev. Mod. Phys. **46** (1974) 815.
erratum:
Y-S Tsai, Rev. Mod. Phys. **49** (1977) 421.

[103] L. Gladilin, private communication, August 1998.

[104] ZEUS Collaboration, M. Derrick et al., Zeits. f. Phys., **C72** (1996) 399.

[105] J. Heller, "Catch-22", Jonathan Cape (1961).

[106] V. Noyes et al., "ZEUS Interaction Region Upgrade", ZEUS Note 97-035 (05/97)

[107] ZEUS Collaboration, "A Microvertex Detector for ZEUS", ZEUS Note 97-006 (01/97)

[108] G. Abbiendi, J. M. Butterworth, R. Graciani, "High p_T Charm Photoproduction", DESY 96-191.